No d'ordre : 2528

# THESE

PRESENTEE A

# L'UNIVERSITE BORDEAUX I

ECOLE DOCTORALE DES SCIENCES CHIMIQUES

Par **Chai-Won KWON**

POUR OBTENIR LE GRADE DE

# DOCTEUR

SPECIALITE : PHYSICOCHIMIE DE LA MATIERE CONDENSEE

---

## NOUVEAUX MATERIAUX D'ELECTRODES HYBRIDES OU NANOCRISTALLINS POUR BATTERIES AU LITHIUM

---

**Soutenue le 5 juillet 2002**

**Après avis de :**

| | | | |
|---|---|---|---|
| **MM. P. GOMEZ ROMERO** | Directeur de Recherche au C.S.I.C. | *Rapporteurs* |
| **D. GUYOMARD** | Directeur de Recherche au C.N.R.S. | |

**Devant la Commission d'Examen composée de :**

| | | | |
|---|---|---|---|
| **MM.** | **J. ETOURNEAU** | Professeur à l'Université de Bordeaux I | *Président* |
| | **P. GOMEZ ROMERO** | Directeur de Recherche au C.S.I.C. | *Rapporteur* |
| | **D. GUYOMARD** | Directeur de Recherche au C.N.R.S. | *Rapporteur* |
| | **M. SUBRAMANIAN** | Directeur de Recherche à DUPONT | *Examinateurs* |
| | **K. ZAGHIB** | Directeur de Recherche à Hydro-Québec | |
| | **G. CAMPET** | Directeur de Recherche au C.N.R.S. | |
| | **J. PORTIER** | Directeur de Recherche au C.N.R.S. | |
| **Mlle.** | **C. LABRUGERE** | Ingénieur de Recherche au C.N.R.S. | |

**-2002-**

# *Acknowledgements*

This work is a small but solid fruit realized in *Institut de Chimie de la Matière Condensée de Bordeaux* (I.C.M.C.B.) with aids of many splendid collaborations in the world including *Centre for Materials for Electronics Technology* (C.M.E.T.) in India, *Institute of General and Inorganic Chemistry* in Bulgaria, *Laboratoire de Chimie Organique et Organométallique* (L.C.O.O.) and *Laboratoire de Physico-Chimie Moléculaire* (L.P.C.M.) in Université Bordeaux I, and Seoul National University in Korea.

I would like to express my sincere gratitute to all jury members :

I am very grateful to monsieur J. Etourneau, *Professor à l'Université de Bordeaux I*, who offered me the opportunity to work in the I.C.M.C.B. laboratory and took charge of the *Président* in jury of my thesis.

During this study, I owe an enomous debt of the heart to my supervisor of thesis, Monsieur G. CAMPET, *Directeur de Recherche au C.N.R.S.* He is always so kind to discuss whenever I need him. I cannot overestimate his aid to be integrated in french life. In addition, he proposed many academic opportunity like participation in prestigious international meetings.

I should also convey my earnest thanks to Monsieur J. PORTIER, *Directeur de Recherche au C.N.R.S.* His wide and deep insight on materials chemistry helped me significantly to understand the electronic structure of oxides. Furthermore, I cannot forget the nice time spent at his house in Bretagne although I could not catch any fish.

I am very grateful to Monsieur P. GOMEZ ROMERO, *Directeur de Recherche au C.S.I.C.*, and to Monsieur D. GUYOMARD, *Directeur de Recherche au C.N.R.S.*, for accepting the participation in the jury of my thesis as *Rapporteurs* and *Examinateurs*. I should show appreciation to them for their careful reading and valuable comments on my thesis.

Monsieur M. SUBRAMANIAN, *Directeur de Recherche à DUPONT de Nemours*, and Monsieur K. ZAGHIB, *Directeur de Recherche à Hydro-Québec*, are gratefully acknowledged for participating in the jury as *Examinateurs* and gave me valuable advice to the point.

I would like to acknowledge Mademoiselle C. LABRUGERE, *Ingénieur de Recherche au C.N.R.S.*, for measuring XPS on numerous samples and for taking part in the jury of this thesis.

If there were not energetic cooperation and help of many colleagues, this work would not be done. Dr. T. TOUPANCE and Dr. B. JOUSSEAUME in *Université Bordeaux I*, generously gave me fluorind-doped tin oxide samples and helped me for BET measurement. Dr. R. STOYANOVA and Dr. E. ZHECHEVA in *Institute of General and Inorganic Chemistry* in Bulgaria, performed EPR experiments for my vanadium oxide samples and still keep up precious discussion. Dr. P. V. HUONG in *Université Bordeaux I*, is also deeply appreciated for his energetic cooperation and kind advice for micro-Raman experiments for manganese oxide samples. A. Vadivel MURUGAN in *Centre for Materials for Electronics Technology* (C.M.E.T.) in India, sent me the a lot of hybrid samples and our collaboration still continue. I will never forget their help and kindness.

Munificent support from many friends and colleagues in the I.C.M.C.B. laboratory also played a great part for the completion of this work. The discussion with Dr. M. H. DELVILLE, Dr. E. DUGUET and Dr. M. TREGUER-DELAPIERRE has been always useful and helpful. Dr. S. MORNET helped me to synthesize maghemite samples and Dr. F. GRASSET aided magnetism measurement. The limitless help of A. POQUET can never be appreciated enough. I believe that the memory of excellent moments spent at his house and Cognac festival with him and C. ARNAUD will give me happiness and vitality forever.

I should also truly be thankful for much help from my Korean friends and colleagues. Professor Jin-Ho CHOY, *Professor in Seoul National University*, who was the supervisor during my Master course in Korea, is gratefully acknowledged. He encouraged me to continue this study and provided opportunity to carry out spectroscopic analysis. This work may not be achieved without the help of Hyun JUNG, Hyo-Suk PARK, Jae-Up CHANG and Seung-Min PAEK. It is unquestionable that they will become excellent researchers in the field of their subject. And I also feel boundless gratefulness to my seniors, Dr. Seung-Joo KIM, Dr. Joo-Byung YOON, Dr. Seong-Ju HWANG, Dr. Young-Sik HONG and Kun-Pyo HONG, who shared and helped very much my life in France. Especially, the aids of Dr. Seung-Joo KIM, Kun-Pyo HONG and their families are extremely helpful for my daily french life.

Most importantly, the deepest thanks from the bottom of my heart should be dedicated to my parents and sister.

**Chai-Won KWON**

15th July, 2002

# *Resumé en Français*

De nos jours, le développement de la technologie nécessite un stockage avancé de l'énergie sous forme, par exemple, de batteries au lithium utilisées pour les appareils portables. Généralement on utilise comme électrodes des matériaux lamellaires bien cristallisés ($LiCoO_2$, graphite). Mais la capacité reste limitée par les matériaux d'électrodes. Il est donc nécessaire de rechercher de nouveaux matériaux en s'appuyant sur de nouveaux concepts dans le but d'augmenter cette capacité.

En conséquence, je propose trois stratégies d'étude. Elles concernent respectivement :

i) des systèmes hybrides à structure lamellaire synthétisés par intercalation de monomères organiques

ii) des hybrides constitués d'oxydes de métaux de transition enrobés par des polymères conducteurs (particules 'core-shell')

iii) des matériaux nanocristallins

Dans le cadre de la première stratégie, une nouvelle série de matériaux d'électrodes à base de poly(3,4-éthylènedioxythiophène) (PEDOT) et de $V_2O_5$ a été synthétisée par 'réaction d'intercalation et de polymérisation rédox simultanées'. La distance inter-feuillets de $V_2O_5$ augmente de 4,4 Å à 13,8 Å dans une première étape et atteint 19,0 Å dans un second stade suivant la quantité de macromolécules intercalées. Les tests électrochimiques ont montré qu'aucun changement de structure important se produit pendant l'intercalation des ions $Li^+$, contrairement à $V_2O_5$ non traité qui présente divers plateaux distincts.

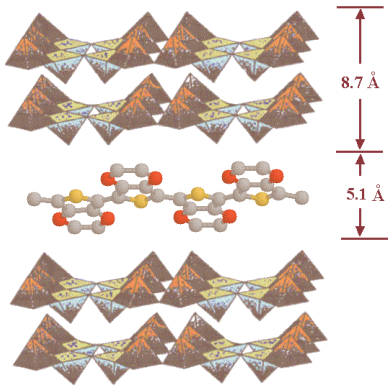


On en conclut donc que la présence des macromolécules dans l'espace inter-feuillet semble stabiliser la structure lamellaire de $V_2O_5$. Les électrodes hybrides délivrent jusqu'a 328 mAh/g entre 2 et 4,4 V vs. Li alors que $V_2O_5$ lui-même est limité à seulement à 241 mAh/g pour la seconde décharge.


La deuxième stratégie porte sur des nanohybrides de type 'core-shell', c'est à dire constitués de nanoparticules d'oxydes enrobées par des polymères conducteurs. Des nanoparticules de maghémite ont été modifiées par polymérisation du pyrrole sur leur surface. Les propriétés électrochimiques sont exaltées en raison de la présence du polymère, bien que celui ci soit présent en faible quantité (3,5% en mole) et que sa capacité électrochimique 'intrinsèque' soit faible. Le principal résultat remarquable est le changement des propriétés physiques induit par l'enrobage. La température de blocage superparamagnétique est augmentée d'environ 8 K en raison de la diminution des interactions entre les particules. La capacité électrochimique a été augmentée et atteint 270 mAh/g dans une gamme de potentiel de 1,3 à 4,3 V *vs.* $Li^+/Li$.

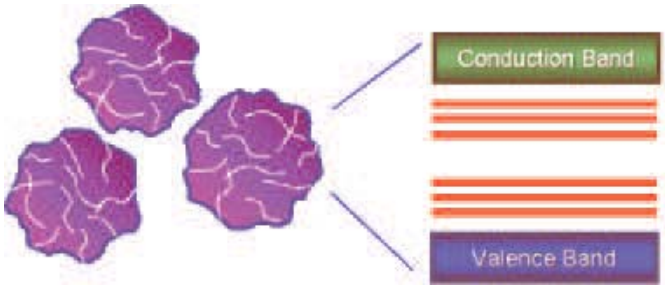


La troisième voie de recherche explore des oxydes nanocristallins originaux. Deux nouveaux matériaux d'électrode ont été mis en évidence :

- Le premier est l'oxyiodure de manganèse amorphe à base de potassium et de lithium qui délivre ~ 340 mAh/g. Cela montre la réversibilité des couples rédox $Mn^{3+/4+}$ et $Mn^{2+/3+}$. Ce résultat diffère de celui obsérvé pour les autre oxydes de manganèse pour lesquels seule la réversibilité du couple rédox $Mn^{3+/4+}$ intervient.
- Le second est l'oxyde d'étain nanocristallin dopé par le fluor préparé par thermolyse d'un xérosol dérivé d'un précurseur moléculaire original. Le rapport atomique F/Sn a été estimé par analyse élémentaire. L'état d'oxydation de l'étain et la conductivité ont été déterminés par spectroscopie Mössbauer et par mesures électriques. Les études électrochimiques ont montré une capacité réversible pouvant atteindre 800 mAh/g.

Pour expliquer le comportement électrochimique de ce genre du matériaux, un modèle schématique est suggéré : il fait intervenir le greffage réversible des ions lithium sur la surface des nanograins.

# *SOMMAIRE*


*page*

***General Introduction*** 1

==========

***Chapter 1. New Organic-Inorganic Poly(3,4-ethylenedioxythiophene)/$V_2O_5$ Hybrid as a Lithium Insertion Electrode*** 5

==========

**1-1. Introduction** 7

**1-2. Experimental Section** 10

1-2-1. Materials 10

1-2-2. Sample Preparation 11

1-2-3. Physico-Chemical Characterization 11

1-2-4. Electrochemistry 12

**1-3. Basic Characterization of PEDOT/$V_2O_5$ Hybrids** 13

1-3-1. Determination of Chemical Composition 13

1-3-2. X-ray Diffraction Study 15

1-3-3. Infrared Spectroscopy 18

1-3-4. Electron Microscopy 20

1-3-5. Electrical Conductivity 22

**1-4. Electrochemistry** 23

1-4-1. Cyclic voltammetry 25

1-4-2. Discharge/Charge Properties 27

**1-5. EPR Study of PEDOT/$V_2O_5$ Hybrids** 30

**1-6. Conclusion** 34

**1-7. References** 35

***Publications Related to Chapter 1*** 41

- "Poly(3,4-ethylenedioxythiophene)/$V_2O_5$ hybrids for lithium batteries", Electrochem. Commun. (2002), vol. 4, n° 5, pp. 384-387. 43

- "Synthesis and characterization of a new organo-inorganic poly(3,4-ethylene dioxythiophene) PEDOT/$V_2O_5$ nanocomposite by intercalation", J. Mater. Chem. (2001), vol. 11, n° 10, pp. 2470-2475. 47

- "Electrochemical lithium insertion into a poly(3,4-ethylenedioxythiophene)/ $V_2O_5$ nanocomposite", J. Power Sources (2002), vol. 105, n° 1, pp. 1-5. 53

*Chapter 2. New Organic-Inorganic Polypyrrole/$\gamma$-$Fe_2O_3$ Hybrid and Its Electrochemical Behaviors* 59

**2-1. Introduction** 61

**2-2. Experimental Section** 62

2-2-1. Materials 62

2-2-2. Sample Preparation 62

2-2-3. Sample Characterization 65

2-2-4. Electrochemistry 65

2-2-5. Magnetism Measurement 66

2-2-6. X-ray Photoelectron and X-ray Absorption Spectroscopy 66

**2-3. Results and Discussion** 67

2-3-1. Evaluation of Chemical Composition 67

2-3-2. Powder XRD Analysis 68

2-3-3. Infrared Spectroscopy 69

2-3-4. Transmission Electron Microscopy 71

2-3-5. Magnetism Measurement 73

2-3-6. Electrochemistry 75

2-3-7. X-ray Photoelectron and X-ray Absorption Spectroscopy 78

**2-4. Conclusion** 81

**2-5. References** 81

*Publications Related to Chapter 2* 85

- "A new polypyrrole/maghemite hybrid as a lithium insertion electrode", Electrochem. Commun. (2002), vol. 4, n° 2, pp. 197-200. 87

- "Conductive Polymer/Transition Metal Oxide Hybrid Materials for Lithium Batteries", Mater. Res. Soc. Symp. Proc. (2002), vol. 726, in press. 91

*Chapter 3. Nanocrystalline Materials for Lithium Batteries* 97

**3-1. Introduction** 99

3-1-1. Nanocrystalline $LiMn_2O_4$ as a Li-Insertion Electrode 100

3-1-2. Amorphous or Nanocrystalline Li-Na-Mn-O-I as a Li-Cathode 104

**3-2. New Potassium-Based Nanocrystalline Manganese Oxyiodide Cathode Prepared in Aqueous Solution** 106

3-2-1. Experimental 107

3-2-2. Powder XRD and Chemical Analysis 109

3-2-3. Electrochemical Performance 111

3-2-4. Local structure Inverstigation Using Raman

and X-ray Absorption Spectroscopy 116
3-2-5. The Role of Iodine Explored by I $L_I$-Edge XANES Analysis 125
**3-3. A New Single Morlecular Precursor Route to Fluorine-Doped Nanocrystalline Tin Oxide Anode for Lithium Batteries** 127
3-3-1. Experimental 129
3-3-2. Results and Discussion 130
**3-4. Nano-Sized Maghemite as a Lithium Insertion Electrode** 135
3-4-1. Experimental 135
3-4-2. Results and Discussion 136
**3-5. Electrochemical Grafting Model** 137
**3-6. Conclusion** 139
**3-7. References** 139

***Publications Related to Chapter 3*** 145

- "Nanocristalline materials for lithium batteries", NATO Advanced Study Institute, New Trends in Intercalation Compounds for Energy Storage, eds. Julien, C., Monchilov, A., and Pereira-Ramos, J.P., Kluwer, in press. 147

- "Local crystal structure around manganese in new potassium-based nanocrystalline manganese oxyiodide", J. Phys. Chem. B. (2002), vol. 106, n° 16, pp. 4053-4060. 160

- "Micro-Raman spectroscopic study on layered lithium manganese oxide and its delithiated/relithiated derivatives", Electrochem. Solid State Lett. (2001), vol. 4, n° 12, pp. A213-A216. 168

- "A new single molecular precursor route to fluorine-doped nanocrystalline tin oxide anodes for lithium batteries", Int. J. Inorg. Mater. (2001), vol. 3, n° 3, pp. 211-214. 172

***General Conclusion*** 177

# General Introduction

# *General Introduction*

The rapid development of modern electronic technology creates a strong demand for portable power sources. For example, popular portable electronic devices such as notebook computers, camcorders and cellular phones require small, but efficient and reliable batteries. Lithium batteries are considered to be the best choice, as they provide high output power and moderate lifetime. Generally, the lithium batteries are composed of cathode, anode, electrolyte, separator and packaging unit. Especially, electrode materials are of strong importance, because the capacity is mostly limited by the electrode materials. Traditional electrode materials are based on the redox potential difference of the electrode in the course of intercalation/deintercalation reactions. They are generally well-crystalline host compounds either with layered structure such as graphite, $LiCoO_2$ and $LiNiO_2$, or with tunnel structure like $LiMn_2O_4$. For the last decade, much effort has been made to improve the performance of the electrode materials. But, conventional synthetic methods are always restricted by the electrode material itself, and it is therefore necessary to search for new materials based on new concepts in order to increase the capacity. In this regard, we have studied three different approaches as follows :

1) bi-dimensional (lamellar) transition metal oxides intercalated by conductive polymers (intercalation strategy)

2) tri-dimensional transition metal oxide nanoparticles coated by conductive polymers (core-shell strategy)

3) nanocrystalline materials

The organic-inorganic hybrid materials are, currently, exploited by its possibility of integrating different desirable properties of organic and inorganic components in a unique material. Here we choose conductive polymers as an organic component and 3d-transition metal oxides as an inorganic counterpart. The conductive polymers have high electric conductivity but their processability and capacity are not sufficient for battery application, and most of the 3d-transition metal oxides are beneficial lithium cathodes with processability but have some shortcoming such as low conductivity and structural instability during lithium insertion/extraction.

The last strategy deals with electrochemistry of nanocrystalline materials in general. For a long time, only well crystalline materials have been considered as good electrodes for lithium-ion cells. Nanocrystalline materials are, however, being re-evaluated recently as ‘nanoscience’ advances. The electrochemistry of this kind of materials is much different from that of traditional crystalline ones because of their significant ‘surface effects’. The nanocrystalline materials are reported to have an enhanced electrochemical activity when the first electrochemical step is insertion of Li ions (discharge process). As illustrative examples, electrochemical behaviors of some nanocrystalline materials such as $\gamma$-$Fe_2O_3$, fluorine-doped tin oxide and potassium manganese oxyiodide, are presented and compared with their well-crystalline homologues. XRD, XPS and X-ray absorption spectroscopy were used as probe tools to differentiate the bulk (core) and local (surface) states. The “electrochemical grafting” concept will be given as a plausible explanation.

# Chapter 1

# New Organic-Inorganic Poly(3,4-ethylenedioxythiophene) /$V_2O_5$ Hybrid as a Lithium Insertion Electrode

## 1-1. INTRODUCTION

Recent progress in 'nano-chemistry' gives birth to a new emerging area, so-called 'hybrid' or 'nanocomposite', which is a challenge for combining properties of two or more different species into a unique material [1-4]. Especially, in the field of lithium battery application, conducting polymer/$V_2O_5$ hybrids have received a considerable attention over the past several years to integrate profitably many desirable properties of the vanadium oxide and of the polymeric counterpart [5-12]. $V_2O_5$ is one of the most beneficial lithium cathodes with processability and high capacity, whereas conducting polymers have advantages including flexibility and conductivity. In addition, from an academic point of view, there are also many interesting things to be investigated such as oxidation state of the vanadium, doping character of the polymer and the nature of interaction between the polymer and the vanadium oxide. These hybrids are generally prepared by mixing $V_2O_5$ gel with monomers of the corresponding conducting polymer such as polyaniline (PANI),

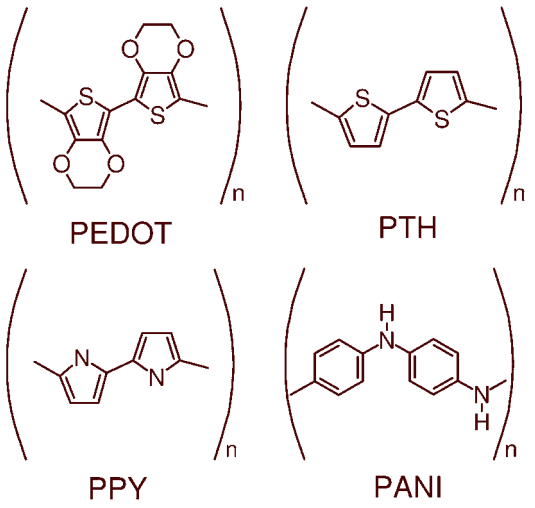


*Figure 1-1. Chemical structure of some selected conductive polymers : PEDOT (poly(3,4-ethylenedioxythiophene)), PTH (polythiophene), PPY (polypyrrole) and PANI (polyaniline).*

polypyrrole (PPY) or polythiophene (PTH) [5-15]. For some selected conducting polymers, their chemical structure is drawn in Figure 1-1.

Among them, PANI/$V_2O_5$ xerogel system is the most intensively studied one [5,6,10-15]. The reaction between aniline and $V_2O_5$ xerogel proceeds via oxidative intercalation and subsequent polymerization of the aniline monomer concomitant with the reduction of V(V) to V(IV) in the xerogel host. Kanatzidis and collaborators found that the growth of polymer goes on mainly within interlamellar space with the consumption of molecular oxygen [15]. Aging in air causes both partial reoxidation of the inorganic host, that is auto-recovery of V(V) from V(IV), and the post-polymerization of the organic intercalate. In this context, it is not surprising that the electrochemical performance of the PANI/$V_2O_5$ xerogel hybrid was found to be improved by a mild oxygen treatment. Leroux et al. could augment the lithium capacity of $PANI_{0.40}V_2O_5$ from 0.85 F/mol to 1.35 F/mol at ~ 10 mA/g after oxygen treatment at 150 °C for 8h [5,6]. They assigned this increase to the regeneration of ~ 2.9 V sites of the $V_2O_5$ host due to the recovery of $V^{5+}$. Lira-Cantú et al. optimized the oxygen treatment condition and reported that the thermal treatment under oxygen over 80 °C for more than 5h may destroy the polymer chain [10-12]. Under optimized condition, 302 mAh/g (2.72 F/mol) at ~ C/48 could be achieved. This enhancement is attributed to the evasion of the degradation of polymer chain, leading to the formation of new ~ 2.3 V-sites probably related to the polymer.

On the contrary, hybrid systems based on PPY/$V_2O_5$ or PTH/$V_2O_5$ are relatively less studied. The position of heteroatom makes distinction in chemistry and physico-chemical properties between PANI on one side and PPY or PTH on other side

[16]. The N atom of PANI is outside the ring and participates directly in the polymerization process, whereas the heteroatom N or S for PPY or PTH, respectively, is one of the ring component members and, instead, the alpha carbon takes part in the polymer linkage. Concerning PPY/$V_2O_5$ hybrids, it was reported that only a partial reoxidation was attained even after 72h $O_2$ exposure at 150 °C, and moreover the capacity decreased owing to the polymer degradation [6,7]. On the other hand, the hybrids prepared under reflux conditions have fully oxidized vanadium, and show an improved performance. To $PPY_{0.40}V_2O_5$ prepared under reflux condition, about 1.8 Li/mol could be inserted at ~ 10 mA/g.

As for the PTH/$V_2O_5$ hybrids, the thiophene monomer is not easy to insert directly into $V_2O_5$, because thiophene has a greater redox potential (~ 3.8 V vs. $Li^+$/Li) than that of $V_2O_5$ (~ 3.4 V vs. $Li^+$/Li). G. R. Goward et al. made several types of the PTH/$V_2O_5$ hybrids with bithiophene, terthiophene, 3-methyl thiophene and 2,5-methyl thiophene, and examined their electrochemical properties [7]. Regarding 3-methyl thiophene, the methylation in the 3-position facilitates α-α' coupling and thereupon more regular structure, whereas in the case of 2,5-dimethyl thiophene, α-β' or/and β-β' coupling deteriorates polymeric order, leading to a decrease in the electrochemical capacity. The hybrids made from terthiophene and 3-methyl thiophene exhibit a better capacity of ~ 0.95 Li/mol at 10 mA/g than those from bithiophene (~ 0.70 Li/mol) and from 2,5-dimethyl thiophene (~ 0.58 Li/mol). The hybrids seem to be sensitive to both polymer nature and overall order in the material. In this standpoint, poly(3,4-ethylenedioxythiophene) (PEDOT) is expected to form a hybrid system with better electrochemical properties, as its cap in 3 and 4 positions with ethylenedioxy group will

lead to a more regular polymeric order [16,17].

We have currently succeeded in the preparation of a new series of PEDOT/$V_2O_5$ [18-20]. To our knowledge, this is the first conducting polymer/$V_2O_5$ hybrid system synthesized starting with well-crystalline vanadium oxide. Furthermore, the PEDOT is probably the conducting polymer of choice, as it has been reported to exhibit excellent electrical conductivity up to 550 S/cm with air-stability superior to PANI, PPY and PTH [16,17]. We observed that these hybrids showed enhanced electrochemical capacities and that their lithium insertion behaviors were not similar to those of crystalline $V_2O_5$ but to those of other hybrid systems based on $V_2O_5$ gel. Here I will describe a systematic study of preparation, characterization and electrochemical lithium insertion into the hybrids. A special discussion will be focused on the relationship between electrochemical properties and structural formation including arrangement of vanadium oxide layers and polymer chains.

## 1-2. EXPERIMENTAL SECTION

### 1-2-1. Materials

Vanadium pentoxide (99.9 %), lithium metal foil (99.9 %), $LiClO_4$ (99.99 %), polytetrafluoroethylene (PTFE, 99.99 %), propylene carbonate (PC, 99.9 %) and dimethyl carbonate (DMC, 99%) from Aldrich were used without further purification. 3,4-ethylenedioxythiophene (EDOT, Bayer AG Germany) was distilled under vacuum prior to use. Ethylene carbonate (EC, Prolabo 99%) and ketjenblack were used as

received. All the experiments were conducted with deionized water.

### 1-2-2. Sample Preparation

The PEDOT/$V_2O_5$ hybrids were synthesized by insertion and subsequent polymerization of EDOT into $V_2O_5$. A given amount of EDOT was dissolved in 25 ml of distilled water, and this solution was mixed and refluxed with 2 g of vanadium pentoxide for 12 h. The nominal molar ratio of EDOT to $V_2O_5$ was adjusted to 0.02 (VP1), 0.04 (VP2), 0.08 (VP3), 0.40 (VP4) or 0.60 (VP5). After completion of the reaction, the solid was filtered off and washed repeatedly with water and acetone until the initial light yellow color in the filtrate disappeared totally, and the resulting bluish black powder was dried in air.

For comparison, $Cl^-$ doped PEDOT was also prepared as reported in Ref. 21. A given amount of EDOT was added in $FeCl_3$ aqueous solution at a molar ratio of $FeCl_3$ : EDOT = 2.5 : 1, and stirred during 24 hours.

### 1-2-3. Physico-Chemical Characterization

The incorporation of the polymer into the $V_2O_5$ was confirmed by powder X-ray diffractometer (Phillips PW-1050) using Ni-filtered Cu-K$\alpha$ radiation ($\lambda$ = 1.5418 Å). Fourier transform infrared (FTIR) spectra of powder samples diluted with KBr were recorded with a Bruker FTIR spectrometer in transmission mode. The variation of particle morphology upon the intercalation was monitored by a scanning electron

micrograph (SEM, Philips XL-30) or by a transmission electron microscope (TEM, JEOL 2000 FX) operating at an accelerating voltage of 200 kV. The molar fraction of polymer per $V_2O_5$ was determined by thermal analysis with a Shimadzu TGA-50 system from room temperature to 800 °C at a rate of 10 °C/min under oxygen. Electrical conductivity was measured by a conventional four-probe method using conducting silver paint for contacts. Elemental analysis was carried out using inductively coupled plasma optical emission spectroscopy (ICP-OES, Perkin-Elmer 1000) and E-Instruments-EA 1110 CHNS-O Analyser.

The EPR spectra were registered as the first derivative of the absorption signal with an ERS-220/Q spectrometer (ex-GDR) within the temperature range between 85 K and room temperature. The g-factors were established with respect to a $Mn^{2+}$/ZnS standard. The signal intensity was determined by double integration of the experimental EPR spectrum. Recordings at different microwave power were used to distinguish the EPR signals.

### 1-2-4. Electrochemistry

The electrochemical measurements were performed using button-type two-electrode cells with aid of a computer-controlled PGS201T (Tacussel) potentiostat/galvanostat system. The composite cathodes were made by intimately mixing 70% (by mass) of the active material, 25 % of Ketjenblack and 5% of PTFE. The surface area of electrodes and mass of active material were adjusted to ~ 1 $cm^2$ and ~ 20 mg respectively for reproducibility. These electrodes were dried under vacuum at ~

80 °C for more than 3 hours, and introduced into an Argon-filled glove box without any exposure to air. The electrolyte was a 1M solution of $LiClO_4$ in a 1:1 mixture (by volume) of EC/DMC. Lithium foil was used as an anode. For discharge/charge experiments, a constant current of 15 mA/g was applied between 2.0 and 4.2 V for $V_2O_5$ or between 2.0 and 4.4 V (*vs.* $Li^+/Li$) for the hybrids. For cyclic voltammetry, the voltage cycled with a sweep rate of 0.5 mV/s between 2.2 V and 3.8 V.

## 1-3. BASIC CHARACTERIZATION OF PEDOT/$V_2O_5$ HYBRIDS

### 1-3-1. Determination of Chemical Composition

As already well known in the field of intercalation chemistry, all the guest reactant would not be always intercalated into the host. The determination of chemical composition of the intercalation compounds is important for this reason. The chemical composition of the PEDOT/$V_2O_5$ hybrid samples was estimated from ICP, CHNS and thermal analysis.

Table 1-1. Results of ICP and CHNS elemental anaylsis.

| | Nominal EDOT/$V_2O_5$ ratio | C/V atomic ratio | S/V atomic ratio |
|---|---|---|---|
| VP1 | 0.02 | 0.08 | 0.00606 |
| VP2 | 0.04 | 0.129 | 0.0102 |

| | | | |
|---|---|---|---|
| VP3 | 0.08 | 0.202 | 0.0442 |
| VP4 | 0.40 | 0.659 | 0.174 |
| VP5 | 0.60 | 0.858 | 0.229 |

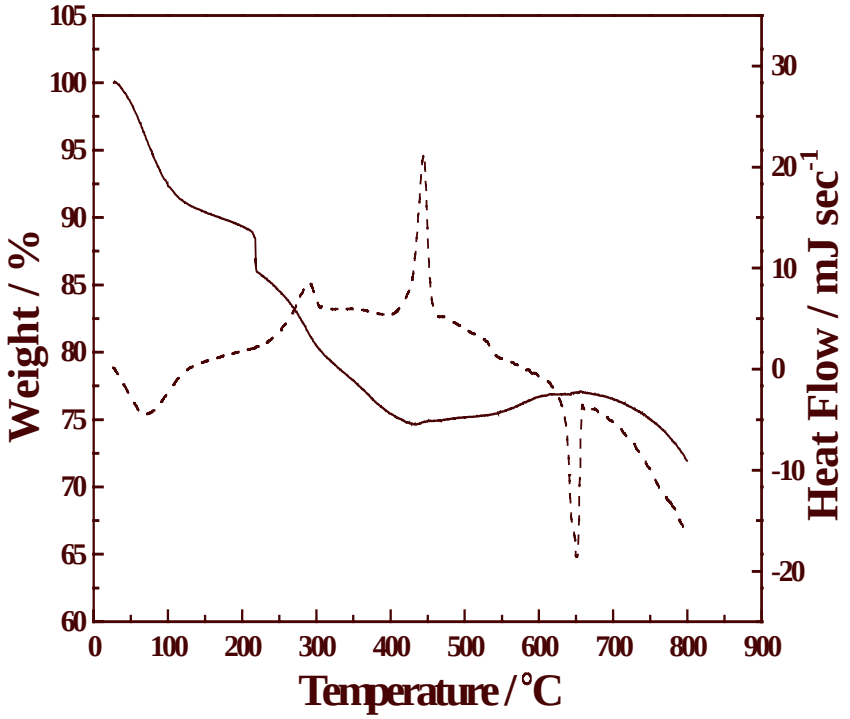


*Figure 1-2. Thermogravimetry (solid line) and differential scanning calorimetry (dashed line) curves for VP3 sample as a representive.*

Figure 1-2 presents the thermogravimetry (TG) and differential scanning calorimetry (DSC) curves of the VP3 sample as a representative. The TG curves can be divided into three temperature domains of 25~130, 130~420 and 420~650 °C.

The first step up to 130 °C, is attributed to removal of water, confirmed by the endothermic peak of the DSC curve. Next weight loss until 420 °C is due to the combustion of the polymer component, which is well corresponding to the exothermic DSC peak. The abrupt weight loss around 210 °C is assigned to the decomposition of the ethylenedioxy groups of the polymer. A mass gain to 650 °C is ascribed to the endothermic oxygen uptake, which occurs together with the conversion of $V^{4+}$ into $V^{5+}$ [6]. This result proposes that the insertion and polymerization of EDOT monomer is accompanied by a 'sacrificial' reduction of the $V_2O_5$ layers. Based on results of elemental and thermal analysis, the formula of the hybrids are evaluated and listed in Table 1-2.

Table 1-2. Nominal EDOT/$V_2O_5$ ratio and corresponding chemical composition for the hybrid samples.

| | Nominal EDOT/$V_2O_5$ | Output/Input ratio | Chemical composition* |
|---|---|---|---|
| VP1 | 0.02 | 1 | $(C_6H_4O_2S)_{0.02}V_2O_{4.9}$ |
| VP2 | 0.04 | 0.75 | $(C_6H_4O_2S)_{0.03}V_2O_{4.8}$ |
| VP3 | 0.08 | 0.625 | $(C_6H_4O_2S)_{0.05}V_2O_{4.7}$ |
| VP4 | 0.40 | 0.45 | $(C_6H_4O_2S)_{0.18}V_2O_{4.6}$ |
| VP5 | 0.60 | 0.42 | $(C_6H_4O_2S)_{0.25}V_2O_{4.6}$ |

* The surface-adsorbed water contents are ignored.

### 1-3-2. X-Ray Diffraction Study

The change of crystal structure upon the incorporation of the polymer into $V_2O_5$ was monitored by powder X-ray diffraction. Series of well-developed (00*l*) peaks can be observed, and the d-spacing increases from 4.3 Å to 13.8 Å and further to 19.0 Å depending on the amount of the incorporated macromolecules (Figure 1-3). The net interlayer expansion increases from 5.1 Å for VP1 to 10.3 Å for VP5 respectively, assuming the $V_2O_5$ slab is composed of two vanadium oxide sheets like that of vanadium oxide xerogel [22,23]. This would indicate that the expansion proceeds in two steps, first forming monolayer of polymer and then double layers. It is noted that (*hk0*) reflections of the hybrids correspond to those of the pristine $V_2O_5$ and that some of them, such as (*110*) and (*310*), show a diffuse peak shape, rising rather rapidly and then declining slowly toward high angle side. This feature suggests that the compounds have a random layer stacking structure, which consists of equidistant and parallel (*a*-*b*) layers, but randomly rotated about the normal *c*-axis [24]. Such characteristics have been already found for $V_2O_5$ compounds prepared by

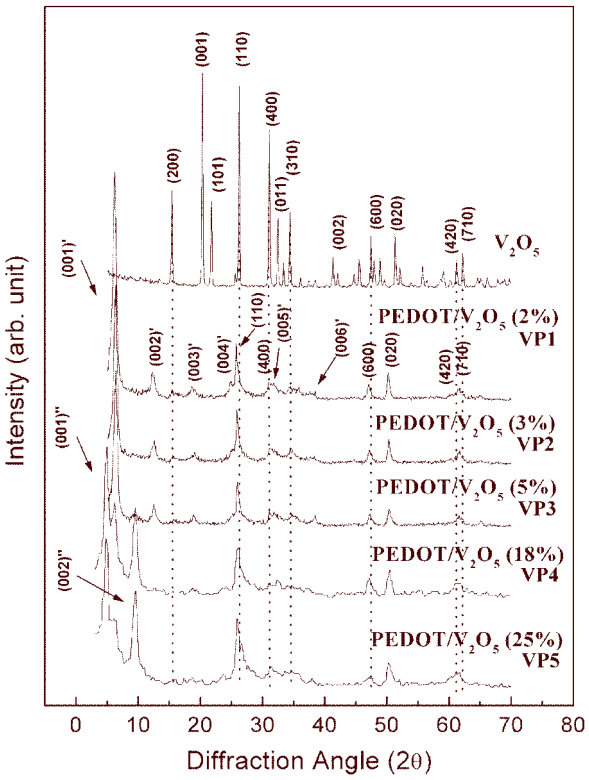


*Figure 1-3. Powder X-ray diffraction patterns of pristine $V_2O_5$, VP1, VP2, VP3, VP4 and VP5.*

electrolysis or ozone-oxidation of $VOSO_4$ or by the reaction of metallic vanadium and hydrogen peroxide [25-29]. These $V_2O_5$ compounds have so-called 'bidimensional' structure, which is stabilized by interlayer water molecules. Such structural characteristics would be similar to those of PEDOT/$V_2O_5$ hybrids, except the replacement of water molecules by hydrophobic polymer chains. For simplicity and clarity, these kinds of $V_2O_5$ will be denoted as 2D-$V_2O_5$ below. Effects of these structural properties on electrochemical behaviors will be discussed in the electrochemistry section (*vide infra*).

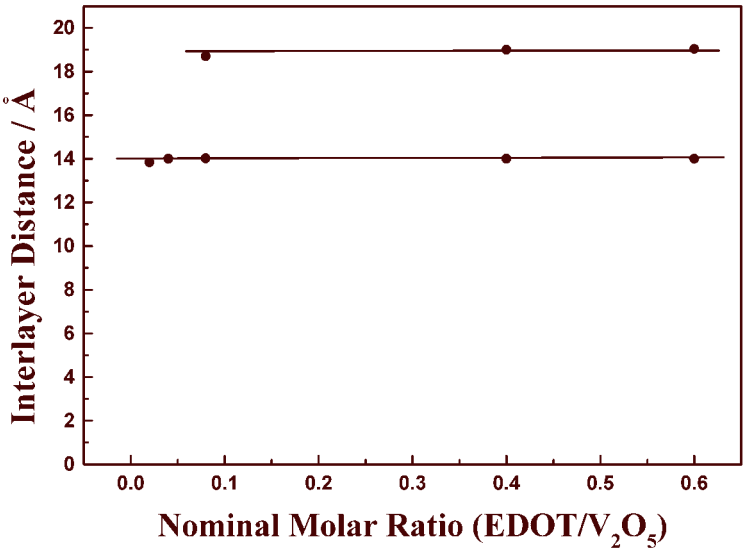


*Figure 1-4. Evolution of interlayer distance upon increasing nominal molar ratio of EDOT to $V_2O_5$.*

The details are summarized in Table 1-3 with the results of elemental analysis.

Table 1-3. Nominal EDOT/$V_2O_5$ ratio, corresponding chemical composition and d-spacing for the the pristine $V_2O_5$ and hybrid samples.

| | Nominal EDOT/$V_2O_5$ | Chemical composition | d-spacing (Å) |
|---|---|---|---|
| $V_2O_5$ | · | $V_2O_5$ | 4.37 * |
| VP1 | 0.02 | $(C_6H_4O_2S)_{0.02}V_2O_{4.9}$ | 13.8 |
| VP2 | 0.04 | $(C_6H_4O_2S)_{0.03}V_2O_{4.8}$ | 14.0 |
| VP3 | 0.08 | $(C_6H_4O_2S)_{0.05}V_2O_{4.7}$ | 14.0 |
| VP4 | 0.40 | $(C_6H_4O_2S)_{0.18}V_2O_{4.6}$ | 17.8 |
| VP5 | 0.60 | $(C_6H_4O_2S)_{0.25}V_2O_{4.6}$ | 19.0 |

* If two slabs of layer is taken as a block, the d-spacing would be ~ 8.7 Å (Ref. 22,23).

### 1-3-3. Infrared Spectroscopy

In order to examine the oxidation state of vanadium and doping state of the polymer, Fourier transform infrared (FTIR) spectra were recorded. The spectra of the hybrids shown in Figure 1-5 display the characteristic bands corresponding to both PEDOT and $V_2O_5$. Vibrations around 1520, 1450 and 1380 $cm^{-1}$ are assigned to the stretching of C=C and C-C in the thiophene ring, and those at 1130 and 1090 $cm^{-1}$ to the stretching of ethylenedioxy group (Figure 1-5a) [30-36]. These peaks increase as the amount of incorporated polymer augments, which proves the presence of the PEDOT in these materials. The absence of peak at 1490 and 1190 $cm^{-1}$ implies that the organics are not in monomer form but in polymeric form. The peaks around 1260 and 1090 $cm^{-1}$ indicate that the polymer is in doped state, leading to an increased conductivity [31,36]. The changes in position and shape of the vibrational peaks of the vanadium oxide framework are also significant.

Bands around 530 and 810 $cm^{-1}$ are attributed to V-O-V stretching modes and those

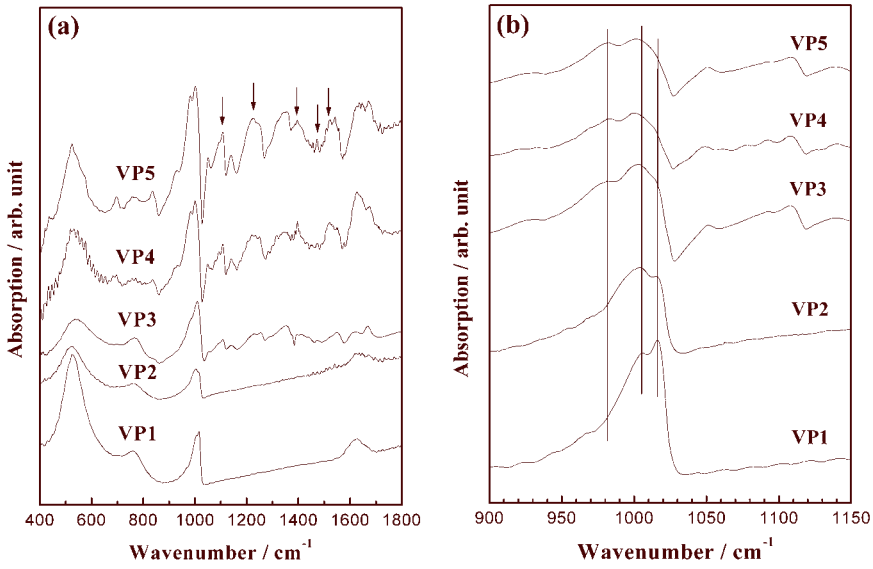


*Figure 1-5. Infrared spectra for VP1, VP2, VP3, VP4 and VP5 in the range of (a) 400~1800 $cm^{-1}$ and (b) 900~1150 $cm^{-1}$ (enlargement). The samples were diluted with KBr and pressed into a pellet. Some important peaks from polymer are marked with arrows.*

around 1000 $cm^{-1}$ to V=O stretching. Compared with well-crystalline $V_2O_5$, the V=O peak shifts from 990 to 1000 $cm^{-1}$ and the V-O-V vibrational peaks shift from 850 and 550 $cm^{-1}$ to 810 and 530 $cm^{-1}$, respectively, accounting for the greater number of $V^{4+}$ centers in the hybrids. The mechanism of this remarkable all-solid-state intra-lamellar polymerization is presumed to be coupled to the ability of vanadium centers to activate oxygen which is the primary electron acceptor in this process. Therefore, vanadium oxide plays a direct role in this redox event, which is consistent with its ability to

catalyze several oxidation reactions of organic molecules [37]. A deeper inspection finds that the 985 $cm^{-1}$ peak increases and the 1015 $cm^{-1}$ peak decreases inversely as the amount of incorporated polymer augments (Figure 1-5b), which suggests a strong interaction (*e.g.* hydrogen bonding) between vanadyl group and the incorporated polymer, like PPY/$V_2O_5$ xerogel hybrid [8].

### 1-3-4. Electron Microscopy

The influence of this modification on particle morphology was observed with scanning and transmission electron microscopy. The SEM micrograph of VP3 together with that of the pristine $V_2O_5$ is illustrated in Figure 1-6. It is apparent that the PEDOT/$V_2O_5$ hybrid forms a continuous and relatively homogeneous matrix with a clean lamellar surface, which evidences the incorporation of PEDOT into the $V_2O_5$ in agreement with the results of XRD patterns. More importantly, the SEM micrographs also suggest that there is no bulk deposition of polymer alone between the micro-crystallites. A deeper observation of particle morphology was realized using transmission electron microscopy. The pristine $V_2O_5$ consists of thick agglomerated particles with irregular sizes of micrometer order (Figure 1-7a), whereas the particles of hybrids are composed of well-developed (*a*-*b*) planes stacked along with c-axis (Figure 1-7b-d). The stacking length in *c*-direction is much shorter compared with *a* and *b* directions for the hybrids, which would be considered as the enhancement of 'bidimensionality'. The interlayer spacing of VP1 has been estimated by measuring the

length from one dark line to the nearest one, which gives ~14 Å in good agreement with XRD result.

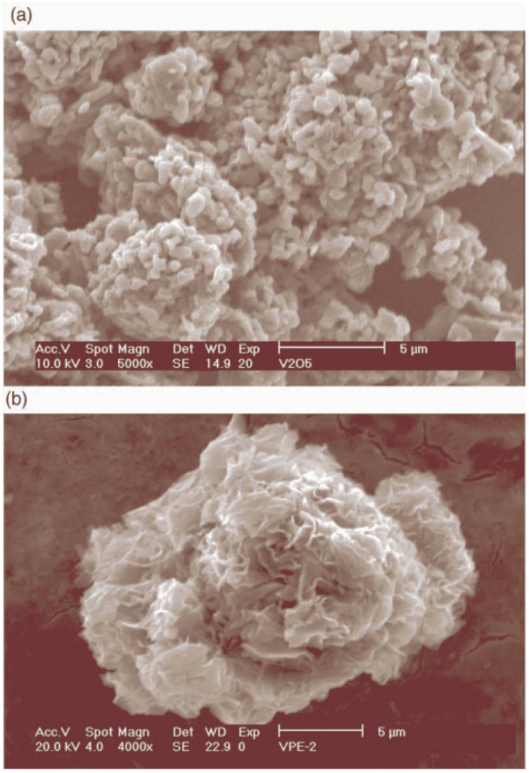


*Figure 1-6. SEM micrographs of (a) pristine $V_2O_5$ and (b) VP3.*

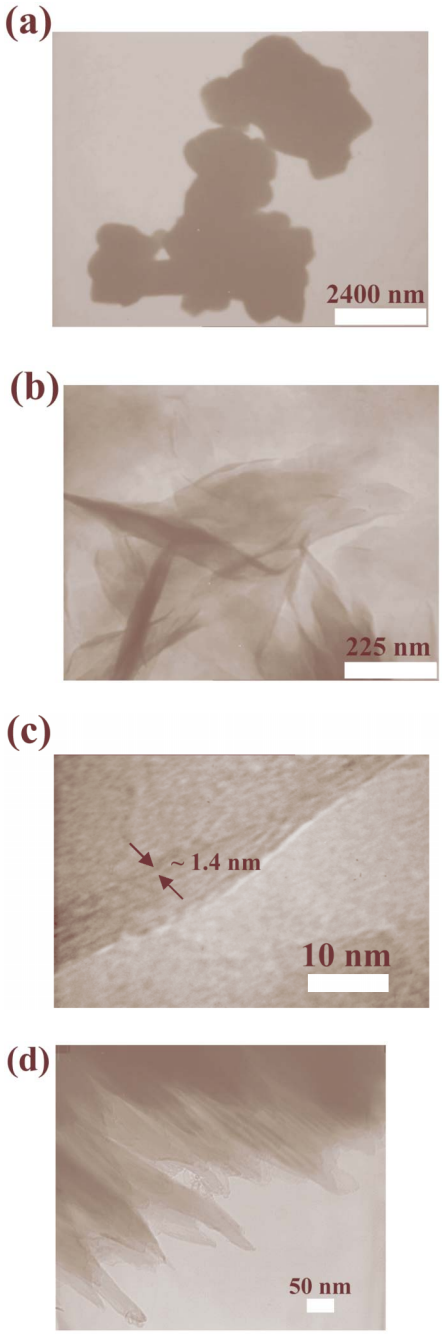


*Figure 1-7. Transmission electron micrographs for (a) pristine $V_2O_5$, (b) and (c) VP1, and (d) VP5.*

### 1-3-5. Electrical Conductivity

The electrical transport behaviors of the hybrids could be understood by considering the insertion of PEDOT into $V_2O_5$ powder as a hybrid system where two different types of low-dimensional electronic conductors coexist at the molecular level in a dimensionally constrained environment. Two types of charge carriers may be present in these material, small polarons (electrons) associated with the $d^1$ ($V^{4+}$) centers on the vanadium oxide lattice, and large polarons on the PEDOT backbone. The actual nature of charge transport would depend on the relative mobility of these two different-kind of carriers as demonstrated by the fact that the electronic conductivity of PEDOT/$V_2O_5$ hybrids is up to 4 orders of magnitude higher than that of pristine $V_2O_5$. In all samples, the conductivity increases with rising temperature as has been observed in most intercalated compounds and conjugated polymers [15,38]. The conductivity raises from $10^{-5}$ to $10^{-1}$ S $cm^{-1}$ as the amount of incorporated polymer augments from VP1 to VP5, although the exact mechanism may be more complex as due to the smaller particle size contribution towards grain conductivity. In this case, however, the increase in conductivity is probably due to a continued process of growth of the organic polymer network. The detailed results are summarized in Table 1-4.

Table 1-4. Nominal EDOT/$V_2O_5$ ratio, chemical compositions, d-spacing and electrical conductivity for the pristine $V_2O_5$ and hybrids.

| | Nominal EDOT/$V_2O_5$ ratio | Chemical composition | d-spacing (Å) | Conductivity ($S \cdot cm^{-1}$) |
|---|---|---|---|---|
| $V_2O_5$ | · | $V_2O_5$ | 4.3 | $8.78 \times 10^{-5}$ |
| VP1 | 0.02 | $(C_6H_4O_2S)_{0.02}V_2O_{4.9}$ | 13.8 | $2.92 \times 10^{-3}$ |
| VP2 | 0.04 | $(C_6H_4O_2S)_{0.03}V_2O_{4.8}$ | 14.0 | $6.97 \times 10^{-3}$ |
| VP3 | 0.08 | $(C_6H_4O_2S)_{0.05}V_2O_{4.7}$ | 14.0 | $3.84 \times 10^{-2}$ |
| VP4 | 0.40 | $(C_6H_4O_2S)_{0.18}V_2O_{4.6}$ | 17.8 | $9.82 \times 10^{-2}$ |
| VP5 | 0.60 | $(C_6H_4O_2S)_{0.25}V_2O_{4.6}$ | 19.0 | $1.01 \times 10^{-1}$ |

## 1-4. ELECTROCHEMISTRY

Vanadium oxide host lattice has been considered as one of the best cathode materials in secondary Li-batteries, mainly due to its layered structure immensely suitable for Li-insertion [39-41]. For battery applications, the rate limiting step is reported to be the reduction of $V_2O_5$ material during discharge accompanied by $Li^+$ insertion [42]. One common strategy to achieve higher efficiency and lithium uptake is to use high surface area materials, so that the distance over which $Li^+$ must diffuse through the host material is minimized [40,41]. In this case, an innegligible amount of Li can be reversibly grafted on large surface materials. This strategy will be focused in Chapter 3. Another approach that has not been completely explored yet, is to manipulate the interlayer spacing in these layered materials by using various intercalants so as to

enhance the rate of $Li^+$ migration since generally intercalation leads to changes in the interlayer spacing for layered materials [43,44]. Examples of such intercalants include pyrrole and aniline, all of which are known to oxidatively polymerize when intercalated into highly oxidizing materials such as $V_2O_5$ [6-8]. The electrochemical insertion of Li in $V_2O_5$ material can be described by the following redox reaction.

$$xLi^+ + xe^- + V_2O_5 \leftrightarrow Li_xV_2O_5$$

For PEDOT/$V_2O_5$ hybrids, analogous electrochemical reactions would be applicable as follows.

(Reduction of PEDOT)

$$[PEDOT^+]_xV_2O_5^{x-} + x\,Li^+ + x\,e^- \leftrightarrow Li_x[PEDOT]_xV_2O_5^{\,x-}$$

(Reduction of $V_2O_5^{x-}$)

$$Li_x[PEDOT]_xV_2O_5^{x-} + y\,Li^+ + y\,e^- \leftrightarrow Li_{x+y}[PEDOT]_xV_2O_5^{\,-(x+y)}$$

The open-circuit voltage (OCV) of the composites versus lithium metal anode is found to vary depending on the PEDOT/$V_2O_5$ ratio and obviously all hybrids give higher OCV values (3.77 to 3.61 V) than that observed (3.43 V) for pure $V_2O_5$ (Table 1-5). This can be explained by two factors. One is that the electrochemical potential for incorporated PEDOT (~ 3.8 V vs. $Li^+$/Li) is higher than that of $V_2O_5$ (~ 3.4 V vs. $Li^+$/Li), and consequently all the hybrids exhibit higher OCV than pristine $V_2O_5$. The other

factor is that the increased amount of incorporated polymer gives augmented number of $V^{4+}$ centers, as observed in the IR spectra, and thereby among the hybrid samples, the monolayer-incorporated hybrids (VP1, VP2 and VP3) deliver higher OCV than the doublelayer-incorporated ones (VP4 and VP5).

Table 1-5. Nominal EDOT/$V_2O_5$ ratio, corresponding chemical composition and open circuit voltage vs. $Li^+/Li$ for the pristine $V_2O_5$ and hybrid samples.

| | Nominal EDOT/$V_2O_5$ | Chemical composition | Open circuit voltage (V) |
|---|---|---|---|
| $V_2O_5$ | · | $V_2O_5$ | 3.43 |
| VP1 | 0.02 | $(C_6H_4O_2S)_{0.02}V_2O_{4.9}$ | 3.74 |
| VP2 | 0.04 | $(C_6H_4O_2S)_{0.03}V_2O_{4.8}$ | 3.76 |
| VP3 | 0.08 | $(C_6H_4O_2S)_{0.05}V_2O_{4.7}$ | 3.77 |
| VP4 | 0.40 | $(C_6H_4O_2S)_{0.18}V_2O_{4.6}$ | 3.62 |
| VP5 | 0.60 | $(C_6H_4O_2S)_{0.25}V_2O_{4.6}$ | 3.61 |

### 1-4-1. Cyclic Voltammetry

Cyclic voltammograms in Figure 1-8 illustrate a drastic change of electrochemical properties induced by the polymer insertion. During the first cathodic scan, from the open-circuit voltage to 2.2 V, the crystalline $V_2O_5$ undergoes well-known phase transformations and stabilization occurs after the third cycle (Figure 1-8a).

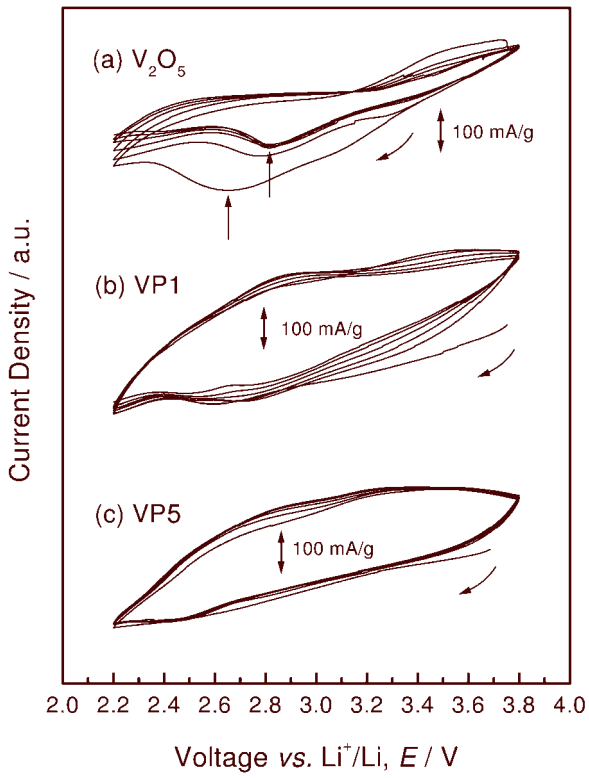


*Figure 1-8. Cyclic voltammograms of (a) pristine $V_2O_5$, (b) VP1 and (c) VP5 at 0.5 mV/s between 2.2 and 3.8 V vs. $Li^+/Li$.*

The irreversible shift of the cathodic peak from 2.65 V (first cathodic scan) to 2.82 V (third and following cathodic scans) means that the structural change is irreversible, which is well corresponding to the literatures [45-48]. In contrast, for the PEDOT/$V_2O_5$ hybrids, there is no sign for any irreversible structural change (Figure 1-8b and c). Their diagrams show broad cathodic peaks, which resemble those of 2D-$V_2O_5$ compounds [25-29]. The broad and diffuse peak shape can, therefore, be correlated with the disturbed layer stacking derived by the polymer incorporation, as previously deduced from X-ray diffraction data. It is also worthwhile to compare these lithium insertion features with those of $V_2O_5$ gel systems such as xerogel, aerogel and ambigel, whose structure is similarly based on the 'bi-dimensionality'. The xerogel shows three intercalation peaks at 2.85, 2.55 and 2.33 V, and, regarding the $V_2O_5$ aerogel and ambigel two reversible insertion peaks appear at 2.85 and 2.35 V, but for extraction process, 2.95 V peak disappears and 3.3 V peak shifts to 3.5 V after first step [40,49-53].

## 1-4-2. Discharge/Charge Properties

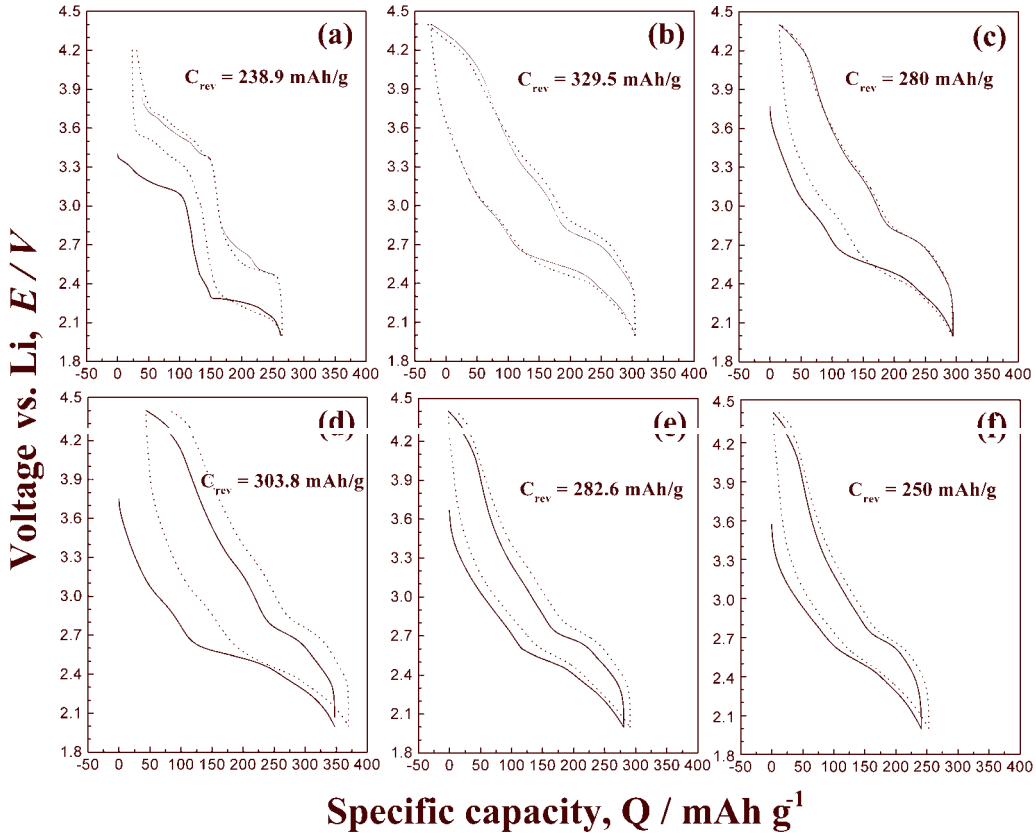


*Figure 1-9. Potential vs. specific capacity curves for the first two cycles of (a) pristine $V_2O_5$, (b) VP1, (c) VP2, (d) VP3, (e) VP4 and (f) VP5. The potential range was set to 2.0 ~ 4.2 V vs. Li for $V_2O_5$, and to 2.0 ~ 4.4 V for the hybrids. The current density was fixed to 15 mA/g.*

Figure 1-9 demonstrates potential *vs.* Li composition curves for the first two cycles carried out at 15 mA/g in the voltage range of 2.0 ~ 4.2 V (vs. $Li^+/Li$) for $V_2O_5$ and 2.0 ~ 4.4 V for the hybrids, corresponding to uptake of ~ 2 lithium per $V_2O_5$ unit. The pristine $V_2O_5$ shows distinctive plateaus due to structural changes from $\alpha$-$V_2O_5$ to

ε-$Li_xV_2O_5$, then further to δ-$Li_xV_2O_5$ [45], whereas the potential decreases more smoothly down to ~ 2.7 V for the hybrid samples. Similar continuous decrease in potential has been also observed for $V_2O_5$ xerogel [49-52], 2D-$V_2O_5$ [25-29] and polymer/$V_2O_5$ xerogel hybrids [5-12], of which common structural feature is the separation of vanadium oxide layers owing to the presence of interlayer molecules. It would be, hence, a plausible explanation that the disturbed layer stacking derived by the separation of layers would make structural disorders, *e.g.* reduced covalency of bondings between some vanadium and oxygen atoms, which thereby creates empty sub-bandgap $V^{5+}$:$3d^0$ energy states rather uniformly distributed between ~ 3.7 and ~ 2.7 V [54,55].

The next lithium insertion into the pristine $V_2O_5$ occurs at ~ 2.3 V and is accompanied by the irreversible structural changes to γ-$Li_xV_2O_5$ phase [45,48], leading to a transformation of curve shape in second cycle, while the hybrids display a plateau at ~ 2.5 V like $V_2O_5$ xerogel or 2D-$V_2O_5$. The fact that about 2.1 moles of lithium could be inserted per $V_2O_5$ unit, similar to the case of 2D-$V_2O_5$ compounds, also advocates above-mentioned assertion. VP1 and VP5 deliver 328 and 251 mAh/g, respectively, but the pristine $V_2O_5$ produces 241 mAh/g on the second discharge. It is worth to mention that the VP1 reveals a larger capacity in the first charge process than in the first discharge. It would be accounted for the presence of $V^{4+}$, which can be easily oxidized by an electrochemical method, as already observed in the case of PPY/$V_2O_5$ and PTH/$V_2O_5$ hybrids [7]. It is noted that VP1 shows the largest reversible capacity (~ 330 mAh/g) among the hybrids, while VP5 delivers the smallest one (~ 250 mAh/g). It is probably due to the fact that the formula weight of VP1 (~185 g/mol) is smallest and

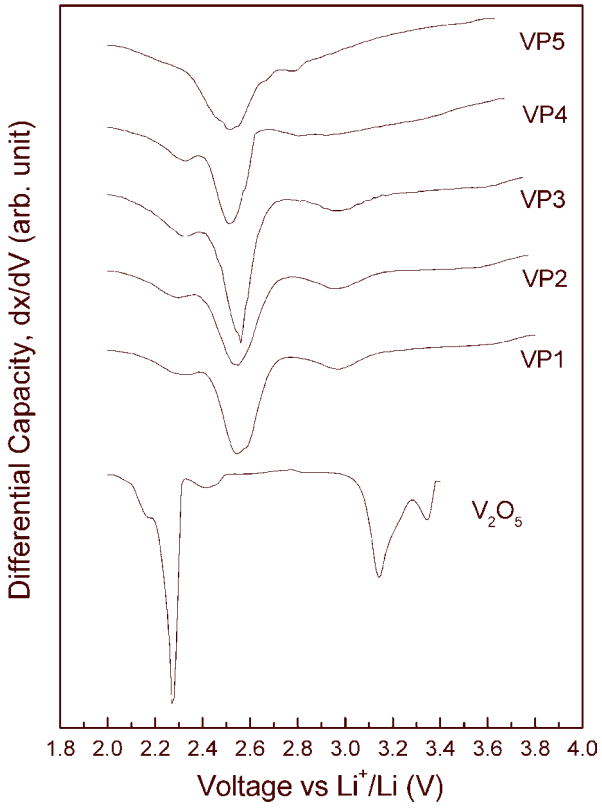


*Figure 1-10. The first differential capacity profiles of the first discharges of the pristine $V_2O_5$ and hybrids.*

that of VP5 (~217 g/mol) is largest.

A more accurate inspection of insertion voltage is accomplished by analysis of differential capacity profiles of the first discharges (Figure 1-10). The sharp peaks of pristine $V_2O_5$ are typical traits of the phase transformations, while on the contrary the hybrids exhibit broad peaks, which would sustain our above argumentation on the sub-bandgap states. VP1 shows three peaks at 2.9, 2.5 and 2.3 V analogous to PPY/$V_2O_5$ and PANI/$V_2O_5$ hybrids [5-7,10,11]. In the case of PANI/$V_2O_5$ hybrids, the 2.3 V peaks could be increased after appropriate oxygen treatment, which was attributed to the polymer [10,11]. But in our case, the hybrids also display 2.3 V peak although PEDOT has no redox capacity around 2.3 V. We, therefore, suggest a possibility that the origin of the 2.3 V capacity might come from the synergetic interaction between $V_2O_5$ layers and polymer chains, not from the polymers alone. For VP5, the 2.9 V peak shifts down to 2.7 V, and 2.3 V peak is less obvious, which also supports this thought. Consequently, the origin of 2.3 V peak has needs to be treated with a special care for further studies.

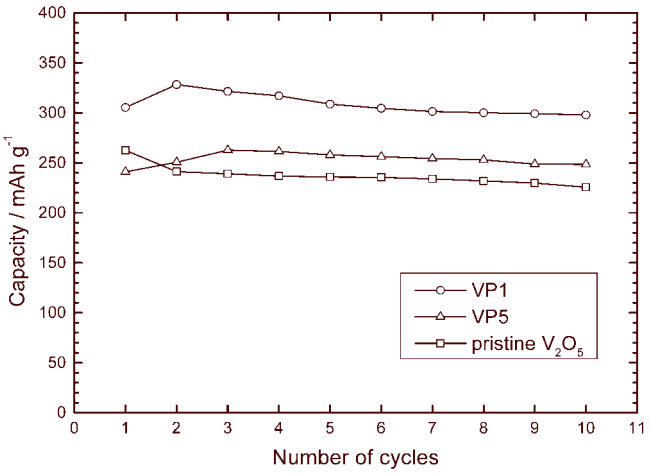


*Figure 1-11. Evolution of discharge capacity with the number of cycles for pristine $V_2O_5$, VP1 and VP5. The data were obtained at a current density of 15 mA/g. The potential range was set to 2.0 ~ 4.2 V vs. Li for $V_2O_5$, and to 2.0 ~ 4.4 V for VP1 and VP5.*

In order to clarify the role of the polymer incorporation on the electrochemical performance for extended cycling, the variation of discharge capacities were measured on VP1 and VP5 as a representative for monolayer and double-layer incorporated system, respectively (Figure 1-11). VP1 maintains capacities over 300 mAh/g for ten cycles. All the hybrids provide larger capacity and better cyclability than the pristine $V_2O_5$. The improved performances are presumably due to a higher electrical conductivity and to the separation between vanadium oxide layers, leading to an enhanced bidimensionality.

## 1-5. EPR STUDY OF PEDOT/$V_2O_5$ HYBRIDS

EPR study of PEDOT/$V_2O_5$ hybrids throws further light on the redoxy processes during EDOT insertion and polymerization between the $V_2O_5$ layers. Figures 1-12 compares the EPR spectra of PEDOT/$V_2O_5$ hybrids with that of pristine $V_2O_5$ and PEDOT polymer doped with $Cl^-$. The EPR spectrum of the pristine $V_2O_5$ shows a single

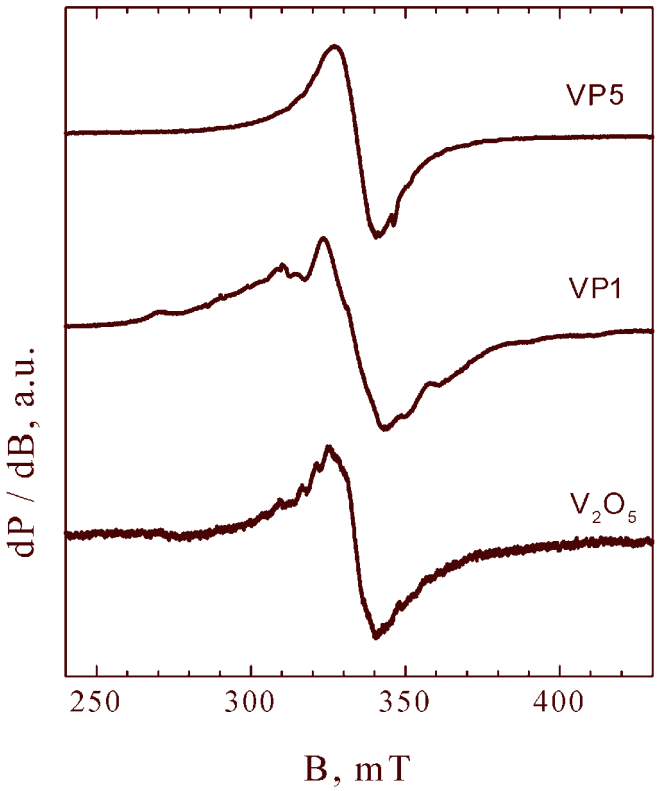


*Figure 1-12. EPR spectra at 85K of $V_2O_5$, VP1 and VP5.*

Lorentzian line with g=1.978 and line-width varying between 13 and 15 mT (In this regard, the exact chemical formula of this $V_2O_5$ would be $V_2O_{5-\delta}$ or $V_{2+\varepsilon}O_5$).

On cooling, a weak fine structure superimposed on the Lorentzian line becomes more pronounced. According to numerous EPR studies on amorphous and crystalline $V_2O_5$ compositions, this signal originates from impurity vanadyl complexes, $VO^{2+}$, which consists of a $V^{4+}$ ion ($d^1$ configuration) and close oxide shell, $O^{2-}$ [56,57]. The fine structure of the EPR spectrum of $VO^{2+}$ is due to the interaction of the unpaired electron (attached to $V^{4+}$, S=1/2) and the vanadium nucleus (I=7/2). The lack of well-resolved fine structure of the EPR spectrum of pristine $V_2O_5$ can be related with non-isolated $VO^{2+}$ complexes. This means that the impurity $VO^{2+}$ complexes are located close one to another, thus giving rise to develop dipole-dipole and exchange magnetic interactions between them.

The EPR spectrum of $Cl^-$ doped PEDOT consist of a broad Lorentzian line (g=2.03 and line width $\Delta H_{pp}$=55 mT) and two low-intensity signals at g=4.2 and g=2.00, as shown in

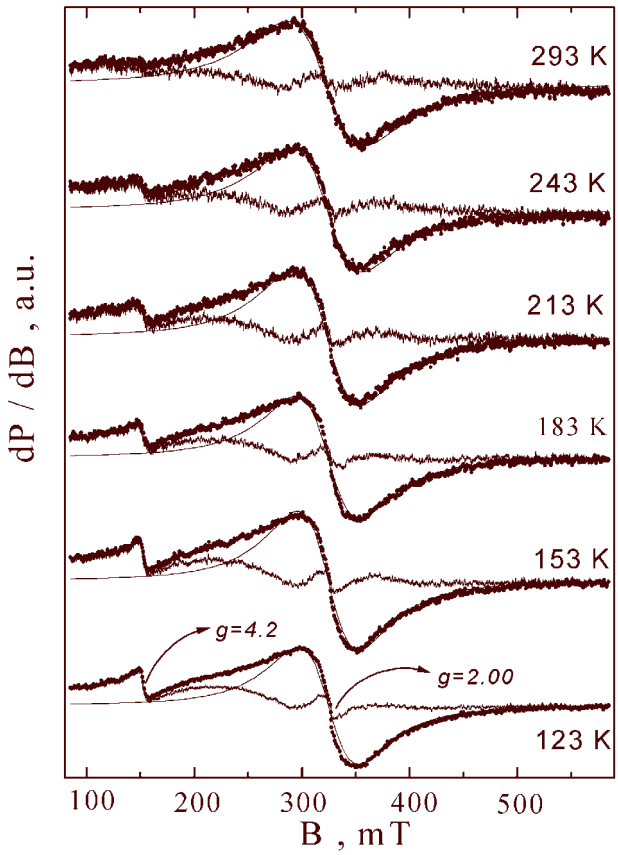


*Figure 1-13. Temperature evolution of the EPR spectrum of PEDOT doped with $Cl^-$. Thick lines correspond to the experimental spectrum, gray lines gives the broad Lorentzian line and the difference between experimental and broad Lorentzian line is shown by thin black line.*

Figure 1-13. The origin of the broad signal is not clear, but it may be tentatively associated with the conductive properties of the PEDOT polymer, maybe related to delocalized polarons and/or bipolarons. The low-intensity signal at g=2.00 can be assigned to free radicals (maybe related to localized polarons), while the signal at g=4.2 comes from $Fe^{3+}$ ions, most probably of $FeCl_3$ oxidizing agent.

During the EDOT insertion into $V_2O_5$, an EPR signal from $VO^{2+}$ is detectable only. The intensity of the signal increases about 200 times as compared to that of unreacted $V_2O_5$. In addition, the signal intensity correlates with the amount of the incorporated polymer: the relative intensity is 1.0 and 3.4 for VP1 and VP5 samples, respectively. Irrespective of the strong increase in the signal intensity, a well-resolved fine structure is observed for the VP1 sample only (Figure 1-12).

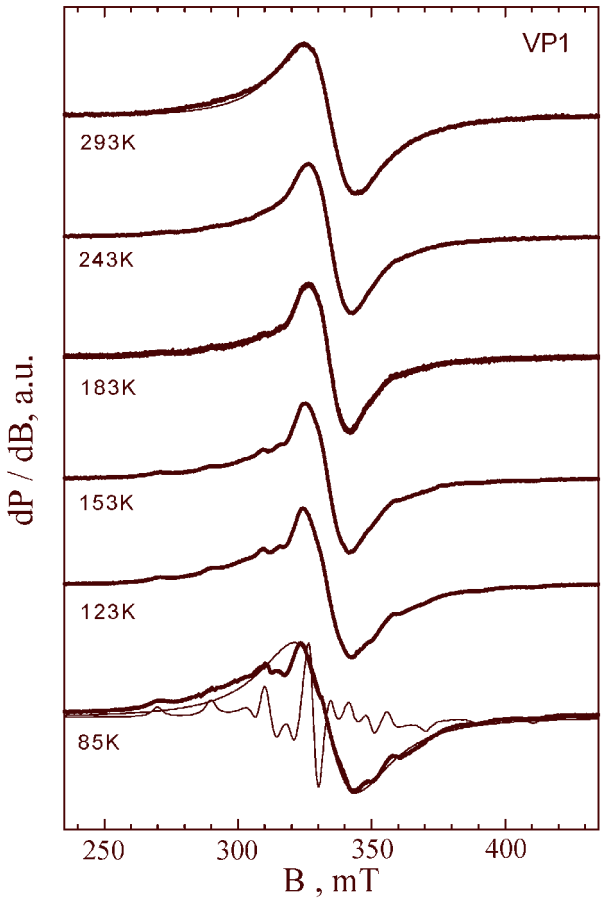


*Figure 1-14. Temperature evolution of the EPR spectrum of VP1. Thick lines correspond to the experimental spectrum, gray fine-structured and thin lines represent the isolated and non-isolated $VO^{2+}$ complexes, respectively.*

The fitting of the experimental spectrum enables to differentiate two signals, the ratio between them being dependent on the recording temperature (Figure 1-14). At 85 K, there is a signal with tetragonally symmetric g- and hyperfine tensor ($g_{\perp}$=1.9913; $g_{||}$=1.9399 and $A_{\perp}$= 66 x $10^{-4}$; $A_{||}$=180 x $10^{-4}$ $cm^{-1}$), as well as a single line with Lorentzian shape and g=1.983 and $\Delta H_{pp}$=23.3 mT. While increasing the recording temperature, the single Lorentzian accounts mainly for the EPR profile of VP1. The two signals can be assigned to the isolated and non-isolated $VO^{2+}$ complexes, respectively. The observed g- and A-tensor of isolated $VO^{2+}$ in VP1 are close to that of $VO^{2+}$ in $[VO(H_2O)_5]^{2+}$ ($g_{\perp}$=1.980,1981; $g_{||}$=1.913 and $A_{\perp}$= 71, 72 x $10^{-4}$; $A_{||}$=180 x $10^{-4}$ $cm^{-1}$), indicating an ionic character of the bond between $VO^{2+}$ and the equatorial ligands.

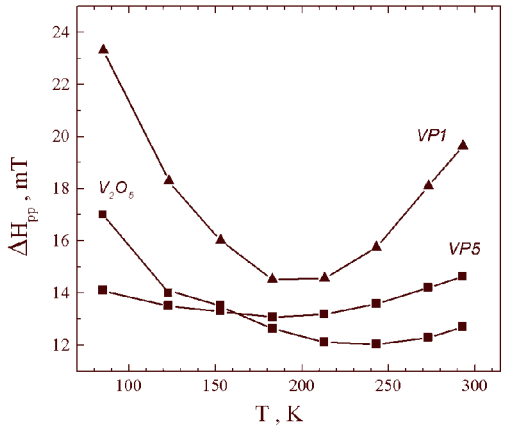


*Figure 1-15. Temperature evolution of the EPR line width of non-isolated $VO^{2+}$ complexes for pristine $V_2O_5$, VP1 and VP5.*

By raising the content of the inserted polymer, the EPR spectrum of VP5 displays a single Lorentzian line with g=1.973 due to non-isolated $VO^{2+}$ (Figure 1-12). The line width decreases on cooling from 293 to 183K, passing through minimum and then increases again below 183K (Figure 1-15). A similar temperature evolution of the EPR line width is also observed for non-isolated $VO^{2+}$ complexes in VP1. However, the competition between dipole-dipole and exchange interactions may account for the observed differences in the line width of non-isolated $VO^{2+}$ complexes. This clearly indicates differences in the distribution of $VO^{2+}$ complexes. It seems that incorporated polymers mainly control the distribution of $VO^{2+}$.

## 1-6. CONCLUSION

We have found a novel method of inserting PEDOT between the layers of $V_2O_5$ using a soft process of intercalation. The reaction takes place with the *in-situ* polymerization of EDOT within the framework of crystalline $V_2O_5$ with different nominal EDOT/$V_2O_5$ ratios. XRD expriments proves the interlayer distance of $V_2O_5$ expands upon the incorporation of polymer step-by-step, first forming monolayer and

then double layers depending on the amount of incorporated polymer. The insertion reaction results in a random layer stacking structure, leading to broadening of the energy state distribution. IR spectra suggest the occurrence of $V^{4+}$ centers upon the insertion reaction and a strong interaction between vanadyl group and the incorporated polymer. From the electron microscopy results, it has been found that the incorporation of PEDOT increases bidimensionality of the $V_2O_5$ host by the layer separation. According to electrochemical measurements, the hybrids showed reversible specific capacities up to ~330 mAh/g at 15 mA/g between 2 ~ 4.4 V vs. $Li^+$/Li. This improvement of electrochemical performance compared with pristine $V_2O_5$ is attributed to higher electric conductivity and enhanced bidimensionality. The origin of enhanced conductivity has been also investigated by EPR spectroscopy, which gives evidence for the two types of $VO^{2+}$ complexes, that is, one is isolated and the other is non-isolated. The observed increasing trend in the fraction of isolated and non-isolated $VO^{2+}$ can be related with the growing tendency of conductivity from VP1 to VP5 samples.

## 1-7. REFERENCES

[1] C. Sanchez, G. J. de A. A. Soler-Illia, F. Ribot, T. Lalot, C. R. Mayer and V. Cabuil, Chem. Mater., 13 (2001), 3061-3083.

[2]. J. Portier, G. Campet, N. Treuil, A. Poquet, Y. I. Kim, S. J. Kwon, S. Y. Kwak and J. H. Choy, J. Korean Chem. Soc., 42 (1998), 487-500.

[3] R. Gangopadhyay and A. De, Chem. Mater., 12 (2000), 608-622.

[4] V. L. Colvin, M. C. Schlamp and A. P. Alivisatos, Nature (London), 370 (1994), 354.

[5] F. Leroux, B. E. Koene and L. F. Nazar, J. Electrochem. Soc., 143 (1996), L181.

[6] F. Leroux, G. Goward, W. P. Power and L. F. Nazar, J. Electrochem. Soc., 144 (1997) 3886.

[7] G. R. Goward, F. Leroux and L. F. Nazar, Electrochim. Acta., 43 (1998), 1307.

[8] H. P. Wong, B. C. Dave, F. Leroux, J. Harreld, B. Dunn and L. F. Nazar, J. Mater. Chem., 8 (1998), 1019.

[9] J. H. Harreld, B. Dunn and L. F. Nazar, Int. J. Inorg. Mater., 1 (1999), 135.

[10] M. Lira-Cantu and P.Gomez-Romero, Int. J. Inorg. Mater., 1 (1999), 111.

[11] M. Lira-Cantu and P.Gomez-Romero, J. Electrochem. Soc., 146 (1999), 2029.

[12] M. Lira-Cantu and P.Gomez-Romero, J. Solid State Chem., 147 (1999), 601.

[13] M. G. Kanatzidis and C. G. Wu, J. Am. Chem. Soc. 111 (1989) 4141.

[14] Y. J. Liu, D. C. DeGroot, J. L. Schindler, C. R. Kannewurf and M. G. Kanatzidis, J. Chem. Soc. Chem. Commun., 593 (1993).

[15] C. G. Wu, D. C. Degroot, H. O. Marcy, J. L. Schindler, C. R. Kannewurf, Y. J . Liu, W. Hirpo and M. G. Kanatzidis, Chem. Mater., 8, 1992 (1996).

[16] For general reviews on conductive polymers, see : Handbook of Organic Conductive Molecules and Polymers, Vols. 1-4, H. S. Nalwa (Ed.), Wiley, Chichester, UK (1997).

[17] L. B. Groenedaal, F. Jonas, F. Freitag, H. Pielartzik and J. R. Reynolds, Adv. Mater., 12 (2000), 481.

[18] A. V. Murugan, B. B. Kale, C. W. Kwon, G. Campet and K. Vijayamohanan, J. Mater. Chem. 11 (2001) 2470.

[19] A. V. Murugan, C. W. Kwon, G. Campet, B. B. Kale, T. Maddanimath and K. Vijayamohanan, J. Power Sources, 105 (2002), 1.

[20] C. W. Kwon, A. V. Murugan, G. Campet, J. Portier, B.B. Kale, K. Vijaymohanan and J. H. Choy, Electrochem. Commun., 4 (2002), 384.

[21] R. Corradi and S. P. Armes, Synth. Met., 84 (1997), 453.

[22] P. Aldebert, N. Baffier, N. Gharbi and J. Livage, Mater. Res. Bull., 16 (1981), 669.

[23] J. Livage, Solid State Ionics, 86-88 (1996), 935.

[24] B. E. Warren, Phys. Rev., 59 (1941,) 693.

[25] Y. Sato, T. Nomura, H. Tanaka and K. Kobayakawa, J. Electrochem. Soc., 138 (1991), L37.

[26] Y. Sato, T. Asada, H. Tokugawa and K. Kobayakawa, J. Power Sources, 68 (1997), 674.

[27] Y. Sato, T. Matsueda, H. Tokugawa and K. Kobayawa, Chem. Lett., (1993), 901.

[28] M. Ugaji, M. Hibino and T. Kudo, J. Electrochem. Soc., 142 (1995), 3664.

[29] M. Hibino, M. Ugaji, A. Kishimoto and T. Kudo, Solid State Ionics, 79 (1995), 239.

[30] J. C. Gustafsson, B. Liedberg and O. Inganas, Solid State Ionics, 69 (1994), 145.

[31] C. Kvarnstrom, J. Neugebauer, S. Blomquist, H. J. Ahonen, J. Kankare and A. Ivaska, Electrochem. Acta., 44 (1999), 2739.

[32] V. Hernandez, F. J. Ramirez, T. F. Otero and J. T. Lopez Navarrete, J. Chem. Phys., 100 (1994), 114.

[33] K. E. Aasmundtveit, E. J. Samuelson, L. A. A.Pettersson, O. Inganas, T. Johansson and R. Feidenhans'l, Synth. Met., 101 (1999), 561.

[34] K. E. Aasmundtveit, E. J. Samuelson, O. Inganas, L. A. A.Pettersson, T. Johansson

and S. Ferrer, Synth. Met., 113 (2000), 93.

[35] G. Zotti, S. Zecchin, G. Schiavon and L. B. Groenendaal, Chem. Mater., 12 (2000), 2996.

[36] F. Tran-Van, S. Garreau, G. Louarn, G. Froyer and C. Chevrot, J. Mater. Chem., 11 (2001), 1378.

[37] R. A. Ross and C. Fairbridge, Can. J. Chem., 62 (1984), 1483.

[38] H. H. Javadi, K. R. Cromack, A. G. McDiarmid and A. Epstein, Phys. Rev. B, 39 (1989), 3579.

[39] M. S. Whittingham in "Lithium Ion Batteries", M. Wakihara and O. Yamamoto (Eds.), Kodansha, Tokyo, 1998, Ch. 3.

[40] D. B. Le, S. Passerini, A. L. Tipton, B. B. Owens and W. H. Smyrl, J. Electrochem. Soc., 142 (1995), L102.

[41] D. B. Le, S. Passerini, A. L. J. Guo, J. Ressler, B. B. Owens and W. H. Smyrl, J. Electrochem. Soc., 143 (1996), 2099.

[42] Rechargeable Lithium and Lithium Ion Batteries, S. Megahed, B. M. Barnett and L. Xie (Eds.), Electrochemical Society, New Jersey, 1995, Electrochemical Society Proceedings Series PV 94-28.

[43] J. P. Lemmon and M. M. Lerner, Chem. Mater., 6 (1994), 207.

[44] C. O. Oriakhi and M. M. Lerner, Chem. Mater., 8 (1996), 2016.

[45] J. M. Cocciantelli, M. Broussely, J. P. Doumerc, J. Labat and M. Pouchard, J. Power Sources, 34 (1991), 103.

[46] A. Tranchant, J. M. Blengino, J. Farcy and R. Messina, J. Electrochem. Soc., 139 (1992), 1243.

[47] K. West, B. Zachau-Christiansen, T. Jacobsen and S. Skaarup, Solid State Ionics, 76 (1995), 15.

[48] J. M. Cocciantelli, M. Ménétrier, C. Delmas, J. P. Doumerc, M. Pouchard, M. Broussely and J. Labat, Solid State Ionics, 78 (1995), 143.

[49] H. K. Park and W. H. Smyrl, J. Electrochem. Soc., 141 (1994), L25.

[50] K. Salloux, F. Chaput, H. P. Wong, B. Dunn and M. W. Breiter, J. Electrochem. Soc., 142 (1995), L191.

[51] F. Coustier, S. Passerini and W. H. Smyrl, J. Electrochem. Soc., 145 (1998), L73.

[52] J. H. Harreld, W. Dong and B. Dunn, Mater. Res. Bull., 33 (1998), 561.

[53] W. Dong, D. R. Rolison and B. Dunn, Electrochem. Solid-State. Lett., 3 (2000), 457.

[54] Amorphous Semiconductors, 2nd ed., M. H. Brodsky (Ed.), Topics in Applied Physics Vol. 36, Springer-Verlag, Berlin (1985).

[55] G. Campet, S. J. Wen, S. D. Han, M. C. R. Shastry, J. Portier, C. Guizard, L. Cot, Y. Xu and J. Salardennet, Mater. Sci. Eng. B,18 (1993), 201.

[56] B. Pecquenard, D. Gourier and N. Baffier, Solid State Ionics, 78 (1995), 287.

[57] P. E. Stallworth, F. S. Johnson, S. G. Greenbaum, S. Passerini, J. Flowers, W. Smyrl and J. J. Fontanella, Solid State Ionics, 146 (2002), 43.

# *Publications Related to Chapter 1*

- "Poly(3,4-ethylenedioxythiophene)/$V_2O_5$ hybrids for lithium batteries", Electrochem. Commun. (2002), vol. 4, n° 5, pp. 384-387.

- "Synthesis and characterization of a new organo-inorganic poly(3,4-ethylene dioxythiophene) PEDOT/$V_2O_5$ nanocomposite by intercalation", J. Mater. Chem. (2001), vol. 11, n° 10, pp. 2470-2475.

- "Electrochemical lithium insertion into a poly(3,4-ethylenedioxythiophene)/$V_2O_5$ nanocomposite", J. Power Sources (2002), vol. 105, n° 1, pp. 1-5.

ELSEVIER

Electrochemistry Communications 4 (2002) 384–387

electrochemistry communications

www.elsevier.com/locate/elecom

# Poly(3,4-ethylenedioxythiophene)$V_2O_5$ hybrids for lithium batteries

Chai-Won Kwon [a], A. Vadivel Murugan [b], Guy Campet [a,*], Josik Portier [a], B.B. Kale [b], K. Vijaymohanan [c], Jin-Ho Choy [d]

[a] *Institut de Chimie de la Matière Condensée de Bordeaux (ICMCB), 87 Avenue du Dr. A. Schweitzer, 33608 Pessac, France*
[b] *Centre for Materials for Electronics Technology, Ministry of Information Technology, Government of India, Pashan Road, Pune 411 008, India*
[c] *Physical and Materials Chemistry Division, National Chemical Laboratory, Pune 411 008, India*
[d] *National Nanohybrid Materials Laboratory, School of Chemistry and Molecular Engineering, Seoul National University, Seoul 151-747, Republic of Korea*

Received 13 February 2002; received in revised form 25 February 2002; accepted 25 February 2002

**Abstract**

A series of hybrid electrode materials, poly(3,4-ethylenedioxythiophene)/$V_2O_5$, has been synthesized using an oxidative insertion and polymerization reaction. FTIR, X-ray diffraction and transmission electron microscopy studies have shown that the incorporation of polymer between $V_2O_5$ slabs leads to an enhanced bidimensionality. The electrochemical lithium capacity has been increased up to ~330 mAh/g at the second discharge in the range of 2.0–4.4 V vs. Li. This improvement of electrochemical performance compared to pristine $V_2O_5$ is attributed to the higher electric conductivity and enhanced bidimensionality. © 2002 Elsevier Science B.V. All rights reserved.

*Keywords:* Vanadium oxide; Poly(3,4-ethylenedioxythiophene); Lithium battery; Electrode material; Hybrid; Bidimensionality

## 1. Introduction

Conductive polymer/$V_2O_5$ hybrids have received a considerable attention over past several years to integrate profitably many desirable properties of both vanadium oxide and the polymeric counterpart [1–7]. $V_2O_5$ is one of the most beneficial lithium cathodes with processability and high capacity, whereas conductive polymers have advantages in flexibility and conductivity. These hybrids are generally prepared by mixing $V_2O_5$ gel with monomers of the corresponding conductive polymer such as polyaniline (PANI) [1–3], polypyrrole (PPY) [3–5] or polythiophene (PTH) [5]. Recently, we have succeeded in the first synthesis of poly(3,4-ethylenedioxythiophene) (PEDOT)/$V_2O_5$ hybrids starting from well-crystalline $V_2O_5$ unlike other hybrid, and reported their possible use as an electrode material [6,7]. In this study, we describe their outstanding electrochemical performance and attempt to explain the origin of the enhancement.

## 2. Experimental

The PEDOT/$V_2O_5$ hybrids were synthesized by dissolving 3,4-ethylenedioxythiophene (EDOT, Bayer) in 25 ml of distilled water and mixing with 2 g of $V_2O_5$ (99.9%, Aldrich) under reflux condition for 12 h. The nominal molar ratio of EDOT to $V_2O_5$ was adjusted to 0.02 (VP1), 0.04 (VP2), 0.08 (VP3), 0.40 (VP4) or 0.60 (VP5). The detailed synthetic method has already been published [6].

The crystal structure of samples was examined by a powder X-ray diffractometer (Phillips PW-1050) using graphite-monochromated Cu-K$\alpha$ radiation ($\lambda$ = 1.5418 Å). Fourier transform infrared (FTIR) spectra of powder samples diluted with KBr were recorded with a Bruker FTIR spectrometer in transmission mode. The variation of particle morphology on the intercalation was monitored by a transmission electron microscope (JEOL 2000 FX) operating at an accelerating voltage of 200 kV.

* Corresponding author. Tel.: +33-05-5684-6297; fax: +33-05-5684-2761.
*E-mail address:* campet@icmcb.u-bordeaux.fr (G. Campet).


PII: S1388-2481(02)00316-8

Table 1
Nominal EDOT/$V_2O_5$ ratio, chemical compositions, *d*-spacing and electrical conductivity for the pristine $V_2O_5$ and hybrids

| | Nominal EDOT/$V_2O_5$ ratio | Chemical composition[a] | *d*-spacing (Å) | Conductivity[b] (S · cm$^{-1}$) |
|---|---|---|---|---|
| $V_2O_5$ | – | $V_2O_5$ | 4.3 | $8.78 \times 10^{-5}$ |
| VP1 | 0.02 | $(C_6H_4O_2S)_{0.02}V_2O_5$ | 13.8 | $2.92 \times 10^{-3}$ |
| VP2 | 0.04 | $(C_6H_4O_2S)_{0.03}V_2O_5$ | 14.0 | $6.97 \times 10^{-3}$ |
| VP3 | 0.08 | $(C_6H_4O_2S)_{0.05}V_2O_5$ | 14.0 | $3.84 \times 10^{-2}$ |
| VP4 | 0.40 | $(C_6H_4O_2S)_{0.18}V_2O_5$ | 17.8 | $9.82 \times 10^{-2}$ |
| VP5 | 0.60 | $(C_6H_4O_2S)_{0.25}V_2O_5$ | 19.0 | $1.01 \times 10^{-1}$ |

[a] Evaluated from thermogravimetry and elemental analysis.
[b] Measured by four probe method using conducting silver paste for contacts.

Electrochemical experiments were performed based on the configuration of 'Li |1 M $LiClO_4$ in EC (ethylene carbonate)/DMC (dimethyl carbonate) (1:1 v/v)| composite electrode'. The composite electrodes were made by intimately mixing 70% (by mass) of the active material, 25% of Ketjenblack and 5% of polytetrafluoroethylene (PTFE). These electrodes were dried under vacuum at 80 °C for 3 h, and introduced into an Argon-filled glove box without any exposure to air. Charge/discharge experiments were carried out in a galvanostatic mode at a current density of 15 mAh/g using a computer-controlled PGS201T (Tacussel) system.

## 3. Results and discussion

The incorporation of the polymer into the $V_2O_5$ was examined by powder X-ray diffraction. Series of well-developed (0 0 *l*) peaks can be observed, and the *d*-spacing increases from 4.3 to 13.8 Å and further to 19.0 Å depending on the amount of the incorporated macromolecules. The net interlayer expansion increases from 5.1 Å for VP1 to 10.3 Å for VP5, respectively, assuming the $V_2O_5$ slab is composed of two vanadium oxide sheets like that of vanadium oxide xerogel [8]. This would indicate that the expansion proceeds in two steps, first forming monolayer of polymer and then double layers. It is noted that (*h k* 0) reflections of the hybrids correspond to those of the pristine $V_2O_5$ and that some of them, such as (1 1 0) and (3 1 0), show a diffuse peak shape, rising rather rapidly and then declining slowly toward high angle side. This feature suggests that the compounds have a random layer stacking structure, which consists of equidistant and parallel (*a*-*b*) layers, but randomly rotated about the normal *c*-axis [9]. The details are summarized in Table 1 with the results of elemental analysis and conductivity, but curve figures are not presented here because they have been already published elsewhere [6].

In order to examine the oxidation state of vanadium and doping state of the polymer, Fourier transform infrared (FTIR) spectra were recorded. Vibrations around 1520, 1450 and 1380 cm$^{-1}$ are assigned to the stretching

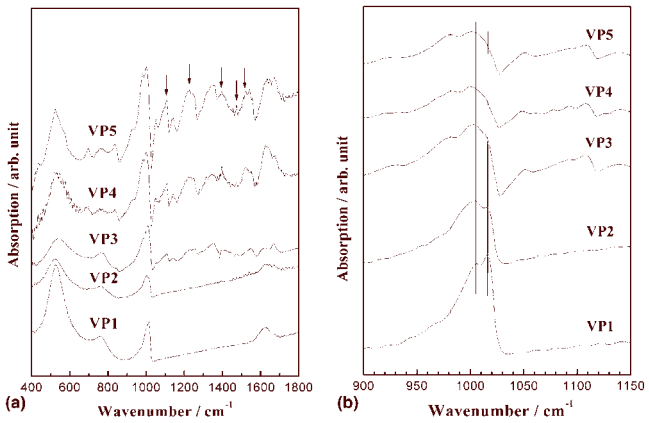


Fig. 1. Infrared spectra for VP1 (bottom), VP2, VP3 (middle), VP4 and VP5 (top) in the range of (a) 400–1800 cm$^{-1}$ and (b) 900–1150 cm$^{-1}$ (enlargement). The samples were diluted with KBr and pressed into a pellet. Some important peaks from polymer are marked with arrows.

of C=C and C–C in the thiophene ring, and those at 1130 and 1090 $cm^{-1}$ to the stretching of ethylenedioxy group (Fig. 1(a)) [10,11]. These peaks increase as the amount of incorporated polymer augments, which proves the presence of the PEDOT in these materials. The absence of peak at 1490 and 1190 $cm^{-1}$ implies that the organics are not in monomer form but in polymeric form [10,11]. The peaks around 1260 and 1090 $cm^{-1}$ indicate that the polymer is in doped state as expected in the improved conductivity [10,11]. Bands around 530 and 810 $cm^{-1}$ are attributed to V–O–V stretching modes and those around 1000 $cm^{-1}$ to V=O stretching. A deeper inspection finds that the 985 $cm^{-1}$ peak increases and the 1015 $cm^{-1}$ peak decreases inversely as the amount of incorporated polymer augments (Fig. 1(b)), which suggests a strong interaction (e.g. hydrogen bonding) between vanadyl group and the incorporated polymer, like PPY/$V_2O_5$ xerogel hybrid [4]. A further study with XPS is under investigation.

The influence of this modification on particle morphology was monitored with transmission electron microscopy. The pristine $V_2O_5$ consists of thick agglomerated particles with irregular sizes of micrometer order (Fig. 2(a)), whereas the particles of hybrids are composed of well-developed (*a*-*b*) planes stacked along with *c*-axis (Figs. 2(b–d)). The stacking length in *c*-direction is much shorter compared with *a* and *b* directions for the hybrids, which would be considered as the enhancement of 'bidimensionality'. The interlayer spacing of VP1 has been estimated by measuring the length from one dark line to the nearest one, which gives ~14 Å in good agreement of XRD result.

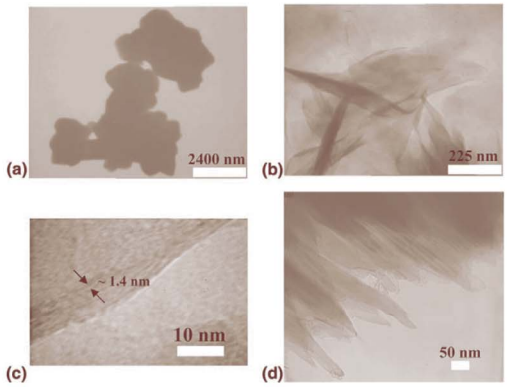


Fig. 2. Transmission electron micrographs for (a) pristine $V_2O_5$, (b) and (c) VP1, and (d) VP5.

Fig. 3 demonstrates potential vs. capacity curves of the first two cycles for the pristine $V_2O_5$ and hybrids. The pristine $V_2O_5$ shows distinctive plateaus due to structural changes [12], whereas the potential decreases more smoothly down to ~2.7 V for the hybrid samples. Similar continuous decrease in potential has been also observed for $V_2O_5$ xerogel [13,14], 2D-$V_2O_5$ [15] and conductive polymer/$V_2O_5$ xerogel hybrids [2–5], of

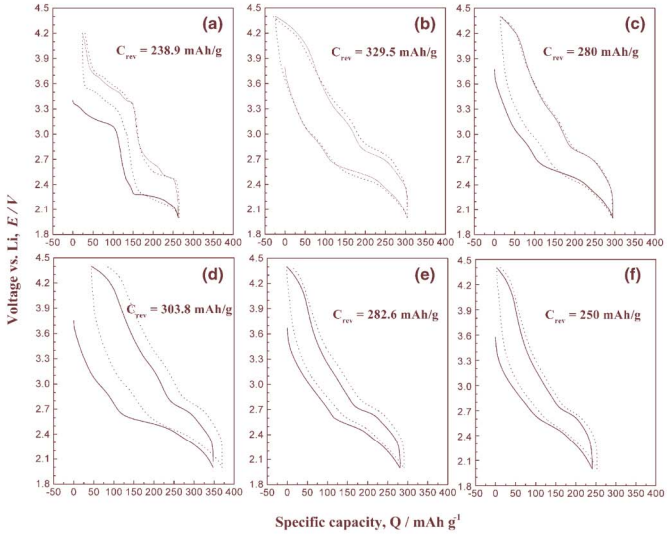


Fig. 3. Potential vs. specific capacity curves for the first two cycles of (a) pristine $V_2O_5$, (b) VP1, (c) VP2, (d) VP3, (e) VP4 and (f) VP5. The potential range was set to 2.0–4.2 V vs. Li for $V_2O_5$, and to 2.0–4.4 V for the hybrids. The current density was fixed to 0.15 mA/g.

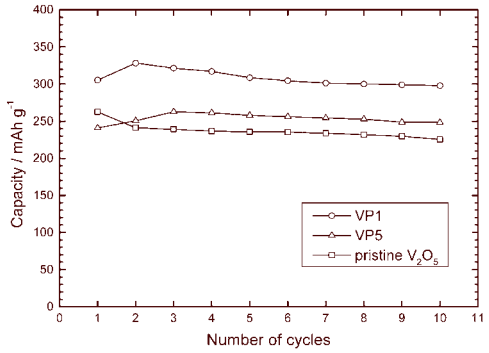


Fig. 4. Evolution of discharge capacity with the number of cycles for pristine $V_2O_5$, VP1 and VP5. The data were obtained at a current density of 0.15 mA/g. The potential range was set to 2.0–4.2 V vs. Li for $V_2O_5$, and to 2.0–4.4 V for VP1 and VP5.

which common structural feature is the separation of vanadium oxide layers owing to the presence of interlayer molecules. It would be, hence, a plausible explanation that the disturbed layer stacking derived by the separation of layers would make structural disorders, e.g. reduced covalency of bondings between some vanadium and oxygen atoms, which thereby creates empty sub-bandgap $V^{5+}$:$3d^0$ energy states rather uniformly distributed between ~3.7 and ~2.7 V [16,17]. The next lithium insertion into the pristine $V_2O_5$ occurs at ~2.3 V and is accompanied by the irreversible structural changes to $\gamma$–$Li_xV_2O_5$ phase [12], while the hybrids display a plateau at ~2.5 V like $V_2O_5$ xerogel or 2D-$V_2O_5$. It is worth to mention that the VP1 reveals a larger capacity in the first charge process than in the first discharge. It would be accounted for the presence of $V^{4+}$, which can be easily oxidized by an electrochemical method, as already observed in the case of PPY/$V_2O_5$ and PTH/$V_2O_5$ hybrids [2–5]. It is noted that VP1 shows the largest reversible capacity (~330 mAh/g) among the hybrids, while VP5 delivers the smallest one (~250 mAh/g). It is probably due to the fact that the formula weight of VP1 (~185 g/mol) is smallest and that of VP5 (~217 g/mol) is largest. In order to clarify the role of the polymer incorporation on the electrochemical performance for extended cycling, the variation of discharge capacities measured on VP1 and VP5 as a representative for monolayer and double-layer incorporated system, respectively. All the hybrids provide larger capacity and better cyclability than the prisinte $V_2O_5$, as shown in Fig. 4. The improved performances are presumably due to a higher electrical conductivity and to the separation between vanadium oxide layers, leading to an enhanced bidimensionality.

## 4. Conclusion

A series of hybrid electrode materials, PEDOT/$V_2O_5$, has been synthesized and subjected to various characterization. The interlayer distance of $V_2O_5$ expands upon the incorporation of polymer, which thereby results in a random layer stacking structure. IR spectra suggest a strong interaction between vanadyl group and the incorporated polymer. From the TEM results, it has been found that the incorporation of PEDOT increases bidimensionality of the $V_2O_5$ host by the layer separation. According to electrochemical measurements, the hybrids showed reversible specific capacities up to ~330 mAh/g at 15 mA/g. This improvement of electrochemical performance compared with pristine $V_2O_5$ is attributed to higher electric conductivity and enhanced bidimensionality.

## Acknowledgements

The authors are grateful to B. Dunn (UCLA) for his helpful discussion. C.W. Kwon thanks the CROUS of Bordeaux (France) for grant.

## References

[1] M.G. Kanatzidis, C.G. Wu, J. Am. Chem. Soc. 111 (1989) 4141.
[2] M. Lira-Cantu, P. Gomez-Romero, J. Electrochem. Soc. 146 (1999) 2029.
[3] F. Leroux, G. Goward, W.P. Power, L.F. Nazar, J. Electrochem. Soc. 144 (1997) 3886.
[4] H.P. Wong, B.C. Dave, F. Leroux, J. Harreld, B. Dunn, L.F. Nazar, J. Mater. Chem. 8 (1998) 1019.
[5] G.R. Goward, F. Leroux, L.F. Nazar, Electrochim. Acta 43 (1998) 1307.
[6] A.V. Murugan, B.B. Kale, C.W. Kwon, G. Campet, K. Vijayamohanan, J. Mater. Chem. 11 (2001) 2470.
[7] A.V. Murugan, C.W. Kwon, G. Campet, B.B. Kale, T. Maddanimath, K. Vijayamohanan, J. Power, Sources 105 (2002) 1.
[8] J. Livage, Solid State Ion. 86–88 (1996) 935.
[9] B.E. Warren, Phys. Rev. 59 (1941) 693.
[10] C. Kvarnstrom, H. Neugebauer, S. Blomquist, H.J. Ahonen, J. Kankare, A. Ivaska, Electrochim. Acta 44 (1999) 2739.
[11] F. Tran-Van, S. Garreau, G. Louarn, G. Fryer, C. Chevrot, J. Mater. Chem. 11 (2001) 1378.
[12] J.M. Cocciantelli, M. Menetrier, C. Delmas, J.P. Doumerc, M. Pouchard, M. Broussely, J. Labat, Solid State Ion. 78 (1995) 143.
[13] H.K. Park, W.H. Smyrl, J. Electrochem. Soc. 141 (1994) L25.
[14] K. Salloux, F. Chaput, H.P. Wong, B. Dunn, M.W. Breiter, J. Electrochem. Soc. 142 (1995) L191.
[15] M. Ugaji, M. Hibino, T. Kudo, J. Electrochem. Soc. 142 (1995) 3664.
[16] M.H. Brodsky (Ed.), Amorphous Semiconductors, 2nd ed., Topics in Applied Physics, vol. 36, Springer-Verlag, Berlin, 1985.
[17] C.W. Kwon, A. Poquet, S. Mornet, G. Campet, J. Portier, J.H. Choy, Electrochem. Commun. 4 (2002) 197.

JOURNAL OF Materials CHEMISTRY

# Synthesis and characterization of a new organo–inorganic poly(3,4-ethylene dioxythiophene) PEDOT/$V_2O_5$ nanocomposite by intercalation

**A. Vadivel Murugan,*[a] B. B. Kale,[a] Chai-Won Kwon,[b] Guy Campet[b] and K. Vijayamohanan*[c]**

[a]*Centre for Materials for Electronics Technology, Ministry of Information Technology Govt. of India, Panchavati, Off Pashan Road, Pune 411 008, India. E-mail: vadivel12@hotmail.com*
[b]*Institut de Chimie de la Matiere Condensee de Bordeaux du CNRS, Chateau Brivazac, avenue du Dr. A. Schweitzer, 33608 Pessac, France*
[c]*Physical and Materials Chemistry Division, National Chemical Laboratory, Pune 411 008, India*

***Received 19th January 2001, Accepted 19th June 2001***
***First published as an Advance Article on the web 31st August 2001***

We have developed a novel nanocomposite material, PEDOT/$V_2O_5$ by inserting poly(3,4-ethylene dioxythiophene) PEDOT in $V_2O_5$ layers using oxidative polymerization/intercalation in air. A systematic study of the synthesis of the nanocomposites by direct *in situ* reaction of 3,4-ethylene dioxythiophene (EDOT) with $V_2O_5$ fine powder shows that upon intercalation, the interlayer spacing of $V_2O_5$ expands in two stages, *i.e.*, first from 4.32 to 13.84 Å and further to 19.04 Å. The interlayer separation is consistent with the existence of two phases in the PEDOT/$V_2O_5$ system corresponding to the intercalation of one and two monolayers of PEDOT, respectively, in the $V_2O_5$ framework. The unique properties of the organo–inorganic composites are investigated by electronic conductivity measurements, X-ray diffraction, FTIR spectroscopy, thermogravimetric analysis and SEM. The application potential of these composites as cathode materials in rechargeable lithium batteries is also demonstrated by the electrochemical intercalation of lithium into the PEDOT/$V_2O_5$ nanocomposites, where an enhancement in the discharge capacity (240 mA h $g^{-1}$) is observed compared to that (140 mA h $g^{-1}$) observed for $V_2O_5$.

## Introduction

Recently, soft chemistry ("*Chimie douce*") has been shown to be an effective method for the preparation of conducting polymer based nanocomposites for several applications such as light emitting diodes, supercapacitors, chemical sensors, and nonlinear optics.[1–4] The low temperature processing of such nanocomposites is especially relevant in the area of rechargeable lithium batteries where the composition and structure can be modulated to obtain many advantages such as the formation of amorphous matrices to facilitate lithium ion transport, flexibility with respect to fabrication, high energy density, good cycle life, *etc.*[5–8] Although the early studies on two-dimensional or layered oxides/sulfides of transition metals primarily involved the intercalation of simple, small molecules or ions into van der Waals gaps, later several new classes of these materials were developed based on the extension of these concepts, including the incorporation of macromolecular species.[9,10] In particular, the insertion of conjugated polymers has been examined extensively over the past few years.[11–23] One approach is based on the oxidation of the polymer backbone (p-doping), where the method provides materials that are highly conductive, and poses fascinating questions as to the change in their properties upon intercalation. For example, the degree to which the polymer–polymer interactions in the bulk are affected by the polymer host is not clear and questions related to how the polymer–host interactions sequester the polymer chains affecting either the polymer conformation, chain length, and/or bulk electron-transport properties are not fully elucidated. In addition, there is also the possibility of electron or hole transfer between the polymer and the inorganic component especially if the latter is a transition metal oxide with conductive properties.[24] More significantly, the application of either conjugated polymers[25] or transition metal oxides[26] individually as positive electrodes in rechargeable lithium batteries also suggests that when these polymer/oxide materials are blended together at a "nanoscale" level new properties are possible due to synergistic effects.

During the past several years many conducting polymers have been inserted into layered transition metal oxides to form nanocomposites. For example, Kanatzidis, Gomez-Romero, and their co-workers have inserted polyaniline, one of the few conducting polymers that is completely air stable in the p-doped form into $V_2O_5$ to form a nanocomposite.[27–30] Unfortunately, owing to the possible presence of benzidine moieties in the polymer backbone, the application of these systems is limited since they might yield toxic (carcinogenic) products upon degradation.[31] Numerous industrial and academic groups have considered alternatives to polyaniline including the (hetero) aromatic polypyrrole and polythiophene, two more "environment friendly" systems.[32] In this context it may be better to use poly(3,4-ethylene dioxythiophene) (PEDOT), one of the recently found excellent conducting polymers, as it has been reported to exhibit greatly enhanced stability compared to polypyrrole and polyaniline.[33,34] Indeed, it appears to be one of the most stable conducting polymers currently available[35] and has been attracting growing interest for applications in supercapacitors[36,37] and lithium ion batteries.[38–40]

In this communication we report the successful preparation of PEDOT/$V_2O_5$ nanocomposites by a soft method of intercalation, where the resulting nanocomposite shows improved room temperature conductivity and enhanced lithium ion mobility compared to the polymer free vanadium oxide. The primary objective is to characterize the redox intercalation reaction of EDOT with $V_2O_5$ powder and the subsequent

 DOI: 10.1039/b100714i

polymerization chemistry associated with this system to demonstrate the existence of two phases in the PEDOT/$V_2O_5$ system corresponding to the intercalation of one or two monolayers of PEDOT into $V_2O_5$. These observations are supported by several physicochemical data and the microstructure of PEDOT/$V_2O_5$ nanocomposites, attributed in part, to the polymer propping open the inorganic layers, effectively reducing electrostatic and steric effects which hinder lithium diffusion through the material. Preliminary measurements on the PEDOT/$V_2O_5$ nanocomposite system during few initial charge–discharge cycles show an excellent capacity of 240 mA h $g^{-1}$ compared to 140 mA h $g^{-1}$ observed for $V_2O_5$, after coupling these nanocomposites as cathodes with a lithium metal anode using 1 M $LiClO_4$ in a mixed electrolyte of ethylene carbonate and dimethyl carbonate. To our knowledge, this is the first study of electrochemical Li-insertion into a PEDOT/vanadium oxide nanocomposite, which shows that the improved capacity is related to the presence of the conducting polymer in the interlamellar region.

## Experimental

### Materials

Vanadium pentoxide (99%), lithium metal foil (99.9%), $LiClO_4$ (99.99%) and dimethyl carbonate (DMC, 99%), purchased from Aldrich were used without further purification. Ethylene dioxythiophene (Bayer AG Germany) was distilled under vacuum prior to use; ethylene carbonate (EC, Prolabo 99%), Chevron Carbon black and PTFE (Teflon) binder were used as received. All the experiments were conducted with double distilled water.

### Characterization

Fourier transform infrared (FTIR) spectra were recorded from pressed KBr pellets using a Perkin-Elmer spectrum-2000 FTIR spectrometer. The X-ray powder diffraction studies were carried out with a Bruker AXS D5005 instrument in the range 3–80° using Cu-K$\alpha$ radiation. Thermogravimetric analysis (TGA/DTA) was performed with a Shimadzu TGA-50 thermal analysis system using dry oxygen as a carrier gas. The TGA experiments were conducted from room temperature to 800 °C at a linear heating rate of 10 °C $min^{-1}$. Electronic conductivity measurements were made on compactions of powder in pellet form by using a four probe conductivity method, while scanning electron microscopy (SEM) images were taken on a Philips XL-30 microscope after mounting samples on Al stubs with gold coatings. The electrochemical measurements were performed using a computer controlled Tacussel, PGS 201T model, potentiostat/galvanostat. Elemental analysis was carried out using inductively coupled plasma optical emission spectroscopy (ICP-OES, Perkin-Elmer 1000) and using a CE-Instruments-EA 1110 CHNS-O Analyser.

### Synthesis of PEDOT/$V_2O_5$ nanocomposites

Insertion of PEDOT into $V_2O_5$ by a soft process in aqueous medium was carried out by dissolving a given amount of EDOT in double distilled water and refluxing this with crystalline vanadium pentoxide for 12 h. The molar ratio of EDOT/$V_2O_5$ was varied from 0.02 to 0.6 in five different compositions. After completion of the reaction, the solid was filtered off and washed repeatedly with water and acetone until the initial light yellow color in the filtrate was totally absent, and the bluish black powder was dried in air. The vanadium content was determined by applying ICP-OES analysis to the sample solution that was prepared by placing the composite powder in a concentrated sulfuric acid solution to dissolve the $V_2O_5$ in the composite, followed by dilution with water and filtration to remove the dispersed polymer. Elemental analysis of nanocomposites: $(C_6H_4O_2S)_{0.02}\cdot V_2O_5$ **A**: C, 0.84%; H, 1.15%; S, 0.17%; V, 44.53%. $(C_6H_4O_2S)_{0.04}\cdot V_2O_5$ **B**: C, 1.35%; H, 1.48%; S, 0.28%; V, 43.67%. $(C_6H_4O_2S)_{0.08}\cdot V_2O_5$ **C**: C, 2.12%; H, 1.61%; S, 1.09%; V, 39.15%. $(C_6H_4O_2S)_{0.40}\cdot V_2O_5$ **D**: C, 6.92%; H, 1.54%; S, 3.77%; V, 34.36%. $(C_6H_4O_2S)_{0.60}$ $V_2O_5$ **E**: C, 9.01%; H, 1.07%; S, 4.86%; V, 33.66%.

### Electrochemical measurements

Electrochemical measurements were carried out using composite cathodes, prepared by mixing the PEDOT/$V_2O_5$ nanocomposite powder with carbon black and PTFE binder (70:25:5 by weight), followed by compaction and drying under a primary vacuum for 3 h at 80 °C. This composite cathode was coupled with a lithium foil anode in 1 M $LiClO_4$ dissolved in a mixture of ethylene carbonate and dimethyl carbonate (50/50 by volume) to form the electrochemical cell. All charge–discharge measurements were performed in galvanostatic mode using a computer controlled potentiostat/galvanostat. All manipulations of air sensitive materials as well as the cell assemblies were carried out in an inert atmosphere of an argon filled glove box.

## Results and discussion

The intercalation of EDOT in $V_2O_5$ powder is a redox reaction in which EDOT is oxidatively polymerized, concomitantly reducing vanadium during the refluxing conditions to form a relatively quasi-crystalline layered material, and is associated with a dramatic color change to dark blue. Generally if the solvent containing EDOT is able to swell the $V_2O_5$ powder, the intercalation reaction is observed to be fast whilst there was no swelling (or intercalation) if $V_2O_5$ was refluxed with neat EDOT. Water is reported to be a good solvent for the completion of polymeric intercalation in oxide layers, in comparison with organic solvents;[29] water molecules can be expelled from the slightly hydrophobic intragallery space during intercalation, allowing more polymer to be inserted. The composites obtained from the reaction between EDOT and $V_2O_5$ in aqueous medium showed good lamellar order, as judged by the following physicochemical characterization techniques.

### X-Ray diffraction and SEM studies

Fig. 1 shows a comparison of the powder XRD patterns for the series of PEDOT/$V_2O_5$ composites and $V_2O_5$ to demonstrate the subtle structural changes upon intercalation. The strongest peak observed at low angle corresponding to the (001) plane of the layered $V_2O_5$ structure is directly related to the interlayer spacing. The main features of the $V_2O_5$ diffraction pattern in the composites are clearly modified by the appearance of a sharp diffuse scattering feature and an increase in the intensity of the (001) peak. Within the series of nanocomposites, a clear change in the position of the peak takes place, which indicates differences between samples. Samples **A**–**C** with EDOT/$V_2O_5$ ratios of 0.02–0.08 show the (001) peak at $2\theta$ 6.6–6.4°, which corresponds to an interlayer spacing of 13.84–14.02 Å, respectively, *cf.* the interlayer spacing of $V_2O_5$ of 4.32 Å. More interestingly, this peak in the patterns for **D** and **E** has shifted to lower angle, 5.0 to 4.5°, corresponding to an interlayer spacing of 17.8 and 19.04 Å, respectively, which is substantially larger than that found for the samples **A**–**C**.

This behavior is summarized in Fig. 2 (also see inset), where the evolution of the *c* parameter is shown in relation to the nominal EDOT/$V_2O_5$ ratio used in the preparation of each sample. There are two regions with qualitatively different features, which confirm the existence of phases with distinct structures. This suggests that PEDOT intercalation occurs in

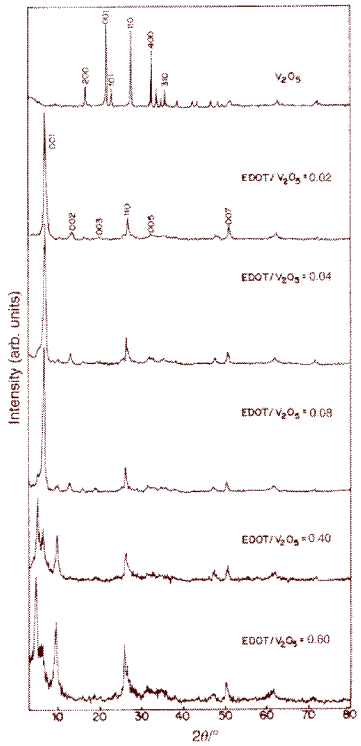


**Fig. 1** Powder X-ray diffraction patterns of $V_2O_5$ powder and PEDOT/$V_2O_5$ nanocomposites **A**–**E** synthesized with different ratios of EDOT/$V_2O_5$.

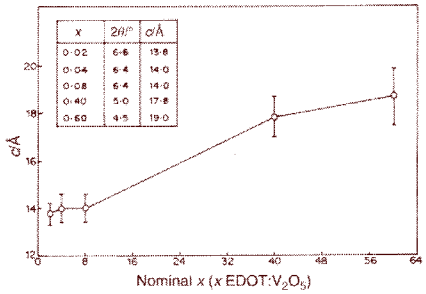


**Fig. 2** Plot of interlayer spacing in $V_2O_5$ ($c$ parameter in Å, calculated from the position of 001 peaks) *vs.* the EDOT/$V_2O_5$ ratio as derived from Fig. 1.

two steps, leading to the formation of two correspondingly different phases. The first one represents an expansion from 4.32 to 13.84 Å and can be explained by monolayer formation of PEDOT. On the other hand, the formation of the second phase, associated with an additional expansion of the $c$ parameter to 19.04 Å indicates double the amount of PEDOT between layers per $V_2O_5$ unit as reported recently for the PANI/$V_2O_5$ system.[30] Thus it is likely that these materials constitute a new PEDOT/$V_2O_5$ composite phase consisting of a double layer of PEDOT chains intercalated within the $V_2O_5$ interlayer spacing. (see Scheme 1)

SEM micrographs of $V_2O_5$ and a synthesized PEDOT/$V_2O_5$ composite are illustrated in Fig. 3. It is apparent that PEDOT/$V_2O_5$ composites form a continuous and relatively homogeneous matrix with a clearly lamellar morphology. It is evident that the incorporation of PEDOT into the $V_2O_5$ leads to morphological changes in agreement with the results of XRD patterns, but these can be seen only at high resolution. More significantly, the SEM micrographs also suggest that there is no bulk deposition of polymer on the surface of the micro-crystallites.

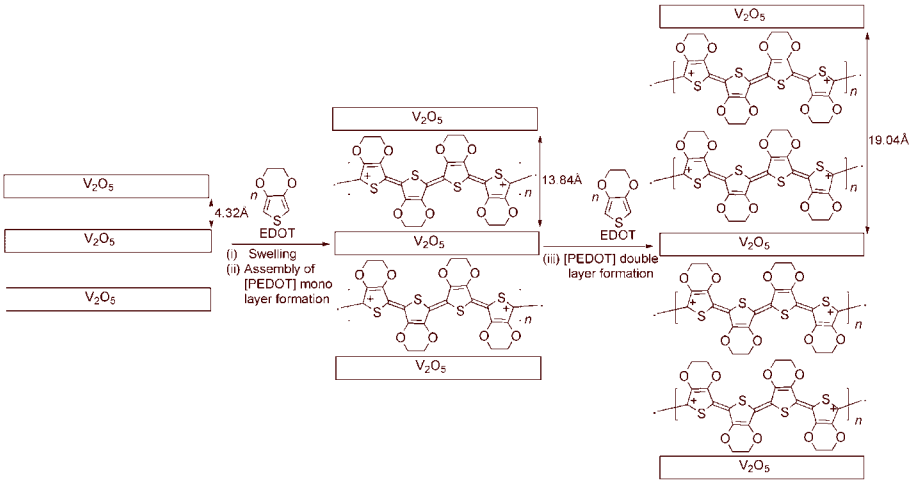


**Scheme 1** Schematic diagram of the swelling and assembly process of monolayer and double-layer formation of PEDOT into the $V_2O_5$ layers during preparation of the nanocomposites.

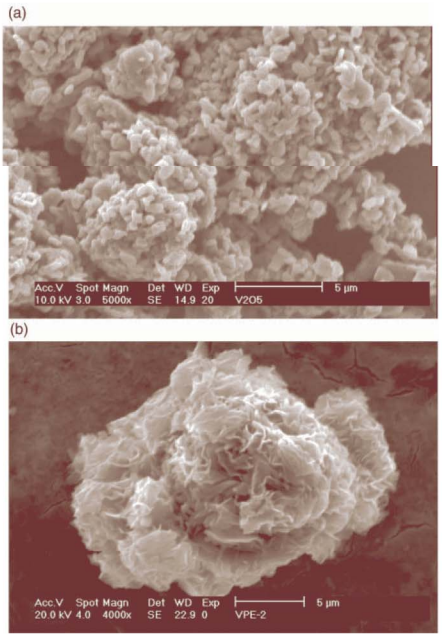


**Fig. 3** SEM micrographs of (a) $V_2O_5$ and (b) PEDOT/$V_2O_5$ nanocomposite **C** synthesized with EDOT/$V_2O_5$ = 0.08.

### FTIR spectroscopic studies

Fig. 4 shows the FTIR spectra of different samples of PEDOT/$V_2O_5$ nanocomposites synthesized with various amounts of EDOT as described above. The spectrum for **C** (EDOT/$V_2O_5$ = 0.08), is discussed as a representative example, which presents the characteristic bands corresponding to PEDOT (bands in the range 1049–1600 $cm^{-1}$) as well as bands at lower frequencies assigned to $V_2O_5$ (523 and 759 $cm^{-1}$ for V–O–V stretching modes and 1003 $cm^{-1}$ for V=O stretching). The changes in position and shape of the vibrational peaks of the vanadium oxide framework are also significant. The V=O peak shifts from 990 to 1003 $cm^{-1}$ while the V–O–V vibrational peaks shift from 852 and 530 $cm^{-1}$ to 758 and 523 $cm^{-1}$, respectively. These changes are attributed to the greater number of $V^{4+}$ centers present in the nanocomposite. The mechanism of this remarkable all-solid-state intra-lamellar polymerization is presumed to be coupled to the ability of vanadium centers[41] to activate oxygen. Therefore, vanadium oxide plays a direct role in this redox event, which is consistent with its ability to catalyze several oxidation reactions of organic molecules.[42] The qualitative differences between spectra of **D** and **E** relative to nanocomposites **A**–**C** relate to bands at 1218 and 1105 $cm^{-1}$ owing to the presence of excess PEDOT in these two samples.

### Thermogravimetric analysis

The thermal stability of these materials in air was examined by TGA experiments. Two distinct stages were observed in the thermogravimetry and differential thermal analysis (TGA–DTA) curves as shown in Fig. 5. The first step, up to 120 °C, corresponds to the removal of the reversibly bound water, whereas the second step at ~215 °C corresponds to the loss of more strongly bound water between the layers. This is followed by a continuous weight loss up to ~420 °C which can be attributed to the combustion of the organic polymer component, in agreement with the exothermic peak in the DTA curve. A subsequent mass gain up to 650 °C can be attributed to the formation of orthorhombic $V_2O_5$. Crystallization of this phase was evidenced from the DTA curve which showed a relatively sharp endotherm peak at 650 °C. These results suggest that the insertion and polymerization of the 3,4-ethylene dioxythiophene (EDOT) monomer is accompanied by 'sacrificial' reduction of the $V_2O_5$ layers.

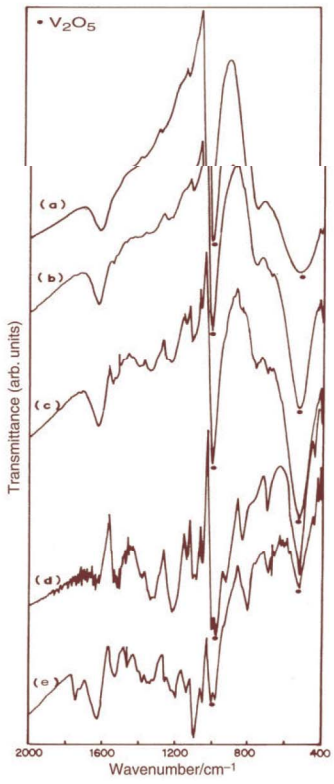


**Fig. 4** FTIR spectra of the PEDOT/$V_2O_5$ nanocomposites **A**–**E** obtained with different EDOT/$V_2O_5$ ratios; (a) 0.02, (b) 0.04, (c) 0.08, (d) 0.40, (e) 0.60; peaks assigned to $V_2O_5$ are indicated by filled circles.

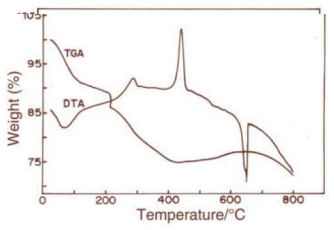


**Fig. 5** TGA–DTA curves of PEDOT/$V_2O_5$ composite **C** (ratio of 0.08), as a representative example.

**Table 1** Comparison of room temperature conductivity, interlayer spacing and open circuit voltage with EDOT/$V_2O_5$ ratio in composites **A–E**

| | Nanocomposite | EDOT : $V_2O_5$ ratio | Interlayer spacing/Å | Electronic conductivity, $\sigma$/S cm$^{-1}$ | Open circuit voltage[a]/V |
|---|---|---|---|---|---|
| 1. | $V_2O_5$ | | 4.32 | $8.78 \times 10^{-5}$ | 3.43 |
| 2. | **A** | 0.02 | 13.84 | $2.92 \times 10^{-3}$ | 3.74 |
| 3. | **B** | 0.04 | 14.00 | $6.97 \times 10^{-3}$ | 3.76 |
| 4. | **C** | 0.08 | 14.02 | $3.84 \times 10^{-2}$ | 3.77 |
| 5. | **D** | 0.40 | 17.80 | $9.82 \times 10^{-2}$ | 3.62 |
| 6. | **E** | 0.60 | 19.04 | $1.01 \times 10^{-1}$ | 3.61 |

[a]The open circuit voltage is obtained from the charge–discharge measurements of $V_2O_5$ and PEDOT/$V_2O_5$ nanocomposites synthesized from EDOT/$V_2O_5$ (ratio 0.02–0.6), as a cathode material by coupling with a lithium metal anode using 1 M $LiClO_4$ in a mixed electrolyte of ethylene carbonate and dimethyl carbonate.

### Electronic conductivity

The electrical transport behavior of nanocomposites can be understood by considering the insertion of poly(3,4-ethylene dioxythiophene) in $V_2O_5$ powder as a composite system in which two different types of low-dimensional electronic conductors coexist at the molecular level in a dimensionally constrained environment. Two types of charge carriers can be present in these materials, small polarons (electrons) associated with the $d^1$ ($V^{4+}$) centers on the vanadium oxide lattice, and large polarons on the poly(3,4-ethylene dioxythiophene) backbone. The actual nature of charge transport would depend on the relative mobility of these two different types of carriers as demonstrated by the fact that the electronic conductivity of PEDOT/$V_2O_5$ is $10^4$ times higher than that of pristine $V_2O_5$. In all samples, the conductivity is almost exclusively electronic under our experimental conditions, and increases with temperature as has been observed in most intercalated compounds and conjugated polymers.[12–42] For similar PEDOT/$V_2O_5$ samples synthesized with different nominal EDOT/$V_2O_5$ ratios, the room temperature conductivity varies from $10^{-1}$ to $10^{-5}$ S cm$^{-1}$. In this case the increase in conductivity is probably due to a continued process of growth of the organic polymer network. The conductivity increases as the length of polymer chain increases from **A–E** although the exact mechanism may be complex (see Table 1)

### Electrochemical lithium insertion

Vanadium oxide host lattice has been proposed as a good cathode material in secondary Li-batteries, mainly due to its layered structure which is highly suitable for Li-insertion.[43,44] For battery applications, the rate limiting step is reported to be the reduction of $V_2O_5$ material during discharge accompanied by $Li^+$ insertion.[45] One common strategy to achieve higher efficiency and lithium uptake is to use high surface area materials, so that the distance over which $Li^+$ must diffuse through the host material is minimized.[46–50] For example, $V_2O_5$ nanotubes have been recently reported to give rise to a discharge capacity of 186 mA h g$^{-1}$ compared to 140 mA h g$^{-1}$ observed for the bulk oxide.[51] Another approach that has not been completely explored yet is to manipulate the interlayer spacing in these layered materials by using various intercalants so as to enhance the rate of $Li^+$ migration (it is well-known that intercalation leads to changes in the interlayer spacing for layered materials).[52,53] Examples of such intercalants include pyrrole and aniline, which are known to oxidatively polymerize when intercalated into highly oxidizing materials such as $V_2O_5$.[15–23] The electrochemical insertion of Li in $V_2O_5$ material can be described by the redox couple of eqn. (1).

$$x\mathrm{Li}^+ + x\mathrm{e}^- + \mathrm{V_2O_5} \leftrightarrow \mathrm{Li}_x\mathrm{V_2O_5} \quad (1)$$

For PEDOT/$V_2O_5$ nanocomposites, we can write analogous electrochemical reactions [eqns. (2) and (3)] after incorporating lithium ions between the layers

$$[\mathrm{PEDOT}^+]_x\mathrm{V_2O_5}^{x-} + x\mathrm{Li}^+ + x\mathrm{e}^- \underset{\text{Reduction of PEDOT}}{\longleftrightarrow} \mathrm{Li}_x[\mathrm{PEDOT}]_x\mathrm{V_2O_5}^{x} \quad (2)$$

$$\mathrm{Li}_x[\mathrm{PEDOT}]_x\mathrm{V_2O_5}^{x-} + y\mathrm{Li}^+ + y\mathrm{e}^- \underset{\text{Reduction of } \mathrm{V_2O_5}^{x-}}{\longleftrightarrow} \mathrm{Li}_{x+y}[\mathrm{PEDOT}]_x\mathrm{V_2O_5}^{-(x+y)} \quad (3)$$

The open-circuit voltage (OCV) of the composites when coupled with a lithium metal anode is found to be a function of the PEODT/$V_2O_5$ ratio and clearly all nanocomposites give higher OCV values (3.61–3.77) than that observed (3.43) for pure $V_2O_5$ (Table 1). The discharge process of the Li/$V_2O_5$ cell seems to be thermodynamically more favorable as the deviation from open circuit voltage is less for a given current density. However, the discharge capacity is found to be significantly enhanced (240 mA h $g_{composite}^{-1}$ for PEDOT/$V_2O_5$ nanocomposites compared to 140 mA h g$^{-1}$ for pure $V_2O_5$) under similar experimental conditions. A typical example is illustrated in Fig. 6 showing the charge–discharge behavior of pure $V_2O_5$ and a representative example of a nanocomposite, **A** (EDOT/$V_2O_5$ ratio of 0.02). Better reversibility for the composite is also suggested by the reduced overpotentials reflected in both charge and discharge curves. This indicates that the effect of PEDOT intercalated into the $V_2O_5$ framework in enhancing the discharge capacity of $V_2O_5$ material can be attributed to the changes in the interlayer spacing due to more facile lithium ion diffusion.

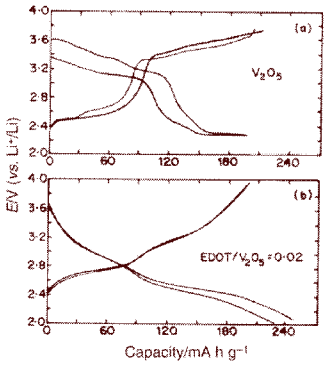


**Fig. 6** Typical charge–discharge curves of (a) $V_2O_5$ and (b) PEDOT/$V_2O_5$ nanocomposite **A** (EDOT/$V_2O_5$ ratio of 0.02), as a cathode material by coupling with a lithium metal anode using 1 M $LiClO_4$ in a mixed electrolyte of ethylene carbonate and dimethyl carbonate using a constant current density of 15 mA g$^{-1}$ (electrode surface area is ~1 cm$^2$).

## Conclusions

We have found a novel method of interleaving poly(3,4-ethylene dioxythiophene) between the layers of $V_2O_5$ using a soft process of intercalation. The reaction takes place with the *in situ* polymerization of EDOT within the framework of $V_2O_5$ with different nominal EDOT/$V_2O_5$ ratios to give two distinct phases. These two phases can be distinguished by their different interlayer spacings as detected from powder X-ray diffraction patterns. The fact that two distinct phases rather than a continuum of compositions are obtained in this system suggest the existence of a significant interaction between the host and guest beyond simple insertion into van der Waals gaps and is closer to the formation of true compounds. The experimental data presented here suggest that polymerization proceeds concomitantly with intercalation. The polymer chains appear fixed in the interlamellar space, and the ring flips observed in the bulk form of PEDOT are frozen in these materials. Therefore, there is considerable bonding interaction between the organic and inorganic components, probably due to hydrogen bonding. We observed that the influence of intercalants on $Li^+$ diffusion rates and charge capacity in the PEDOT/$V_2O_5$ nanocomposite was increased relative to $V_2O_5$. The results also suggest that the polymer nanocomposites act as better cathode materials than the pristine $V_2O_5$ oxide material by enhancing lithium diffusion.

## Acknowledgements

A. V. M. would like to thank Dr B. K. Das (Executive Director, C-MET) and gratefully acknowledge to Messrs Bayer AG, Germany, Mr S. D. Joshi (Bayer India Ltd. Mumbai) and Dr Tanay Seth for SEM analysis, Mr S. K. Apte for FTIR analysis, Mr P. Sasidharan, Mr S. N. Potty for XRD analysis and Mrs S. D. Adyanthaya (NCL) for thermogravimetric analysis.

## References

1 V. L. Colvin, M. C. Schlamp and A. P. Alivisatos, *Nature*, 1994, **370**, 354.
2 C. Arbizzani, M. Mastragostino, L. Meneghello and R. Paraventi, *Adv. Mater.*, 1996, **8**, 331.
3 M.-I. Baraton, L. Merhara, J. Wang and K. E. Gonsalves, *Nanotechnology*, 1998, **9**, 356.
4 B. R. Mattes, E. T. Knobbe, P. D. Fuqua, F. Nishid, E. W. Chang, B. M. Pierce, B. Dunn and R. B. Karner, *Synth. Met.*, 1991, **43**, 3183.
5 S. Kakuda, T. Momma, T. Osaka, B. G. Appetecchi and B. Scrosati, *J. Electrohem. Soc.*, 1995, **142**, L1.
6 F. Leroux, B. E. Koene and L. F. Nazar, *J. Electrochem. Soc.*, 1996, **143**, L181.
7 E. Shouji and A. D. Buttry, *Langmuir*, 1999, **15**, 669.
8 A. J. Jacobson and M. S. Whittingham, *Intercalation Chemistry*, Academic Press, New York, 1982.
9 J. P. Pereira-Ramos, *J. Power Sources*, 1995, **54**, 120.
10 J. P. Pereira-Ramos, N. Baffier and G. Pistoia, in *Lithium batteries, New Materials, Developments and Perspectives*, ed. G. Pistoia, Elsevier, Amsterdam, 1994, p. 281.
11 E. Ruiz-Hitzky, *Adv. Mater.*, 1993, **5**, 334.
12 H. H. Javadi, K. R. Cromack, A. G. Mac Diarmid and A. Epstein, *J. Phys. Rev. B*, 1989, **39**, 3579.
13 H. H. S. Javadi, R. Laversanne, A. J. Epstein, R. K. Kohli, E. M. Sherr and A. G. Mac Diarmid, *Synth. Met.*, 1989, **29**, E439.
14 F. Zuo, M. Angelopoulos, A. G. Mac Diarmid and A. Epstein, *J. Phys. Rev. B*, 1989, **39**, 3570.
15 M. G. Kanatzidis, C.-G. Wu, H. O. Marcy and C. R. Kannewurf, *J. Am. Chem. Soc.*, 1989, **111**, 4139.
16 C.-G. Wu, M. G. Kanatzidis, H. O. Marcy, D. C. Degroot and C. R. Kannewurf, *Polym. Mater. Sci. Eng.*, 1989, **61**, 969.
17 C.-G. Wu, M. G. Kanatzidis, H. O. Marcy, D. C. Degroot and C. R. Kannewurf, *NATO Advanced Study Institute, Lower Dimensional Systems and Molecular Devices*, ed. R. M. Metzger, Plenum Press, New York, 1991, p. 427.
18 M. G. Kanatzidis, H. O. Marcy, D. C. Degroot and C. R. Kannewurf, *Chem. Mater.*, 1990, **2**, 221.
19 C.-G. Wu and M. G. Kanatzidis, *Symposium on Solid State Ionics* ed. G. Nazri, R. A. Huggins, D. F. Shriver and M. Balkanski, *MRS Symp. Proc.*, 1991, **210**, 429.
20 D. C. Degroot, J. L. Schindler, C. R. Kannewurf, Y.-J. Liu, C.-G. Wu and M. G. Kanatzidis, *Symposium on Submicron Multiphase Materials*, ed. R. Baney, L. Gilliom, H. Schmidt, and S.-I. Hirano, *Mater. Res. Soc. Symp. Proc.*, 1992, 133.
21 C.-G. Wu, D. C. Degroot, H. O. Marcy, J. L. Schindler, C. R. Kannewurf, T. Bakas, V. Papaefthymiou, W. Hirpo, J. Yes-nowski, Y.-J. Liu and M. G. Kanatzidis, *J. Am. Chem. Soc.*, 1995, **117**, 9229.
22 M. G. Kanatzidis, C.-G. Wu, H. O. Marcy, D. C. Degroot, J. L. Schindler, C. R. Kannewurf, M. Benz and E. L. Goff, *Supramolecular Chemistry in Two and Three Dimensions*, ed. T. Bein, *ACS Symp. Ser.*, 1992, **499**, 194.
23 M. G. Kanatzidis, C.-G. Wu, D. C. Degroot, J. L. Schindler, M. Benz, E. L. Goff and C. R. Kannewurf, *NATO Advanced Study Institute in Chemical Physics of Intercalation*, ed. P. Bernier, J. E. Fischer, S. Roth and S. Solin, Plenum Press, New York, 1993, p. 63.
24 P. Day, *Philos. Trans. R., Soc. London A*, 1985, **314**, 145.
25 F. Bonino and B. Scrosati, in *Materials for Solid State Batteries*, ed. B. V. R. Chowdari and S. Radhakrishna, World Scientific, Singapore, 1986, p. 53.
26 J. Desilvestro and O. Haas, *J. Electrochem. Soc.*, 1990, **137**, 5C.
27 Y. J. Liu, D. C. DeGroot, J. L. Schlindler, C. R. Kannewurf and M. G. Kanatzidis, *J. Chem. Soc., Chem. Commun.*, 1993, 593.
28 M. G. Kanatzidis and C. Wu, *J. Am. Chem. Soc.*, 1989, **111**, 4139.
29 C.-G. Wu, D. C. DeGroot, H. O. Marcy, J. L. Schindler, C. R. Kannewurf, Y.-J. Liu, W Hirpo and M. G. Kanatzidis, *Chem. Mater.*, 1996, **8**, 1992.
30 P. Gomez-Romero and M. Lira-Cantu, *J. Solid State Chem.*, 1999, **147**, 601.
31 F. Lux, *Farbe + Lack*, 1998, **104**, 32.
32 L. B. Groenendaal, F. Jonas, D. Freitag, H. Pielartzik and R. J. Reynolds, *Adv. Mater.*, 2000, **12**, 481.
33 G. Heywang and F. Jonas, *Adv. Mater.*, 1992, **4**, 116.
34 H. Yamato, M. Ohwa and W. Wernet, *J. Electroanal. Chem.*, 1995, **397**, 163.
35 I. Winter, C. Reese, J. Hormes, G. Heywang and F. Jonas, *Chem. Phys.*, 1995, **194**, 207.
36 S. Ghosh and O. Inganas, *Adv. Mater.*, 1999, **11**, 1214.
37 P. Novak, O. Inganas and R. Bjorklund, *J. Electrochem. Soc.*, 1987, **134**, 1341.
38 P. Novak, K. Muller, K. S. V. Santhanam and O. Haas, *Chem. Rev.*, 1997, **97**, 207.
39 M. Dietrich, J. Heinze, G. Heywang and F. Jonas, *J. Electroanal. Chem.*, 1994, **369**, 87.
40 T. Nakamura and M. Inagaki, *The 39th Battery Symposium in Japan, Nov. 25 27, 1998*, Sendai, pp. 283 284.
41 G. Geneti, D. Pinelli and F. Trifiro, *J. Mol. Catal.*, 1990, **59**, 221.
42 R. A. Ross and C. Fairbridge, *Can. J. Chem.*, 1984, **62**, 1483.
43 D. B. Le, S. Passerini, A. L. Tipton, B. B. Owens and W. H. Smyrl, *J. Electrochem. Soc.*, 1995, **142**, L102.
44 D. B. Le, S. Passerini, J. Guo, J. Ressler, B. B. Owens and W. H. Smyrl, *J. Electrochem. Soc.*, 1996, **143**, 2099.
45 *Rechargeable Lithium and Lithium ion Batteries*, ed. S. Megahed, B. M. Barnett and L. Xie, Electrochemical Society, New Jersey, 1995; *Electrochemical Society Proceedings Series PV* 94-28.
46 D. B. Le, S. Passerini, J. Guo, J. Ressler, B. B. Owens and W. H. Smyrl, *J. Electrochem. Soc.*, 1996, **143**, 2099.
47 M. S. Wittingham and A. J. Jacobson, *Intercalation Chemistry*, Academic Press, New York, 1982.
48 F. R. Gamble, F. J. Disalvo, R. A. Klemn and T. H. Geballe, *Science*, 1970, **168**, 568.
49 D. W. Murphy and G. W. Hull, *J. Chem. Phys.*, 1975, **62**, 973.
50 A. Lerf and R. Schollhorn, *Inorg. Chem.*, 1977, **11**, 2950.
51 M. E. Spahr, P. Stoschitzki-bitterli, R. Nesper, O. Haas and P. Novak, *J. Electrochem. Soc.*, 1999, **146**(8), 2780.
52 J. P. Lemmon and M. M. Lerner, *Chem. Mater.*, 1994, **6**, 207.
53 C. O. Oriakhi and M. M. Lerner, *Chem. Mater.*, 1996, **8**, 2016.

ELSEVIER

Journal of Power Sources 105 (2002) 1–5

JOURNAL OF POWER SOURCES

www.elsevier.com/locate/jpowsour

# Electrochemical lithium insertion into a poly(3,4-ethylenedioxythiophene)PEDOT/$V_2O_5$ nanocomposite

A. Vadivel Murugan[a,*], Chai-Won Kwon[b], Guy Campet[b], B.B. Kale[a], Trupti Maddanimath[c], K. Vijayamohanan[c]

[a]*Centre for Materials for Electronics Technology, Ministry of Information Technology, Government of India, Panchwati, Pashan Road, Pune 411 008, India*
[b]*Institut de Chimie da Ia Matiere Condensee de Bordaeaux du CNRS, Chateau Brivazac, Avenue du Dr. A. Schweitzer, 33608 Pessac, France*
[c]*Physical and Materials Chemistry Division, National Chemical Laboratory, Pune 411 008, India*

Received 10 July 2001; accepted 30 July 2001

**Abstract**

A nanocomposite comprised of conductive poly(3,4-ethylene dioxythiophene)PEDOT chains interleaved between the layers of crystalline $V_2O_5$ powder has been synthesized by direct in situ oxidation. The interlayer spacing of $V_2O_5$ expands from 4.32 to 13.84 Å and this interlayer separation is consistent with the existence of a monolayer of PEDOT in the $V_2O_5$ framework. The nanocomposite is coupled with a large-area Li foil counter electrode and a Li wire reference electrode in 1 M $LiClO_4$ in a mixture of ethylene and dimethylcorbonate (50/50 by volume), the discharge capacity is ≥300 m Ah $g^{-1}$ which is larger than that of pristine $V_2O_5$. The significant difference in capacity is explained on the basis of lithium ions insertion/de-insertion between the layers of $V_2O_5$. © 2002 Elsevier Science B.V. All rights reserved.

*Keywords:* Lithium insertion; PEDOT/$V_2O_5$ nanocomposite; Cathode material

## 1. Introduction

Research on active electrode materials for rechargeable lithium batteries is intense at present [1]. Recently, electronically conducting polymer-based molecular nanocomposites with transition metal oxide and sulfide have been synthesized by different approaches [2–7]. Vanadium oxide has been selected as the host lattice mainly because of its well-known performance as a good cathode material for rechargeable Li-batteries. This is due to its layered structure which is immensely suitable for Li insertion [8,9]. For battery applications, the rate-limiting step is reported to be the reduction of $V_2O_5$ during discharge accompanied by $Li^+$ insertion [10]. One common strategy to achieve higher efficiency and lithium uptake is to use high surface-area materials, so that the distance over which $Li^+$ must diffuse through the host material is minimized [11,12]. For example, $V_2O_5$ nanotubes have been reported [13] to give 186 mAh $g^{-1}$ compared with 140 mAh $g^{-1}$ observed for bulk oxide. Another approach that has not been completely explored yet is to manipulate the interlayer spacing in these layered materials using various intercalants so as to enhance the rate of $Li^+$ migration since it is well-known that intercalation leads to changes in the interlayer spacing for layered materials [14–16]. Examples of such conducting polymer intercalants, e.g. polyaniline have certain limitations such as the possible presence of benzidine moieties in the polymer backbone which might yield toxic (carcinogenic) products upon degradation [17]. Consequently, it is important to develop new nanocomposites based on the (hetero) aromatic thiophene monomer, which are known to be more "eco-friendly" systems to undergo oxidative polymerization when intercalated into highly oxidizing materials such as $V_2O_5$. Poly(3,4-ethylene dioxythiophene), hitherto referred to as PEDOT, is one of the recently found excellent conducting polymers and has been attracting growing interest for applications in supercapacitor and lithium-ion batteries [18–21]. Hence, we have selected this to design a new nanocomposite by intercalation into a $V_2O_5$ host and the results indicate that the nanocomposite is highly attractive for applications such as cathodes in lithium-batteries due to several improved properties, viz. room temperature conductivity and lithium-ion transport.

To our knowledge, this is the first study of preparation and electrochemical Li-insertion using such a nanocomposite, based on the PEDOT/$V_2O_5$ system. We find that PEDOT/$V_2O_5$ nanocomposites display higher discharge capacities and greater reversibility for Li-insertion than those observed for $V_2O_5$ alone.

* Corresponding author. Tel.: +91-20-589-8390; fax: +91-20-589-8180.
*E-mail address:* vadivel12@hotmail.com (A.V. Murugan).

0378-7753/02/$ – see front matter 
PII: S0378-7753(01)00992-2

## 2. Experimental

The PEDOT/$V_2O_5$ nanocomposites were prepared by the soft process of refluxing an aqueous solution which contained crystalline $V_2O_5$ powder and 3,4-Ethylene dioxy thiophene (EDOT) (0.02–0.08 molar ratio) under air for 12 h. After completion of the reaction, the solid was filtered off and washed repeatedly with water and acetone, and then dried at room temperature. Powder X-ray diffraction was performed (Bruker AXS D5005 using Cu Kα radiation) to study the formation of a polymer monolayer in the $V_2O_5$ layer upon intercalation. Fourier transform-infra red (FT-IR) spectra were recorded on Perkin-Elmer spectrum 2000 and thermogravimetric analysis was conducted using a Shimadzu TGA-50 instrument. The room temperature conductivity measurements were made on compactions of powder in pellets form by using a standard four-probe method. Electrochemical experiments were conducted with similar pellets of the nanocomposite (70 wt.% mixed with 5 wt.% polytetrafluoro ethylene and 25 wt.% acetylene black) as the working electrode. The electrode had a geometric area of 1 $cm^2$ and contained ~20 mg. This was coupled to a Li foil counter electrode of larger area and a Li wire references electrode in 1 M $LiClO_4$ in a mixture of ethylene and dimethyl carbonate (50/50 by volume) to form the cell. A constant current of 15 mAh $g^{-1}$ was applied between 2.0 and 4.2 V (versus $Li^+$/Li) for $V_2O_5$ or between 2.0 and 4.4 V for the hybrids. All charge-discharge and cyclic voltammetry measurements were performed using a compute-controlled potentiostat/galvanostat (Tacussel, PGS 201T model). The cell assemblies were carried out in an inert atmosphere of an argon filled glove box.

## 3. Results and discussion

### 3.1. FT-IR spectroscopic studies

Fig. 1 shows the FT-IR spectra of different samples of PEDOT/$V_2O_5$ nanocomposites synthesized with various amounts of EDOT as presented above. The spectrum for C (EDOT/$V_2O_5$ is 0.08) as a representative example, which shows the characteristic bands corresponding to PEDOT (bands in range 1049–1600 $cm^{-1}$) as well as bands in lower frequency range assigned to $V_2O_5$ (523 and 759 $cm^{-1}$ for V–O–V stretching modes and 1003 $cm^{-1}$ for V=O stretching). The changes in position and shape of the vibrational peaks of the vanadium oxide framework are also significant. The V=O peak shifts from 990 to 1003 $cm^{-1}$ while the V–O–V vibrational peaks shift from 852 and 530 $cm^{-1}$ to 758 and 523 $cm^{-1}$, respectively. These changes are attributed to the greater number of $V^{4+}$ centers present in the nanocomposite.

### 3.2. X-ray diffraction

The powder XRD diffraction patterns (Fig. 2) of the layered structure of PEDOT/$V_2O_5$ composites and crystalline $V_2O_5$

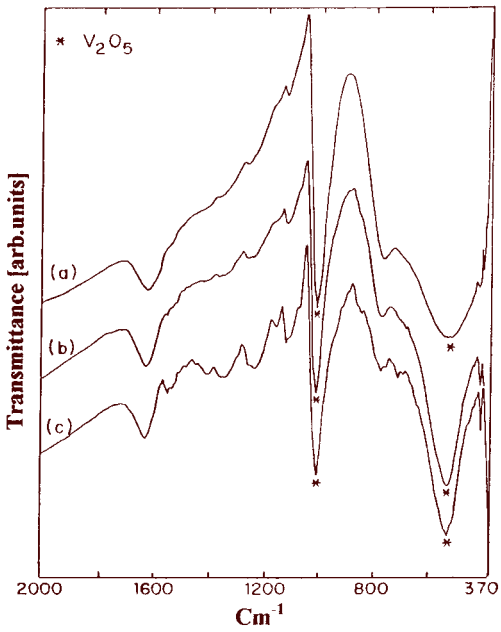


Fig. 1. FT-IR spectra of PEDOT/$V_2O_5$ nanocomposites obtained with different EDOT/$V_2O_5$ ratios: (a) 0.02, (b) 0.04, (c) 0.08. Peaks assigned to $V_2O_5$ are indicated by asterisks.

to demonstrate the subtle structural changes upon intercalation. The strongest peak observed at the low angle of 6.5° corresponding to the (*0 0 1*) plane of the layered $V_2O_5$ structure is directly related to the interlayer spacing. This interlayer spacing upon intercalation of crystalline $V_2O_5$ powder expands from 4.32 to 13.84 Å. Incorporation of PEDOT in $V_2O_5$ and increases the interlayer spacing to form the monolayer. Both effects are advantages for the Li-insertion process.

### 3.3. Thermal studies

Thermal stability measurements of these materials in air show that two distinct stages are present in the thermograms and also in the differential thermal analysis (TGA-DTA) curves, as shown in Fig. 3. The first step, up to 120° C, corresponds to the removal of the reversibly bound water, whereas, the second step at ~215 °C corresponds to the loss of more strongly bound water between the layers. A weight loss is observed at 435 °C in the PEDOT/$V_2O_5$ composite which corresponds to the combustion of the organic polymer component, followed by a gain in mass up to 600 °C, where orthorhombic $V_2O_5$ is formed. This mass increase is due to oxygen uptake by the $V^{4+}$ centers in the inorganic lattices that were generated during the formation of the nanocomposites in this latter redox reaction. The 3,4-Ethylene dioxy

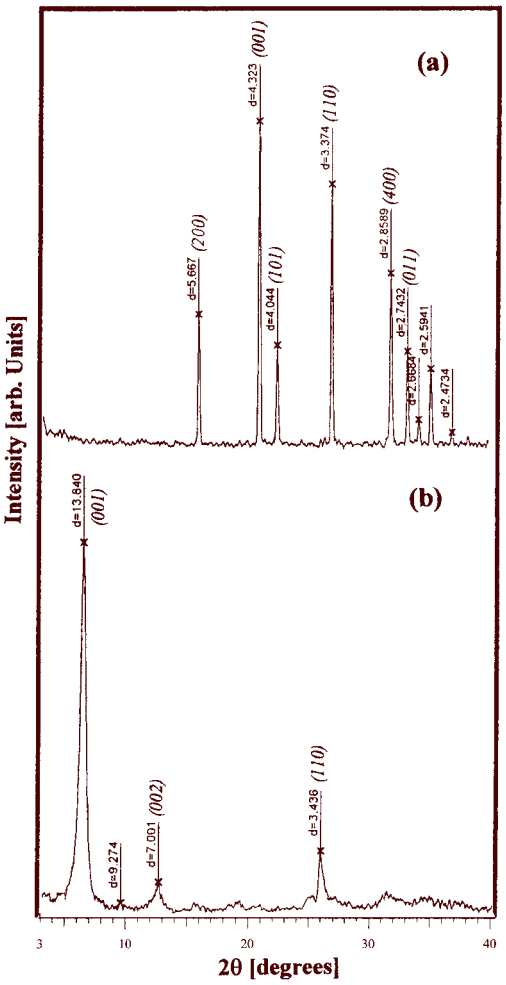


Fig. 2. Powder X-ray diffraction patterns of (a) $V_2O_5$, (b) PEDOT/$V_2O_5$ nanocomposite.

thiophene (EDOT) is oxidatively polymerized to poly(3,4-ethylene dioxythiophene) by sacrificial reduction of the $V_2O_5$ layers. Furthermore, evidence from the DTA curves also shows a large, relatively sharp exotherm at ~450 °C due to the degradation of the organic PEDOT between the layers, followed by another endotherm. We attribute this endothermic peak at 650 °C to oxygen uptake by the $V^{4+}$ centers, which thus changes into $V^{5+}$ to form $V_2O_5$.

### 3.4. Electronic conductivity

For PEDOT/$V_2O_5$ samples synthesized with different nominal EDOT/$V_2O_5$ ratios, the room temperature conductivity

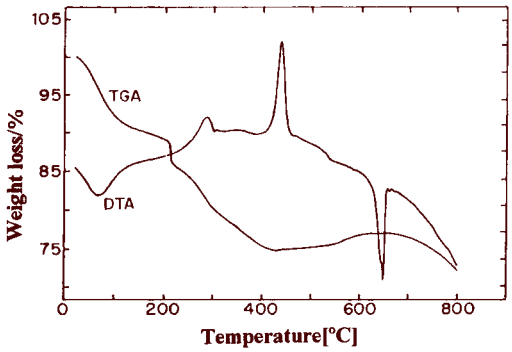


Fig. 3. TGA-DTA curves for PEDOT/$V_2O_5$ composite with a ratio of 0.08.

varies from $10^{-2}$ to $10^{-5}$ S $cm^{-1}$. In this case, the increase in conductivity is probably due to a continued process of growth of the organic polymer network, as evidenced from the X-ray diffraction patterns. The electrical transport behavior of the nanocomposite can be understood by considering the insertion of poly(3,4-ethylene dioxythiophene) in $V_2O_5$ powder as a composite system in which two different type of low-dimensional electronic conductors coexist at the molecular level in a dimensionally constrained environment. Two types of charge carrier can be present in these materials, namely: small polarons (electrons) associated with the $d^1$ ($V^{4+}$) centers on the vanadium oxide lattice, and massive polarons on the poly(3,4-ethylene dioxythiophene) backbone.

### 3.5. Electrochemical lithium insertion

For cyclic voltammetry, the voltage was cycled at a scan rate of 100 mV $s^{-1}$ between 2.2 and 3.8 V Li reference. The cyclic voltammograms in Fig. 4 illustrate a drastic change in

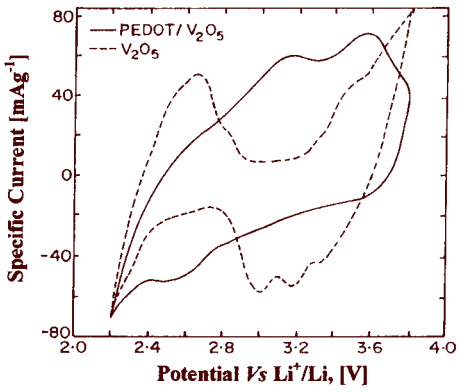


Fig. 4. Superimposed cyclic voltammograms of (a) $V_2O_5$ powder, and (b) PEDOT/$V_2O_5$ composite coupled with Li foil counter and Li wire reference electrodes in 1 M $LiClO_4$/EC and DMC; scan rate 100 mV $s^{-1}$.

electrochemical properties induced by the polymer insertion. During the first cathodic scan, from the open-circuit voltage to 2.2 V, pristine $V_2O_5$ undergoes well-known phase transformations [22]. The irreversible shift of the cathodic peak from 2.65 to 2.82 V means that the structural change is irreversible, which is in agreement with reports in the literature [22]. By contrast, the voltammogram for the PEDOT/$V_2O_5$ nanocomposite shows no sign for any irreversible structural change and has broad cathodic peaks. The broad and diffuse peak shape can, therefore, be correlated with the disturbed layer stacking derived by polymer incorporation, as previously deduced from X-ray diffraction data.

Potential versus capacity curves for the first two cycles down to 2.0 V (versus $Li^+/Li$), corresponding to uptake of ~2 Li per $V_2O_5$ unit, are presented in Fig. 5. pristine $V_2O_5$ shows distinctive plateau due to structural changes from α-$V_2O_5$ to ε-$Li_xV_2O_5$, then finally to the γ-$Li_xV_2O_5$ phase [22]. By contrast, the potential decreases more smoothly without any sign of phase transformation for the hybrid samples. A similar continuous decrease in potential has been also observed for $V_2O_5$ xerogel, 2D-$V_2O_5$ and other polymer/$V_2O_5$ hybrids whose common structural feature is the separation of the vanadium oxide layers due to the presence of interlayer molecules [23,24]. It should be noted that the PEDOT/$V_2O_5$ nanocomposite gives a higher capacity in the first charge process than in the first discharge. This is associated with the presence of $V^{4+}$, which can be easily oxidized by an electrochemical method, as already observed in the case of PPY/$V_2O_5$ and PTH/$V_2O_5$ hybrids [23,25]. A study of the effects of the initial charge process and oxygen treatment is in progress.

A more accurate inspection of insertion voltage is accomplished by analysis of the differential capacity profiles of the first discharges (insets in Fig. 5). The sharp peaks for pristine $V_2O_5$ are typical signs of the phase transformations, whereas the hybrids exhibit gross peaks. The PEDOT/$V_2O_5$

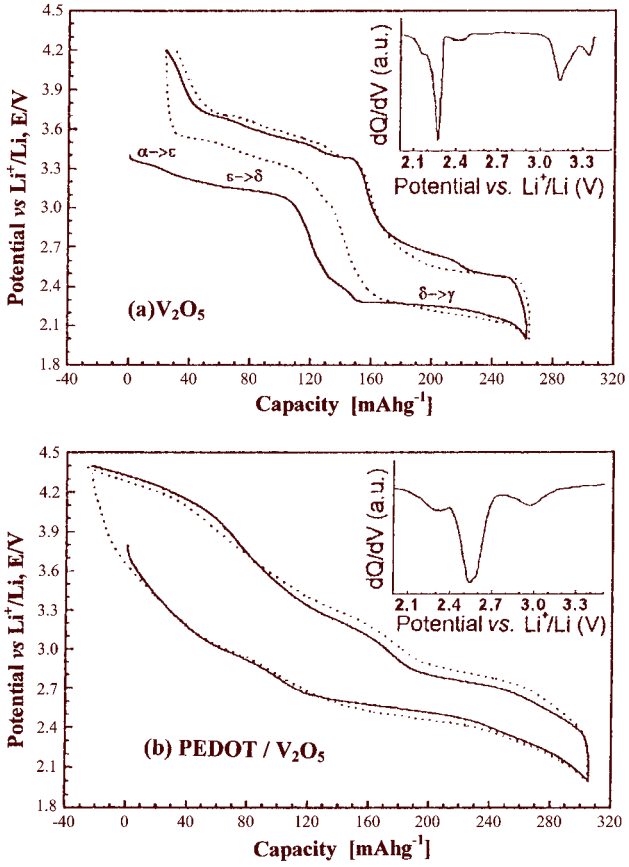


Fig. 5. Potential vs. capacity curves for first two cycles of (a) $V_2O_5$ and (b) PEDOT/$V_2O_5$ nanocomposite, as a cathode material coupled with Li foil counter and Li wire reference electrodes in 1 M $LiClO_4$/EC and DMC. Insets show corresponding differential profiles of first discharge.

nanocomposite shows three peaks at 2.9, 2.5 and 2.3 V analogous to PPY/$V_2O_5$ hybrids [23,25]. The discharge capacity of PEDOT/$V_2O_5$ nanocomposite is found to be $\geq$300 mAh $g^{-1}$ which is larger than pristine $V_2O_5$. The improved performances is presumably the result of the larger separation between vanadium oxide layers due to the presence of the polymer, which gives a structural stabilization. Therefore, we would like to suggest that judicious polymer incorporation into $V_2O_5$ is a way to improve its electrochemical properties by suppressing phase transformation and increasing the interlayer distance.

## 4. Conclusions

Interleaving poly(3,4-ethylene dioxythiophene) between the layers of $V_2O_5$ framework using a soft process of *in situ* polymerization gives a novel nanocomposite. Formation of the nanocomposite can be identified by IR fingerprints, and especially by the different interlayer spacing upon intercalation as detected by powder X-ray diffraction patterns, where a unique shift towards lower angle is observed and corresponds to monolayer formation. A PEDOT/$V_2O_5$ hybrid sample gives larger capacities and better reversibility than pristine $V_2O_5$.

The improved performance is presumably due to structural stabilization which results from incorporation of the polymer between vanadium oxide layer. The results also suggest that the polymer nanocomposite acts as a better cathode material than pristine $V_2O_5$ oxide material by enhancing lithium diffusion.

## References

[1] M. Winter, J.O. Besenhard, M.E. Spahr, P. Novak, Adv. Mater. 10 (1998) 725.
[2] S. Ye, D. Belanger, J. Phys. Chem. 100 (1996) 15848.
[3] E. Shouji, Y. Yokoyama, J.M. Pope, N. Oyama, D.A. Buttry, J. Phys. Chem. B 101 (1997) 2861.
[4] K. Naoi, K.-i. Kawase, M. Mori, M. Komiyama, J. Electrochem. Soc. 144 (1997) L173.
[5] S. Kuwabata, T. Idzu, C.R. Martin, H. Yoneyama, J. Electrochem. Soc. 145 (1998) 2707.
[6] F. Leroux, G. Goward, W.P Power, L.F. Nazar, J. Electrochem. Soc. 144 (1997) 3886.
[7] T.A. Kerr, H. Wu, L.F. Nazar, Chem. Mater. 8 (1996) 2005.
[8] D.B. Le, S. Passerini, A.L. Tipton, B.B. Owens, W.H. Smyrl, J. Electrochem. Soc. 142 (1995) L102.
[9] D.B. Le, S. Passerini, J. Guo, J. Ressler, B.B. Owens, W.H. Smyrl, J. Electrochem. Soc. 143 (1996) 2099.
[10] S. Megahed, B.M. Barnett, L. Xie (Eds.), Rechargeable Lithium and Lithium-ion Batteries, Electrochemical Society New Jersey Electrochemical Society; Proceedings Series PV 94–28, 1995.
[11] M.S. Wittingham, A.J. Jacobson, Intercalation Chemistry, Academic Press, New York, 1982.
[12] F.R. Gamble, F.J. Disalro, R.A. Klemn, T.H. Geballe, Science 168 (1970) 568.
[13] M.E. Spahr, P. Stoschitzki-bitterli, R. Nesper, O. Haas, P. Novak, J. Electrochem. Soc. 146 (8) (1999) 2780.
[14] J.P. Lemmon, M.M. Lerner, Chem. Mater. 6 (1994) 207.
[15] C.O. Oriakhi, M.M. Lerner, Chem. Mater. 8 (1996) 2016.
[16] A. Vadivel Murugan, B.B. Kale, Chai-Won Kwon, Guy Campet, K. Vijayamohanan, J. Mater. Chem. 11 (2001) 2470.
[17] F. Lux, Farbe & Lack 104 (1998) 32.
[18] P. Novak, O. Inganas, R. Bjorklund, J. Electrochem. Soc. 134 (1987) 1341.
[19] P. Novak, K. Muller, K.S.V. Santhanam, O. Hass, Chem. Rev. 97 (1997) 207.
[20] S. Ghosh, O. Inganas, Adv. Mater. 11 (1999) 1214.
[21] L.B. Groenendaal, F. Jonas, D. Freitag, H. Pielartzik, R.J. Reynolds, Adv. Mater. 12 (2000) 481.
[22] J.M. Cocciantelli, M. Ménétrier, C. Delmas, J.P. Doumerc, M. Pouchard, M. Broussely, J. Labat, Solid State Ionics 78 (1995) 143.
[23] G.R. Goward, F. Leroux, L.F. Nazar, Electrochem. Acta 43 (1998) 1307.
[24] Y. Sato, T. Asada, H. Tokugawa, K. Kobayakawa, J. Power Sources 68 (1997) 674.
[25] H.P. Wong, B.C. Dave, F. Leroux, J. Harreld, B. Dunn, L.F. Nazar, J. Mater. Chem. 8 (1998) 1019.

# Chapter 2

# New Organic-Inorganic Polypyrrole/γ-$Fe_2O_3$ Hybrid and Its Electrochemical Behaviors

## 2-1. INTRODUCTION

The birth of 'nano-technology' is one of the most fruitful scientific progresses in the last half of the 20th century [1]. This contemporary advance endows mankind to handle and interpret the structure of matters based on molecular or cluster level. Exploration below a critical size found many curious phenomena such as quantum size effects, superparamagnetism and so on. In recent years, considerable efforts have been devoted to the development of methods for the preparation of hybrid particles consisting of inorganic nano-cores covered with shells of organic polymers with functionality or *vice versa* [2-3]. Especially, magnetic nanoparticular cores are of great interest because of their unique applications such as information storage, magnetic refrigeration, ferrofluids, high-gradient magnetic separation (HGMS), medical diagnosis and targeting for drug delivery [4-8]. For example, the HGMS technique uses nano-sized magnetic particles coupled to the target species for removal of by using a high-gradient magnetic field device [4,5]. Generally, the iron oxide nanoparticles are used as magnetic core and they are covered by in-situ polymerization of corresponding monomer. But, the chemistry of nanoparticles is different from that of their well-crystalline analogues owing to the large surface area. Here begins the necessity for investigating more profoundly the 'surface effects' of the nanoparticles to make hybrids with appropriate functionality.

First row transition metal oxides such as $MnO_2$, $TiO_2$ and $V_2O_5$, have been the focus for lithium insertion electrodes [9-11]. We have selected maghemite (γ-$Fe_2O_3$) as a starting compound because its synthetic methods for nanoparticles with regular size distribution are well established, and because it displays excellent magnetic properties

[12-15]. Furthermore, it could be considered to be one of the best cathode candidates for Li-batteries by virtue of its environmental affinity and low price. In spite of such merits, electrochemical behaviors of the maghemite have been relatively less studied due to its low conductivity, the insufficient electrochemical potential and most importantly its frustrating cyclability. In this study, we describe for the first time, to our knowledge, an attempt to change electrochemical and magnetic properties of nano-sized maghemite by surface modification.

## 2-2. EXPERIMENTAL SECTION

### 2-2-1. Materials

$FeCl_2 \cdot 4H_2O$ (99.9 %), $FeCl_3 \cdot 6H_2O$ (99.9 %), $Fe(NO_3)_3 \cdot 9H_2O$ (99.9 %) were purchased from Aldrich. Pyrrole (99.9 %, Aldrich), ethylene carbonate (EC, Prolabo 99.9 %), dimethyl carbonate (DMC, Aldrich, 99.9 %) and Ketjenblack were used as received. Lithium perchlorate ($LiClO_4$, 99.99 %, Aldrich) and polytetrafluoroethylene (PTFE, 99.99 %, Aldrich) was dried at 120 °C in vacuum for 24 hours prior to use.

### 2-2-2. Sample Preparation

#### Synthesis of maghemite (γ-$Fe_2O_3$) nanoparticles

The maghemite nanoparticles were prepared by the method of Massart et al

[16,17]. First, magnetite ($Fe_3O_4$) was precipitated by alkalizing an aqueous iron chloride solution containing $Fe^{2+}/Fe^{3+}$ = 0.5 with $NH_4OH$, leading to a magnetic colloid formation as following reaction equation.

$$2\,FeCl_3 + FeCl_2 + 4NH_4OH \xrightarrow[\text{stirring 15 min.}]{T = 50\,^\circ C} 4\,HCl + 4\,NH_4Cl + Fe_3O_4 \downarrow$$

316 mmol, 143 ml | 158 mmol, 170 ml, 1.5 M HCl | 8.6 M, 300 ml | magnetic decantation

In this reaction, the kind of base, addition kinetics, concentration, temperature, stirring, precursors are all important parameters which determine the distribution of size and phase of the product. For a typical run, 143 ml of 2.21 M $FeCl_3$ aqueous solution (containing 316 mmol $FeCl_3$) and 170 ml 1.5 M HCl solution with 158 mmol $FeCl_2$ were prepared separately, and mixed into a 5 L plastic vessel and diluted with 3.5 L of distilled water. The solution was heated to 50 °C, and then 300 ml of 8.6 M $NH_4OH$ solution was quickly added into it, followed by strong agitation for 15 min. This process gives ~ 36 g of $Fe_3O_4$ normally.

The inverse spinel structure of magnetite ($[Fe^{3+}]_{tetra}[Fe^{3+}Fe^{2+}]_{octa}O_4$) is prone to oxidize, so we transform it via full-oxydation step to maghemite which is more stable and of the same structure but possess one third of octahedral vacancy sites ($[Fe^{3+}]_{tetra}[Fe^{3+}_{5/3}\square_{1/3}]_{octa}O_4$). After washing several times to remove chloride ions, the particles were treated with nitric acid .

$$Fe_3O_4 + HNO_3 \xrightarrow[\text{stirring 15 min.}]{} [Fe^{III}]_{tetra}[Fe^{III}\,Fe^{II}_{1-x}\square_x]_{octa}O_4 \downarrow$$

m = 36g | 2M, 200 ml | magnetic decantation

This step permits to acidify the surface of nanoparticles by replacing the flocculating counterions $NH^{4+}$ for nitrate ions $NO^{3-}$ and by allowing the access of ferric ions in solution by superficial oxidation. The final step consists of addition of the particles to a ferric nitrate solution at boiling temperature.

$$[Fe^{III}]_{tetra}[Fe^{III}\ Fe_{1-x}{}^{II}\ \square_x]_{octa}O_4 \quad + \quad Fe(NO_3)_3 \quad \xrightarrow[\text{stirring 30 min.}]{T_b} \quad \gamma\text{-}Fe_2O_3 \downarrow$$

0.33 M
600 ml

magnetic decantation

The products was washed with water and acetone 4 times and dried at 40 °C. Typically, the final product is ~ 30 g.

**Preparation of Maghemite/PPY Hybrids**

1.7 g of maghemite was dispersed in liquid pyrrole and excess pyrrole was removed, leaving only the surface of maghemite powder wet. The remaining pyrrole was about 1.3 g. This mixture was added to 200 ml of 0.15 M $FeCl_3$ ethanol solution under stirring. Polymerization lasted for 30 min, followed by filtration and washing with ethanol repeated times. The separation between modified maghemite and polypyrrole without maghemite was done as follows: The modified maghemite particles were decanted down in the solution using a magnet and the polypyrrole, which is not magnetic, was removed by repeated washing with ethanol and acetone. Bulk polypyrrole (PPY) was also prepared, for comparison, with 1.3 g of pyrrole in the 200

ml of 0.30 M $FeCl_3$ ethanol solution for 4 hours. The products were dried and preserved at 40 °C.

### 2-2-3. Sample Characterization

The crystal structure of samples was examined by a powder X-ray diffractometer (Phillips PW-1050) using graphite-monochromated Cu-Kα radiation (λ = 1.5418 Å). Fourier transform infrared (FTIR) spectra were recorded with a Bruker EQUINOX 55 spectrometer in reflection mode diluted with KBr. The variation of particle morphology on the intercalation was monitored by a transmission electron microscope (JEOL 2000 FX) operating at an accelerating voltage of 200 kV. The fraction of volatile content (polymer and Cl) to maghemite (γ-$Fe_2O_3$) was determined by thermal analysis with a Setaram TGA-DSC system. The PPY/maghemite sample was heated from room temperature to 600 °C at a rate of 2 °C/min under oxygen.

### 2-2-4. Electrochemistry

Electrochemical experiments were performed based on the configuration of 'Li | 1M $LiClO_4$ in EC/DMC (1:1 v/v) | composite electrode'. The composite electrodes were made by intimately mixing 70% (by mass) of the active material, 25 % of Ketjenblack and 5% of polytetrafluoroethylene (PTFE). The surface area of the electrodes and mass of active material were adjusted to 1 $cm^2$ and 20 mg respectively for reproductivity. These electrodes were dried under vacuum at 80 °C for more than 3

hours, and introduced into an Argon-filled glove box without any exposure to air. A computer-controlled PGS201T (Tacussel) potentiostat/galvanostat system was used for data collection. Charge/discharge experiments were carried out in a galvanostatic mode at 8 mA/g in the voltage range of 1.3 ~ 4.3 V (vs. $Li^+/Li$).

### 2-2-5. Magnetism Measurement

Magnetization measurements were performed using a SQUID magnetometer (Quantum Design MPMS-5S) at fields ranging from 0 to 5000 G and at temperature ranging from 15 to 350 K. For zero-field-cooling (ZFC) magnetization, the sample was cooled to 5 K with the magnetic field set to zero. After stabilization at this low temperature for ~ 15 min, a weak magnetization of 50 G was applied. The magnetization was measured while stepping the temperature up to 350 K. Then, the samples was progressively re-cooled recording the magnetization for field-cooling (FC) experiments. The blocking temperature ($T_b$) was estimated from the temperature at which the ZFC magnetization curve shows a peak maximum ($T_{max}$) using the following equation:

$$T_{max} = \beta T_b$$

where β is a constant related to the size distribution of the particles [13-15].

### 2-2-6. X-ray Photoelectron and X-ray Absorption Spectroscopy

The XPS data were collected using a VG 220i-XL Escalab spectrometer with a monochromatized Al Kα source (hν = 1486.6 eV) whose spot size is about 500 μm. The pressure in the analysis chamber during measurements was maintained at around $10^{-8}$ Pa. The powder samples were put onto small indium foils.

The XAS experiments were performed using the EXAFS facility installed at the beam line 7C at the Pohang Light Source in Pohang, Korea operated with electron storage ring energy of 2.5 GeV and the electron current of about 340 mA. The X-rays are monochromatized by a Si (111) double crystal for all the present XAS data. All the present spectra were obtained at room temperature in a transmission mode using gas-ionization detectors with a spacing of ~ 0.4 eV for the XANES region and ~ 1.5 eV for the EXAFS one. The powder samples for XAS experiments were prepared in the form of pellet, in which the finely ground samples were diluted with boron nitride in order to obtain an optimum absorption jump ($\Delta\mu \cdot t \cong 1$). All spectral data were calibrated by measuring the spectra of Fe metal foil. The data analysis for the experimental spectra was carried out by the standard procedure using computer program UWXAFS version 2.0 [18,19].

## 2-3. RESULTS AND DISCUSSION

### 2-3-1. Evaluation of Chemical Composition

As the amount of PPY attached to maghemite is unknown, the determination of ratio of PPY to maghemite is important. The chemical composition of the PPY/$Fe_2O_3$ hybrid samples was estimated from thermogravimetry and electron probe micro-

analysis (EPMA). Figure 2-1 shows the thermogravimetry (TG) curve of PPY/maghemite hybrid. The TG curve can be divided into four temperature domains of 25~130, 130~480, 480~500 and 500~600 °C. The first region, up to 130 °C, is attributed to removal of water on surface. Next weight loss until 480 °C is assigned to the volatile components (PPY and Cl). A sudden decrease in mass at *ca.* 490 °C is due to the oxygen loss during the phase transformation to magnetite ($Fe_3O_4$). The fraction of volatile content (polymer and Cl) to maghemite is evaluated to be 3.5 wt %. From EPMA experiments, the Cl/Fe atomic ratio was estimated to be ca. 0.22 % for pristine maghemite and ca. 1.6 % for PPY/maghemite. The exact ratio of Cl/Fe is difficult to know due to the inhomogeneity of the sample surface. The existence of Cl on the surface of maghemite can be rationalized by the fact that it was synthesized from iron chloride solution. Based on above findings, the composition of PPY/maghemite is approximately estimated to be $Py_{0.07}Cl_{0.03}Fe_2O_3$, where Py abbreviates a pyrrole unit.

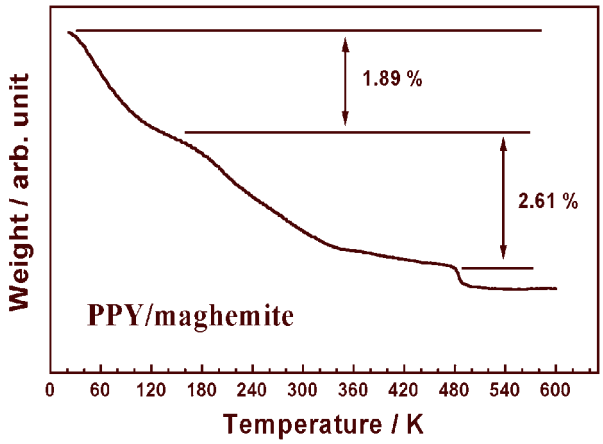


*Figure 2-1. Thermogravimetry curve for PPY/maghemite hybrid.*

**2-3-2. Powder XRD Analysis**

The crystal structure of samples was examined by a powder X-ray diffractometer

(Phillips PW-1050) using graphite-monochromated Cu-Kα radiation (λ = 1.5418 Å). The X-ray powder diffraction patterns in Figure 2-2 proves that the PPY/maghemite sample has the same crystal structure as maghemite. Peaks at 2θ = 18.4, 30.3, 35.7, 43.3, 53.8 and 57.3 degree are well indexed to (111), (220), (311), (400), (422) and (511) reflections of a cubic system with the cell parameter *a* = 8.35 Å respectively [20]. Such

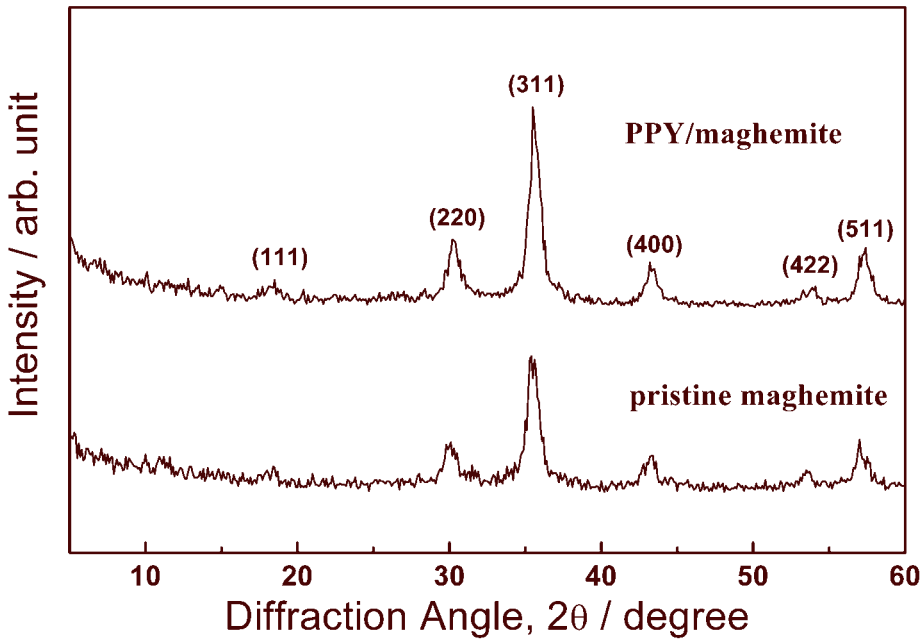


*Figure 2-2. X-ray diffraction patterns of PPY/maghemite compared with pristine maghemite*

characteristics mean that our treatment with pyrrole kept the core structure of the modified sample, that is to say, a surface modification.

### 2-3-3. Infrared Spectroscopy

The FTIR spectrum of PPY/maghemite in Figure 2-3 displays a combination of characteristic patterns of both pristine maghemite and bulk PPY, suggesting the growth

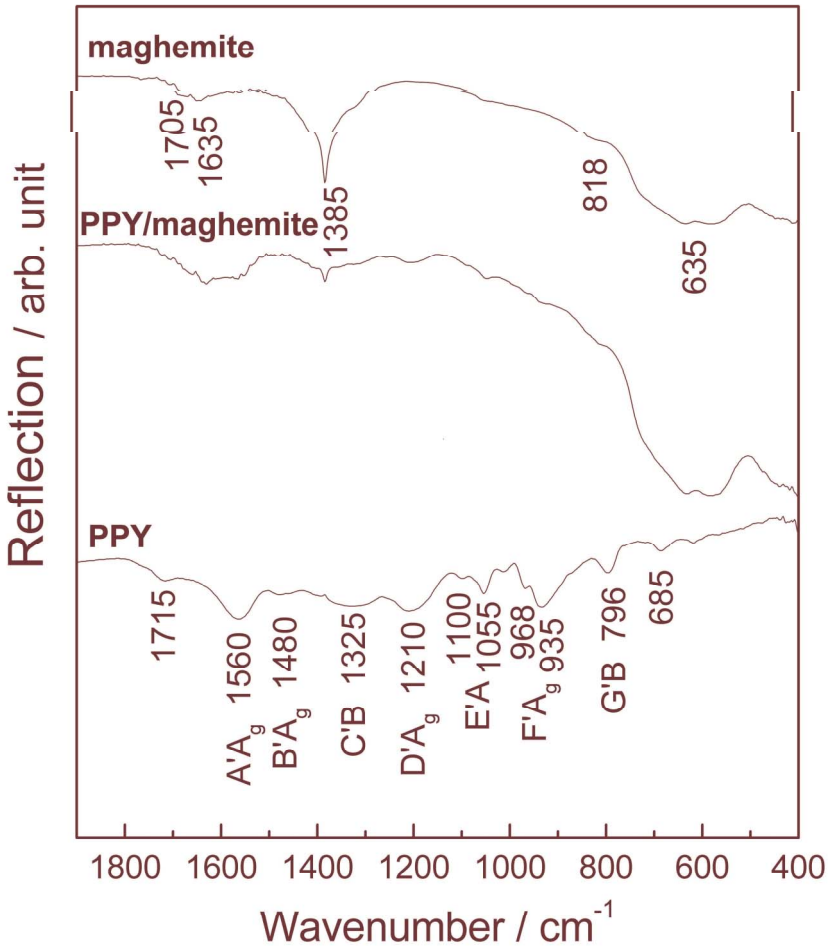


*Figure 2-3. FTIR spectra of maghemite, PPY/maghemite and bulk PPY in diffuse reflection mode. Peaks from PPY are assigned based on the effective conjugation coordinate (ECC) theory in Ref. 21 and 22. The samples were diluted with KBr.*

of polypyrrole onto the surface of maghemite nanoparticles. Peaks from PPY are assigned with designations based on the effective conjugation coordinate (ECC) theory, which predicts well how the intensities and position of the IR bands change to the extent of delocalization along the polymer chain [21,22]. The A' band at 1560 $cm^{-1}$ is due to C-C & C=C stretching and the B' band at 1480 $cm^{-1}$ is from C-N stretching of polypyrrole. C. R. Martin et al. established a relationship that the A'/B' ratio is inversely proportional to the conjugation length and doping level of polypyrrole [23,24].

It is noted that the 1385 $cm^{-1}$ band due to the adsorbed nitrate in the course of synthesis decreases considerably for the PPY/maghemite sample compared with the pristine maghemite, which signifies the removal of most of surface $-NO_3^-$ groups by the polypyrrole coverage.

### 2-3-4. Transmission Electron Microscopy

The influence of this modification on particle morphology was monitored with transmission electron microscope (JEOL 2000 FX) operating at an accelerating voltage of 200 kV. The particles are almost spherical with relatively regular size of *ca.* 8 nm for both samples, but the aggregation of grains is more significant for the pristine

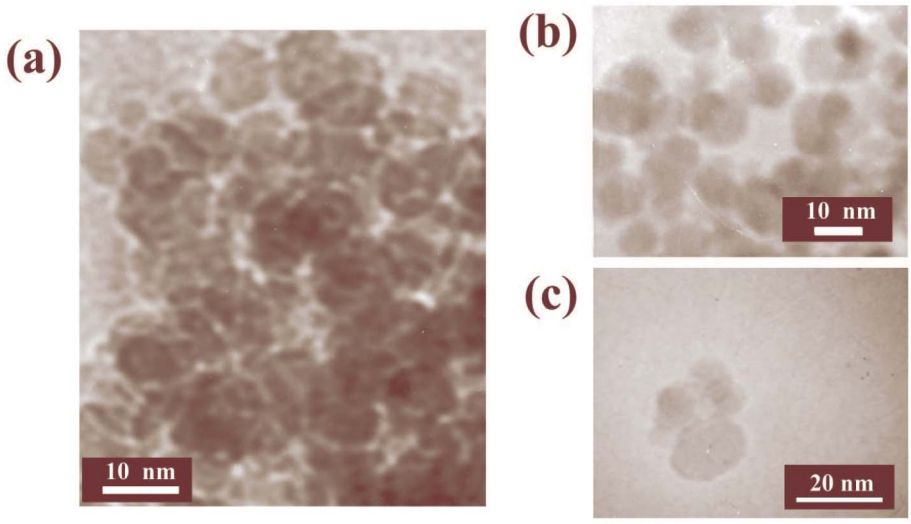


*Figure 2-4. TEM micrographs of (a) pristine maghemite and (b-c) PPY/maghemite*

maghemite (Figure 2-4a) than for the modified one (Figure 2-4b,c). Furthermore, somewhat less dark regions around each particle can be found in the right figure, which

evidences the presence of polymer cover. The origin of the particle segregation for PPY/maghemite, is therefore probably due to the presence of polypyrrole on intergrain surface. It is worthwhile to mention that the similar particle sizes of the two samples indicate the extreme shortness of polypyrrole chain, confirming the interpretation of IR analysis. To guess the quantity of polymers on the surface, a simple and rough calculation was conducted as follows. Assuming a particle is spherical with a diameter of 80 Å, the particle has a volume of 270 $nm^3$ containing 460 unit cells of maghemite. A unit cell contains $Fe_{64/3}O_{32}$, so a particle has 9800 Fe atoms. If the outermost shell has a thickness of *ca.* 2 Å, it has 1400 Fe atoms. From the composition $Py_{0.07}Cl_{0.03}Fe_2O_3$, a

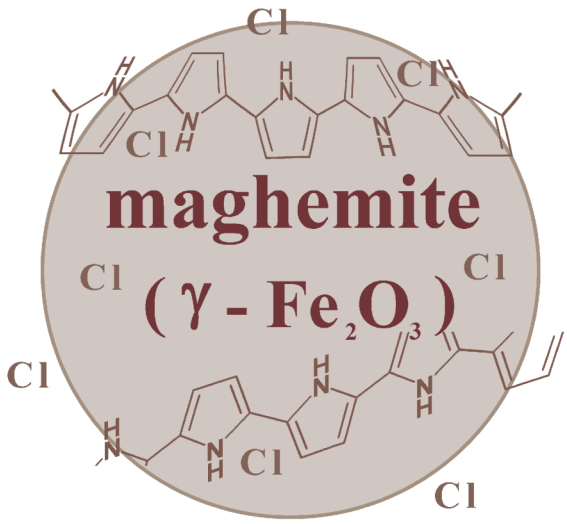


*Figure 2-5. A schematic model of PPY/maghemite.*

particle has 340 pyrrole units. Therefore, we believe that the polypyrrole does partially cover the surface of maghemite. A schematic model is illustrated in Figure 2-5.

## 2-3-5. Magnetism Measurement

To examine particle size and surface modification effects, magnetic properties were measured by observing magnetization depending on applied field. Bulk maghemite is a ferrimagnet, but the bulk characteristics disappear below a critical size as the particle size decreases. Such particles are called superparamagnetic [25]. As shown in Figure 2-6, the magnetization vs. applied filed curve at 290 K (upper figure) exhibits no hysterisis, implying the direction of magnetization can easily flip with thermal activation. Both remanence ($M_r$) and coercivity ($H_c$) are zero, consistent with the superparamagnetic behavior and the nanoscale dimensions of the particles : The particles are small enough that their anisotropy energy barrier is overcome by thermal fluctuation, permitting the magnetization direction become reverse [25].

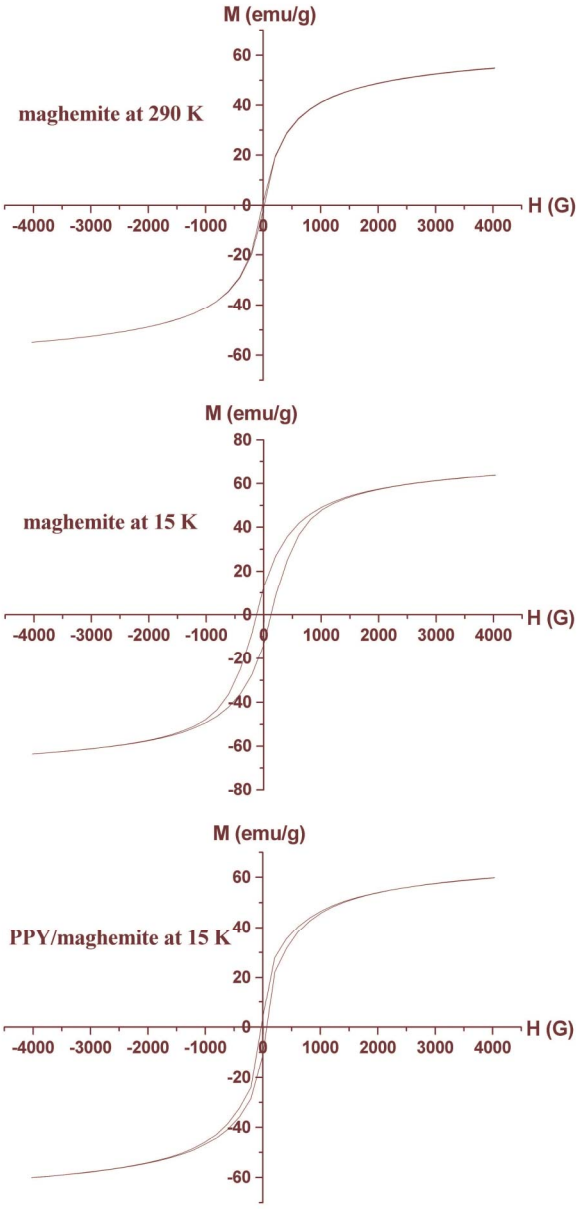


*Figure 2-6. Magnetization vs. Applied field plots at 290 K and 15 K for pristine maghemite or PPY/maghemite hybrid.*

As the temperature goes down to 15 K, the magnetization increases and a hysterisis loop appears. At this temperature, the magnetic moment remains frozen to the direction of the former external field. The system is thus left with a net remanence magnetization that decay very slowly compared to the time scale of the measurement (~ 30s). To make the net magnetization be zero, a coercive magnetic field needs to be applied. Typical $H_c$ values for bulk γ-$Fe_2O_3$ range from 250 to 400 Oe [14,15,26], while our nanoparticular sample has $H_c$ = 130 Oe (48 Oe) and $M_r$ = 13.2 emu/g (7.3 emu/g) at 15 K for pristine maghemite (or PPY/maghemite hybrid). The hybrid sample displays smaller $H_c$ and $M_r$ values because their particles are more separated than the pristine ones [12,14].

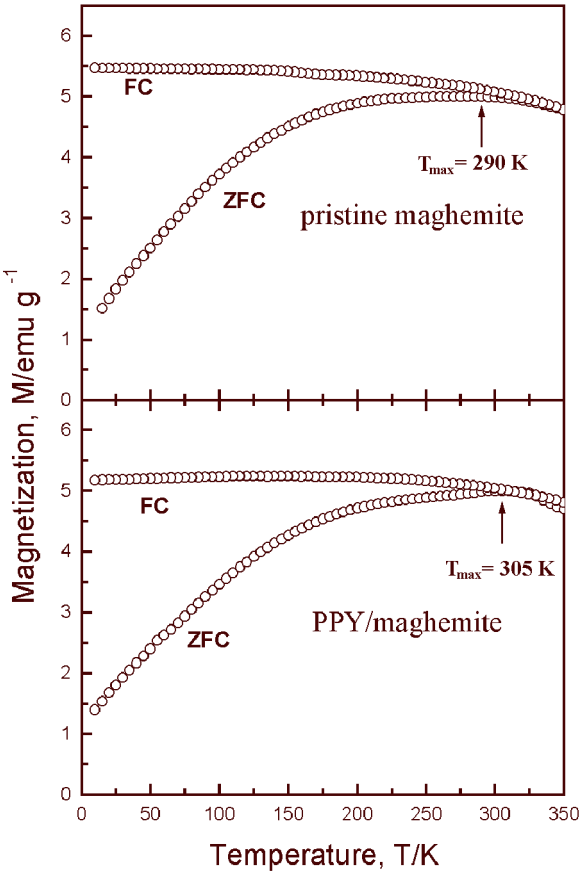


*Figure 2-7. Magnetization ZFC/FC curves of pristine maghemite (upper) and PPY/maghemite (bottom). The arrows indicate the temperature maximum of the ZFC curves. The applied field is 50 G.*

For zero-field-cooling (ZFC) magnetization, the sample was first cooled to 15 K in a zero field and, after stabilization, a weak magnetic field of 50 G was applied. The magnetization was measured while stepping the temperature up to 350 K. Then, the samples were progressively

re-cooled recording the magnetization for field-cooling (FC) experiments. For the pristine maghemite sample, the temperature maximum ($T_{max}$) of the ZFC curve is 290 K (Figure 2-7), which suggests that their average particle size is *ca.* 8 nm [12-14], confirming the TEM observation. The blocking temperature ($T_b$) is obtained from the equation $T_{max} = \beta T_b$, where β typically in the range of 1.5 ~ 2.0, accounts for size distribution [12-15]. The magnetic nanoparticles are in a ferromagnetic state below $T_b$, whereas exhibit superparamagnetic behaviors above $T_b$. The $T_b$ values are, thereby, assessed to be *ca.* 170 K and *ca.* 178 K for the pristine and modified samples, respectively. Such increase in $T_b$ value can be normally discovered in polymer-diluted nanoparticle systems, depending on the concentration of the magnetic particles due to the reduction of interparticle interactions [12,14]. In this case, however, with only the small amount of polypyrrole, the blocking temperature is increased by *ca.* 8 K, which results from diminution of the interparticle interactions.

### 2-3-6. Electrochemistry

Figure 2-8 illustrates potential *vs.* capacity curves for the first four discharges carried out in a galvanostatic mode at 8 mA/g in the voltage range of 1.3 ~ 4.3 V (vs. Li). The electrochemical Li insertion into the maghemite, who has a defective spinel structure written as $[Fe^{3+}]_{8a}[Fe^{3+}_{5/3}\square_{1/3}]_{16d}O_4$ in the spinel notation [27,28], starts with the filling of the octahedral vacancies. Then, a distinctive plateau at 2.7 V appears due to the structural transformation into a layered rocksalt-like structure along with the lithium-insertion into 16c sites, including a major rearrangement of 8a tetrahedral $Fe^{3+}$

ions, also, to the 16c octahedral sites [28]. Finally, lithium ions enter to the rest 16c sites with falling of the voltage until 1.3 V.

In contrast, the 2.7 V plateau is less obvious for the polypyrrole-modified sample and, in addition, the potential decreases more smoothly. This would imply that electrochemical properties could be drastically changed by the little surface modification. The improvement by the surface modification is more evident for the cyclability. The capacity of the pristine maghemite still diminishes during the first four cycles, but the modified one is somewhat stabilized after the first cycle. It is also interesting to note that our results on the electrochemical lithium-insertion for the maghemite differ somewhat from those of previous literatures. M. Pernet et al. reported that the phase transformation started at 1.6 V and x ~ 0.4 in $Li_xFe_2O_3$ [28], but this difference stems from kinetic reasons in our opinion. Our maghemite sample is nano-sized with *ca.* 8 nm, but they used well crystalline one with 0.8 μm in length. Such difference is presumably important for this kinetically diffusion-limited

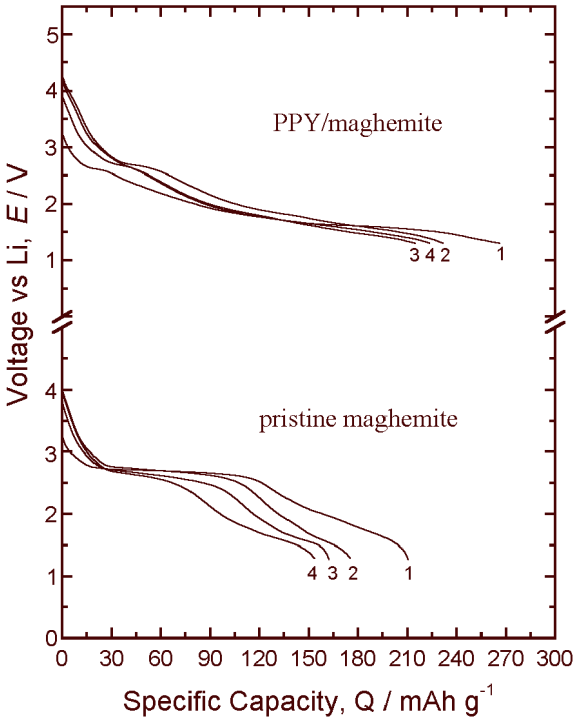


*Figure 2-8. Variation of the voltage vs. Li for the first four discharges of maghemite and PPY/maghemite. The current density and potential range were 8 mA/g and 1.3 ~ 4.3 V, respectively.*

situation, that is, the rearrangement of $Fe^{3+}$ ions from tetrahedral sites into octahedral sites. Therefore, in the above-mentioned publication, the authors found no plateau although the reaction proceeds via two phases, implying a significant over-potential [29]. This assertion is also supported by the fact that potassium-β-ferrite $K_{1.33}Fe_{11}O_{17}$ with the spinel block shows a 2.3 V plateau at 60 °C, whereas its potential slowly decreases to 1.5 V at 25 °C without any plateau [30]. Therefore, we would like to suggest that the nanoparticles can be advantageously used for the purpose of overcoming kinetic problems in lithium insertion electrodes in the absence of catalytic decomposition of solvent.

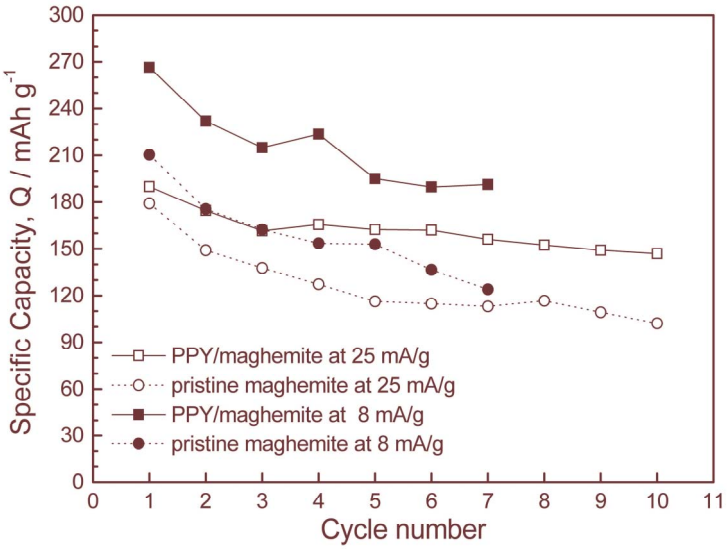


*Figure 2-9. Variation of discharge capacities with cycle for PPY/maghemite (squares) and maghemite (circles) between 1.3 ~ 4.3 V. The capacities at 8 mA/g and 25 mA/g are represented as filled and open marks, respectively.*

In order to clarify the role of the surface modification of maghemite nanoparticles on the electrochemical performance for extended cycling, the variation of discharge capacities measured at 8 and 25 mA/g for the first 7 and 10 cycles, respectively, is presented in Figure 2-9. The magemite shows the first discharge capacity of 179 mAh/g, but the capacity rapidly decreases to 100 mAh/g after 10 cycles at 25 mA/g. In contrast, the PPY/magemite exhibits rather good cyclability to deliver

185 and 155 mAh/g at the first and 10th cycle respectively at the same current density. This suggests that the surface modification with polypyrrole not only increases the capacity but also enhances reversibility of maghemite nanoparticles.

### 2-3-7. X-ray Photoelectron and X-ray Absorption Spectroscopy

To examine the oxidation state of iron ion and the nature of interaction between PPY and maghemite, a comparative study of XPS and XAS was performed. XPS survey spectra of PPY/maghemite is presented in Figure 2-10. The presence of PPY is

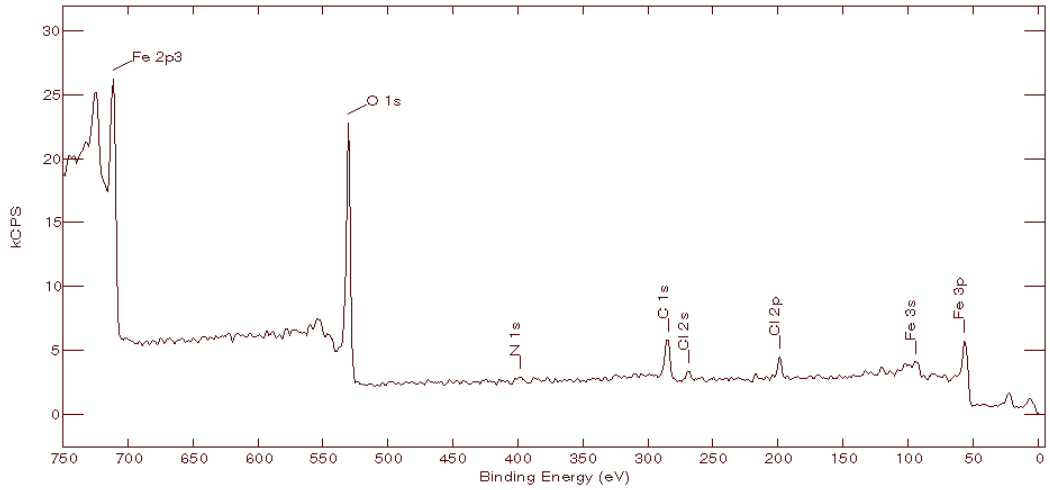


*Figure 2-10. XPS survey spectrum of PPY/maghemite hybrid.*

evidenced by the nitrogen and carbon peaks. The atomic ratio of Fe, O, N, C, Cl is measured to be 16.1 %, 55.7 %, 1.9 %, 22.8 % and 3.5 %, respectively. Assuming that the N 1s signals are entirely from PPY, those results agree well with the EPMA and thermogravimetry analysis. The amount of carbon is somewhat overestimated and that of iron is underevaluated, but it can be rationalized when considering that the polymer cover containing carbon is outer side than iron oxide and the sampling depth of XPS is 2 ~ 5 nm [31].

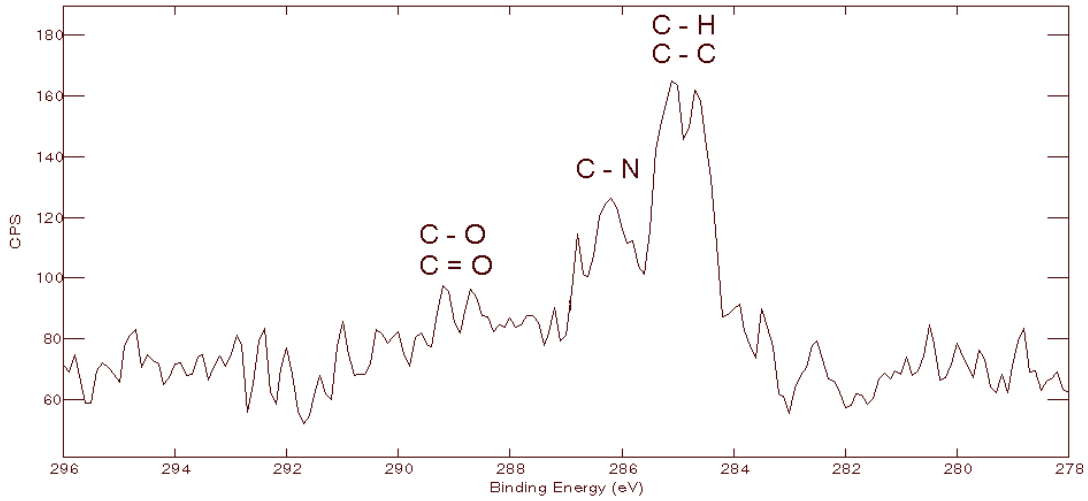


*Figure 2-11. C 1s core-line spectrum for PPY/maghemite.*

Figure 2-11 illustrates C 1s core-line spectrum of PPY/maghemite hybrid. Three main peaks are assigned to C—C/C—H (~ 285 eV), C—N (~ 286.2 eV) and C—O/C=O (~ 289 eV) bonds [31,32]. The small peak around 289 eV suggests the interaction between oxygen of maghemite and carbon of PPY. Considering the amount of oxygen is very much, this small peak also implies that this interaction is weak and that the participating

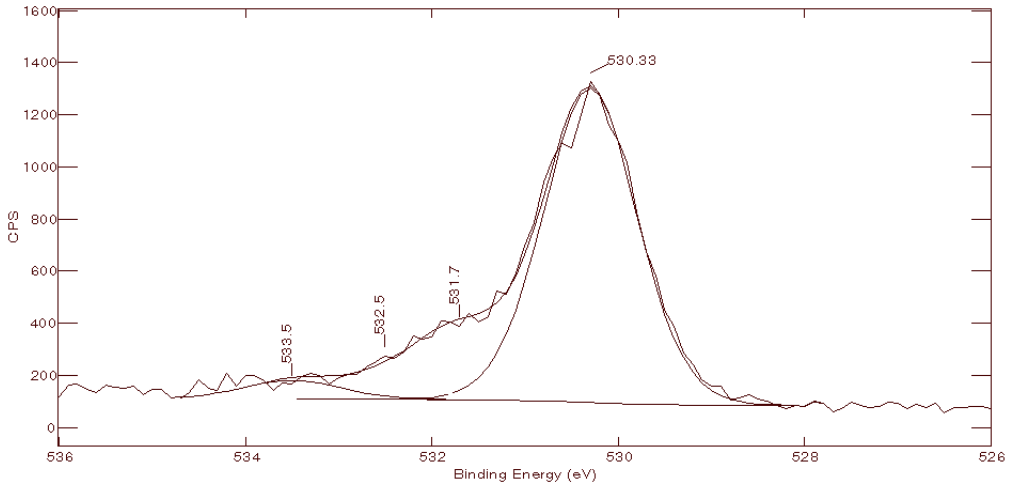


*Figure 2-12. O 1s core-line spectrum for PPY/maghemite hybrid.*

oxygen is not much.

The O 1s core-line spectrum is displayed in Figure 2-12.

The experimental peak is fitted by four reference peaks centered at 530.33, 531.7, 532.5 and 533.5 eV. The largest peak is, of course, attributed to the Fe-O bond, but the origin of the other peaks is not clear. There are several possible interactions like N···O, C···O and Cl···O. From the strength of electronegativity, peaks at 531.7, 532.5 and 533.5 eV are assigned to C···O, Cl···O and N···O interactions, respectively. At this point, it should be discussed on the bonding nature between PPY and maghemite. Among those three interactions, C···O and N···O bonds may combine PPY and maghemite, but the N···O bond is not so feasible. But, there is not so much possibility that the C···O bonding forms covalently because we just add pyrrole monomer and and $FeCl_3$ ethanol solution as an oxidant. Therefore, we believe that the origin of interaction between PPY

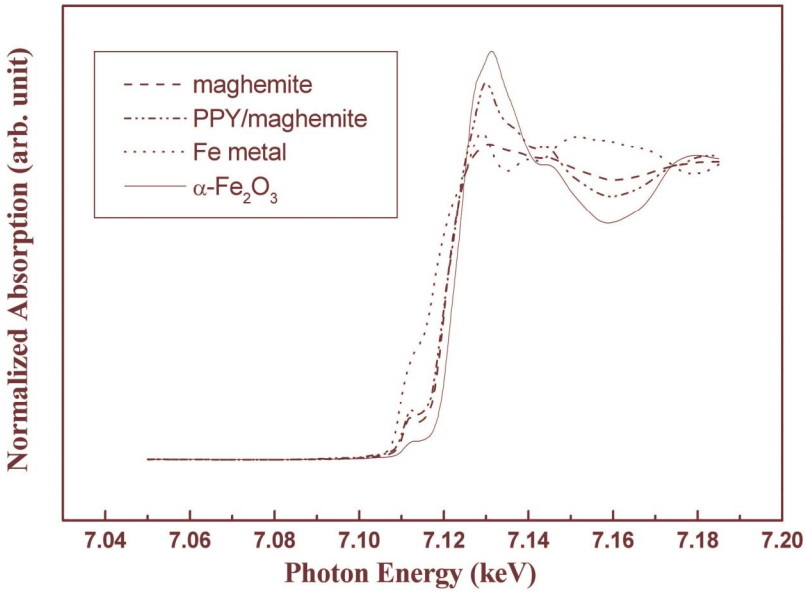


*Figure 2-13. Fe K-edge X-ray absorption spectra for the pristine maghemite and PPY/maghemite hybrid compared with iron metal and α-$Fe_2O_3$ references.*

and maghemite is the physisorption of carbon in PPY and oxygen in maghemite, which would explain the weak interaction suggested by Figure 2-11.

To investigate the oxidation state of iron ion after the surface modification with polypyrrole, the Fe K-edge X-ray absorption measurements were carried out. As shown in Figure 2-13, the PPY/maghemite exhibit the same main-edge position as the pristine maghemite. However, the peak shapes are somewhat different, which supposes the change of electronic band structure by the polypyrrole modification. This result well corresponds to the electrochemical lithium insertion experiments.

## 2-4. CONCLUSION

The PPY/maghemite was prepared by the polymerization of pyrrole on the surface of maghemite nanoparticles. IR and XRD experiments showed that it was a surface modification keeping the core particles unchanged. From the chemical composition analysis and TEM results, it was found that the polypyrrole partially covers the maghemite particles. Electrochemical measurements showed that nanoparticles can be advantageously used to overcome kinetic problems in lithium insertion, and that the surface modification with polypyrrole not only increases the capacity but also enhances reversibility of maghemite nanoparticles. Based on XPS and X-ray absorption spectroscopy, the interaction between maghemite and PPY would be due to physisorption of nitrogen in PPY to oxygen in maghemite, and the iron ions remain +3 oxidation state after the polypyrrole modification.

## 2-5. REFERENCES

[1] Special issue dedicated to nanomaterials, Chem. Mater., 8 (1996), 1569-2194.

[2] R. Gangopadhyay and A. De, Chem. Mater., 12 (2000), 608.

[3] C. Sanchez, G. J. de A. A. Soler-Illia, F. Ribot, T. Lalot, C. R. Mayer and V. Cabuil, Chem. Mater., 13 (2001), 3061.

[4] S. Kurinoby, J. Uesugi, Y. Utumi and H. Kasagara, IEEE Trans. Magn., 35 (1999), 4067.

[5] J. W. M. Bulte, L. D. Ma, R. L. Magin, R. L. Kamman, C. E. Hulstaert, K. G. Go, T. H. The and L. Deleij, Magn. Reson. Med., 29 (1993), 32.

[6] S. Mornet, A. Vekris, J. Bonnet, E. Duguet, F. Grasset, J. -H. Choy and J. Portier, Mater. Lett., 42 (2000), 183.

[7] M. Kryszewski and J. K. Jeszka, Synth. Met., 94 (1998), 99.

[8] R. F. Ziolo, E. P. Giannelis, B. A. Weinstein, M. P. O'Horo, B. N. Ganguly, V. Mehrotra, M. R. Russel and D. R. Huffman, Science, 257 (1992), 219.

[9] M. M. Thackeray, Prog. Solid State Chem., 25 (1997), 1.

[10] T. Ohzuku, Z. Takehara and S. Yoshizawa, Electrochim. Acta, 12 (1982), 1263.

[11] A. Tranchant, J. M. Blengino, J. Farcy and R. Messina, J. Electrochem. Soc., 139 (1992), 1243.

[12] J. L. Dormann, F. D'Orazio, F. Lucari, E. Tronc, P. Prené, J. P. Jolivet, D. Fiorani, R. Cherkaoui and M. Noguès, Phys. Rev. B, 53 (1996), 14291.

[13] O. Jarjayes and P. Auric, J. Magn. Magn. Mater., 138 (1994), 115.

[14] S. Mϕrup, F. Bϕdker, P. V. Hendriksen and S. Linderoth, Phys. Rev. B, 53 (1996), 287.

[15] B. Z. Tang, Y. Geng, J.W. Y. Lam, B. Li, X. Jing, X. Wang, F. Wang, A. B. Pakhomov and X. X. Zhang, Chem. Mater., 11 (1999), 1581.

[16] R. Massart, IEEE Trans. Magn., 17 (1981), 1247.

[17] R. Massart, S. Neveu, V. Cabuil-Marchal, R. Brossel, J. M. Fruchart, T. Bouchami, J. Roger, A. Bee-Debras, J. N. Pons, M. Carpentier, French Patent 1990, No. 2662539.

[18] A. Frenkel, E.A. Stern, A. Voronel, M. Qian and M. Newville, Phys. Rev. B, 49 (1994), 11662.

[19] P.A. O'Day, J.J. Rehr, S.I. Zabinsky and G.E. Brown Jr., J. Am. Chem. Soc., 116 (1994), 2938.

[20] Joint Committee on Powder Diffraction Standards (JCPDS) file No. 39-1346.

[21] B. Tian and G. Zerbi, J. Chem. Phys., 92 (1990), 3886.

[22] B. Tian and G. Zerbi, J. Chem. Phys., 92 (1990), 3892.

[23] J. Lei, Z. Cai and C. R. Martin, Synth. Met., 46 (1992), 53.

[24] J. Lei, Z. Cai and C. R. Martin, Synth. Met., 48 (1992), 301.

[25] Nanomagnetism, A. Hernando (Ed.), Klewer acedemic publishers, Dordrecht, The Netherlands, 1993.

[26] Y. S. Kang, S. Risbud, J. F. Rabolt and P. Stroev, Chem. Mater., 8 (1996), 2209.

[27] H. M. Ho, E. Goo and G. Thomas, J. Appl. Phys., 59 (1986), 1606.

[28] M. Pernet, P. Strobel, B. Bonnet, P. Bordet and Y. Chabre, Solid State Ionics, 66 (1993), 259.

[29] W. R. McKinnon in: P. G. Bruce (Ed.), Solid State Electrochemistry, Cambridge, University Press, Cambridge, 1995, Ch. 7.

[30] S. Ito, K. Ui, N. Koura and K. Akashi, Solid State Ionics, 113 (1998), 17.

[31] G. Beamson and D. Briggs, High-Resolution XPS of Organic Polymers, Wiley, Chichester, 1992.

[32] M. A. Khan, S. P. Armes, C. Perruchot, H Ouamara, M. M. Chehimi, S. J. Greaves and J. F. Watts, Langmuir, 16 (2000), 4171.

# *Publications Related to Chapter 2*

- "A new polypyrrole/maghemite hybrid as a lithium insertion electrode", Electrochem. Commun. (2002), vol. 4, n° 2, pp. 197-200.

- "Conductive Polymer/Transition Metal Oxide Hybrid Materials for Lithium Batteries",
  Mater. Res. Soc. Symp. Proc. (2002), vol. 726, in press.

ELSEVIER

Electrochemistry Communications 4 (2002) 197–200

electrochemistry communications

www.elsevier.com/locate/elecom

# A new polypyrrole/maghemite hybrid as a lithium insertion electrode

Chai-Won Kwon [a], Armel Poquet [a], Stéphane Mornet [a], Guy Campet [a,*], Josik Portier [a], Jin-Ho Choy [b]

[a] *Institut de Chimie de la Matière Condensée de Bordeaux (ICMCB), 87 Avenue du Dr. A. Schweitzer, 33608 Pessac, France*
[b] *National Nanohybrid Materials Laboratory, School of Chemistry and Molecular Engineering, Seoul National University, Seoul 151-747, South Korea*

Received 17 December 2001; received in revised form 31 December 2001; accepted 31 December 2001

**Abstract**

A new polypyrrole (PPY)/maghemite (γ-$Fe_2O_3$) hybrid was prepared by modification of the surface of maghemite nanoparticles using polymerization of pyrrole on the surface. Fourier transform infrared (FTIR), X-ray diffraction and electron microscopy studies have proven that it was only a surface modification, keeping the core structure unchanged. Transmission electron micrographs have shown the presence of PPY on the intergrain surface between maghemite particles, leading to reduction of particle aggregation. The electrochemical lithium capacity has increased up to 270 mAh/g in the potential range between 1.3 and 4.3 V vs. Li at 8 mA/g. The modified samples showed an enhanced cyclability compared to the pristine one. © 2002 Published by Elsevier Science B.V.

*Keywords:* Maghemite; Lithium battery; Electrode material; Polypyrrole; Hybrid; Nanoparticle

## 1. Introduction

As the 'nanoscience' advances recently, 'surface effects' become more and more important because nanoparticles have a much larger surface area than traditional crystalline ones. The electrochemistry field is not an exception. O'Regan and Grätzel [1] proposed dye-sensitized solar cells based on nanostructured $TiO_2$ particles surface-tailored with photoreceptor dyes. Kim and collaborators [2] reported that amorphous manganese oxyiodide $Li_{1.5}Na_{0.5}MnO_{2.85}I_{0.12}$ showed excellent reversibility involving both the $Mn^{3+/4+}$ and $Mn^{2+/3+}$ couples unlike most other manganese oxide systems, which generally show reversibility only for the $Mn^{3+/4+}$ couple. They attributed this feature to the presence of small amount of iodine may be on the intergrain surface. We have currently announced that the electrochemical behaviors of nanocrystalline $LiMn_2O_4$ are different from those of corresponding crystalline ones due to the 'electrochemical grafting' of surface [3], and that F-doped $SnO_2$ nanoparticles seem to provide a more effective way to form Li–Sn alloy than classical well-crystallized ones [4]. Here begins the necessity to modify the surface of nanoparticles appropriate to the purpose.

First row transition metal oxides such as $MnO_2$ and $V_2O_5$ have been the focus as a lithium insertion electrode. Among them, iron oxide like maghemite or magnetite is thought to be one of the best candidates by virtue of its environmental affinity and low price. In this regard, we have selected maghemite (γ-$Fe_2O_3$) as a starting compound because its synthetic methods for nanoparticles with regular size distribution are well established. In spite of such merits, electrochemical behaviors of this iron oxide have been relatively less studied due to its low conductivity, insufficient electrochemical potential and most importantly its frustrating cyclability. In this study, we describe for the first time, to our knowledge, an attempt to improve electrochemical properties of nano-sized maghemite by surface modification.

## 2. Experimental

The maghemite nanoparticles were prepared by the method of Massart et al. [5,6]. Briefly, magnetite ($Fe_3O_4$) was precipitated by alkalizing an aqueous iron chloride solution containing $Fe^{2+}/Fe^{3+} = 0.5$ with $NH_4OH$, followed by acidification and oxidation using

* Corresponding author. Tel.: +33-5-5684-6297; fax: +33-5-5684-2761.
*E-mail address:* campet@icmcb.u-bordeaux.fr (G. Campet).

1388-2481/02/$ - see front matter © 2002 Published by Elsevier Science B.V.
PII: S1388-2481(02)00250-3

$HNO_3$ and $Fe(NO_3)_3$. The surface area was ca. 130 $m^2/g$, measured by BET nitrogen adsorption method. 1.7 g of maghemite was dispersed in liquid pyrrole and excess pyrrole was removed, leaving only the surface of maghemite powder wet. The remaining pyrrole was about 1.3 g. This mixture was added to 200 ml of 0.15 M $FeCl_3$ ethanol solution under stirring. Polymerization lasted for 30 min, followed by filtration and washing with ethanol repeated number of times. The separation between modified maghemite and polypyrrole (PPY) without maghemite was done as follows: the modified maghemite particles were decanted down in the solution using a magnet and the PPY, which is not magnetic, was removed by repeated washing with ethanol and acetone. Bulk PPY was also prepared, for comparison, with 1.3 g of pyrrole in the 200 ml of 0.30 M $FeCl_3$ ethanol solution for 4 h.

The crystal structure of samples was examined by a powder X-ray diffractometer (Phillips PW-1050) using graphite-monochromated Cu-Kα radiation ($\lambda = 1.5418$ Å). Fourier transform infrared (FTIR) spectra of powder samples diluted with KBr were recorded with a Bruker EQUINOX 55 spectrometer in diffuse reflection mode. The variation of particle morphology on the intercalation was monitored by a transmission electron microscope (JEOL 2000 FX) operating at an accelerating voltage of 200 kV. The fraction of volatile content (polymer and Cl) to maghemite ($\gamma$-$Fe_2O_3$) was determined to be 3.5 wt% by thermal analysis with a Setaram TGA–DSC system. The PPY/maghemite sample was heated from room temperature to 600 °C at a rate of 2 °C/min under oxygen. From electron probe microanalysis (EPMA) experiments, the Cl/Fe atomic ratio was estimated to be ca. 0.22% for pristine maghemite and ca. 1.6% for PPY/maghemite. Based on above findings, the composition of PPY/maghemite is approximately estimated to be $Py_{0.07}Cl_{0.03}Fe_2O_3$, where Py abbreviates a pyrrole unit. Electrochemical experiments were performed based on the configuration of 'Li | 1 M $LiClO_4$ in ethylene carbonate (EC)/dimethyl carbonate (DMC) (1:1 v/v) | composite electrode'. The composite electrodes were made by intimately mixing 70% (by mass) of the active material, 25% of Ketjenblack and 5% of polytetrafluoroethylene (PTFE). These electrodes were dried under vacuum at 80 °C for 3 h, and introduced into an argon-filled glove box without any exposure to air. Charge/discharge experiments were carried out in a galvanostatic mode using a computer-controlled PGS201T (Tacussel) system between 1.3 and 4.3 V vs. Li.

### 3. Results and discussion

The FTIR spectrum of PPY/maghemite in Fig. 1 displays a combination of characteristic patterns of both pristine maghemite and bulk PPY, suggesting the

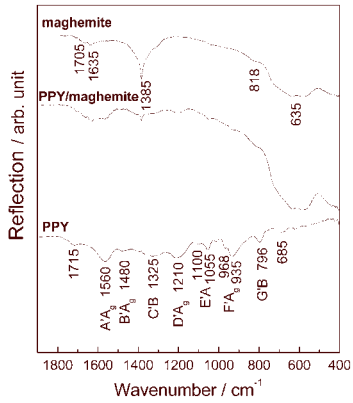


Fig. 1. FTIR spectra of maghemite, PPY/maghemite and bulk PPY in diffuse reflection mode. Peaks from PPY are assigned based on the ECC theory in [7,8]. The samples were diluted with KBr.

growth of PPY onto the surface of maghemite nanoparticles. Peaks from PPY are assigned with designations based on the effective conjugation coordinate (ECC) theory, which predicts well how the intensities and position of the IR bands change to the extent of delocalization along the polymer chain [7,8]. The A′ band at 1560 $cm^{-1}$ is due to C—C and C=C stretching and the B′ band at 1480 $cm^{-1}$ is from C—N stretching of PPY. Martin and co-workers [9,10], established a relationship that the A′/B′ ratio is inversely proportional to the conjugation length and doping level of PPY. Using these results, the doping ratio of chloride ion of the bulk PPY is obtained to be ca. 0.2 per pyrrole unit, deduced from the A′/B′ ratio of 5.1. But, the B′ band is not so obvious for the PPY/maghemite sample, which means the extreme shortness of PPY chain. It is noted that the 1385 $cm^{-1}$ band due to the adsorbed nitrate in the course of synthesis decreases considerably for the PPY/maghemite sample compared to the pristine maghemite, which signifies the removal of most of the surface $-NO_3^-$ groups by the PPY coverage.

The X-ray powder diffraction (XRD) patterns in Fig. 2 prove that the PPY/maghemite sample has the same crystal structure as maghemite. Peaks at $2\theta = 18.4°$, 30.3°, 35.7°, 43.3°, 53.8° and 57.3° are well indexed to (1 1 1), (2 2 0), (3 1 1), (4 0 0), (4 2 2) and (5 1 1) reflections of a cubic system with the cell parameter $a = 8.35$ Å, respectively [11]. Such characteristics mean that our treatment with pyrrole kept the core structure of the modified sample, that is to say, a surface modification.

The influence of this modification on particle morphology was monitored with transmission electron microscopy. The particles are almost spherical with a relatively regular size of ca. 8 nm for both samples, but the aggregation of grains is more significant for the

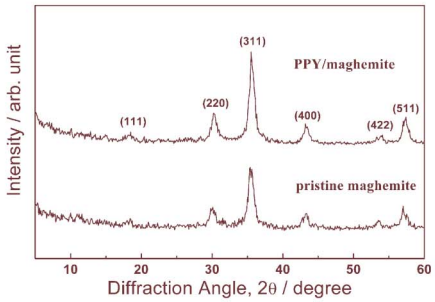


Fig. 2. X-ray diffraction patterns of PPY/maghemite compared with pristine maghemite.

pristine maghemite (Fig. 3(a)) than for the modified one (Fig. 3(b)). Furthermore, a deeper inspection of the PPY/maghemite (Fig. 3(c)) finds a somewhat bright region between darker round spheres, which evidences the presence of the PPY between maghemite particles. The origin of the particle separation for PPY/maghemite is therefore probably due to the presence of PPY on intergrain surface. It is worthwhile to mention that the TEM micrographs show the extreme shortness of PPY chain, confirming the interpretation of IR analysis. To guess the quantity of polymers on the surface, a simple and rough calculation was conducted as follows. Assuming a particle is spherical with a diameter of 80 Å, the particle has a volume of 270 $nm^3$ containing 460 unit cells of maghemite. A unit cell contains $Fe_{64/3}O_{32}$, so a particle has 9800 Fe atoms. If the outermost shell has a thickness of ca. 2 Å, it has 1400 Fe atoms. From the composition $Py_{0.07}Cl_{0.03}Fe_2O_3$, a particle has 340 pyrrole units. Therefore, we believe that the PPY does partially cover the surface of maghemite. The nature of interactions among maghemite, PPY and Cl is still under investigation.

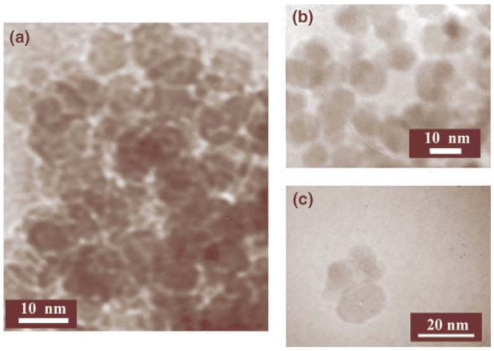


Fig. 3. TEM micrographs of (a) pristine maghemite and (b), (c) PPY/maghemite.

Fig. 4 illustrates potential vs. capacity curves for the first four discharges carried out in a galvanostatic mode at 8 mA/g in the voltage range 1.3–4.3 V (vs. Li). The electrochemical Li insertion into the maghemite, which has a defective spinel structure written as $[Fe^{3+}]_{8a}\,[Fe^{3+}_{5/3}\square_{1/3}]_{16d}O_4$ in the spinel notation [12,13], starts with the filling of the octahedral vacancies. Then, a distinctive plateau at 2.7 V appears due to the structural transformation into a layered rocksalt-like structure along with the lithium insertion into 16c sites, including a major rearrangement of 8a tetrahedral $Fe^{3+}$ ions, also, to the 16c octahedral sites [13]. Finally, lithium ions enter the rest of the 16c sites with falling of the voltage until 1.3 V. In contrast, the 2.7 V plateau is less obvious for the PPY-modified sample and, in addition, the potential decreases more smoothly. This would imply that the electrochemical properties could be drastically changed by the little surface modification. The improvement by the surface modification is more evident for the cyclability. The capacity of the pristine maghemite still diminishes during the first four cycles, but the modified one is somewhat stabilized after the first cycle. It is also interesting to note that our results on the electrochemical lithium insertion for the maghemite differ somewhat from those of previous literatures. Pernet et al. [13], reported that the phase transformation started at 1.6 V and $x \sim 0.4$ in $Li_xFe_2O_3$, but this difference stems from kinetic reasons in our opinion. Our maghemite sample is nanosized with ca. 8 nm, but they used a well-crystalline one with 0.8 μm in length. Such a difference is presumably important for this kinetically diffusion-

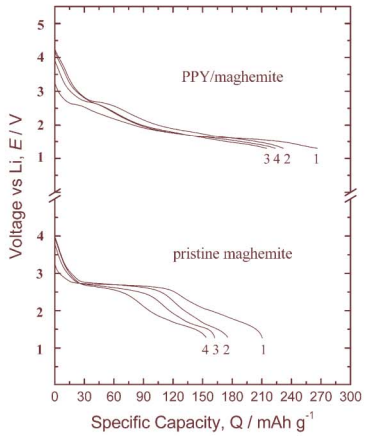


Fig. 4. Variation of the voltage vs. Li for the first four discharges of maghemite and PPY/maghemite. The current density and potential range were 8 mA/g and 1.3–4.3 V, respectively.

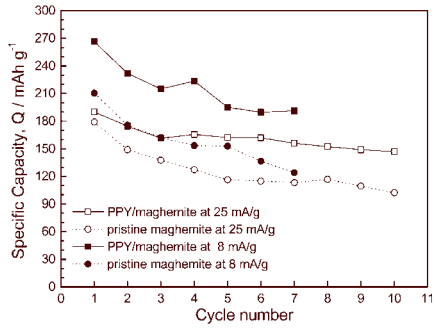


Fig. 5. Variation of discharge capacities with cycle for PPY/maghemite (squares) and maghemite (circles) between 1.3 and 4.3 V. The capacities at 8 and 25 mA/g are represented as filled and open marks, respectively.

limited situation, that is, the rearrangement of $Fe^{3+}$ ions from tetrahedral sites into octahedral sites. Therefore, in the above-mentioned publication, the authors found no plateau although the reaction proceeds via two phases, implying a significant over-potential [14]. This assertion is also supported by the fact that potassium–β-ferrite $K_{1.33}Fe_{11}O_{17}$ with the spinel block shows a 2.3 V plateau at 60 °C, whereas its potential slowly decreases to 1.5 V at 25 °C without any plateau [15]. Therefore, we would like to suggest that the nanoparticles can be advantageously used for the purpose of overcoming kinetic problems in lithium insertion electrodes. In order to clarify the role of surface modification of maghemite nanoparticles on the electrochemical performance for extended cycling, the variation of discharge capacities measured at 8 and 25 mA/g for the first 7 and 10 cycles, respectively, is presented in Fig. 5. The maghemite shows the first discharge capacity of 185 mAh/g, but the capacity rapidly decreases to 120 mAh/g after 10 cycles at 25 mA/g. In contrast, the PPY/maghemite exhibits a rather good cyclability to deliver 178 and 155 mAh/g at the first and 10th cycles, respectively, at the same current density. This suggests that the surface modification with PPY not only increases the capacity but also enhances reversibility of maghemite nanoparticles.

## 4. Conclusion

The PPY/maghemite was prepared by the polymerization of pyrrole on the surface of maghemite nanoparticles. IR and XRD experiments showed that it was a surface modification keeping the core particles unchanged. From the chemical composition analysis and TEM results, it was found that the PPY partially covers the maghemite particles. Electrochemical measurements showed that the nanoparticles can be advantageously used to overcome kinetic problems in lithium insertion, and that the surface modification with PPY not only increases the capacity but also enhances reversibility of maghemite nanoparticles.

## Acknowledgements

C.W. Kwon is indebted to CROUS of Bordeaux (France) for the financial support.

## References

[1] B. O'Regan, M. Grätzel, Nature (London) 353 (1991) 737.
[2] J. Kim, A. Manthiram, Nature (London) 390 (1997) 265.
[3] N. Treuil, C. Labrugère, M. Menetrier, J. Portier, G. Campet, A. Deshayes, J.C. Frison, S.J. Hwang, S.W. Song, J.H. Choy, J. Phys. Chem. B 103 (1999) 2100.
[4] C.W. Kwon, G. Campet, J. Portier, A. Poquet, L. Fournès, C. Labrugère, B. Jousseaume, T. Toupance, J.H. Choy, M.A. Subramanian, Int. J. Inorg. Mater. 3 (2001) 211.
[5] R. Massart, IEEE Trans. Magn. 17 (1981) 1247.
[6] R. Massart, S. Neveu, V. Cabuil-Marchal, R. Brossel, J.M. Fruchart, T. Bouchami, J. Roger, A. Bee-Debras, J.N. Pons, M. Carpentier, French Patent 1990, No. 2662539.
[7] B. Tian, G. Zerbi, J. Chem. Phys. 92 (1990) 3886.
[8] B. Tian, G. Zerbi, J. Chem. Phys. 92 (1990) 3892.
[9] J. Lei, Z. Cai, C.R. Martin, Synth. Met. 46 (1992) 53.
[10] J. Lei, Z. Cai, C.R. Martin, Synth. Met. 48 (1992) 301.
[11] Joint Committee on Powder Diffraction Standards (JCPDS) File No. 39-1346.
[12] H.M. Ho, E. Goo, G. Thomas, J. Appl. Phys. 59 (1986) 1606.
[13] M. Pernet, P. Strobel, B. Bonnet, P. Bordet, Y. Chabre, Solid State Ionics 66 (1993) 259.
[14] W.R. McKinnon, in: P.G. Bruce (Ed.), Solid State Electrochemistry, Cambridge University Press, Cambridge, 1995, Chapter 7.
[15] S. Ito, K. Ui, N. Koura, K. Akashi, Solid State Ionics 113 (1998) 17.

**Mat. Res. Soc. Symp. Proc. Vol. 726 © 2002 Materials Research Society**

## Conductive Polymer/Transition Metal Oxide Hybrid Materials for Lithium Batteries

Chai-Won Kwon[1], Armel Poquet[1], Stéphane Mornet[1], Guy Campet[1], Josik Portier[1], A. Vadivel Murugan[2], B. B. Kale[2], K. Vijayamohanan[3] and Jin-Ho Choy[4]
[1]Institut de Chimie de la Matière Condensée de Bordeaux, 87 av. A. Schweitzer, 33608 Pessac Cedex, France
[2]Center for Materials for Electronics Technology, Ministry of Information Technology, Govt. of India, Panchwati, Pashan Road, Pune 411 008, India
[3]National Chemical Laboratory, CSIR, Pashan Road, Pune 411 008, India
[4]National Nanohybrid Materials Laboratory, School of Chemistry, Seoul National University, Seoul 151-747, South Korea

### ABSTRACT

Organic-inorganic hybrid materials were synthesized for use of lithium battery electrode by two strategies: 1) core-shell strategy for tri-dimensional transition metal oxide and 2) intercalation strategy for bi-dimensional (lamellar) transition metal oxide. We choose conductive polymers as an organic component for high electric conductivity and 3d-transition metal oxides as an inorganic counterpart for large capacity and processibility. Polypyrrole/maghemite and poly(3,4-ethylenedioxythiophene) (PEDOT)/vanadium pentoxide hybrids will be presented and compared with their pristine materials for core-shell and intercalation strategies, respectively. Polypyrrole/maghemite showed an enhanced electrochemical reversibility and capacity up to ~270 mAh/g in the potential range between 1.3 and 4.3 V *vs.* Li at 8 mA/g. PEDOT/vanadium pentoxide also exhibited improved reversibility and capacity up to ~330 mAh/g at 15 mA/g between 2.0 ~ 4.4 V vs. Li on the second discharge. XRD, IR, electron microscopy, XPS and X-ray absorption spectroscopy were used to characterize the samples, and to examine oxidation state of the transition metals, doping character of the polymer and the nature of interaction between the polymer and the transition metal oxides.

### INTRODUCTION

The rapid development of modern electronic technology creates a strong demand for portable power sources. For example, popular portable electronic devices such as notebook computers, camcorders and cellular phones require small, but efficient and reliable batteries. Lithium batteries are considered to be the best choice, as they provide high output power and moderate lifetime. Generally, the lithium batteries are composed of cathode, anode, electrolyte, separator and packaging unit. Especially, electrode materials are of strong importance, because the capacity is mostly limited by the electrode materials. Traditional electrode materials are based on the redox potential difference of the electrode in the course of intercalation / deintercalation reactions. They are generally well-crystalline host compounds either with layered structure such as graphite, $LiCoO_2$ and $LiNiO_2$, or with tunnel structure like $LiMn_2O_4$. For the last decade, much effort has been made to improve the performance of the electrode materials. But, conventional synthetic methods are always restricted by the electrode material itself, and it is therefore necessary to search for new materials based on new concepts in order to increase the capacity. In this regard, we have studied organic-inorganic hybrid materials for this purpose.

The hybrid materials are, currently, exploited by its possibility of integrating different desirable properties of organic and inorganic components in a unique material [1]. Here we choose conductive polymers as an organic component and 3d-transition metal oxides as an inorganic counterpart. The conductive polymers have high electric conductivity but their processability and capacity are not sufficient for battery application, and most of the 3d-transition metal oxides are beneficial lithium cathodes with processability but have some shortcoming such as low conductivity and structural instability during lithium insertion/extraction. Consequently, we propose following two strategies for combining advantages of these two components:
1) tri-dimensional transition metal oxide nanoparticles coated by conductive polymers (core-shell strategy)
2) bi-dimensional (lamellar) transition metal oxides intercalated by conductive polymers (intercalation strategy)
In this report we present a brief overview of our works on the use of hybrid materials as lithium insertion electrodes. As illustrative examples, polypyrrole (PPY)/maghemite and poly(3,4-ethylenedioxythiophene) (PEDOT)/$V_2O_5$ hybrid systems will be presented and compared with their corresponding pristine materials for core-shell and intercalation strategies, respectively.

## PPY/MAGHEMITE HYBRID BY CORE-SHELL STRATEGY

The maghemite nanoparticles were prepared by a modification of Massart's method [2,3]. Briefly, maghemite nanoparticles were synthesized by alkalizing an aqueous iron chloride solution containing $Fe^{2+}/Fe^{3+} = 0.5$ with $NH_4OH$, and by following acidification and oxidation using $HNO_3$ and $Fe(NO_3)_3$. The surface modification was realized by wetting the surface of maghemite with liquid pyrrole and polymerizing in ethanol solution containing $FeCl_3$ for 30 min [3]. The separation between modified maghemite and polypyrrole without maghemite was done by decantation using a magnet. The surface area of the pristine maghemite and PPY/maghemite was calculated to be ~130 and ~95 $m^2/g$, respectively, from nitrogen adsorption isotherm curves at 77K by BET method. The chemical composition of PPY/maghemite is approximately estimated from thermal analysis and electron probe microanalysis (EPMA) to be $Py_{0.07}Cl_{0.03}Fe_2O_3$, where Py abbreviates a pyrrole unit.

To examine the influence of this modification on the crystal structure, X-ray powder diffraction has been performed, which proves that the PPY/maghemite sample has the same crystal structure as maghemite. Peaks at d-spacing of 4.82, 2.95, 2.52, 2.09, 1.70 and 1.61 Å are well indexed to (111), (220), (311), (400), (422) and (511) reflections respectively, with a cubic system having the cell parameter $a$ = 8.35 Å. Such a characteristic means that our treatment with pyrrole kept the core structure of the modified sample, that is to say, a surface modification.

In order to examine the doping state of the polymer, FTIR spectrum of PPY/maghemite has been recorded in comparison with pristine maghemite and bulk PPY alone. The PPY/maghemite hybrid displays a combination of characteristic patterns of both pristine maghemite and bulk PPY, suggesting not the adsorption of monomeric pyrrole but the growth of polypyrrole onto the surface of maghemite nanoparticles. It is well established that the ratio of 1560 $cm^{-1}$ peak (C-C & C=C stretching) to 1480 $cm^{-1}$ one (C-N stretching) of PPY are inversely proportional to conjugation length [4]. From this relationship, the quite small 1480 $cm^{-1}$ peak of PPY/ maghemite implies the extreme shortness of PPY chain.

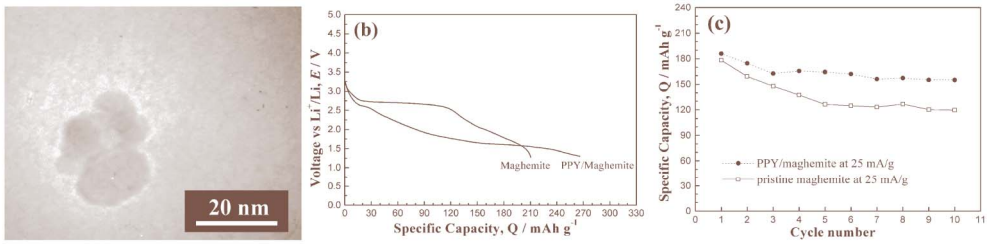


**Figure 1**. (a) TEM micrographs of the PPY/maghemite, (b) Voltage *vs.* capacity profile for the first discharges of pristine maghemite and PPY/maghemite at 8 mA/g between 1.3 ~ 4.3 V, (c) Variation of the discharge capacities during the first 10 discharges for PPY/maghemite (filled circles) and maghemite (open circles) between 1.3 ~ 4.3 V at 25 mA/g.

The influence of this modification on particle morphology was monitored with transmission electron microscope (JEOL 2000 FX) operating at an accelerating voltage of 200 kV. Both samples are of similar size and almost spherical, but somewhat less dark regions around each particle can be found for PPY/maghemite, which evidences the presence of polymer cover (Figure 1(a)). Owing to the presence of PPY between particles, the particle segregation is less significant for PPY/maghemite, which is expected to give better characteristics for electrochemical lithium insertion. The thickness of polymer cover is not so homogeneous but around 1 nm. To guess the quantity of polymers on the surface, a simple and rough calculation was conducted as follows: Assuming a particle is spherical with a diameter of 80 Å, the particle has a volume of 270 $nm^3$ containing 460 unit cells of maghemite. A unit cell contains $Fe_{64/3}O_{32}$, so a particle has 9800 Fe atoms. If the outermost shell has a thickness of *ca.* 2 Å, it has 1400 Fe atoms. From the composition $Py_{0.07}Cl_{0.03}Fe_2O_3$, a particle has 340 pyrrole units. Therefore, we believe that the polypyrrole does partially cover the surface of maghemite. It can be rationalized that the surface chloride ions probably play an important role for polymerizing the pyrrole on the surface of maghemite and that inhomogeneous distribution of chloride ion induces the only partial coverage. The determination of active sites for polymerization is under investigation.

Figure 1(b) illustrates potential *vs.* capacity curves for the first discharges carried out in a galvanostatic mode at 8 mA/g in the voltage range of 1.3 ~ 4.3 V (*vs.* $Li^+/Li$). The electrochemical Li insertion into the maghemite, who has a defective spinel structure written as $[Fe^{3+}]_{8a}[Fe^{3+}_{5/3}\square_{1/3}]_{16d}O_4$ in the spinel notation, starts with the filling of the octahedral vacancies. Then, a distinctive plateau at 2.7 V appears due to the structural transformation into a layered rocksalt-like structure along with the lithium-insertion into 16c sites, including a major rearrangement of 8a tetrahedral $Fe^{3+}$ ions, also, to the 16c octahedral sites. Finally, lithium ions enter to the rest 16c sites with falling of the voltage until 1.3 V [3,5]. In contrast, the 2.7 V plateau is less obvious for the polypyrrole-modified sample and the potential decreases more smoothly. In addition, the discharge capacity is increased much from ~210 mAh/g for pristine maghemite to ~270 mAh/g for PPY/maghemite. This would propose that overall electrochemical properties could be drastically changed by the little surface modification.

In order to clarify the role of the surface modification of maghemite nanoparticles on the electrochemical performance for extended cycling, the variation of discharge capacities measured at 25 mA/g for the first 10 cycles is presented in Figure 1(c). The pristine magemite shows the first discarge capacity of 178 mAh/g, but the capacity rapidly decreases to 120 mAh/g after 10 cycles at 25 mA/g. In contrast, the PPY/magemite exhibits rather good cyclability to

deliver 185 and 155 mAh/g at the first and 10th cycles, respectively, at the same current density. This suggests that the surface modification with polypyrrole not only increases the capacity but also enhances reversibility of maghemite nanoparticles.

## PEDOT/$V_2O_5$ HYBRID BY INTERCALATION STRATEGY

Conductive polymer/$V_2O_5$ hybrids have received a considerable attention over past several years to integrate profitably many desirable properties of both vanadium oxide and the polymeric counterpart. $V_2O_5$ is one of the most beneficial lithium cathodes with processability and high capacity, whereas conductive polymers have advantages in flexibility and conductivity. These hybrids are generally prepared by mixing $V_2O_5$ gel with monomers of the corresponding conductive polymer such as polyaniline (PANI), polypyrrole or polythiophene (PTH) [6]. Recently, we have succeeded in the first synthesis of poly(3,4-ethylenedioxythiophene) (PEDOT)/$V_2O_5$ hybrids starting from well-crystalline $V_2O_5$ unlike other hybrid, and reported their possible use as an electrode material [7,8].

The PEDOT/$V_2O_5$ hybrids were synthesized by dissolving 3,4-ethylenedioxythiophene (EDOT, Bayer) in 25 ml of distilled water and mixing with 2 g of $V_2O_5$ (99.9 %, Aldrich) under reflux condition for 12h. The nominal molar ratio of EDOT to $V_2O_5$ was adjusted to 0.02. The detailed synthetic method has already been published elsewhere [7].

The incorporation of the polymer into the $V_2O_5$ was examined by powder X-ray diffraction. Series of well-developed (00*l*) peaks can be observed, and the d-spacing increases from 4.4 Å to 13.8 Å. The net interlayer expansion increases from 5.1 Å, assuming the $V_2O_5$ slab is composed of two vanadium oxide sheets (8.7 Å) like that of vanadium oxide xerogel [8]. This would indicate that the expansion proceeds with the formation of monolayer of polymer. It is noted that (*hk0*) reflections of the hybrid correspond to those of the pristine $V_2O_5$ and that some of them, such as (*110*) and (*310*), show a diffuse peak shape, rising rather rapidly and then declining slowly toward high angle side. This feature suggests that the compounds have a random layer stacking structure, which consists of equidistant and parallel (*a*-*b*) layers, but randomly rotated about the normal *c*-axis [8]. The details are summarized in Table I with the results of elemental analysis and conductivity, but curve figures are not presented here because they have been already published elsewhere [7].

In order to examine the oxidation state of vanadium and doping state of the polymer, Fourier transform infrared (FTIR) spectra were recorded. Vibrations around 1520, 1450 and 1380 $cm^{-1}$ are assigned to the stretching of C=C and C-C in the thiophene ring, and those at 1130 and 1090 $cm^{-1}$ to the stretching of ethylenedioxy group, which proves the presence of the PEDOT in the material. The absence of peak at 1490 and 1190 $cm^{-1}$ implies that the organics are not in monomer form but in polymeric form. The peaks around 1260 and 1090 $cm^{-1}$ indicate that the polymer is in doped state as expected in the improved conductivity. Bands around 530 and 810 $cm^{-1}$ are attributed to V-O-V stretching modes and those around 1000 $cm^{-1}$ to V=O stretching.

**Table I**. Nominal EDOT/$V_2O_5$ ratio, chemical compositions, d-spacing and electrical conductivity for the pristine $V_2O_5$ and PEDOT/$V_2O_5$ hybrid.

| | Nominal EDOT/$V_2O_5$ ratio | Chemical composition | d-spacing (Å) | Conductivity ($S \cdot cm^{-1}$) |
|---|---|---|---|---|
| $V_2O_5$ | - | $V_2O_5$ | 4.4 | $8.78 \times 10^{-5}$ |
| PEDOT/$V_2O_5$ | 0.02 | $(C_6H_4O_2S)_{0.02}V_2O_5$ | 13.8 | $2.92 \times 10^{-3}$ |

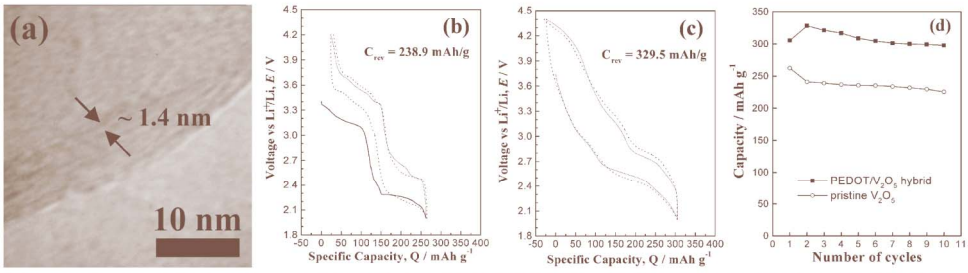


**Figure 2**. (a) TEM micrographs of the PEDOT/$V_2O_5$, Voltage *vs.* capacity profile for the first two cycles of (b) pristine $V_2O_5$ and (c) PEDOT/$V_2O_5$ at 15 mA/g, and (d) Variation of the discharge capacities during the first 10 discharges for pristin $V_2O_5$ (open circles) and PEDOT/$V_2O_5$ (filled squares) at 15 mA/g.

The influence of this modification on particle morphology was monitored with transmission electron microscopy. The pristine $V_2O_5$ consists of thick agglomerated particles with irregular sizes of micrometer order, whereas the particles of PEDOT/$V_2O_5$ hybrid are composed of well-developed (*a*-*b*) planes stacked along with c-axis. The stacking length in *c*-direction is much shorter compared with *a* and *b* directions for the hybrids, which would be considered as the enhancement of 'bidimensionality'. As shown in Figure 2(a), the interlayer spacing of PEDOT/$V_2O_5$ has been estimated by measuring the length from one dark line to the nearest one, which gives ~14 Å in good agreement of XRD result.

The electrochemical measurements were performed based on the configuration of 'Li | 1M $LiClO_4$ in EC/DMC (1:1 v/v) | composite electrode'. The composite electrodes were made by intimately mixing 70% (by mass) of the active material, 25 % of Ketjenblack and 5% of polytetrafluoroethylene (PTFE). These electrodes were dried under vacuum at 80 °C for more than 3 hours. Figure. 2(b) and (c) demonstrate potential *vs*. capacity curves of the first two cycles for the pristine $V_2O_5$ and PEDOT/$V_2O_5$ hybrid. The pristine $V_2O_5$ shows distinctive plateaus due to structural changes, whereas the potential decreases more smoothly down to ~ 2.7 V for the hybrid samples. The next lithium insertion into the pristine $V_2O_5$ occurs at ~2.3 V and is accompanied by the irreversible structural changes to γ-$Li_xV_2O_5$ phase, while the PEDOT/$V_2O_5$ hybrid display a plateau at ~ 2.5 V like $V_2O_5$ xerogel or 2D-$V_2O_5$ [8]. It is worth to mention that the PEDOT/$V_2O_5$ reveals a larger capacity in the first charge process than in the first discharge. It would be accounted for the presence of $V^{4+}$, which can be easily oxidized by an electrochemical method, as already observed in the case of PPY/$V_2O_5$ and PTH/$V_2O_5$ hybrids [10].

For the purpose of clarifying the role of the polymer incorporation on the electrochemical performance for extended cycling, the variation of discharge capacities measured on the PEDOT/$V_2O_5$ hybrid and pristine $V_2O_5$. The hybrid provides larger capacity and better cyclability than the prisinte $V_2O_5$, as shown in Figure (d). The improved performances are presumably due to a higher electrical conductivity and to the separation between vanadium oxide layers, leading to an enhanced bidimensionality.

## CONCLUSION

The design of organic/inorganic hybrids offers a new door to new materials with multifunctionality and enhanced performance. For the purpose of electrode materials, here we presented two examples, that is, PPY/maghemite and PEDOT/$V_2O_5$. We showed the maghemite nanoparticles partially coated with PPY can be advantageously used for the purpose of overcoming kinetic problems in lithium insertion electrodes. The PEDOT/$V_2O_5$ lamellar hybrid maintains capacities about 300 mAh/g for the first ten cycles. It is clear that the hybrid samples give larger capacities and better cyclability than the pristine ones. The improved performances are presumably giving positive sign to the use of hybrid materials as a lithium insertion electrode.

## REFERENCES

1. C. Sanchez, G. J. de A. A. Soler-Illia, F. Ribot, T. Lalot, C. R. Mayer and V. Cabuil, Chem. Mater. **13**, 3061 (2001).
2. R. Massart, IEEE Trans. Magn. **17**, 1247 (1981).
3. C. W. Kwon, A. Poquet, S. Mornet, G.. Campet, J. Portier and J. H. Choy, Electrochem. Commun. **4**, 197 (2002).
4. J. Lei, Z. Cai and C. R. Martin, Synth. Met. **46**, 53 (1992); **48**, 301 (1992).
5. M. Pernet, P. Strobel, B. Bonnet, P. Bordet and Y. Chabre, Solid State Ionics **66**, 259 (1993).
6. M. G. Kanatzidis and C. G. Wu, J. Am. Chem. Soc. **111**, 4141 (1989).
7. A. V. Murugan, B. B. Kale, C. W. Kwon, G. Campet and K. Vijayamohanan, J. Mater. Chem. **11**, 2470 (2001).
8. C. W. Kwon, A. V. Murugan, G. Campet, J. Portier, B. B. Kale, K. Vijayamohanan and J. H. Choy, Electrochem. Commun. **4**, 384 (2002).
9. H. P. Wong, B. C. Dave, F. Leroux, J. Harreld, B. Dunn and L. F. Nazar, J. Mater. Chem. **8**, 1019 (1998).
10. F. Leroux, G. Goward, W. P. Power and L. F. Nazar, J. Electrochem. Soc. **144**, 3886 (1997); M. Lira-Cantu and P.Gomez-Romero, ibid. **146**, 2029 (1999).

# Chapter 3

# Nanocrystalline Materials for Lithium Batteries

## 3-1. INTRODUCTION

The rapid development of modern electronic technology creates a strong demand for portable power sources. Lithium batteries are considered to be the best choice, as they provide high output power and moderate lifetime. But, their capacity is limited mostly by the electrode materials. In this respect, much effort has been made to improve the performance of the electrode materials. Traditional electrode materials are based on the redox potential difference of the electrode in the course of intercalation/deintercalation reactions [1,2]. They are generally well-crystalline host compounds either with layered structure such as graphite, $LiCoO_2$ and $LiNiO_2$, or with tunnel structure like $LiMn_2O_4$. For a long time, only well crystalline materials have been considered as good electrodes for lithium-ion cells, because their crystal regularity insures the easy diffusion of Li ion in the iono-covalent lattices in the viewpoint of "solid state ionics". Nanocrystalline materials are, however, being re-evaluated recently as 'nanoscience' advances. The electrochemistry of this kind of materials is much different from that of traditional crystalline ones because of their significant 'surface effects'. Recently, it has been found that the nanocrystalline $LiMn_2O_4$ has an enhanced electrochemical activity when the first electrochemical step is insertion of Li ions (discharge process) [3-7]. Furthermore, Kim et al. reported that amorphous manganese oxyiodide $Li_{1.5}Na_{0.5}MnO_{2.85}I_{0.12}$ showed excellent reversibility involving both the $Mn^{3+/4+}$ and $Mn^{2+/3+}$ couples, unlike most other manganese oxide systems which generally show reversibility only for the $Mn^{3+/4+}$ couple [8-14]. In this chapter, a brief overview on the aforementioned compounds — that is, $LiMn_2O_4$ and

$Li_{1.5}Na_{0.5}MnO_{2.85}I_{0.12}$ — will be described first as a research background, followed by our works on the electrochemical behaviors of alkali-metal-based manganese oxyiodide, fluorine-doped tin oxide and γ-$Fe_2O_3$. Finally the "electrochemical grafting" concept will be given as a plausible explanation.

### 3-1-1. Nanocrystalline $LiMn_2O_4$ as a Li-Insertion Electrode

Lithium manganese oxide spinel $Li_xMn_2O_4$ is one of promising cathodes for rechargeable lithium batteries by virtue of its low cost, high electrochemical potential and environmental affinity. It delivers 4 V *vs.* Li in the range $0 < x < 1$ and 3 V in the range $1 < x < 2$ [15-17]. However, studies on its utilization have mainly focused on the 4V domain, because the capacity fades severely in the 3 V range due to the occurrence of Jahn-Teller distortion when the average valence of Mn falls below +3.5. Lithium insertion into $Li_xMn_2O_4$ electrodes ($x > 1$) is, therefore, accompanied by the formation of a tetragonal phase [15,17].

The use of nanocrystalline material to overcome this shortcoming was first attempted by Bruce's group [3]. They prepared the $LiMn_2O_{4.1}$ from manganese acetate and lithium carbonate at 200 °C in air; electrodes prepared either with or without carbon additive cycled well between 3.7 and 2.0 V at C/2. But, they didn't explain why the nanocrystalline materials show such different characteristics from their well-crystalline analogues. Recently, our group has reported a comparative study between spinel $LiMn_2O_4$ prepared at low and high temperatures in order to examine the difference of electrochemical properties depending on synthetic conditions [4]. The combinational

experiments of XPS with X-ray absorption found that a lowering of synthetic temperature gave rise to an increase of structural disorder and of the average oxidation state of manganese, which was more significant at the surface than in the bulk (Table 3-1). Such a result suggest that the modification of surface property induced by a decrease of particle size is closely related to the electrochemical performance. The nanocrystalline $LiMn_2O_4$ prepared at 250 °C showed excellent cyclability in the 3 V region whereas it shows smaller capacities in the 4V domain (Figure 3-1). This phenomenon is reversal of that of well-crystalline homologue prepared at 700 °C.

Table 3-1. Relative proportion of $Mn^{IV+}/Mn^{III+}$, average particle size, coordination number (CN), and bond distance of $LiMn_2O_4$ prepared at 250 °C and 700 °C. (From Ref. 4)

| Sintering temperature | | 250 °C | 700 °C |
|---|---|---|---|
| $C_{Mn}^{III+}$ | | 41.0 % | 55.5 % |
| $C_{Mn}^{IV+}$ | | 59.0 % | 44.5 % |
| Average particle size | | ~ 5 nm | ~ 100 nm |
| (Mn-O) | CN | 5.6 | 6.0 |
| | R (Å) | 1.90(4) | 1.91(5) |
| (Mn-Mn) | CN | 5.2 | 6.0 |
| | R (Å) | 2.88(9) | 2.89(5) |

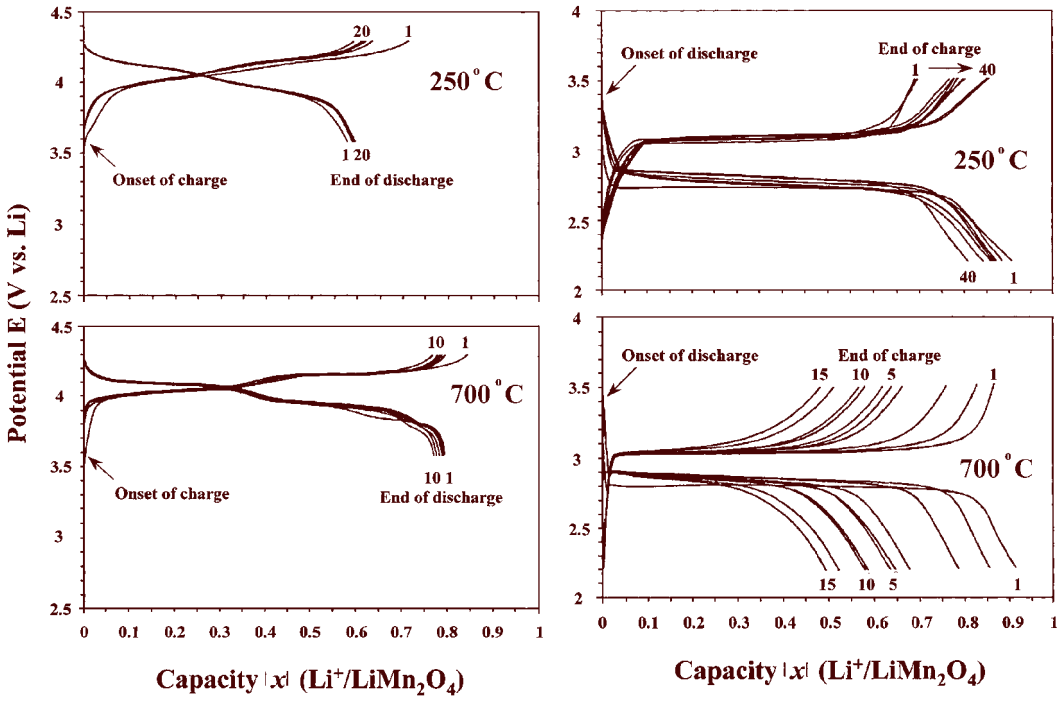


*Figure 3-1. Galvanostatic discharge and charge curves for $LiMn_2O_4$ prepared at low temperature (250 °C, top) and high temperature (700 °C, bottom). Left figures present cycling for 4V domain and right ones do for 3V domain. (From Ref. 4)*

For the purpose of examining the evolution of the chemical bonding nature of inserted lithium, $^7$Li MAS NMR study was performed for both the spinel compounds before and after the insertion of 0.2 mol $Li^+$ per formula unit. While the insertion did not induce any remarkable spectral change for the well-crystalline $LiMn_2O_4$, it led to a dramatic suppression of the NMR signal for the nanocrystalline one, indicating that the $Li^+$ insertion into the latter phase results in significant modifications of the chemical environment of lithium (Figure 3-2). It can be thus argued that the lowering of synthetic temperature modifies the surface properties and overall chemical environment of ions (lithium ions, of course, but also probably manganese and oxygen ions), which in turn changes the electrochemical properties, that is, the better cyclability in the 3V domain.

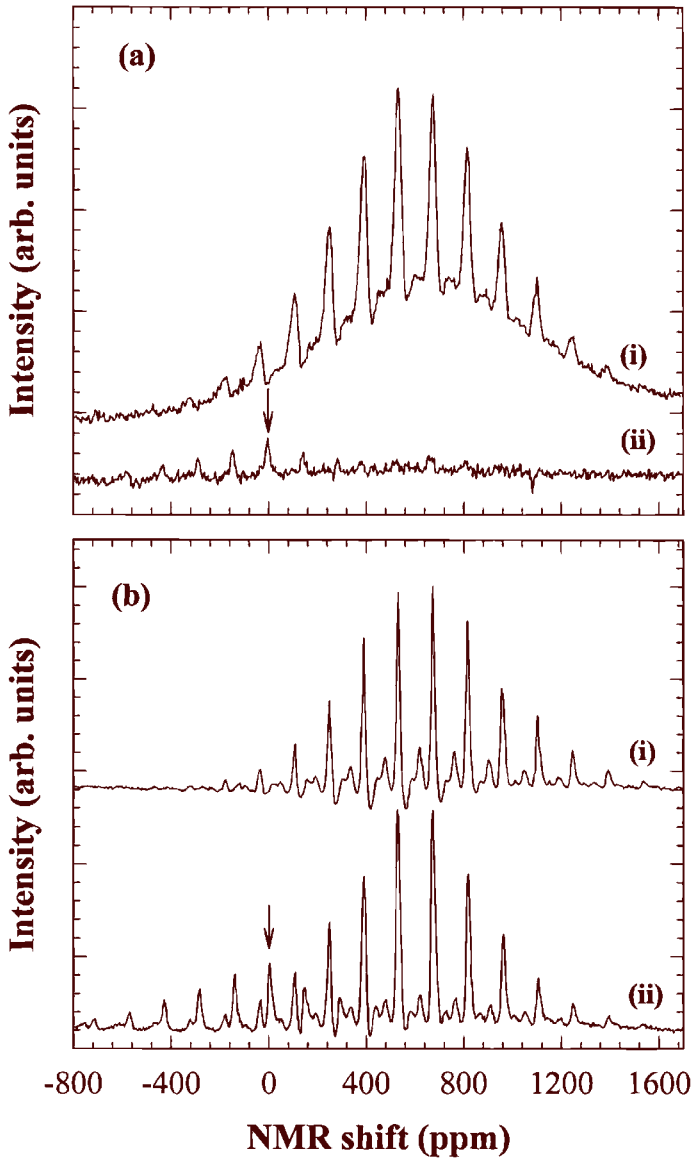


*Figure 3-2. A comparison $^{7}Li$ MAS NMR spectra of $^{7}Li$ MAS NMR spectra (i) before and (ii) after Li intercalation for (a) 250 °C sample and (b) 700 °C one. The arrows indicate the additional signals from the trace of salt and/or passivating film. (From Ref. 4)*

This assertion is supported by Goodenough group's recent work. At the first stage, they found that $Li[Li_yMn_{2-y}]O_4$ spinel powders prepared by either a sol-gel or an aqueous solution method, showed excellent cyclability in the 3V range (2.4-3.4 V) [5,6]. In their further study, it was observed that even the well-crystalline spinel displayed improved capacity retention after sufficiently lasted ball-milling process to mix active material and carbon [7]. As an explanation, the ball-milling of well-crystalline spinel powders would generate nanograins, intraparticular strain and increased manganese oxidation state, resulting in an enhanced cyclability in the 3V domain. Such results can be also understood in the same context of the electrochemical grafting.

### 3-1-2. Amorphous or Nanocrystalline Li-Na-Mn-O-I as a Li-Cathode

As already mentioned above, thermodynamically stable spinel phase is well-known to suffer from capacity fading during repeated charge–discharge cycling. The capacity loss of this cathode material is closely related to the structural transition from cubic spinel to tetragonal one, leading to a structural breakdown and to a formation of electronically isolated zones [15,18]. In fact, this sort of problems originating from the phase transition are considered to be more or less inevitable for well-crystalline lithium manganese oxides. Such a speculation gives an impetus to develop amorphous phases as an alternative cathode material, since this type of compounds would be much more tolerable for the repeated Li insertion–deinsertion processes. Consequently, numerous amorphous or nanocrystalline manganese oxides have been developed by precipitation

or sol-gel route [19-21]. Among these nanocrystalline materials, sodium-based manganese oxyiodides possess a quite large discharge capacity and excellent cyclability.

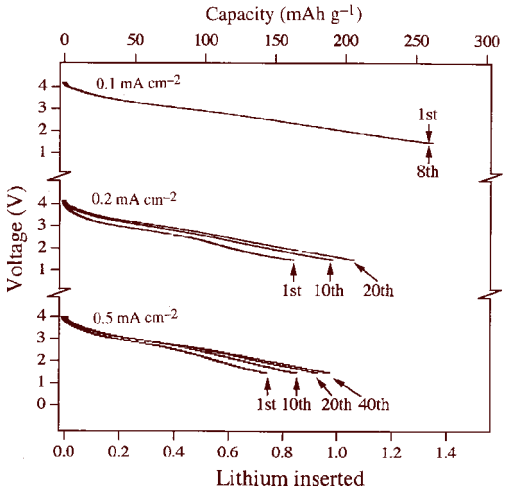


*Figure 3-3. Discharge curves and cyclability of $Li_{1.5}Na_{0.5}MnO_{2.85}I_{0.12}$ recorded at various current densities. (From Ref. 8)*

While many research groups have studied $LiMn_2O_4$, alkali metal manganese oxyiodides have been investigated mainly by Manthiram's group. First, they announced $Li_{1.5}Na_{0.5}MnO_{2.85}I_{0.12}$ prepared by reacting $NaMnO_4$ with LiI in acetonitrile and following heat-treatment at 250 °C. This material showed a large reversible capacity of 260 mAh/g in the range 1.5 ~ 4.3 V vs. Li at a current density of 0.1 mA/cm$^2$, as drawn in Figure 3-3 [8]. The enhanced performance was attributed to the amorphous nature of the material, which led to reversibility in $Mn^{2+/3+}$ electrochemical couple. This phenomemon is different from that of other well-crystalline manganese oxides which show reversilibity only for $Mn^{3+}/Mn^{4+}$ couple. However, the capacity was found to be decreased on increasing current density; the first discharge capacity was ~ 140 mAh/g at a current density of 0.5 mA/cm$^2$. Further systematic investigation of the product discovered that ball-milling could improve the electrochemical properties. In an optimized process, the 40 min. ball-milled sample exhibited 275 mAh/g even at a higher current density of 0.5 mA/cm$^2$ [10]. These findings directed to research for analogous synthesis in aqueous solution for next step,

because water is cheaper and more environmentally friendly than organic solvents. Several papers reported the reaction of $NaMnO_4$ with LiI (or NaI) in aqueous solution and subsequent heat-treatment at 500 °C or 600 °C [9,11,14]. Firing at rather high temperature led to evaporatation of the iodine contents and somewhat crystallized the samples. XRD patterns proved the co-existence of $LiMn_2O_4$ and $Na_xMnO_2$ phases as main components. It was also found that $Na_{0.5}MnO_2$ with tunnel structure formed on firing at ≥ 600 °C and $Na_{0.7}MnO_2$ with layered structure was produced at ~ 500 °C. The less-crystalline layered product showed better performance than the tunnel-structured one, which would also imply the same mechanism of electrochemical grafting.

## 3-2. NEW POTASSIUM-BASED NANOCRYSTALLINE MANGANESE OXYIODIDE CATHODE PREPARED IN AQUEOUS SOLUTION

As stated above, the sodium-based manganese oxyiodides possess a quite large discharge capacity and good cyclability. On the other hand, Whittingham *et al.* reported that a potassium-based manganate with rhombohedral layered structure is more stable for electrochemical lithiation–delithiation reaction compared to sodium- or lithium-based ones [22,23]. Despite such contradiction, there is no systematic study on potassium-based nanocrystalline manganese oxyiodide although it is worthwhile to probe the effect of alkali metal on the electrochemical properties of these nanocrystalline manganese oxyiodide. Here we would like to present the preparation of a new potassium-based nanocrystalline manganese oxyiodide in aqueous solution and

characterization of its physico-chemical properties in comparison with those of sodium-based homologue. Generally, it is quite difficult to probe the local cation ordering of amorphous/nanocrystalline compounds because of their X-ray amorphous character. We attempted to determine the local geometric and electronic structures around manganese before and after chemical lithiation using micro-Raman and Mn K-edge X-ray absorption analysis. The chemical bonding characters of iodine species in these nanocrystalline materials was also studied by I $L_I$-edge X-ray absorption near-edge structure (XANES) analysis.

### 3-2-1. Experimental

The nanocrystalline A–Li–Mn–O–I (A = K and Na) samples were prepared by reacting the aqueous solution of $KMnO_4$ or $NaMnO_4 \cdot H_2O$ with 1.5 equiv LiI at room temperature, similar to the previously reported *Chimie Douce* method [8-14]. The mixed solution was maintained for 1 day under constant stirring. The resulting precipitate was washed with water, and dried at 130 °C in vacuum. The chemical lithiation reaction for these amorphous samples was carried out by reacting them with 1.6 M *n*-BuLi in hexane for 48 h. Prior to the physico-chemical characterization, the lithiated-samples were washed thoroughly with hexane and ethanol, and dried in vacuum.

The crystal structures of A–Li–Mn–O–I (A = K and Na) and their chemically lithiated products were studied by X-ray diffraction (XRD) measurement using Ni-filtered Cu $K_\alpha$ radiation with a graphite diffracted beam monochromator. The chemical

compositions of these samples were determined by using atomic absorption (AA) spectrometry, inductive coupled plasma (ICP) spectrometry, and electron probe for micro-analysis (EPMA). The water contents were estimated by performing thermogravimetric analysis (TGA) under $O_2$ flow. The weight losses of ~3% and ~6% up to ~150 °C are observed for the Na- and K-based nanocrystals, respectively, indicating that these materials possess about 0.2–0.4 mole water per unit formula [22]. The electrochemical measurements were performed with the cell configuration of Li | 1M $LiPF_6$ in EC:DEC (50:50 v/v) | composite cathode, which was assembled in a dry-box. The composite cathode was prepared by mixing thoroughly the active A–Li–Mn–O–I (A = K and Na) material (20 mg, 70 wt%) with 25 wt% of Ketjenblack and 5 wt% of PTFE (polytetrafluoroethylene). Charge/discharge experiments were carried out in a galvanostatic mode using a computer-controlled PGS201T (Tacussel) system between 1.5 – 4.3 V at the constant current densities of 0.2 and 0.5 mA/$cm^2$ (10 and 25 mA/g).

The micro-Raman spectra presented here were recorded on a Dilor-Omars microspectrometer coupled with an optical microscope (spatial resolution of 1 $\mu m^2$) and an intensified 1024-channel photodiode array detector. The 514.5 nm line from an argon ion laser Spectra Physics model 2016 was used as an excitation source. All the present spectra were measured by backscattering from the freshly fractured surfaces of the pellet or from the powdered sample. In order to prevent possible thermal damage of the samples, the power of incident laser light was maintained at less than 1 mW. After each measurement, the sample surface was thoroughly checked to remove the possibility of spectral modification caused by surface degradation.

The XAS experiments were performed for nanocrystalline A–Li–Mn–O–I (A = K and Na) compounds and their lithiated derivatives by using the EXAFS facility installed at the beam line 7C at the Photon Factory in Tsukuba, operated with electron storage ring energy of 3.5 GeV and the electron current of about 300 – 360 mA. The X-rays are monochromatized by a Si (111) double crystal for all the present XAS data. All the present spectra were obtained at room temperature in a transmission mode using gas-ionization detectors with a spacing of ~ 0.4 eV for the XANES region and ~ 1.5 eV for the EXAFS one. The powder samples for XAS experiments were prepared in the form of pellet, in which the finely ground samples were diluted with boron nitride in order to obtain an optimum absorption jump ($\Delta\mu \cdot t \cong 1$). All spectral data were calibrated by measuring the spectra of Mn metal foil and KI. The data analysis for the experimental spectra was carried out by the standard procedure using computer program UWXAFS version 2.0 [24,25].

### 3-2-2. Powder XRD and Chemical Analysis

The powder XRD patterns of as-prepared A–Li–Mn–O–I (A = K and Na) compounds are shown in Figure 3-4, together with those of their heated and lithiated products. No distinct reflection can be observed for the nanocrystalline samples heated at 130 °C in vacuum. After the heat-treatment at 600 °C, an amorphous phase is changed into a mixed crystalline phase, that is, a mixture of rhombohedral layered $K_xMnO_2$ [22,23] and cubic-spinel $Li_{1+y}Mn_{2-y}O_4$ for the potassium-based nanocrystal, and a mixture of $Na_{0.7}MnO_2$ [8,11] and cubic-spinel $Li_{1+y}Mn_{2-y}O_4$ for the sodium-based

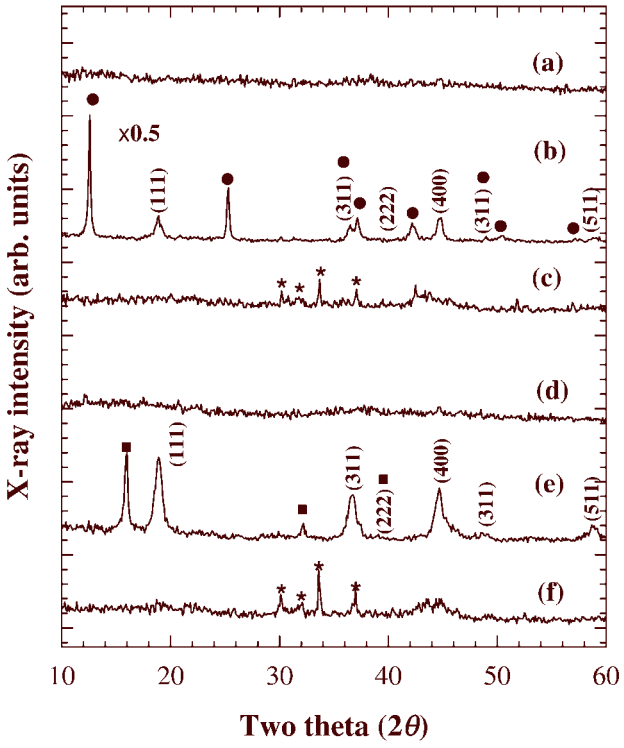


*Figure 3-4. X-ray diffraction patterns of (a) nanocrystalline K-Li-Mn-O-I compound and its derivatives (b) after the heat-treatment at 600 °C, and (c) after lithiation, together with (d-f) the corresponding data of Na-homologues. In (b) and (e), the indexed reflections are assigned on the basis of cubic spinel structure, and the circle and square symbols represent the reflections from $K_xMnO_2{\cdot}yH_2O$ and $Na_{0.7}MnO_2$ phases, respectively. And the asterisk symbols in (c) and (f) denote the peaks originating from $LiOH{\cdot}H_2O$.*

nanocrystal.

In the case of the lithiated derivatives, there is no XRD peak related to the crystalline lithium manganate, except several weak reflections corresponding to small amount of lithium hydroxide hydrate formed by a reaction with *n*-BuLi and water in the samples. This finding indicates that the amorphous structure of the present nanocrystalline manganese oxyiodides is highly tolerable for Li insertion reaction.

The chemical formulas of the nanocrystalline A–Li–Mn–O–I (A = K and Na) compounds and their lithiated derivatives estimated from AA, ICP, and EPMA analyses

are summarized in Table 3-2. The concentration of alkali metal ion is determined to be smaller for the potassium-based nanocrystal than for the sodium-based one, whereas the iodine content is larger for the former compared to the latter. As listed in Table 3-2, the lithiation process results in the incorporation of about two moles of lithium ions per unit formula commonly for both nanocrystalline materials. This reflects their greater ability to accommodate lithium ions compared to the well-crystallized electrode materials like $LiMn_2O_4$ spinel, even though a fraction of lithium ions are consumed up for the reaction with the sample water, leading to the formation of lithium hydroxide.

Table 3-2. Chemical formulas of nanocrystalline manganese oxyiodides and their lithiated derivatives

| Sample | as-prepared | Lithiated |
|---|---|---|
| K–Li–Mn–O–I | $Li_{0.54}K_{0.31}MnO_{2.5-\delta}I_{0.10}$ | $Li_{2.45}K_{0.34}MnO_{2.5-\delta}I_{0.13}$ |
| Na–Li–Mn–O–I | $Li_{0.52}Na_{0.62}MnO_{2.5-\delta}I_{0.07}$ | $Li_{2.48}Na_{0.79}MnO_{2.5-\delta}I_{0.08}$ |

### 3-2-3. Electrochemical Performance

The cycling characteristics of the nanocrystalline A–Li–Mn–O–I (A = K and Na) compounds have been examined to probe the effect of alkali metal on the electrochemical performance of the lithium manganese oxyiodides. Since both pristine materials possess an open circuit potential of ~3.4 V (vs. $Li/Li^+$), the electrochemical

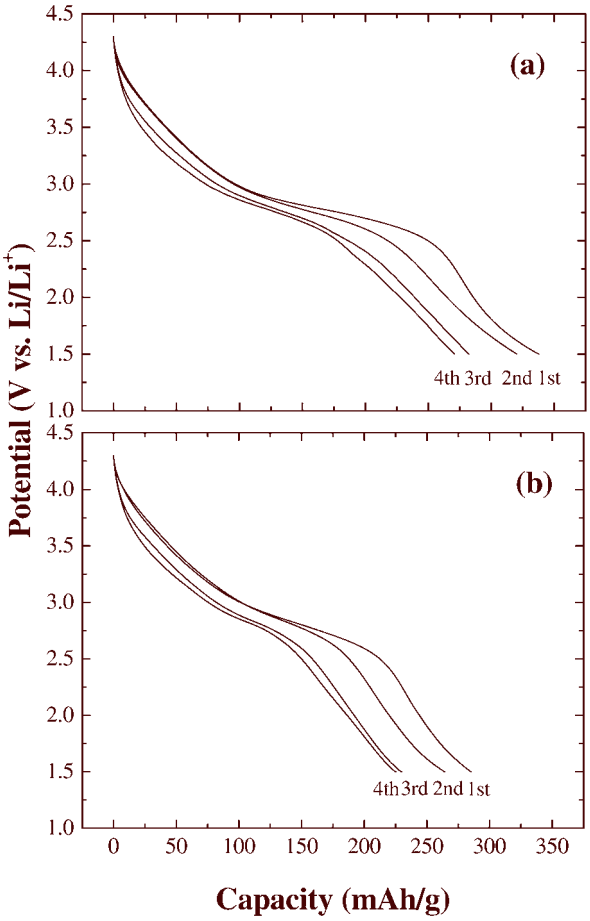


*Figure 3-5. Discharge potential profiles of the nanocrystalline A–Li–Mn–O–I compounds with A = (a) K and (b) Na. The electrochemical measurements were carried out in the potential range of 1.5–4.3 V with the applied current density of 0.2 mA/cm$^2$.*

cycling starts with the first charge process up to 4.3 V.

The discharge potential profiles of the nanocrystalline A–Li–Mn–O–I (A = K and Na) compounds measured at a constant current density of 0.2 mA/cm$^2$ are plotted in Figure 3-5. For both compounds, a small capacity of ~110 mAh/g corresponding to the oxidation of trivalent manganese ions is commonly observed (not shown in the figure), which is much smaller than the capacity of the following discharge process. This underlines that the electrochemical activity of these manganese oxyiodides is attributed mainly to the insertion of lithium ion from Li anode rather than to the re-insertion of lithium ions which already exist in the as-prepared materials. Both nanocrystals show nearly identical curve shape, which is very close to that of the previously reported amorphous manganese dioxide [8-14,19,20], confirming the

amorphous character of the present manganese oxyiodides. The observed smooth decrease of potential during discharge process is a characteristic of nanocrystalline electrode materials such as $SnO_2$, $Fe_2O_3$, etc [26-28].

This can be explained by the fact that the existence of surface defects and/or surface dangling bonds in nanocrystalline materials gives rise to the formation of many sub-bands between valence and conduction bands, leading to a smooth change of Fermi-energy and hence a slow potential change [4]. In comparison with the sodium-based manganese oxyiodide, the potassium-based one shows a greater discharge capacity for each cycle.

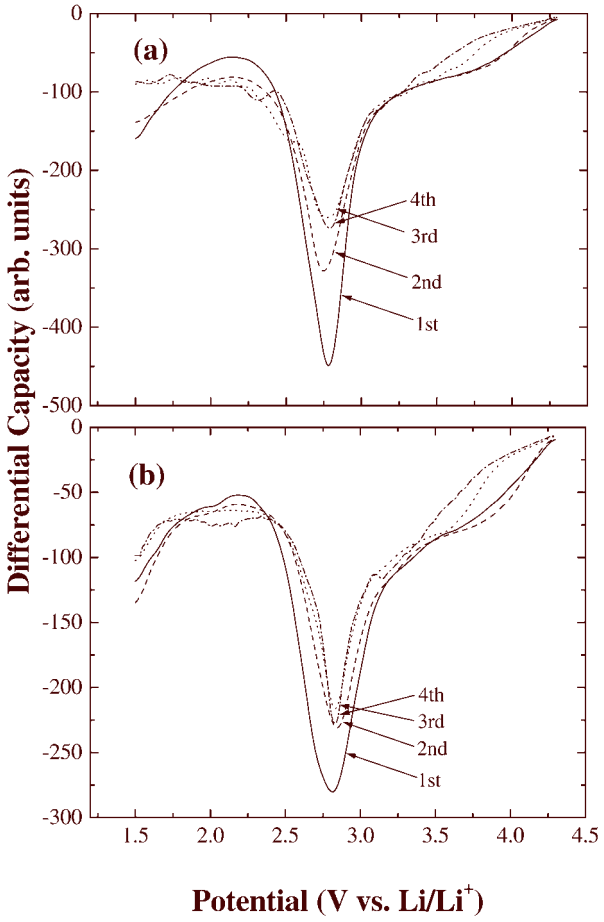


*Figure 3-6. Differential capacity profiles of the nanocrystalline A–Li–Mn–O–I compounds with A = (a) K and (b) Na. The electrochemical measurements were carried out in the potential range of 1.5–4.3 V with the applied current density of 0.2 mA/cm$^2$.*

For a more accurate inspection of discharge behaviors, the differential capacity profiles of the nanocrystalline A–Li–Mn–O–I (A = K and Na) compounds are presented in

Figure 3-6. As the cycle proceeds, no significant change in curve shape, except a slight depression of the peak at ~ 2.7 V, can be observed for both compounds, which suggests that the electrochemical discharge–charge process does not induce any marked structural transition in these nanocrystalline materials. However, it is worthwhile to note that the present nanocrystals commonly show a significant capacity fading, which is fairly contrasted with the previous report on the sodium-based materials prepared in acetonitrile solvent [8,10]. This may be attributed not to the structural transition but to the presence of water leading to the formation of LiOH and HF via the reaction with Li anode and electrolyte respectively. In this context, now we are trying to prepare potassium-based nanocrystal in nonaqueous solvent and to examine the effect of ball milling on its electrochemical property, with a view to improving the cyclability and discharge capacity of this promising nanocrystalline material. On the other hand, we have also measured the electrochemical performances of the present nanocrystalline samples up to 20 cycles with a higher current density of 0.5 $mA/cm^2$, in order to examine the long-term cycling characteristics as well as to probe the effect of current density.

As presented in Figure 3-7, the potassium-based phase shows the high initial discharge capacity of 185 mAh/g with a notable capacity decrease to 120 mAh/g after the 20th cycle, whereas the sodium-based one exhibits a better capacity retention from 178 mAh/g at the first cycle to 155 mAh/g at the 20th cycles. This is surely contrasted with the results obtained with the lower current density of 0.2 $mA/cm^2$. Such different long-term cycle characteristics of these nanocrystals are suggested to originate from their dissimilar water contents and/or from the contribution of other chemical species like

Na/K or iodine to discharge capacity. However, it is quite difficult to conclude here the origin of the observed electrochemical behavior of the present nanocrystals, since there are so many factors to be considered influencing the long-term cycling performance. In order to answer this question, now we are performing the detailed electrochemical measurements with various experimental conditions. In this context, here we limit our further discussion to why the potassium-based phase shows a greater "initial" discharge capacity than the sodium-based one. In fact, prior to the electrochemical measurements, we expected that the potassium-based compound possesses inferior initial discharge capacity to the sodium-based one, judging from the heavier atomic weight of potassium compared to sodium. But this is not true for the nanocrystalline materials presented here. In order to understand such unexpected finding, we have examined the local structure around manganese in both nanocrystalline compounds by performing micro-Raman and XANES/EXAFS tools complementarily.

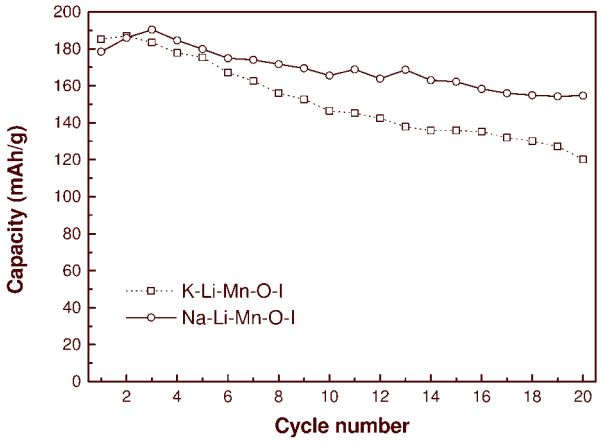


*Figure 3-7. Discharge capacities of the nanocrystalline A–Li–Mn–O–I compounds with A = K (squares) and Na (circles). The electrochemical measurements were carried out in the potential range of 1.5–4.3 V with the applied current density of 0.5 mA/cm$^2$.*

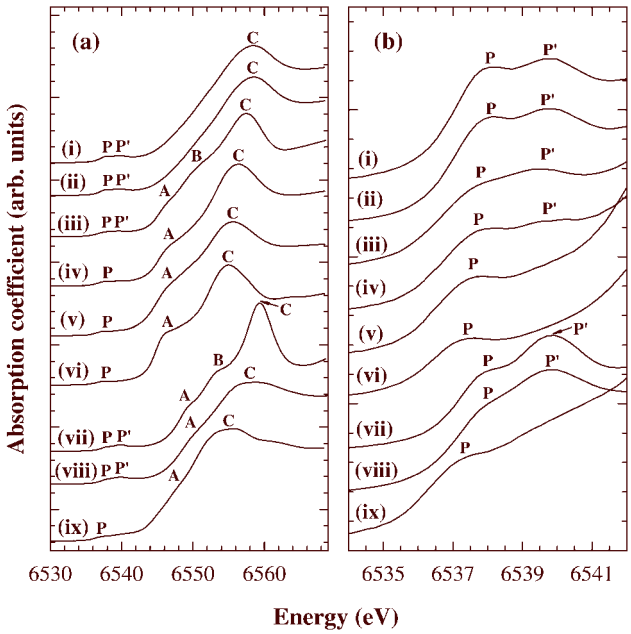


*Figure 3-8. (a) Mn K-edge XANES spectra for the nanocrystalline A–Li–Mn–O–I compounds with A = (i) K and (ii) Na and (iv–v) their lithiated derivatives, in comparison with the references (iii) cubic spinel $LiMn_2O_4$, (vi) tetragonal spinel $Li_2Mn_2O_4$, (vii) λ-$MnO_2$, (viii) nanocrystalline manganese oxide, and (ix) $Mn_2O_3$. The magnified spectra for pre-edge region are presented in (b).*

### 3-2-4. Local Structure Inverstigation Using Raman and X-ray Absorption Spectroscopy

The Mn K-edge XANES spectra of the pristine nanocrystalline A–Li–Mn–O–I (A = K and Na) compounds and their lithiated derivatives are illustrated in Figure 3-8a, in comparison with the reference spectra of cubic spinel $LiMn_2O_4$, tetragonal spinel $Li_2Mn_2O_4$, λ-$MnO_2$, nanocrystalline manganese oxide [29] (This material corresponds to the sample 2 in ref. 29 with composition of $MnO_{1.89}$), and $Mn_2O_3$. The position of the edge jump for the pristine manganese oxyiodides is a little bit higher than that for $LiMn^{+IV}Mn^{+III}O_4$ but slightly lower than that for λ-$Mn^{+IV}O_2$, which indicates that manganese ions in these materials have an average valence state of > +3.5.

Actually the sodium-based manganese oxyiodide has been reported to possess the

average Mn oxidation state of about +3.8 [8]. In case of the lithiated manganese oxyiodides, the edge position is rather in accordance with that of tetragonal spinel $Li_2Mn^{+III}{}_2O_4$, confirming the reduction of manganese ions after the *n*-BuLi-treatment. In the pre-edge region, all the spectra presented here show small pre-edge peaks (denoted P and P'), which are assigned as the transitions from the core 1*s* level to unoccupied 3*d* states. Even though they are not allowed by the electronic dipolar selection rule, $\Delta l = \pm 1$, the pre-edge peaks could be discerned either due to quadrupole-allowed transitions and/or due to the mixing of 4*p* and 3*d* states. In this context, the weak intensity of these features suggests that all the manganese ions in the samples under investigation are stabilized in octahedral site with an inversion center. The position and shape of these pre-edge peaks are well-known to be closely related to the oxidation state of the absorbing ion and the local arrangement of back-scattering ions, respectively. As can be seen clearly from Figure 3-8b, the relative energies of the pre-edge peaks are wholly consistent with the order of the main-edge positions. It is also evident that the spectral shape of pre-edge features in all the samples presented here can be classified into two groups; two pre-edge peaks P and P' are discernible for some materials containing considerable amount of tetravalent manganese ions, whereas only one feature P at lower energy can be observed for the others with trivalent manganese ions. In fact, the latter characteristic pre-edge feature for trivalent manganese compounds can be interpreted as a result of the splitting of $t_{2g}$ and $e_g$ energy levels modified by Jahn-Teller deformation [30]. For the nanocrystalline manganese oxyiodides under investigation, both the pristine materials exhibit nearly the same spectral features in pre-edge region, whereas there are marked spectral differences

between the corresponding lithiated derivatives. That is, the lithiation reaction gives rise to a smaller change in the pre-edge features of the potassium-based nanocrystal compared to the sodium-based one, which suggests that the Jahn-Teller deformation of the $MnO_6$ octahedra is smaller in the former. In the main-edge region, there are some peaks (denoted A, B, and C), which are assigned as the dipole-allowed transitions from the core 1*s* level to unoccupied 4*p* states. In contrast to the well-crystallized $LiMn_2O_4$ and λ-$MnO_2$ [31], both the pristine nanocrystalline compounds do not show the fine features A and B in this region, which is attributed to the absence of long-range crystal order. This finding is well consistent with the recent XANES study for Na-based nanocrystal [12]. On the contrary, a distinct peak A is clearly observed for both the lithiated derivatives as well as for tetragonal spinel $Li_2Mn_2O_4$, although its spectral weight is weaker for the formers than for the latter. Since the strong peak A is an indicator of trivalent manganese ion stabilized in the Jahn-Teller distorted octahedra [32], the observed weak intensity of peak A indicates that the Jahn-Teller deformation around manganese is less prominent for the nanocrystalline manganese oxyiodide than for the well-crystallized tetragonal spinel, as reported recently [12]. Moreover, a closer inspection on the present XANES spectra reveals that K-based nanocrystal exhibits smaller intensity of peak A than Na-based one, which is well correlated with less prominent change of pre-edge features after lithiation in the former. On the other hand, an intense and sharp peak C appears commonly for all the nanocrystalline manganese oxyiodides including the lithiated derivatives as well as for the spinel-structured compounds. Considering the fact that the intensity of this peak is proportional to the relative concentration of edge-shared $MnO_6$ octahedra with respect to corner-shared one

[33], it can be supposed that the crystal structure of nanocrystalline manganese oxyiodides consists of edge-shared $MnO_6$ octahedra like spinel-structured compounds. In contrast, only a broader and less intense peak C can be discerned for another nanocrystalline manganate without iodine and potassium species (sample (viii) in Figure 3-8), indicating this compound has the intergrowth structure of edge- and corner-shared $MnO_6$ octahedra. On the basis of this finding, it can be supposed that iodine and potassium ions may act as stabilizers for edge-shared $MnO_6$ network. It has been known that there are some kinds of lithium manganate phases like spinel $LiMn_2O_4$, layered $LiMnO_2$, etc, whose crystal structures constitute with edge-shared $MnO_6$ octahedra. However, on the basis of the present Mn K-edge XANES results, it is very difficult to determine conclusively the local structure around manganese in the nanocrystalline manganese oxyiodides. In order to solve this problem, we have applied micro-Raman spectroscopy.

The Raman spectra of the nanocrystalline A–Li–Mn–O–I (A = K and Na) compounds are represented in Figure 3-9, together with the reference spectra of rhombohedral layered $LiCoO_2$, cubic spinel $LiMn_2O_4$, monoclinic layered $LiMnO_2$, and tetragonal spinel $Li_2Mn_2O_4$. As predicted by the factor group analysis, the rhombohedral $LiCoO_2$ compound exhibits two $A_{1g}$ and $E_g$ phonon lines at 486 and 596 $cm^{-1}$, whereas three Raman peaks corresponding to Raman-active $2A_g + B_g$ modes are observed for the layered $LiMnO_2$ oxide at 422, 481, and 603 $cm^{-1}$ [34,35]. In the case of spinel-structured compounds, larger number of Raman peaks appear due to their complex crystal structure. As shown in Figure 3-9, the present cubic spinel $LiMn_2O_4$ sample shows four Raman peaks at 270, 340, 454, and 631 $cm^{-1}$, which assigned as $2T_{2g}$,

$E_g$, and $A_{1g}$ mode, respectively, whereas four characteristic phonon lines can be detected for the tetragonal spinel phase in the frequency range 200–650 $cm^{-1}$.

It is worthwhile to mention that the Raman spectrum of tetragonal spinel $Li_2Mn_2O_4$ can be clearly distinguished from that of monoclinic layered $LiMnO_2$, even though both the lithium manganates show almost the same XRD patterns [36]. This is due to the fact that Raman spectrum is strongly dependent on the crystal symmetry rather than the structure factor. In this regard, the Raman spectroscopy enables us to easily identify various lithium manganate phases with closely related crystal structures such as layered $LiMnO_2$ (*C2/m*), tetragonal spinel $Li_2Mn_2O_4$ ($I4_1/amd$), orthorhombic $LiMnO_2$ (*Pmnm*), and etc [34]. In the case of the nanocrystalline manganese oxyiodides, two very broad features are discernible around 490 and 630 $cm^{-1}$. Considering the fact that the nanocrystalline nature and the mixed Mn oxidation state of the

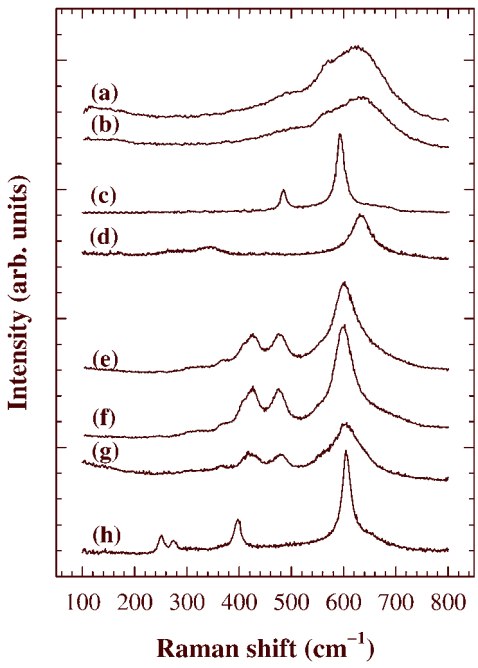


*Figure 3-9. Micro-Raman spectra for the nanocrystalline A–Li–Mn–O–I compounds with A = (a) K and (b) Na and (e–f) their lithiated derivatives, in comparison with the references (c) rhombohedral layered $LiCoO_2$, (d) cubic spinel $LiMn_2O_4$, (g) monoclinic layered $LiMnO_2$, and (h) tetragonal spinel $Li_2Mn_2O_4$.*

present manganese oxyiodides are surely responsible for the very broad Raman feature, the Raman spectra of these nanocrystals are somewhat similar to that of rhombohedral $LiCoO_2$, rather than that of spinel $LiMn_2O_4$. However, the considerable broadness of features makes it very difficult to definitively determine the local structure of nanocrystalline materials on the basis of the present Raman spectra. In this regard, we have also examined the Raman spectra of lithiated manganese oxyiodides, since the lithiation usually increases the signal to noise (S/N) ratio of Raman data by depressing the electrical conductivity. As can be seen clearly from Figure 3-9, there is remarkable spectral consistency between the nanocrystalline materials and the monoclinic layered $LiMnO_2$, highlighting that the lithiated derivatives possess the layered structure with monoclinic distortion. Generally the reduction of Mn oxidation state induces a Jahn-Teller distortion around manganese, giving rise to a structural transition from rhombohedral layered to monoclinic layered, or from cubic spinel to tetragonal spinel. Moreover, it is impossible to change from spinel structure to layered one during lithiation process, since the spinel structure is thermodynamically more stable than the layered one. In this regard, we can conclude that the manganese ion in nanocrystalline manganese oxyiodide crystallizes locally in rhombohedral layered cation ordering not in the spinel-type one, and the lithiation reaction results in a local structural change into monoclinic layered structure.

The local structural variation of the nanocrystalline A–Li–Mn–O–I (A = K and Na) compounds upon chemical lithiation process has been examined quantitatively using Mn K-edge EXAFS spectroscopy. The $k^3$-weighted Mn K-edge EXAFS spectra for the nanocrystalline A–Li–Mn–O–I (A = K and Na) compounds and

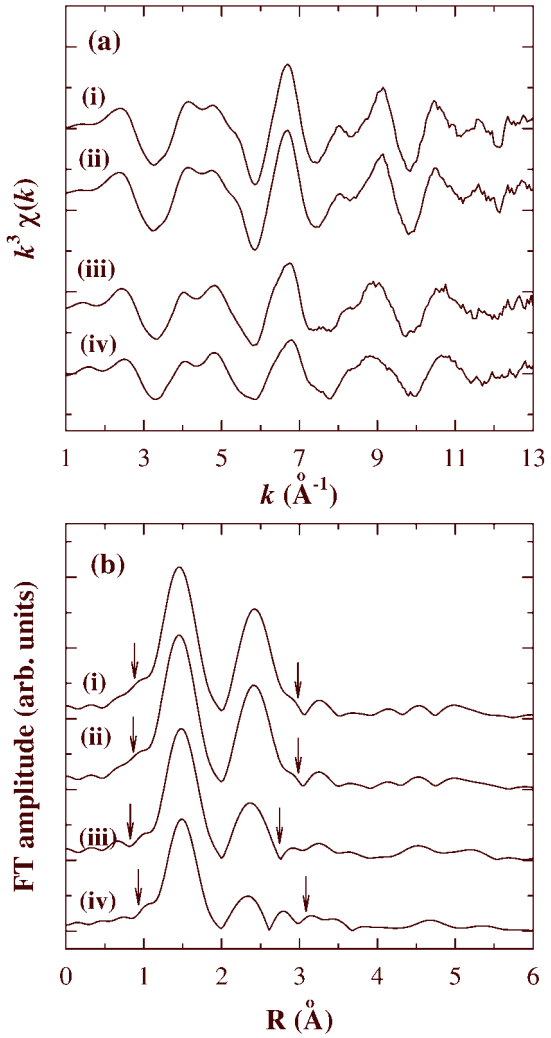


*Figure 3-10. (a) $k^3$-weighted Mn K-edge EXAFS spectra and (b) their Fourier transforms for the nanocrystalline A–Li–Mn–O–I compounds with A = (i) K and (ii) Na, and (iii–iv) their lithiated derivatives. The range over which the Fourier filtering has been made is shown by the arrows.*

their lithiated derivatives are represented in Figure 3-10a, and the corresponding Fourier transforms (FTs) in Figure 3-10b. As can be seen from Figure 3-10a, the overall spectral features of the EXAFS oscillation of the pristine nanocrystalline compounds are quite similar to each other, indicating the same local structure around manganese in both compounds.

On the other hand, the lithiation process gives rise to a spectral change in EXAFS oscillation which is less prominent for K-based material than for Na-based one, as observed in XANES region. In the FT diagrams (Figure 3-10b), the nanocrystalline manganese oxyiodides exhibit two intense FT peaks

at ~1.5 and ~2.5 Å, which are attributed to the (Mn–O) and (Mn–Mn) shells, respectively. Upon lithiation reaction, the FT peaks become depressed especially for (Mn–Mn) shell, which can be understood from the fact that the Jahn-Teller distortion around Mn causes a damping of EXAFS signal. However, in contrast to the previously reported results for the spinel phase [31,37], the splitting of FT peaks corresponding to (Mn–Mn) shells induced by lithiation is not obvious for the present nanocrystalline compounds, which is well correlated with the XANES results [12]. Between both lithiated nanocrystals, the splitting of (Mn–Mn) shells is more well-resolved for Na-based material than for K-based one. These findings can be regarded as further evidence for the excellent endurance of the amorphous character of these nanocrystalline materials during Li insertion reaction, especially for the case of K-based nanocrystal. It is also worthwhile to mention that the peaks at 4–6 Å originated from the multiple scattering paths with focusing effect are nearly suppressed in the present compounds, in contrast to the well-crystalline $LiMnO_2$ and $LiMn_2O_4$ ones [31,32]. This confirms the nanocrystalline nature of the present manganese oxyiodides. In order to determine the structural parameters such as coordination number (*CN*), bond distance (*R*), and Debye-Waller factor ($\sigma^2$), these FT peaks were isolated by inverse Fourier transform to a *k* space and then curve-fitted. In the light of micro-Raman results, we have tried to reproduce the spectra of nanocrystalline manganese oxyiodides and their lithiated derivatives on the basis of the crystal structures of rhombohedral layered and monoclinic layered phases, respectively, in such a way that we were able to get reasonable fitting results (We have also tried to reproduce the experimental EXAFS data of lithiated derivatives on the basis of rhombohedral layered

structure, but it gave poor fits and physically meaningless structural parameters). The best fitting results and the obtained structural parameters are listed in Table 3-3. While the manganese ion in the nanocrystalline A–Li–Mn–O–I (A = K and Na) compounds is stabilized in a regular $MnO_6$ octahedron with six neighboring oxygen ions at the same distance, the manganese ion in the lithiated derivatives exists in a Jahn-Teller distorted $MnO_6$ octahedra, as supposed from micro-Raman study. Moreover, the average (Mn–O) and (Mn–Mn) bond distances of the nanocrystalline materials are found to be elongated by lithiation reaction, confirming the decrease of Mn oxidation state after reaction with *n*-BuLi. In addition, the coordination numbers are determined to be smaller for (Mn–Mn) shells than for (Mn–O) shells, which reflects the nanocrystalline nature of the present samples leading to an incomplete coordination of manganese by distant shells.

Table 3-3. Results of nonlinear least-squares curve-fitting analysis for the Mn K-edge EXAFS spectra of nanocrystalline manganese oxyiodides and their lithiated derivatives

| sample | bond | $CN^{(a)}$ | $R$ (Å) | $\sigma^2$ ($10^{-3} \times$ Å$^2$) |
|---|---|---|---|---|
| K–Li–Mn–O–I | (Mn–O) | 6.0 | 1.90 | 4.89 |
| | (Mn–Mn) | 4.2 | 2.86 | 6.22 |
| Na–Li–Mn–O–I | (Mn–O) | 6.0 | 1.90 | 4.95 |
| | (Mn–Mn) | 4.3 | 2.85 | 6.91 |
| | (Mn–$O_{eq}$) | 4 | 1.90 | 3.21 |

| | | | | |
|---|---|---|---|---|
| lithiated K–Li–Mn–O–I | (Mn–$O_{ax}$) | 2 | 2.33 | 10.60 |
| | (Mn–Mn) | 1.4 | 2.87 | 2.82 |
| | (Mn–Mn) | 2.8 | 3.02 | 9.99 |
| lithiated Na–Li–Mn–O–I | (Mn–$O_{eq}$) | 4 | 1.90 | 4.08 |
| | (Mn–$O_{ax}$) | 2 | 2.27 | 15.31 |
| | (Mn–Mn) | 1.4 | 2.83 | 5.73 |
| | (Mn–Mn) | 2.8 | 3.02 | 15.11 |

[(a)] While the coordination numbers for (Mn–O) shells are fixed to the crystallographic values, those for (Mn–Mn) shells are set as variables in the course of curve-fitting analysis.

### 3-2-5. The Role of Iodine Explored by I $L_I$-Edge XANES Analysis

As described in the Mn K-edge XANES section, another type of nanocrystalline manganate without iodine and potassium species crystallizes with edge- and corner-shared network of $MnO_6$ octahedra, in contrast to the present manganese oxyiodides. In this regard, it is very interesting to question what the role of iodine is. In order to give an answer to this question, we have studied the chemical bonding character of iodine species by performing I $L_I$-edge XANES analysis. The I $L_I$-edge XANES spectra of the nanocrystalline manganese oxyiodides and their lithiated derivatives are presented in Figure 3-11, in comparison with the reference spectra of KI, $I_2$, $KIO_3$, and $KIO_4$.

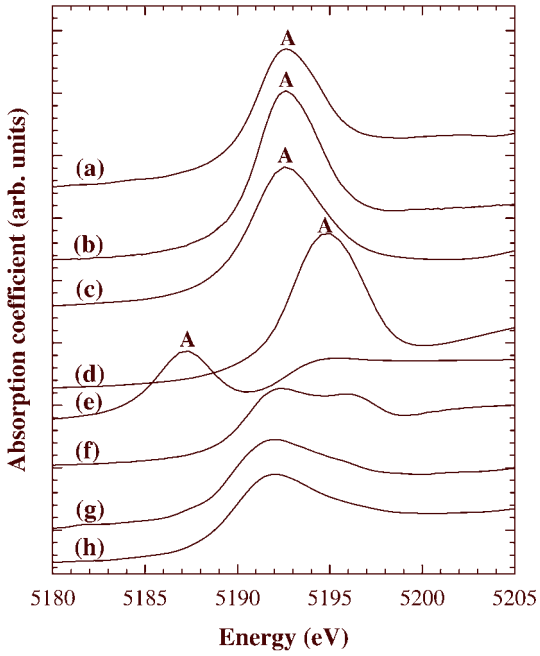


*Figure 3-11. I $L_I$-edge XANES spectra for the nanocrystalline A–Li–Mn–O–I compounds with A = (a) K and (b) Na and (g–h) their lithiated derivatives, in comparison with the references (c) $KIO_3$, (d) $KIO_4$, (e) $I_2$, and (f) KI.*

All the reference spectra except for KI exhibit a characteristic white line (WL) peak at around 5185–5195 eV, which is ascribed to the transition from the 2*s* core level to the unoccupied 5*p* state [38]. Since the intensity of this WL feature is dependent on the density of the unoccupied 5*p* final state, the most intense peak is discernible for both $KIO_3$ and $KIO_4$ references having completely empty I 5*p* orbitals. On the contrary, this 2*s* → 5*p* transition is not possible for KI due to the full occupancy of I 5*p* orbital. In the case of pristine nanocrystalline materials, this WL peak shows almost the same position and intensity as the reference $KIO_3$, which indicates that the iodate species is stabilized in nanocrystalline manganate oxyiodides, as reported very recently [13]. There are two possibilities about the site of $IO_3^-$ cluster in these nanocrystalline compounds; one is the interlayer site and the other is the grain boundary or the sample surface. As shown in Figure 3-11, a notable depression of peak A upon lithiation can be observed for both nanocrystalline materials, suggesting that most of iodate ion is reduced to a negatively charged iodide ion. Considering the electrostatic repulsion

between iodide and oxide anions, it is impossible for iodide ion to exist in the interlayer octahedral site of rhombohedral layered lattice. However, the elemental analyses reveal that there still remain lots of iodine species after lithiation, which implies that most of iodine species in nanocrystalline manganese oxyiodide is located in the grain boundary or on the surface. Since the iodate ion stabilized in the grain boundary prevents an effective crystal growth of lithium manganese oxide grains, it would help to maintain the nanocrystalline nature of this material before and after Li insertion.

Summarizing the present experimental findings, it is evident that manganese ion in the present nanocrystalline compounds is stabilized in the rhombohedral layered-type local structure, which is maintained by the presence of alkali metal pillar rather by the existence of iodate cluster in interlayer space. In this context, a greater initial discharge capacity of K-based nanocrystal compared to Na-based one is interpreted as a result of the expanded interlayer spacing sustained by larger potassium ion, giving a better ability to accommodate the lithium ion in the interlayer space.

## 3-3. A NEW SINGLE MOLECULAR PRECURSOR ROUTE TO FLUORINE-DOPED NANOCRYSTALLINE TIN OXIDE ANODE FOR LITHIUM BATTERIES

Tin oxide is a well-known host material for lithium insertion and extraction. Its electrochemical behaviors in non-aqueous electrolytes have been studied in the view of electrochromism [39]. Recently, it has been reported that several tin oxide-based compounds can be used as an anode for lithium-ion batteries [40-45]. The common

feature between them is that Li irreversibly decomposes the Sn oxides into metallic tin, and then subsequent Li-Sn alloy is formed [41,42]. The second reaction is reversible, leading to a high capacity of about 600 mAh/g. However, the reversible capacity varies severely depending on the synthetic condition and sample state [42-45]. A plausible explanation might be the enormous volume change during Li-Sn alloy formation, inducing large local stress and inhomogeneity, deteriorating the mechanical stability of the electrode [41,46]. In this respect, it is worthwhile to note that, generally, nanocrystalline or/and more conductive (doped) tin oxide powders have larger reversible capacity than well crystalline and undoped ones [42-45].

The way of enhancing the conductivity and electrochemical reversibility by doping Cl, Sb, Mo or F into tin oxide is a well-established strategy [43,47-50]. Among these dopants, the fluorine is known to be the most efficient doping agent for tin oxide to achieve the highest electrical conductivity which is ~ $5 \times 10^3$ $\Omega^{-1}cm^{-1}$ for an optimum atomic F/Sn ratio of ~ 3 % [51]. Preparation of nanostructured $SnO_2$ and its electrochemical properties have already been reported [42], however, to our knowledge, no investigation has been devoted to the synthesis and electrochemistry of similar F-doped tin oxide, although the enhancement of the conductivity due to F-doping may increase the reversible electrochemical capacity of this kind of materials. Furthermore, until recently, the concept of a single molecular precursor of F-doped $SnO_2$ prepared by sol-gel route has rarely been investigated. Recently our group has reported, for the first time, how to stabilize fluoroalcoxytin complexes, which are ideal precursors for preparing highly conductive F-doped $SnO_2$ nanocrystalline powders [52,53].

In this section, I would describe the preparation and electrochemical characteristics of

nanocrystalline F-doped tin oxide powder, obtained from a mixed-valence fluorotin alkoxide.

### 3-3-1. Experimental

The nanocrystalline F-doped $SnO_2$ powder was prepared by the same method as reported in Ref. 53. The simplified procedure is illustrated in Scheme 1. The thermolysis of xerosol was carried out at first by drying the powder at 50°C, and then calcined at 550°C in air for 15 min. For comparison, commercial $SnO_2$ powder was purchased from Aldrich Chemicals (99.9 %).

Scheme 1. The simplified synthetic procedure.

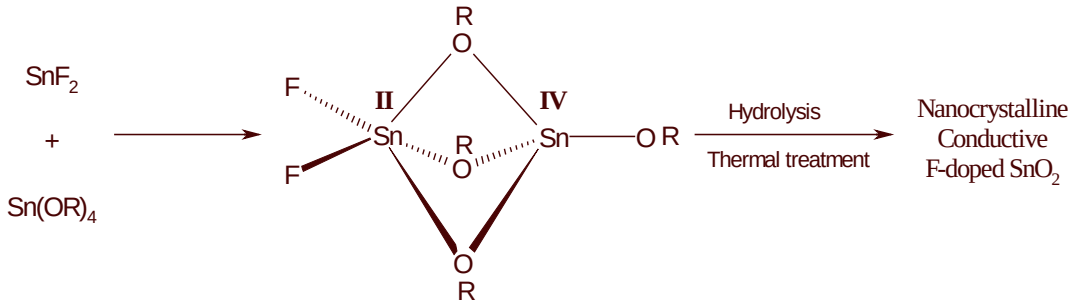


R = -C(CH$_3$)$_3$

Elemental analysis was conducted in the Center of Chemical Analysis of the CNRS (Vernaison, France). The crystallinity and structure of the samples were monitored by powder X-ray diffractometer (Phillips PW1050) using Cu Kα radiation (λ = 1.5418 Å). The sample resistivity was estimated by compacting under pressure (10

tons) a given amount of powder (200 mg) between two stainless steel cylinders. The resistance $R_s$ of the as-pelletized materials (13 mm diameter, 0.42 mm thickness) was measured with a Rhopoint M210 Milli-ohmeter. The measurements were performed under pressure (0.5 ton) using the previous cylinders as contacts. The sample resistivity $\rho_s$ was deduced from $R_s$ by the simple formula $\rho_s = SR_s/t$ where $S$ and $t$ are the surface area and the thickness of the sample, respectively.

The room temperature Mössbauer resonance spectrum was obtained using a Halder-type spectrometer equipped with a $Ca^{119}SnO_3$ source in the constant acceleration mode. The spectrum thus acquired was fitted to the sum of Lorentzians by least square refinements. All isomer shifts given refer to $CaSnO_3$ at 293K.

Electrochemical measurements were performed using a computer-controlled potentiostat/galvanostat (Tacussel, PGS 201T). A button-type cell was used with the configuration of 'Li | 1M $LiClO_4$ in ethylene carbonate (EC) — dimethyl carbonate (DMC) (50:50, v/v) | $SnO_2$ composite electrode'. The composite electrodes were prepared either by intimately mixing the active material with carbon black (25 wt. %) and polytetrafluoroethylene (PTFE, 5 wt. %) or by mixing with carbon black (15 wt. %) and ploy vinylidenedifluoride (PVDF, 10 wt. %) and spreading on Cu foil. All measurements and cell assembly were carried out in an argon-filled dry box. The potential range was set between 0 ~ 2 V vs. $Li^+/Li$ and the current density was fixed at 20 mA/g in a galvanostatic mode.

### 3-3-2. Results and Discussion

Figure 3-12 shows the X-ray diffraction patterns of the dried xerosol precursor, the nanocrystalline F-doped $SnO_2$ and undoped $SnO_2$ powders. For the dried xerosol precursor, no distinguishable peak appears indicating an amorphous state or/and absence of long-range order. After heat-treatment at 550°C in air, as expected, XRD peaks appear to be broader compared to the well-crystalline Aldrich sample. All the XRD reflections are properly indexed with tetragonal symmetry and the cell parameters obtained from the least-square fitting analysis are listed in Table 3-4. It is evident that the cell parameters become smaller for the F-doped nanocrystalline sample. The size of crystallites was estimated to be 7 nm using Scherrer's relation $t=0.9\lambda/(B\cos\theta)$ where $\lambda$ is the X-ray wavelength, $\theta$ is the Bragg angle and B is the angular full-width-half-maximum of the chosen *(hkl)* reflection in radian. For the doped sample, the F/Sn ratio of ~ 0.14, based on the result of elemental analysis, leads to a diminished resistivity of $\rho_s \sim 0.7\ \Omega\cdot$cm. On the contrary, for the undoped $SnO_2$, the resistivity is higher than $10^5\ \Omega$ cm. At this point, it should be noted that the above reported F/Sn ratio of 0.14 is ~ 5 times higher than the maximum value which can be

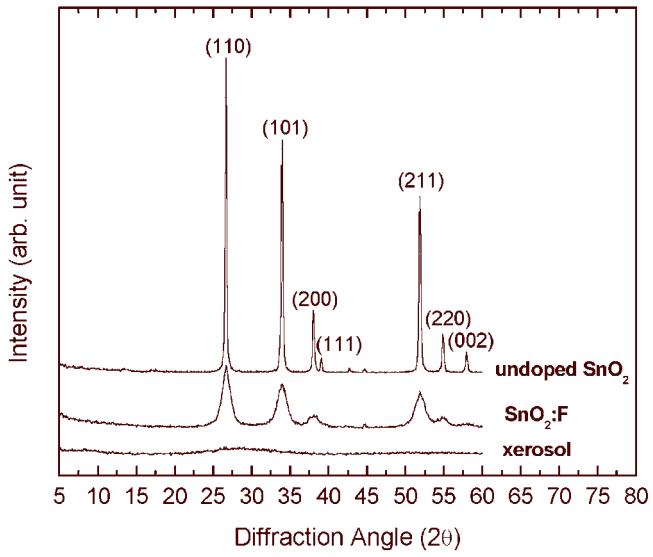


*Figure 3-12. The X-ray diffraction patterns of the dried xerosol precursor, the nanocrystalline F-doped and well-crystalline undoped (Aldrich) $SnO_2$ powders.*

incorporated into the lattice [51]. It might be that some amorphous (as not detected by XRD) secondary phases exist at the grain boundary such as $Sn^{4+}F_4$ [51].

Table 3-4. Elemental analysis, electrical resistivity, crystallite size and cell parameter data of the Aldrich $SnO_2$ and the nanocrystalline F-doped $SnO_2$.

| | | Undoped $SnO_2$ | F-doped $SnO_2$ |
|---|---|---|---|
| Elemental analysis (mole ratio) | F/Sn | · | 0.14 |
| | C/Sn | · | < 0.04 |
| Electrical resistivity | $\rho_s$ (Ω·cm) | $> 10^5$ | 0.7 |
| Crystallite size | *l* (nm) | > 200 | ~ 7 |
| Cell parameters | a (Å) | 4.73(8) | 4.69(3) |
| | c (Å) | 3.18(7) | 3.17(6) |

The oxidation state of tin in the nanocrystalline F-doped $SnO_2$ was determined by Mössbauer spectroscopy at room temperature. The $^{119}Sn$ Mössbauer spectrum of the F-doped nanocrystalline $SnO_2$ and its Lorentzian fits are presented in Figure 3-13. These spectra show the existence of $Sn^{4+}$ state only, although this material was prepared by heating a mixed valence precursor [53]. This finding is consistent with the observed low resistivity (0.7 Ω·cm), which implies indeed that the F-doping into $SnO_2$ may generate mobile electrons in the conduction band, instead of trapped electrons leading to $Sn^{2+}$ formation ($Sn^{4+} + 2e^- \rightarrow Sn^{2+}$ ).

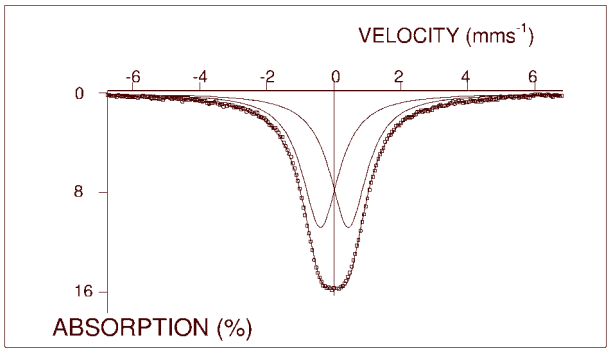


*Figure 3-13. The $^{119}$Sn Mössbauer spectrum of the F-doped nanocrystalline $SnO_2$ and its Lorentzian fits.*

Figure 3-14 shows the first discharge curves for Li | $SnO_2$ cells. A distinctive plateau at about 1.0 V can be observed for the undoped $SnO_2$ sample, which is due to the initial formation of Sn. In contrast, the plateau is less obvious for the doped nanocrystalline sample. For the voltage region over 1.5 V, the F-doped $SnO_2$ shows a capacity of ~30 mAh/g, which is ~6 times larger than that of the undoped sample (~5 mAh/g). A similar phenomenon was also observed in the case of nanocrystalline $SnO_2$ prepared by hydrolysis of $SnCl_4$ and heating at various temperatures [42]. As reported previously by our group, in general, a higher insertion voltage can be observed at the same insertion level for a n-type semiconducting electrode with smaller particles; moreover, the potential decreases more smoothly as the lithium-insertion progresses in these kinds of electrodes composed of nanocrystalline materials such as $Li_xSnO_2$,

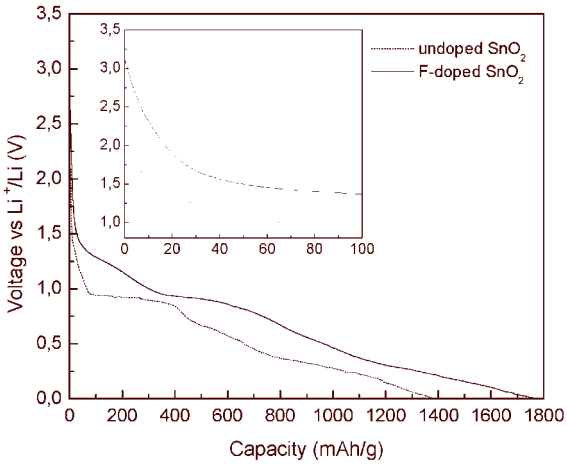


*Figure 3-14. The discharge curves of Li | $SnO_2$ and Li | F-doped nanocrystalline $SnO_2$ cells.*

$Li_xTiO_2$, and $Li_xWO_3$ [54-58]. It suggests that a regular and smooth change of Fermi-energy in the electrode without undergoing any significant structural change, owing to the existence of many sub-band gap states between the valence and conduction band, may be due to surface defects and/or surface dangling bonds [58]. It is worthy to note here that the first discharge capacity (~1800 mAh/g) of the doped sample is larger than the theoretical one (~1490 mAh/g), probably due to the influence of carbon black (25 wt. %). The first two cycling curves of the cells are shown in Fig. 4. The undoped sample shows the reversible capacity of ~600 mAh/g, which corresponds well to the literature values [41-45]. For the F-doped nanocrystalline $SnO_2$, the reversible capacity is close to the expected maximum one (~800 mAh/g) [59]. Thus it seems that highly conductive nanoparticles may provide a way of forming the Li-Sn alloy more effectively, as they reach the ratio of 22:5 ($Li_{22}Sn_5$) [59].

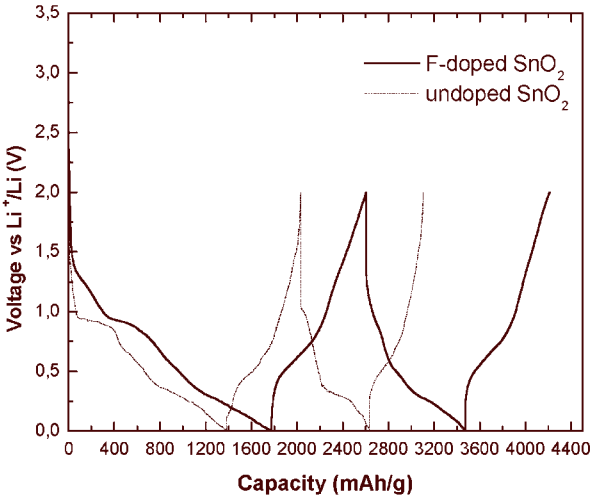


*Figure 3-15. The first two cycle curves of Li/$SnO_2$ and Li/F-doped nanocrystalline $SnO_2$ cells.*

On the whole, it can be rationalized that a nanocrystalline and conductive matrix facilitates the diffusion of Li and the dispersion of Sn atoms in the electrode and that the formation of an alloy around the Sn atoms occurs more intactly. Even though further systematic investigations should be done on the long term cycling behaviors and on the microstructural change induced by dopage of F, the F-doped nanocrystalline $SnO_2$

reported here is expected to be a promising anode material for Li-ion batteries.

## 3-4. NANO-SIZED MAGHEMITE AS A LITHIUM INSERTION ELECTRODE

The preparation and characterization of nanocrystalline nano-sized maghemite ($\gamma$-$Fe_2O_3$) have been already described in the Chapter 2. In this section, I would briefly spotlight different electrochemical behaviors of maghemite nanoparticles compared with well-crystalline ones.

### 3-4-1. Experimental

The maghemite nanoparticles are precipitated by alkalizing an aqueous iron chloride solution containing $Fe^{2+}/Fe^{3+}$ = 0.5 with $NH_4OH$, followed by acidification and oxidation using $HNO_3$ and $Fe(NO_3)_3$, as described in Chapter 2. Electrochemical experiments were performed based on the configuration of 'Li | 1M $LiClO_4$ in EC (ethylene carbonate)/DMC (dimethyl carbonate) (1:1 v/v) | composite electrode'. The composite electrodes were made by intimately mixing 70% (by mass) of the active material, 25 % of Ketjenblack and 5% of polytetrafluoroethylene (PTFE). These electrodes were dried under vacuum at 80 °C for 3 hours, and introduced into an Argon-filled glove box without any exposure to air. Charge/discharge experiments were carried out in a galvanostatic mode using a computer-controlled PGS201T (Tacussel) system between 1.3 ~ 4.3 V vs. $Li^+/Li$.

### 3-4-2. Results and Discussion

Figure 3-16 illustrates potential *vs.* capacity curves for the first four discharges carried out in a galvanostatic mode at 8 mA/g in the voltage range of 1.3 ~ 4.3 V (*vs.* Li). The electrochemical Li insertion into the maghemite, who has a defective spinel structure written as $[Fe^{3+}]_{8a}[Fe^{3+}_{5/3}\square_{1/3}]_{16d}O_4$ in the spinel notation [60,61], starts with the filling of the octahedral vacancies. Then, a distinctive plateau at 2.7 V appears due to the structural transformation into a layered rocksalt-like structure along with the lithium-insertion into 16c sites, including a major rearrangement of 8a tetrahedral $Fe^{3+}$ ions, also, to the 16c octahedral sites [61]. Finally, lithium ions enter to the rest 16c sites with falling of the voltage until 1.3 V. It is interesting to note that our results on the electrochemical lithium-insertion for the maghemite differ somewhat from those of previous literatures. M. Pernet et al. reported that the phase transformation started at 1.6 V and x ~ 0.4 in $Li_xFe_2O_3$ [61], but this difference stems from kinetic reasons in our opinion. Our maghemite sample is nano-sized with *ca.* 8 nm,

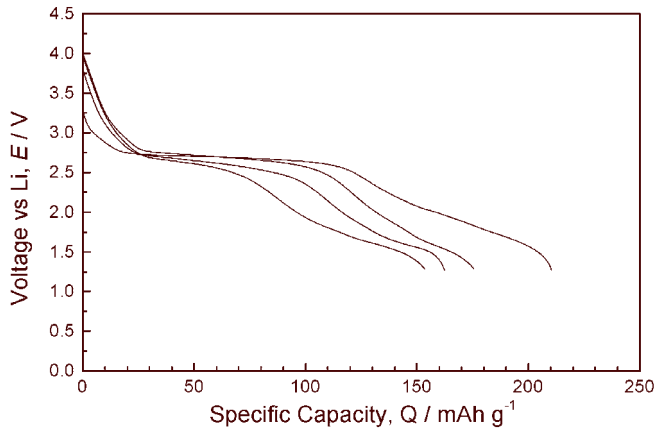


*Figure 3-16. Variation of the voltage vs. Li for the first four discharges of maghemite. The current density and potential range were 8 mA/g and 1.3 ~ 4.3 V, respectively.*

but they used well crystalline one with 0.8 μm in length. Such difference is presumably important for this kinetically diffusion-limited situation, that is, the rearrangement of $Fe^{3+}$ ions from tetrahedral sites into octahedral sites. Therefore, in the above-mentioned publication, the authors found no plateau although the reaction proceeds via two phases, implying a significant over-potential [1]. This assertion is also supported by the fact that potassium-β-ferrite $K_{1.33}Fe_{11}O_{17}$ with the spinel block shows a 2.3 V plateau at 60 °C, whereas its potential slowly decreases to 1.5 V at 25 °C without any plateau [62]. Therefore, we would like to suggest that the nanoparticles can be advantageously used for the purpose of overcoming kinetic problems in lithium insertion electrodes. Moreover, the corresponding electrodes will possess a high electrochemically active surface area leading to enhancement of the capacity due to a reversible electrochemical grafting of Li ions (described below).

## 3-5. ELECTROCHEMICAL GRAFTING MODEL

As mentioned so far, the surface effects of nanocrystalline electrodes exhibit unique electrochemical behaviors distinguished from crystalline ones. It is worth to mention some features of the nanocrystalline electrodes:

(i) They work better when the first electrochemical step is insertion of $Li^+$.

(ii) At the first $Li^+$ insertion step, a higher insertion voltage can be observed at the same insertion level compared to well-crystalline homologues.

(iii) After the first $Li^+$ insertion step, the following cycles are reversible enough.

These trends agree well with our previous reports on n-type semiconducting electrodes composed of nanoparticles such as $Li_xSnO_2$, $Li_xTiO_2$, and $Li_xWO_3$ [54-58]. Based on above phenomenological facts, here we suggest the "electrochemical grafting" model. Figure 3-17 depicts a schematic band model for this electrochemical grafting process. In this model, the nanocrystalline materials have many subband-gap states between the conduction band and valence band owing to their surface defects and/or surface dangling bonds. For example, the metal subband represents deep subband gap energy states arising from cation defects adjacent to an anion vacancy and somewhat lower than the conduction band of metal. The first electrochemical $Li^+$ insertion process fills the subband-gap states, and consequently gives a more smooth discharge curve compared to the well-crystalline homologue. It means a regular and smooth change of Fermi-energy in the electrode without undergoing any significant structural change. Therefore, the nanocrystalline materials can endure better for the structural phase transition. Once the subband-gap states are filled, they are cured and following electrochemical processes would be reversible. In this regard, we named this step the electrochemical grafting. In such a way, nanocrystalline materials can be more efficient

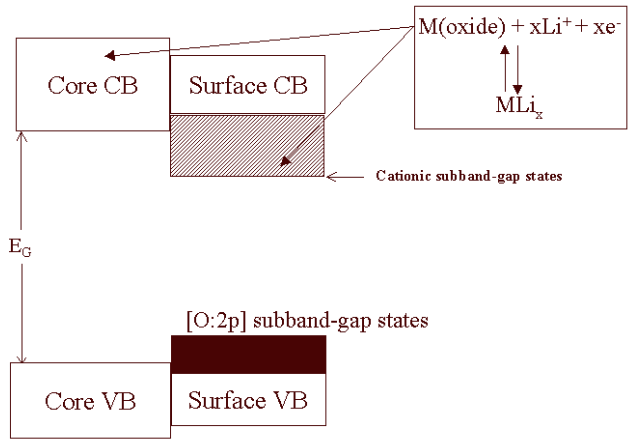


*Figure 3-17. A schematic band model for the electrochemical grafting process.*

than their well-crystalline homologues. We would like to believe that this model can deliver a useful insight to develop more effective electrodes.

## 3-6. CONCLUSION

The electrochemistry of various nanocrystalline materials was investigated especially highlighted on their different behaviors compared with the corresponding well-crystalline analogues. The electrochemistry of nanocrystalline materials differs from that of traditional well-crystalline ones due to their significant surface effects. It is proved that they can be profitably used as lithium insertion electrodes *e.g.* to overcome phase transition problem for potassium manganese oxyiodide, to solve conductivity problem by shortening diffusion length for γ-$Fe_2O_3$, and to facilitate alloy formation with a judicious molecular precursor approach for F-doped $SnO_2$. The above-presented electrochemical grafting concept would be advantageously served for a qualitative comprehension of such “nano-phenomena” occuring at the surface of the nanocrystalline electrodes.

## 3-7. REFERENCES

[1] W. R. McKinnon in “Solid State Electrochemistry”, P. G. Bruce (Ed.), Cambridge University Press, Cambridge, 1995, Ch. 7.

[2] M. S. Whittingham in “Lithium Ion Batteries”, M. Wakihara and O. Yamamoto (Eds.), Kodansha, Tokyo, 1998, Ch. 3.

[3] H. Huang and P. G. Bruce, J. Electrochem. Soc., 141 (1994), L76.

[4] N. Treuil, C. Labrugère, M. Menetrier, J. Portier, G. Campet, A. Deshayes, J. C. Frison, S. J. Hwang, S. W. Song and J. H. Choy, J. Phys. Chem. B, 103 (1999), 2100.

[5] S. H. Kang and J. B. Goodenough, J. Electrochem. Soc., 147 (2000), 3621.

[6] S. H. Kang and J. B. Goodenough, Electrochem. Solid-State Lett., 3 (2000), 536.

[7] S. H. Kang, J. B. Goodenough and L. K. Rabenberg, Chem. Mater., 13 (2001), 1758.

[8] J. Kim and A. Manthiram, Nature (London), 390 (1997), 265.

[9] J. Kim and A. Manthiram, Electrochem. Solid-State Lett., 1 (1998), 207.

[10] J. Kim and A. Manthiram, Electrochem. Solid-State Lett. 2 (1999), 55.

[11] Y. U. Jeong and A. Manthiram, Electrochem. Solid-State Lett., 2 (1999), 421.

[12] C. R. Horne, U. Bergmann, J. Kim, K. A. Streibel, A. Manthiram, S. P. Cramer and E. J. Cairns, J. Electrochem. Soc., 147 (2000), 395.

[13] A. Manthiram, J. Kim and S. Choi, Mater. Res. Soc. Symp. Proc., 575 (2000), 9.

[14] Y. U. Jeong and A. Manthiram, J. Solid State Chem., 156 (2001), 331.

[15] M. M. Thackeray, W. I. F. David, P. G. Bruce and J. B. Goodenough, Mater. Res. Bull., 18 (1983), 461.

[16] J. M. Tarascon, E. Wang, F. K. Shokoohi, W. R. McKinnon and S. Colson, J. Electrochem. Soc., 138 (1991), 2859.

[17] M. M. Thackeray, Prog. Solid State Chem. 25 (1997), 1.

[18] R. J. Gummow, D. C. Liles and J. B. Goodenough, Mater. Res. Bull. 28 (1993), 1249.

[19] J. J. Xu, A. J. Kinser, B. B. Owens and W. H. Smyrl, Electrochem. Solid-State Lett., 1 (1998), 1.

[20] F. Leroux and L. F. Nazar, Solid State Ionics, 100 (1997), 103.

[21] J. W. Long, K. E. Swider-Lyons, R. M. Stroud, and D. R. Rolison, Electrochem. Solid-State Lett., 3 (2000), 453.

[22] R. Chen, and M. S. Whittingham, J. Electrochem. Soc., 144 (1997), L64.

[23] R. Chen, P. Zavalij and M. S. Whittingham, Chem. Mater., 8 (1996), 1275.

[24] A. Frenkel, E.A. Stern, A. Voronel, M. Qian and M. Newville, Phys. Rev. B, 49 (1994), 11662.

[25] P.A. O'Day, J.J. Rehr, S.I. Zabinsky and G.E. Brown Jr., J. Am. Chem. Soc., 116 (1994), 2938.

[26] C. W. Kwon, G. Campet, J. Portier, A. Poquet, L. Fournès, C. Labrugère, B. Jousseaume, T. Toupance, J. H. Choy and M. A. Subramanian, Int. J. Inorg. Mater., 3 (2001), 211.

[27] G. Campet, S. J. Wen, S. D. Han, M. C. R. Shastry, J. Portier, C. Guizard, L. Cot, Y. Xu and J. Salardenne, Mater. Sci. Eng. B, 18 (1993), 201.

[28] S. D. Han, N. Treuil, G. Campet, J. Portier, C. Delmas, J. C. Lassègues and A. Pierre in "Soft Chemistry Routes to New Materials" (eds.) J. Rouxel, M. Tournoux and R. Brec, Materials Science Forum 152-153, Trans Tech Publications, Switzerland, 1994.

[29] C. Tsang, J. Kim and A. Manthiram, J. Solid State Chem., 137 (1998), 28.

[30] C. R. Horne, U. Bergmann, M. M. Grush, R. C. C. Perera, D. L. Ederer, T. A. Callcott, E. J. Cairns and S. P. Cramer, J. Phys. Chem. B, 104 (2000), 9587.

[31] S. J. Hwang, H. S. Park, J. H. Choy and G. Campet, J. Phys. Chem. B, 105 (2001), 335.

[32] S. J. Hwang, H. S. Park, J. H. Choy and G. Campet, G. Chem. Mater., 12 (2000),

1818.

[33] A. Manceau, A. I. Gorshkov and V. A. Drits, Am. Miner., 77 (1992), 1133.

[34] S. J. Hwang, H. S. Park, J. H. Choy, G. Campet, J. Portier, C. W. Kwon and J. Etourneau, Electrochem. Solid-State Lett., 4 (2001), A123.

[35] M. Inaba, Y. Iriyama, Z. Ogumi, Y. Todzuka and A. Tasaka, J. Raman Spectrosc., 28 (1997), 613.

[36] Y. I. Jang, B. Huang, Y. M. Chiang and D. R. Sadoway, Electrochem. Solid-State Lett., 1 (1998), 13.

[37] B. Ammundsen, D. J. Jones, J. Rozière and F. Villain, J. Phys. Chem. B, 102 (1998), 7939.

[38] S. J. Hwang, N. G. Park, D. H. Kim and J. H. Choy, J. Solid State Chem., 138 (1998), 66.

[39] B. Orel, U. L. Stangar, U. Opara, M. Gaberscek and K. Kalcher, J. Mater. Chem., 5 (1995), 617.

[40] Y. Idota, T. Kubota, A. Matsufuji, Y. Maekawa and T. Miyasaka, Science, 276 (1997), 1395.

[41] I. A. Courtney and J. R. Dahn, J. Electrochem. Soc., 144 (1997), 2045.

[42] W. Liu, X. Huang, Z. Wang, H. Li and L. Chen, J. Electrochem. Soc., 145 (1998), 59.

[43] J. Morales and L. Sánchez, J. Electrochem. Soc., 146, 1640 (1999).

[44] R. Retoux, T. Brousse and D. M. Schleich, J. Electrochem. Soc., 146 (1999), 2472.

[45] S. C. Nam, Y. H. Kim, W. I. Cho, B. W. Cho, H. S. Chun and K. S. Yun, Electrochem. Solid State Lett., 2 (1999), 9.

[46] J. Yang, M. Winter and J. O. Besenhard, Solid State Ionics, 90 (1996), 281.

[47] T. Maruyama, K. Tabata, J. Appl. Phys., 68 (1990), 4282.

[48] A. Messad, J. Bruneaux, H. Cachet and J. J. Bruneaux, J. Mater. Sci., 29 (1994), 5095.

[49] J. Bruneaux, H. Cachet, M. Froment and A. Messad, Thin Solid Films, 197 (1991), 129.

[50] J. Bruneaux, H. Cachet, M. Froment and A. Messad, Electrochim. Acta, 39 (1994), 1251.

[51] C. Geoffroy, Doctoral Thesis (1990), University of Bordeaux I.

[52] A. Gamard, B; Jousseaume, T. Toupance and G. Campet, Inorg. Chem., 38 (1999), 4671.

[53] D. Boegeat, B. Jousseaume, T. Toupance, G.Campet, L. Fournès, Inorg. Chem., 39 (2000), 3924.

[54] S. D. Han, N. Treuil, G. Campet, J. Portier, C. Delmas, J. C. Lassègues and A. Pierre, in Soft Chemistry Routes to New Materials, J. Rouxel, M. Tournoux and R. Brec, Editors, Materials Science Forum 152-153, Trans Tech Publications (1994).

[55] S. D. Han, G. Campet, S. Y. Huang, M. C. R. Shastry, J. Portier, J. C. Lassègues and H. S. Dweik, Active and Passive Elec. Comp., 18 (1995), 39.

[56] S. D. Han, S. Y. Huang, G. Campet, S. H. Pulcinnelli and C. V. Santilli, Active and Passive Elec. Comp., 18 (1995), 61.

[57] J. P. Couput, G. Campet, J. M. Chabagno, M. Bourrel, D. Muller, R. Garrié, C. Delmas, B. Morel, J. Portier and J. Salardenne, Int. Appl. Publ. Under PCT. Int. Pat. Class GO2F 1701, FO1 G9/00, C 23C 14/34, WO 9101510 (1989).

[58] G. Campet, S. J. Wen, S. D. Han, M. C. R. Shastry, J. Portier, C. Guizard, L. Cot, Y. Xu and J. Salardennet, Mater. Sci. Eng. B,18 (1993), 201.

[59] R. A. Dunlap, D. A. Small, D. D. MacNeil, M. N. Obrovac and J. R. Dahn, J. Alloys Compd., 289 (1999), 135.

[60] H. M. Ho, E. Goo and G. Thomas, J. Appl. Phys., 59 (1986), 1606.

[61] M. Pernet, P. Strobel, B. Bonnet, P. Bordet, Y. Chabre, Solid State Ionics, 66 (1993) 259.

[62] S. Ito, K. Ui, N. Koura and K. Akashi, Solid State Ionics, 113 (1998), 17.

# *Publications Related to Chapter 3*

- "Nanocristalline materials for lithium batteries",
  NATO Advanced Study Institute, New Trends in Intercalation Compounds for Energy Storage, eds. Julien, C., Monchilov, A., and Pereira-Ramos, J.P., Kluwer, in press.

- "Local crystal structure around manganese in new potassium-based nanocrystalline manganese oxyiodide",
  J. Phys. Chem. B. (2002), vol. 106, n° 16, pp. 4053-4060.

- "Micro-Raman spectroscopic study on layered lithium manganese oxide and its delithiated/relithiated derivatives",
  Electrochem. Solid State Lett. (2001), vol. 4, n° 12, pp. A213-A216.

- "A new single molecular precursor route to fluorine-doped nanocrystalline tin oxide anodes for lithium batteries",
  Int. J. Inorg. Mater. (2001), vol. 3, n° 3, pp. 211-214.

# NANOCRYSTALLINE MATERIALS FOR LITHIUM BATTERIES

C. W. KWON[a], S. J. HWANG[a,b], A. POQUET[a], N. TREUIL[a], G. CAMPET[a], J. PORTIER[a] and J. H. CHOY[b]

[a] *Institut de Chimie de la Matière Condensée de Bordeaux, 87 av. A. Schweitzer, 33608 Pessac, France ;* [b] *Nadhdhtional Nanohybrid Materials Laboratory, School of Chemistry, Seoul National University, Seoul 151-747, Korea*

## ABSTRACT

For a long time, only well crystalline materials have been considered as good electrodes for lithium-ion cells. Nanocrystalline materials are, however, being re-evaluated recently as ‘nanoscience’ advances. The electrochemistry of this kind of materials is much different from that of traditional crystalline ones because of their significant ‘surface effects’. The nanocrystalline materials are reported to have an enhanced electrochemical activity when the first electrochemical step is insertion of Li ions (discharge process). As illustrative examples, electrochemical behaviors of some nanocrystalline materials such as $LiMn_2O_4$, γ-$Fe_2O_3$, fluorine-doped tin oxide and potassium manganese oxyiodide, are presented and compared with their well-crystalline homologues. XRD, XPS, X-ray absorption and NMR spectroscopies were used as probe tools to differentiate the bulk (core) and local (surface) states. The “electrochemical grafting” concept will be given as a plausible explanation.

## 1. Introduction

The rapid development of modern electronic technology creates a strong demand for portable power sources. Lithium batteries are considered to be the best choice, as they provide high output power and moderate lifetime. But, their capacity is limited mostly by the electrode materials. In this respect, much effort has been made to improve the performance of the electrode materials. Traditional electrode materials are based on the redox potential difference of the electrode in the course of intercalation/deintercalation reactions. They are generally well-crystalline host compounds either with layered structure such as $LiCoO_2$ and $LiNiO_2$, or with tunnel structure like $LiMn_2O_4$. As the 'nanoscience' advances recently, however, it is found that the electrochemical behaviors of nanoparticles are much different from those of crystalline ones because they have significant 'surface effects'. O'Regan et al. (1991) proposed dye-sensitized solar cells based on nanostructured $TiO_2$ particles surface-tailored with photoreceptor dyes. Kim et al. (1997) reported that amorphous manganese oxyiodide $Li_{1.5}Na_{0.5}MnO_{2.85}I_{0.12}$ showed excellent reversibility involving both the $Mn^{3+/4+}$ and $Mn^{2+/3+}$ couples, unlike most other manganese oxide systems, which generally show reversibility only for the $Mn^{3+/4+}$ couple. In this report we present a brief overview of our works on the use of nanocrystalline materials as lithium insertion electrodes. A special highlight will be made on the surface effects of the nanocrystalline materials, which makes difference from the traditional crystalline ones.

## 2. $LiMn_2O_4$

Lithium manganese oxide spinel $Li_xMn_2O_4$ is one of promising cathodes for rechargeable lithium batteries by virtue of its low cost, high electrochemical potential and environmental affinity. It delivers 4 V *vs.* Li in the range $0 < x < 1$ and 3 V in the range $1 < x < 2$ (Tarascon et al., 1991). However, studies on its utilization have mainly focused on the 4V domain, because the capacity fades severely in the 3 V range due to the occurrence of Jahn-Teller distortion when the average valence of Mn falls

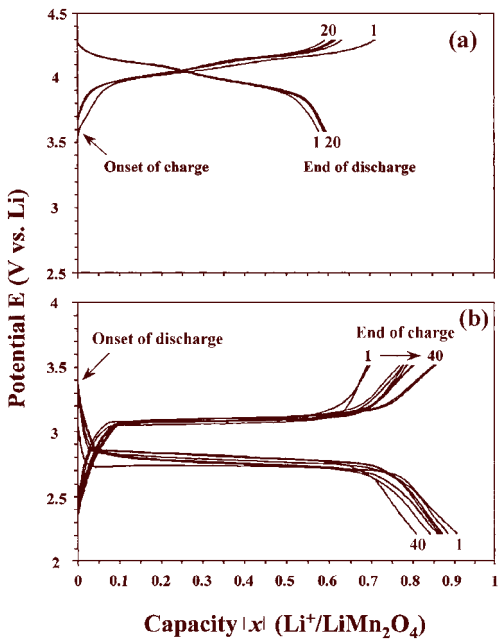


Figure 1. Charge-discharge profiles for $LiMn_2O_4$ prepared at 250 °C (a) in 4V domain and (b) in 3V domain (Treuil et al., 1999).

below +3.5. Lithium insertion into $Li_xMn_2O_4$ electrodes (x > 1) is, therefore, accompanied by the formation of a tetragonal phase (Thackeray et al., 1983). The use of nanocrystalline material to overcome this shortcoming was first attempted by Bruce's group (Huang et al., 1994). They prepared the $LiMn_2O_{4.1}$ from manganese acetate and lithium carbonate at 200 °C in air; electrodes prepared either with or without carbon additive cycled well between 3.7 and 2.0 V at C/2. Recently, we have performed a comparative study between spinel $LiMn_2O_4$ prepared at low and high temperatures in order to examine the difference of electrochemical properties depending on synthetic conditions (Treuil et al., 1999). The comparative experiments between XPS and X-ray absorption found that a lowering of synthetic temperature gives rise to an increase of structural disorder and of the average oxidation state of manganese, which is more significant at the surface than in the bulk (Table 1). Such results suggest that the modification of surface property induced by a decrease of particle size is closely related to the electrochemical performance. The nanocrystalline $LiMn_2O_4$ prepared at 250 °C shows excellent cyclability in the 3 V region whereas it shows smaller capacities in the 4V domain (Figure 1). This phenomenon is reversal of that of well crystalline homologue prepared at 700 °C.

Table 1.Relative proportion of $Mn^{IV+}$ / $Mn^{III+}$ , average particle size, coordination number (CN), and bond distance of $LiMn_2O_4$ prepared at 250 °C and 700 °C.

| Sintering temperature | | 250 °C | 700 °C |
|---|---|---|---|
| $C_{Mn}^{III+}$ | | 41.0 % | 55.5 % |
| $C_{Mn}^{IV+}$ | | 59.0 % | 44.5 % |
| Average particle size | | ~ 5 nm | ~ 100 nm |
| (Mn-O) | CN | 5.6 | 6.0 |
| | R (Å) | 1.90(4) | 1.91(5) |
| (Mn-Mn) | CN | 5.2 | 6.0 |
| | R (Å) | 2.88(9) | 2.89(5) |

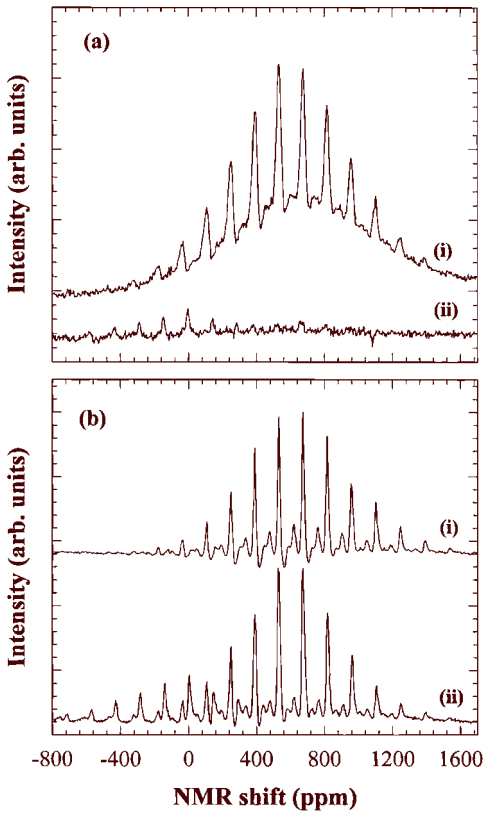


Figure 2. A comparison of $^7Li$ MAS NMR spectra (i) before and (ii) after the insertion of 0.2 mol $Li^+$ for (a) the 250 °C sample and (b) the 700 °C sample. (Treuil et al., 1999).

For the purpose of examining the evolution of the chemical bonding nature of inserted lithium, $^7Li$ MAS NMR studies have been performed for both the spinel compounds before and after the insertion of 0.2 mol $Li^+$. While the insertion does not induce any remarkable spectral change for the well-crystalline $LiMn_2O_4$, it leads to a dramatic suppression of the NMR signal for the nanocrystalline one, indicating that the $Li^+$ insertion into the latter phase results in significant modifications of the chemical environment of lithium. On the basis of present experimental findings, it can be thus

argued that the lowering of synthetic temperature modifies the surface properties and overall chemical environment of ions (lithium ions, of course, but also probably manganese and oxygen ions), which in turn changes the electrochemical properties, that is, the better cyclability in the 3V domain. This phenomenon will be denoted as 'electrochemical grafting' which will be discussed in detail below. Once the grafting process occurs at the first $Li^+$ insertion, the following processes would be reversible enough. Indeed this process, which necessitates a high surface area, will be more efficient for the nanocrystalline samples. Moreover, the grafting and following intercalation processes being reversible, the electrochemical properties in the 3 V region are therefore enhanced for the nanocrystalline $LiMn_2O_4$. This assertion has been supported by Goodenough's group who showed a simple ball-milling of well-crystalline spinel powders generates nanograins and intraparticular strain, and increase manganese oxidation state, which gives a enhanced cyclability in the 3V domain (Kang et al., 2001). Such results can be also understood in the same context of the electrochemical grafting.

### 3. Alkali-metal Manganese Oxyiodide

As mentioned above, the capacity fading problem originating from the phase transition is regarded to be more or less inevitable for the well-crystalline lithium manganese oxides. Such a speculation gives an impetus to develop amorphous phases as alternative cathode materials, since this type of compounds would not suffer from the irreversible phase changes and endure better for the repeated Li insertion-deinsertion processes. Amorphous manganese oxides are normally prepared by reduction and precipitation of permangates such as $NaMnO_4$ or $KMnO_4$ (Xu et al., 1998). Currently, we have synthesized alkali metal-based lithium manganese oxyiodide by reaction the aqueous solution of $KMnO_4$ (or $NaMnO_4$) with 1.5 equivalent LiI at room temperature (Hwang, 2001). Chemical analysis gave the compositions of $Li_{0.54}K_{0.31}MnO_{\sim 2.5}I_{0.10}$ (or $Li_{0.52}Na_{0.62}MnO_{\sim 2.5}I_{0.07}$). X-ray diffraction evidenced that their amorphous character. Electrochemical measurements shows that the potassium-based manganese oxyiodide sample has a great initial capacity

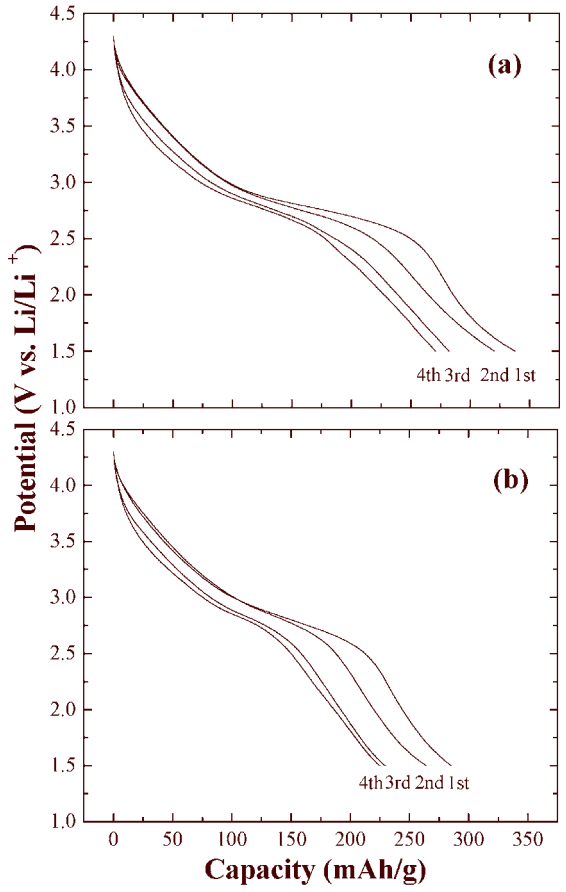


Figure 3. Discharge potential vs. capacity profiles of the A-Li-Mn-O-I compounds with A = (a) K or (b) Na (Hwang, 2001).

of ~ 340 mAh/g between 1.5 ~ 4.3 V *vs.* Li at a constant current density of 0.2 mA/cm$^2$. The local crystal structure around manganese in these compounds has been determined by performing the combinative micro-Raman and X-ray absorption spectroscopy. From the Mn K-edge X-ray absorption near-edge structure and micro-Ramn results, it becomes certain that the manganese ions are stabilized in the rhombohedral layered lattice consisting of edge-shared MnO6 octahedra, and the crystal symmetry is changed into the monoclinic symmetry upon reaction with n-BuLi. The Mn K-edge extended X-ray fine structure analysis reveal that the structural distortion caused by lithiation process is less significant for nanocrystalline compounds than for the spinel lithium manganate, and the crystal structure of K-based nanocrystal is more tolerable for Li insertion than the Na-based one. In this context, the great discharge capacity of potassium-based nanocrystalline material is attributable for the pillaring effect of larger potassium ions, providing an expanded interlayer space available for Li insertion. In addition, the I $L_I$-edge X-ray absorption near edge structure results presented here make it clear that the iodine is stabilized as iodate species on the grain boundary or surface of the nanocrystalline manganese oxyiodide, which helps to maintain the

nanocrystalline nature of the present materials before and after Li insertion.

## 4. γ-$Fe_2O_3$

Although many first row transition metal oxides such as $MnO_2$, $TiO_2$ and $V_2O_5$, have been the focus for lithium insertion electrodes, iron oxides have been relatively less studied due to its low conductivity, insufficient electrochemical potential and most importantly its frustrating cyclability (Thackeray et al., 1982; Pernet et al., 1993). But, the iron oxides are still thought to be one of the best candidates by virtue of its environmental affinity and low price. To improve its performance, we have prepared maghemite (γ-$Fe_2O_3$) nanoparticles because shortening diffusion length may solve its conductivity problem.

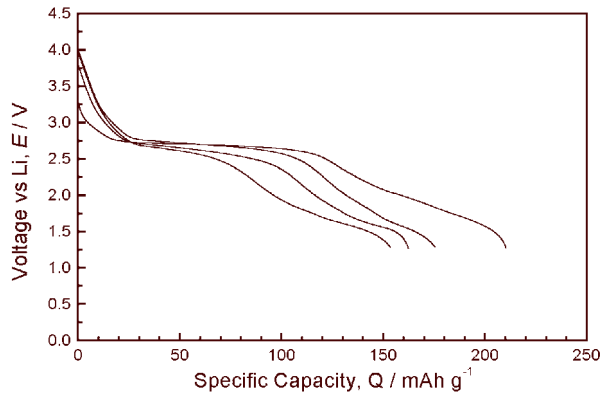


Figure 4. Variation of the voltage vs. Li for the first four discharges of maghemite nanoparticles. The current density and potential range were 8 mA/g and 1.3 ~ 4.0 V, respectively.

The maghemite nanoparticles were prepared by conventional precipitation method mixing $FeCl_2$ and $FeCl_3$ solution at a ratio $Fe^{2+}/Fe^{3+}$ = 0.5 (Massart, 1981). The surface area and size of the obtained particles was *ca.* 8nm and 130 $m^2/g$, respectively. Figure 4 illustrates potential vs. capacity curves for the first four discharges carried out in a galvanostatic mode at 8 mA/g in the voltage range of 1.3 ~ 4.0 V (*vs.* Li). The electrochemical Li insertion into the maghemite, who has a defective inverse spinel structure written as $[Fe^{3+}]_{8a}[Fe^{3+}_{5/3}\square_{1/3}]_{16d}O_4$ in the spinel notation, starts with the filling of the octahedral vacancies. Then, a distinctive plateau at ~2.7 V appears due to the structural transformation

into a layered rocksalt-like structure accompanied by the lithium-insertion into 16c sites, including a major rearrangement of 8a tetrahedral $Fe^{3+}$ ions, also, to the 16c octahedral sites. Finally, lithium ions enter to the rest 16c sites with falling of the voltage until 1.3 V. The capacity of the maghemite diminishes slightly during the first four cycles but it is acceptably reversible. It is very interesting to note that our results on the electrochemical lithium-insertion for the maghemite differ rather from those of previous literatures. Pernet et al. (1993) reported that the phase transformation started at 1.6 V and x ~ 0.4 in $Li_xFe_2O_3$, but this difference stems from kinetic reasons in our opinion. Our maghemite sample is nano-sized with *ca.* 8 nm, but they used well crystalline one with 0.8 μ m in length. Such difference is presumably important for this kinetically diffusion-limited situation, that is, the rearrangement of $Fe^{3+}$ ions from tetrahedral sites into octahedral sites. Therefore, in the above-mentioned publication, the authors found no plateau although the reaction proceeds via two phases, implying a significant over-potential. This assertion is also supported by the fact that potassium-β-ferrite $K_{1.33}Fe_{11}O_{17}$ with the spinel block shows a 2.3 V plateau at 60 °C, whereas its potential slowly decreases to 1.5 V at 25 °C without any plateau (Ito, 1998). Therefore, we would like to suggest that the nanoparticles can be advantageously used for the purpose of overcoming kinetic problems in lithium insertion electrodes.

## 5. Fluorine-doped tin oxide

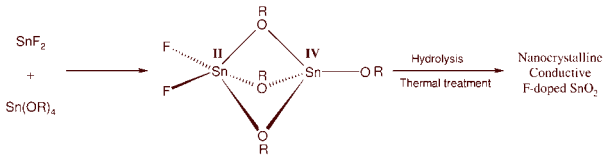


Figure 5. A schematic preparation procedure. R = t-Butyl (Kwon et al., 2001).

Recently, it has been reported that several tin oxide-based compounds can be used as an anode for lithium-ion batteries (Idota, 1997). The common feature is that Li irreversibly decomposes the Sn oxides into metallic tin, and then subsequent Li-Sn alloy formation occurs. The second reaction is reversible, leading to a high capacity of about 600

mAh/g (Courtney, 1997). However, the reversible capacity varies severely depending on the synthetic condition and sample state. Generally, nanocrystalline or/and more conductive (doped) tin oxide powders have larger reversible capacity than well-crystalline and undoped one. Currently, we have prepared nanocrystalline F-doped tin oxide powders obtained by the sol-gel method from the mixed-valence adduct $Sn^{II}Sn^{IV}F_2(OR)_4$ as shown in Figure 5 (Boegeat et al., 2000; Kwon et al., 2001). The electrical resistivity measured by standard four probe method was 0.7 Ω·cm, which is much lower than that of crystalline and undoped sample ($R_s$ > $10^5$ Ω·cm).

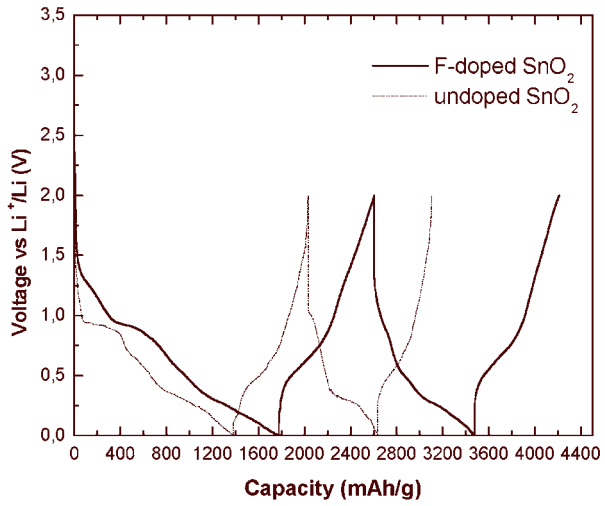


Figure 6. The discharge/charge curves of Li/$SnO_2$ and Li/F-doped nanocrystalline $SnO_2$ cells. (Kwon et al., 2001)

Figure 6 shows the first two cycling curves for nanocrystalline F-doped $SnO_2$ compared with well-crystalline undoped $SnO_2$. A distinctive plateau at ~1.0 V can be observed for the undoped $SnO_2$ sample, which is due to the initial formation of Sn. In contrast, the plateau is less obvious for the F-doped nanocrystalline sample. For the voltage region over 1.5 V, the F-doped $SnO_2$ shows a capacity of ~30 mAh/g, which is ~6 times larger than that of the undoped sample (~5 mAh/g). The undoped sample shows the reversible capacity of ~600 mAh/g, which corresponds well to the literature values. For the F-doped nanocrystalline $SnO_2$, the reversible capacity is close to the expected maximum one (~800 mAh/g). Thus it seems that highly conductive nanoparticles may provide a favorable way of forming the Li-Sn alloy more effectively.

## 6. Electrochemical grafting model

As mentioned so far, the surface effects of nanocrystalline electrodes exhibit unique electrochemical behaviors distinguished from crystalline ones. It is worth to mention some features of the nanocrystalline electrodes:

(i) They work better when the first electrochemical step is insertion of $Li^+$.

(ii) At the first $Li^+$ insertion step, a higher insertion voltage can be observed at the same insertion level compared to well-crystalline homologues.

(iii) After the first $Li^+$ insertion step, the following cycles are reversible enough.

These trends agree well with our previous reports on n-type semiconducting electrodes composed of nanoparticles such as $Li_xSnO_2$, $Li_xTiO_2$, and $Li_xWO_3$ (Campet et al., 1993).

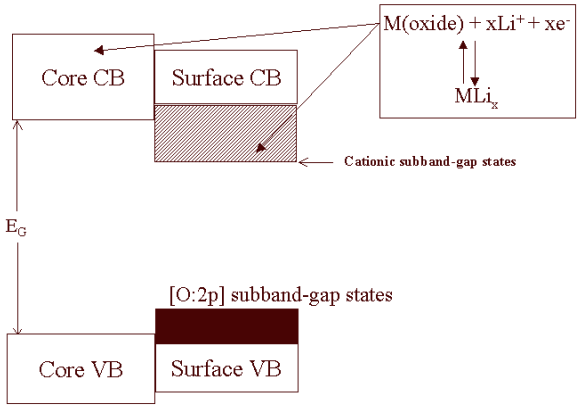


Figure 7. A schematic band model for the electrochemical grafting process.

Based on above phenomenological facts, here we suggest the "electrochemical grafting" model. Figure 7 depicts a schematic band model for this electrochemical grafting process. In this model, the nanocrystalline materials have many subband-gap states between the conduction band and valence band owing to their surface defects and/or surface dangling bonds. For example, the metal subband represents deep subband gap energy states arising from cation defects adjacent to an anion vacancy and somewhat lower than the $\pi^*$ conduction band of metal. The first electrochemical $Li^+$ insertion process fills the subband-gap states, and consequently gives a more smooth discharge curve compared to the well-crystalline homologue. It means a regular and smooth change of Fermi-energy in the electrode

without undergoing any significant structural change. Therefore, the nanocrystalline materials can endure better for the structural phase transition. Once the subband-gap states are filled, they are cured and following electrochemical processes would be reversible. In this regard, we named this step the electrochemical grafting. In such a way, nanocrystalline materials can be more efficient than their well-crystalline homologues. We would like to believe that this model can deliver a useful insight to develop more effective electrodes.

## 7. Conclusion

The electochemistry of nanocrystalline materials differs from that of traditional well-crystalline ones due to their significant surface effects. We have shown that they can be profitably used as lithium insertion electrodes *e.g.* to overcome phase transition problem for $LiMn_2O_4$ or potassium manganese oxyiodide, to solve conductivity problem by shortening diffusion length for $\gamma$-$Fe_2O_3$, and to facilitate alloy formation with a judicious molecular precursor approach for F-doped $SnO_2$. The above-presented electrochemical grafting concept would be advantageously served for a qualitative comprehension of such “nano-phenomena” occuring at the surface of the nanocrystalline electrodes.

## References

Boegeat, D., Jousseaume, B., Toupance, T., Campet, G. and Fournès, L. (2000), “The First Mixed-Valence Fluorotin Alkoxides: New Sol-Gel Precursors of Fluorine-Doped Tin Oxide Materials”, Inorg. Chem., 39, 3924-3927.

Campet, G., Wen, S. J., Han, S. D., Shastry, M. C. R., Portier, J., Guizard, C., Cot, L., Xu, Y. and Salardenne, J. (1993), “Reversible Electrochemical Insertion of Lithium in Fine-Grained Polycrystalline Thin Films of Mixed-Valency Metal Oxides: Application to $Li_xFe_2O_3$ Thin Film Electrodes Prepared by the Sol-Gel Process”, Mater. Sci. Eng.,

B18, 201-208.

Courtney, I. A. and Dahn, J. R. (1997), "Electrochemical and In Situ X-ray Diffraction Studies of the Reaction of Lithium with Tin Oxide Composites", J. Electrochem. Soc., 144, 2045-2052.

Huang, H. and Bruce, P. G. (1994), "A 3 Volt Lithium Manganese Oxide Cathode for Rechargeable Lithium Batteries", *J. Electrochem. Soc.*, 141, L76-L77.

Hwang, S. J. (2001), "Relations entre la Nature de la Liason Chimique et les Propriétes Electrochimiques d'Oxydes Doubles de Lithium et Manganese", Ph. D. Thesis, Bordeaux University I.

Idota, Y., Kubota, T., Matsufuji, A., Maekawa, Y. and Miyasaka, T. (1997), "Tin-Based Amorphous Oxide : A High-Capacity Lithium-Ion_Storage Material", Science, 276, 1395-1397.

Ito, S., Ui, K., Koura, N. and Akashi, K. (1998), "Lithium Secondary Battery Using Potassium-β-Ferrite as a New Cathode Active Material", *Solid State Ionics*, 113-115, 17-21.

Kang, S. H., Goodenough, J. B. and Rabenberg, L. K. (2001), "Efffect of Ball-Milling on 3V Capacity of Lithium-Manganese Oxospinel Cathodes", *Chem. Mater.*, 13, 1758-1764.

Kim, J. and Manthiram, A. (1997), "A Manganese Oxyiodide Cathode for Rechargeable Lithium Batteries", *Nature (London)*, 390, 265-267.

Kwon, C. W., Campet, G., Portier, J., Poquet, A., Fournès, L., Labrugère, C., Jousseaume, B., Toupance, T., Choy, J. H. and Subramanian, M. A. (2001), "A New Single Molecular Precursor Route to Fluorine-Doped Nanocrystalline Tin Oxide Anodes for Lithium Batteries", Int. J. Inorg. Mater., 3, 211-214.

Massart, R. (1981), "Preparation of Aqueous Magnetic Liquids in Alkaline and Acidic Media", *IEEE Trans. Mag.*, 17, 1247-1248.

O'Regan, B. and Grätzel, M. (1991), "A Low-cost, High-efficiency Solar Cell Based on Dye-sensitized Colloidal $TiO_2$ Films", *Nature (London)*, 335, 737-739.

Pernet, M., Strobel, P., Bonnet, B., Bordet, P. and Chabre, Y. (1993), "Structural and Electrochemical Study of Lithium Insertion into γ-$Fe_2O_3$", *Solid State Ionics*, 66, 259-265.

Tarascon, J. M., Wang, E., Shokoohi, F. K., McKinnon, W. R. and Colson, S. (1991), "The Spinel Phase of $LiMn_2O_4$ as a Cathode in Secondary Lithium Cells", *J. Electrochem. Soc.*, 138, 2859-2864.

Thackeray, M. M., David, W. I. F. and Goodenough, J. B. (1982), "Structural Characterization of the Lithiated Iron Oxides $Li_xFe_3O_4$ and $Li_xFe_2O_3$ (0<x<2)", Mater. Res. Bull., 17, 785-793.
Thackeray, M. M., David, W. I. F., Bruce, P. G. and Goodenough, J. B. (1983), "Lithium Insertion into Manganese Spinels", *Mater. Res. Bull.*, 18, 461-472.

Treuil, N., Labrugère, C., Menetrier, M., Portier, J., Campet, G., Deshayes, A., Frison, J. C., Hwang, S. J., Song, S. W. and Choy, J. H. (1999), "Relationship between Chemical Bonding Nature and Electrochemical Property of $LiMn_2O_4$ Spinel Oxides with Various Particle Sizes: Electrochemical Grafting Concept", *J. Phys. Chem. B, 103*, 2100-2106.

Xu, J. J., Kinser, A. J., Owens, B. B. and Smyrl, W. H. (1998), "Amorphous Manganese Dioxide : A High Capacity Lithium Intercalation Host", *Electrochem. Solid State Lett.*, 1, 1-3.

*J. Phys. Chem. B* **2002,** *106,* 4053−4060 

# ARTICLES

## Local Crystal Structure around Manganese in New Potassium-Based Nanocrystalline Manganese Oxyiodide

**Seong-Ju Hwang,[†] Chai-Won Kwon,[†] Josik Portier,[†] Guy Campet,*[,†] Hyo-Suk Park,[‡] Jin-Ho Choy,*[,‡] Pham V. Huong,[§] Masahiro Yoshimura,[∥] and Masato Kakihana[⊥]**

*Institut de Chimie de la Matière Condensée de Bordeaux (ICMCB) du CNRS, 87 Av. du Dr. A. Schweitzer, 33608 Pessac, France, National Nanohybrid Materials Laboratory, School of Chemistry, Seoul National University, Seoul 151-747, Korea, Laboratoire de Physico-Chimie Moléculaire, Université Bordeaux I, 351 Cours de la Libération, 33405 Talence, France, and Department of Materials Science and Engineering, Tokyo Institute of Technology, 4259 Nagatsuta, Midori-ku, Yokohama 226, Japan*

*Received: July 13, 2001; In Final Form: January 17, 2002*

A new nanocrystalline potassium-based lithium manganese oxyiodide has been prepared by using *Chimie Douce* route at room temperature. According to the electrochemical measurements, this nanocrystalline sample shows a large initial capacity up to ~340 mAh/g at a constant current density of 0.2 mA/cm$^2$, which is much larger than that of sodium-based homologue. The X-ray diffraction analysis demonstrates that the amorphous character of the nanocrystalline compounds is maintained before and after chemical lithiation reaction. The local crystal structure around manganese in these materials has been determined by performing the combinative micro-Raman and X-ray absorption spectroscopy. From the Mn K-edge X-ray absorption near-edge structure and micro-Raman results, it becomes certain that manganese ions are stabilized in the rhombohedral layered lattice consisting of edge-shared $MnO_6$ octahedra, and the crystal symmetry is changed into a monoclinic symmetry upon reaction with *n*-BuLi. The Mn K-edge extended X-ray fine structure analysis reveals that the structural distortion caused by lithiation process is less significant for these nanocrystalline compounds than for the spinel lithium manganate. In this context, the great discharge capacity of the nanocrystalline materials is attributable for the pillaring effect of larger alkali metal ion than lithium ion, providing an expanded interlayer space available for Li insertion. In addition, the I $L_I$-edge X-ray absorption near-edge structure results presented here make it clear that iodine is stabilized as iodate species on the grain boundary or the surface of the nanocrystalline manganese oxyiodide, which helps to maintain the nanocrystalline nature of the present materials before and after Li insertion.

### Introduction

Recently, special attention has been paid for lithium manganese oxides as promising cathode materials for lithium rechargeable batteries, which is due to the low toxicity, rich abundance, and low price of manganese.[1] In this context, various types of lithium manganates have been explored for the purpose of developing new cathode materials with better electrochemical performance.[2−4] However, most of lithium manganates experience a common structural modification to a spinel-type cation ordering in the course of electrochemical cycling.[5,6] This thermodynamically stable spinel phase has been well-known to suffer from capacity fading during repeated charge−discharge cycling.[1] The capacity loss of this cathode material is closely related to the structural transition from cubic spinel to tetragonal one, leading to a structural breakdown and to a formation of electronically isolated zones.[7] In fact, this sort of problem originating from the phase transition is considered to be more or less inevitable for well-crystallized lithium metal oxides. Such a speculation gives an impetus to develop amorphous phases as alternative cathode materials, since this type of compounds would be much more tolerable for the repeated Li insertion−deinsertion process. For example, very recently we have found that nanocrystalline spinel compound exhibits an enhanced electrochemical performance for 3 V region corresponding to Li insertion into 16c site in the spinel phase, which would be understood by the grafting mechanism of lithium on the surface of nanocrystalline material.[8] In addition, there have been some reports on nanocrystalline lithium manganese oxides showing superior electrochemical properties over well-crystalline homologues.[9−12] Among these nanocrystalline materials, sodium-based manganese oxyiodides possess a quite large discharge capacity and the best cyclability, and moreover their electrochemical performances can be improved by ball-milling process.[9] On the other hand, Whittingham, M. S. et al. reported

* To whom correspondence should be addressed.Guy Campet: Phone: +33-5-56-84-62-97. Fax: +33-5-56-84-27-61. E-mail: campet@icmcb.u-bordeaux.fr. Jin-Ho Choy: Phone: +82-2-880-6658. Fax: +82-2-872-9864. E-mail: jhchoy@plaza.snu.ac.kr.

[†] Institut de Chimie de la Matière Condensée de Bordeaux (ICMCB) du CNRS.

[‡] Seoul National University.

[§] Université Bordeaux I.

[∥] Tokyo Institute of Technology.

10.1021/jp012704g CCC: $22.00 
Published on Web 03/30/2002

that a potassium-based manganate with rhombohedral layered structure is more stable for electrochemical lithiation−delithiation reaction compared to sodium- or lithium-based ones.[13] Nonetheless, to our knowledge, there is no systematic study on potassium-based nanocrystalline manganese oxyiodide although it is worthwhile to probe the effect of alkali metal on the electrochemical properties of these nanocrystalline manganese oxyiodide. From the viewpoint of solid-state chemistry, it is also important to determine the local structure around manganese and the role of iodine species in understanding the mechanism of Li insertion in this nanocrystalline material. However, it is quite difficult to probe the local cation ordering of nanocrystalline compounds because of their X-ray amorphous character. In our recent papers, it was demonstrated that a combination of micro-Raman and X-ray absorption spectroscopy (XAS) is very effective in probing the local atomic structure of electrode materials with poor crystallinity as well as in examining the effect of Li insertion−deinsertion process on the chemical bonding character of these compounds.[5,14,15]

In this work, we have prepared a new potassium-based nanocrystalline manganese oxyiodide and characterized its physicochemical properties in comparison with those of sodium-based homologue. In addition, an attempt has been made to determine the local geometric and electronic structures around manganese before and after chemical lithiation by using micro-Raman and Mn K-edge XAS analyses.[16] The chemical bonding characters of iodine species in these nanocrystalline materials have also been studied by performing the X-ray absorption near-edge structure (XANES) analysis at I $L_I$-edge.

## Experimental Section

**Sample Preparation.** The nanocrystalline A−Li−Mn−O−I (A = K and Na) samples were prepared by reacting the aqueous solution of $KMnO_4$ or $NaMnO_4{\cdot}H_2O$ with 1.5 equiv LiI at room temperature, similar to the previously reported *Chimie Douce* method.[9,10] The mixed solution was maintained for 1 day under constant stirring. The resulting precipitate was washed with water and was dried at 130 °C in a vacuum. The chemical lithiation reaction for these amorphous samples was carried out by reacting them with 1.6 M *n*-BuLi in hexane for 48 h. Prior to the physicochemical characterization, the lithiated samples were washed thoroughly with hexane and ethanol and were dried in a vacuum.

**Sample Characterization.** The crystal structures of A−Li−Mn−O−I (A = K and Na) and their chemically lithiated products were studied by X-ray diffraction (XRD) measurement using Ni-filtered Cu Kα radiation with a graphite diffracted beam monochromator. The chemical compositions of these samples were determined by using atomic absorption (AA) spectrometry, inductive coupled plasma (ICP) spectrometry, and electron probe for microanalysis (EPMA). The water contents were estimated by performing thermogravimetric analysis (TGA) under $O_2$ flow. The weight losses of ~3% and ~6% up to ~150 °C are observed for the Na- and K-based nanocrystals, respectively, indicating that these materials possess about 0.2−0.4 mole water per unit formula.[13] The electrochemical measurements were performed with the cell configuration of Li/1M $LiPF_6$ in EC:DEC (50:50 v/v)/composite cathode, which was assembled in a drybox. The composite cathode was prepared by mixing thoroughly the active A−Li−Mn−O−I (A = K and Na) material (20 mg, 70 wt %) with 25 wt % of acetylene black and 5 wt % of PTFE (poly(tetrafluoroethylene)). All the experiments were carried out in a galvanostatic mode with Arbin BT 2043 multichannel galvanostat/potentiostat in the voltage range of 1.5−4.3 V at the constant current densities of 0.2 and 0.5 mA/cm² (10 and 25 mA/g).

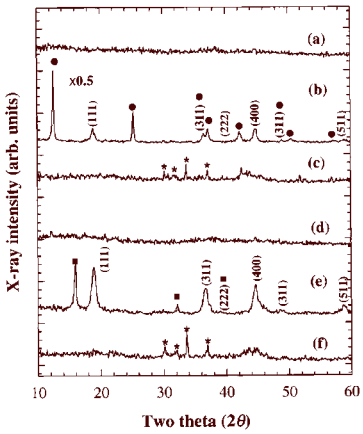


**Figure 1.** X-ray diffraction patterns of (a) nanocrystalline K−Li−Mn−O−I compound and its derivatives (b) after the heat treatment at 600 °C and (c) after lithiation, together with (d−f) the corresponding data of Na-homologues. In (b) and (e), the indexed reflections are assigned on the basis of cubic spinel structure, and the circle and square symbols represent the reflections from $K_xMnO_2{\cdot}yH_2O$ and $Na_{0.7}MnO_2$ phases, respectively. The asterisk symbols in (c) and (f) denote the peaks originating from $LiOH{\cdot}H_2O$.

**Micro-Raman Spectroscopy.** The micro-Raman spectra presented here were recorded on a Dilor-Omars microspectrometer coupled with an optical microscope (spatial resolution of 1 $\mu m^2$) and an intensified 1024-channel photodiode array detector. The 514.5-nm line from an argon ion laser Spectra Physics model 2016 was used as an excitation source. All the present spectra were measured by backscattering from the freshly fractured surfaces of the pellet or from the powdered sample. To prevent possible thermal damage of the samples, the power of incident laser light was maintained at less than 1 mW. After each measurement, the sample surface was thoroughly checked to remove the possibility of spectral modification caused by surface degradation.

**X-ray Absorption Measurement.** The XAS experiments were performed for the nanocrystalline A−Li−Mn−O−I (A = K and Na) compounds and their lithiated derivatives by using the extended X-ray absorption fine structure (EXAFS) facility installed at the beam line 7C at the Photon Factory in Tsukuba.[17] The XAS data were collected at room temperature in a transmission mode using gas-ionization detectors. All the present spectra were calibrated by measuring the spectra of Mn metal foil and KI. The data analysis for the experimental spectra was carried out by the standard procedure as reported previously.[5]

## Results and Discussion

**Powder XRD and Chemical Analyses.** The powder XRD patterns of as-prepared A−Li−Mn−O−I (A = K and Na) compounds are shown in Figure 1, together with those of their heated and lithiated products. No distinct reflection can be observed for the nanocrystalline samples heated at 130 °C in vacuum. After the heat-treatment at 600 °C, an amorphous phase is changed into a mixed crystalline phase, that is, a mixture of rhombohedral layered $K_xMnO_2$[18] and cubic-spinel $Li_{1+y}Mn_{2-y}O_4$ for the potassium-based nanocrystal and a mixture of $Na_{0.7}MnO_2$[19] and cubic-spinel $Li_{1-y}Mn_{2-y}O_4$ for the sodium-based

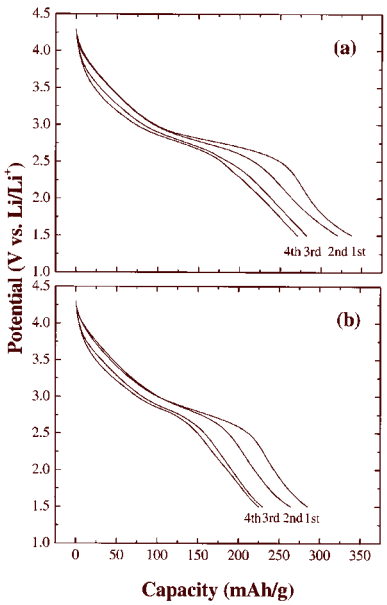


**Figure 2.** Discharge potential profiles of the nanocrystalline A−Li−Mn−O−I compounds with A = (a) K and (b) Na. The electrochemical measurements were carried out in the potential range of 1.5−4.3 V with the applied current density of 0.2 mA/cm$^2$.

**TABLE 1: Chemical Formulas of Nanocrystalline Manganese Oxyiodides and Their Lithiated Derivatives**

| sample | as-prepared | lithiated |
|---|---|---|
| K−Li−Mn−O−I | $Li_{0.54}K_{0.31}MnO_{2.5-\delta}I_{0.10}$ | $Li_{2.45}K_{0.34}MnO_{2.5-\delta}I_{0.13}$ |
| Na−Li−Mn−O−I | $Li_{0.52}Na_{0.62}MnO_{2.5-\delta}I_{0.07}$ | $Li_{2.48}Na_{0.79}MnO_{2.5-\delta}I_{0.08}$ |

nanocrystal. In the lithiated derivatives, there is no XRD peak related to the crystalline lithium manganate, except several weak reflections corresponding to a small amount of lithium hydroxide hydrate formed by a reaction with *n*-BuLi and water of the samples. This finding indicates that the amorphous structure of the present nanocrystalline manganese oxyiodides is highly tolerable for Li insertion reaction.

The chemical formula of the nanocrystalline A−Li−Mn−O−I (A = K and Na) compounds and their lithiated derivatives estimated from AA, ICP, and EPMA analyses is summarized in Table 1. The concentration of alkali metal ion is determined to be smaller for the potassium-based nanocrystal than for the sodium-based one, whereas the iodine content is larger for the former compared to the latter. As listed in Table 1, the lithiation process results in the incorporation of about two moles of lithium ions per unit formula commonly for both nanocrystalline materials. This reflects their greater ability to accommodate lithium ions compared to well-crystallized electrode materials such as $LiMn_2O_4$ spinel, even though a fraction of lithium ions are consumed for the reaction with the sample water, leading to the formation of lithium hydroxide.

**Electrochemical Performance.** The cycling characteristics of the nanocrystalline A−Li−Mn−O−I (A = K and Na) compounds have been examined to probe the effect of alkali metal on the electrochemical performance of the lithium manganese oxyiodides. Since both pristine materials possess an open circuit potential of ~3.4 V (vs Li/Li$^+$), the electrochemical cycling starts with the first charge process up to 4.3 V. The

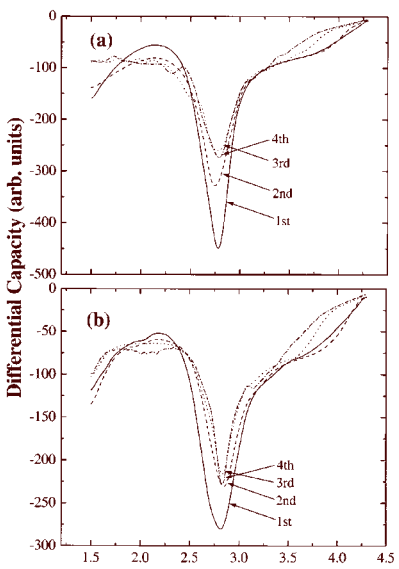


**Figure 3.** Differential capacity profiles of the nanocrystalline A−Li−Mn−O−I compounds with A = (a) K and (b) Na. The electrochemical measurements were carried out in the potential range of 1.5−4.3 V with the applied current density of 0.2 mA/cm$^2$.

discharge potential profiles of the nanocrystalline A−Li−Mn−O−I (A = K and Na) compounds measured at a constant current density of 0.2 mA/cm$^2$ are plotted in Figure 2. For both compounds, a small capacity of ~110 mAh/g corresponding to the oxidation of trivalent manganese ions is commonly observed (not shown in the figure), which is much smaller than the capacity of the following discharge process. This underlines that the electrochemical activity of these manganese oxyiodides is attributed mainly to the insertion of lithium ion from Li anode rather than to the reinsertion of lithium ions which already exist in the as-prepared materials. Both nanocrystals show nearly identical curve shape, which is very close to that of the previously reported amorphous manganese dioxide,[9−11] confirming the amorphous character of the present manganese oxyiodides. The observed smooth decrease of potential during discharge process is a characteristic of nanocrystalline electrode materials such as $SnO_2$, $Fe_2O_3$, and so forth.[20,21] This can be explained by the fact that the existence of surface defects or surface dangling bonds in nanocrystalline materials gives rise to the formation of many sub-bands between valence and conduction bands, leading to a smooth change of Fermi energy and hence a slow potential change.[8] In comparison with the sodium-based manganese oxyiodide, the potassium-based one shows a greater discharge capacity for each cycle. For a more accurate inspection of discharge behaviors, the differential capacity profiles of the nanocrystalline A−Li−Mn−O−I (A = K and Na) compounds are presented in Figure 3. As the cycle proceeds, no significant change in curve shape except a slight depression of the peak at ~2.7 V can be observed for both compounds, which suggests that the electrochemical discharge−charge process does not induce any marked structural transition in these nanocrystalline materials. However, the present nanocrystals commonly show a significant capacity fading, which is fairly contrasted with the previous report on

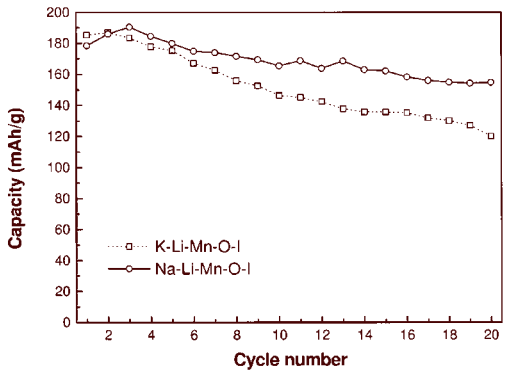


**Figure 4.** Discharge capacities of the nanocrystalline A−Li−Mn−O−I compounds with A = K (squares) and Na (circles). The electrochemical measurements were carried out in the potential range of 1.5−4.3 V with the applied current density of 0.5 mA/cm$^2$.

the sodium-based materials prepared in acetonitrile solvent.[9] This may be attributed not to the structural transition but to the presence of water leading to the formation of LiOH and HF via the reaction with Li anode and electrolyte, respectively. In this context, now we are trying to prepare potassium-based nanocrystal in nonaqueous solvent and to examine the effect of ball milling on its electrochemical property, with a view to improving the cyclability and discharge capacity of this promising nanocrystalline material. On the other hand, we have also measured the electrochemical performances of the present nanocrystalline samples up to 20 cycles with a higher current density of 0.5 mA/cm$^2$, to examine the long-term cycling characteristics as well as to probe the effect of current density. As presented in Figure 4, the potassium-based phase shows the high initial discharge capacity of 185 mAh/g with a notable capacity decrease to 120 mAh/g after the 20th cycle, whereas the sodium-based one exhibits a better capacity retention from 178 mAh/g at the first cycle to 155 mAh/g at the 20th cycle. This is surely contrasted with the results obtained with the lower current density of 0.2 mA/cm$^2$. Such different long-term cycle characteristics of these nanocrystals are suggested to originate from their dissimilar water contents or from the contribution of other chemical species such as Na/K or iodine to discharge capacity. However, it is quite difficult to conclude here the origin of the observed electrochemical behavior of the present nanocrystals, since there are so many factors to be considered influencing the long-term cycling performance. To answer this question, now we are performing the detailed electrochemical measurements with various experimental conditions. In this context, here we limit our further discussion to why the potassium-based phase shows a greater "initial" discharge capacity than the sodium-based one. In fact, prior to the electrochemical measurements, we expected that the potassium-based compound possesses inferior initial discharge capacity to the sodium-based one, judging from the heavier atomic weight of potassium compared to sodium. But this is not true for the nanocrystalline materials presented here. To understand such an unexpected finding, we have examined the local structure around manganese in both nanocrystalline compounds by performing micro-Raman and XANES/EXAFS tools complementarily.

**Mn K-Edge XANES Analysis.** The Mn K-edge XANES spectra of the pristine nanocrystalline A−Li−Mn−O−I (A = K and Na) compounds and their lithiated derivatives are

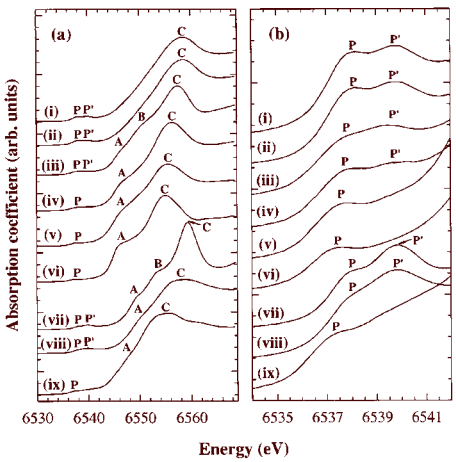


**Figure 5.** (a) Mn K-edge XANES spectra for the nanocrystalline A−Li−Mn−O−I compounds with A = (i) K and (ii) Na and (iv−v) their lithiated derivatives, in comparison with the references (iii) cubic spinel $LiMn_2O_4$, (vi) tetragonal spinel $Li_2Mn_2O_4$, (vii) $\lambda$-$MnO_2$, (viii) nanocrystalline manganese oxide, and (ix) $Mn_2O_3$. The magnified spectra for preedge region are presented in (b).

illustrated in Figure 5a, in comparison with the reference spectra of cubic spinel $LiMn_2O_4$, tetragonal spinel $Li_2Mn_2O_4$, $\lambda$-$MnO_2$, nanocrystalline manganese oxide,[22,23] and $Mn_2O_3$. The position of the edge jump for the pristine manganese oxyiodides is a little bit higher than that for $LiMn^{+IV}Mn^{+III}O_4$ but slightly lower than that for $\lambda$-$Mn^{+IV}O_2$, which indicates that manganese ions in these materials have an average valence state of >+3.5. Actually, the sodium-based manganese oxyiodide has been reported to possess the average Mn oxidation state of about +3.8.[9] In the lithiated manganese oxyiodides, the edge position is rather in accordance with that of tetragonal spinel $Li_2Mn^{+III}{}_2O_4$, confirming the reduction of manganese ions after the *n*-BuLi-treatment. In the preedge region, all the spectra presented here show small preedge peaks (denoted P and P′), which are assigned as the transitions from the core 1s level to unoccupied 3d states. Even though they are not allowed by the electronic dipolar selection rule, $\Delta l = \pm 1$, the preedge peaks could be discerned either because of quadrupole-allowed transitions or because of the mixing of 4p and 3d states.[5] In this context, the weak intensity of these features suggests that all the manganese ions in the samples under investigation are stabilized in octahedral site with an inversion center. The position and shape of these preedge peaks are well-known to be closely related to the oxidation state of the absorbing ion and the local arrangement of backscattering ions, respectively.[5] As can be seen clearly from Figure 5b, the relative energies of the preedge peaks are wholly consistent with the order of the main-edge positions. It is also evident that the spectral shape of preedge features in all the samples presented here can be classified into two groups; two preedge peaks P and P′ are discernible for some materials containing considerable amount of tetravalent manganese ions, whereas only one feature P at lower energy can be observed for the others with trivalent manganese ions. In fact, the latter characteristic preedge feature for trivalent manganese compounds can be interpreted as a result of the splitting of $t_{2g}$ and $e_g$ energy levels modified by Jahn−Teller deformation.[24] For the nanocrystalline manganese oxyiodides under investigation, both the pristine materials exhibit

nearly the same spectral features in preedge region, whereas there are marked spectral differences between the corresponding lithiated derivatives. That is, the lithiation reaction gives rise to a smaller change in the preedge features of the potassium-based nanocrystal compared to the sodium-based one, which suggests that the Jahn−Teller deformation of the $MnO_6$ octahedra is smaller in the former. In the main-edge region, there are some peaks (denoted A, B, and C), which are assigned as the dipole-allowed transitions from the core 1s level to unoccupied 4p states. In contrast to the well-crystallized $LiMn_2O_4$ and $\lambda$-$MnO_2$,[25] both the pristine nanocrystalline compounds do not show the fine features A and B in this region, which is attributed to the absence of long-range crystal order. This finding is well consistent with the recent XANES study for Na-based nanocrystal.[26] On the contrary, a distinct peak A is clearly observed for both the lithiated derivatives as well as for tetragonal spinel $Li_2Mn_2O_4$, although its spectral weight is weaker for the former than for the latter. Since the strong peak A is an indicator of trivalent manganese ion stabilized in the Jahn−Teller distorted octahedra,[5] the observed weak intensity of peak A indicates that the Jahn−Teller deformation around manganese is less prominent for the nanocrystalline manganese oxyiodide than for the well-crystallized tetragonal spinel, as reported recently.[26] Moreover, a closer inspection on the present XANES spectra reveals that K-based nanocrystal exhibits smaller intensity of peak A than Na-based one, which is well correlated with less prominent change of preedge features after lithiation in the former. On the other hand, an intense and sharp peak C appears commonly for all the nanocrystalline manganese oxyiodides including the lithiated derivatives as well as for the spinel-structured compounds. Considering the fact that the intensity of this peak is proportional to the relative concentration of edge-shared $MnO_6$ octahedra with respect to corner-shared one,[27] it can be supposed that the crystal structure of nanocrystalline manganese oxyiodides consists of edge-shared $MnO_6$ octahedra like spinel-structured compounds. In contrast, only a broader and less intense peak C can be discerned for another nanocrystalline manganate without iodine and potassium species (sample viii in Figure 5), indicating this compound has the intergrowth structure of edge- and corner-shared $MnO_6$ octahedra. On the basis of this finding, it can be supposed that iodine and potassium ions may act as stabilizers for edge-shared $MnO_6$ network. It has been known that there are some kinds of lithium manganate phases such as spinel $LiMn_2O_4$, layered $LiMnO_2$, and so forth, whose crystal structures constitute with edge-shared $MnO_6$ octahedra. However, on the basis of the present Mn K-edge XANES results, it is very difficult to determine conclusively the local structure around manganese in the nanocrystalline manganese oxyiodides. To solve this problem, we have applied micro-Raman spectroscopy.

**Micro-Raman Spectroscopy.** The Raman spectra of the nanocrystalline A−Li−Mn−O−I (A = K and Na) compounds are represented in Figure 6, together with the reference spectra of rhombohedral layered $LiCoO_2$, cubic spinel $LiMn_2O_4$, monoclinic layered $LiMnO_2$, and tetragonal spinel $Li_2Mn_2O_4$. As predicted by the factor group analysis, the rhombohedral $LiCoO_2$ compound exhibits two $A_{1g}$ and $E_g$ phonon lines at 486 and 596 $cm^{-1}$, whereas three Raman peaks corresponding to Raman-active $2A_g + B_g$ modes are observed for the layered $LiMnO_2$ oxide at 422, 481, and 603 $cm^{-1}$,[15,28] In the spinel-structured compounds, a larger number of Raman peaks appear because of their complex crystal structure. As shown in Figure 6, the present cubic spinel $LiMn_2O_4$ sample shows four Raman peaks at 270, 340, 454, and 631 $cm^{-1}$, which are assigned as $2T_{2g}$,

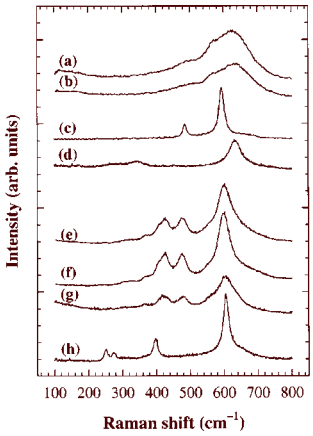


**Figure 6.** Micro-Raman spectra for the nanocrystalline A−Li−Mn−O−I compounds with A = (a) K and (b) Na and (e−f) their lithiated derivatives, in comparison with the references (c) rhombohedral layered $LiCoO_2$, (d) cubic spinel $LiMn_2O_4$, (g) monoclinic layered $LiMnO_2$, and (h) tetragonal spinel $Li_2Mn_2O_4$.

$E_g$, and $A_{1g}$ mode, respectively, whereas four characteristic phonon lines can be detected for the tetragonal spinel phase in the frequency range 200−650 $cm^{-1}$. The Raman spectrum of tetragonal spinel $Li_2Mn_2O_4$ can be clearly distinguished from that of monoclinic layered $LiMnO_2$, even though both the lithium manganates show almost the same XRD patterns.[29] This is because the Raman spectrum is strongly dependent on the crystal symmetry rather than on the structure factor. In this regard, the Raman spectroscopy enables us to easily identify various lithium manganate phases with closely related crystal structures such as layered $LiMnO_2$ (*C*2/*m*), tetragonal spinel $Li_2Mn_2O_4$ ($I4_1/amd$), orthorhombic $LiMnO_2$ (*Pmnm*), and so forth.[15] In the nanocrystalline manganese oxyiodides, two very broad features are discernible around 490 and 630 $cm^{-1}$. Considering that the nanocrystalline nature and the mixed Mn oxidation state of the present manganese oxyiodides are surely responsible for the very broad Raman feature, the Raman spectra of these nanocrystals are somewhat similar to that of rhombohedral $LiCoO_2$ rather than that of spinel $LiMn_2O_4$. However, the considerable broadness of features makes it very difficult to definitively determine the local structure of nanocrystalline materials on the basis of the present Raman spectra. In this regard, we have also examined the Raman spectra of lithiated manganese oxyiodides, since the lithiation usually increases the signal-to-noise (S/N) ratio of Raman data by depressing the electrical conductivity. As can be seen clearly from Figure 6, there is remarkable spectral consistency between the nanocrystalline materials and the monoclinic layered $LiMnO_2$, highlighting that the lithiated derivatives possess the layered structure with monoclinic distortion. Generally the reduction of Mn oxidation state induces a Jahn−Teller distortion around manganese, giving rise to a structural transition from rhombohedral layered to monoclinic layered, or from cubic spinel to tetragonal spinel. Moreover, it is impossible to change from a spinel structure to a layered one during lithiation process, since the spinel structure is thermodynamically more stable than the layered one. In this regard, we can conclude that the manganese ion in nanocrystalline manganese oxyiodide crystallizes locally in rhombohedral layered cation ordering not in the spinel-type one, and the lithiation reaction results in a local structural change into monoclinic layered structure.

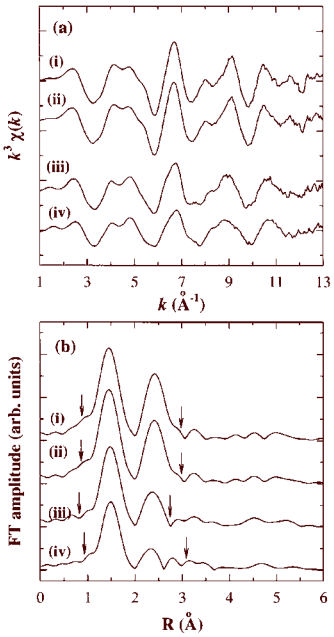


**Figure 7.** (a) $k^3$-weighted Mn K-edge EXAFS spectra and (b) their Fourier transforms for the nanocrystalline A−Li−Mn−O−I compounds with A = (i) K and (ii) Na and (iii−iv) their lithiated derivatives. The range over which the Fourier filtering has been made is shown by the arrows.

**Mn K-Edge EXAFS Analysis.** The local structural variation of the nanocrystalline A−Li−Mn−O−I (A = K and Na) compounds upon chemical lithiation process has been examined quantitatively using Mn K-edge EXAFS spectroscopy. The $k^3$-weighted Mn K-edge EXAFS spectra for the nanocrystalline A−Li−Mn−O−I (A = K and Na) compounds and their lithiated derivatives are represented in Figure 7a and the corresponding Fourier transforms (FTs) in Figure 7b. As can be seen from Figure 7a, the overall spectral features of the EXAFS oscillation of the pristine nanocrystalline compounds are quite similar to each other, indicating the same local structure around manganese in both compounds. On the other hand, the lithiation process gives rise to a spectral change in EXAFS oscillation which is less prominent for K-based material than for Na-based one, as observed in XANES region. In the FT diagrams (Figure 7b), the nanocrystalline manganese oxyiodides exhibit two intense FT peaks at ∼1.5 and ∼2.5 Å, which are attributed to the (Mn−O) and (Mn−Mn) shells, respectively. Upon lithiation reaction, the FT peaks become depressed especially for (Mn−Mn) shell, which can be understood from the fact that the Jahn−Teller distortion around Mn causes a damping of EXAFS signal. However, in contrast to the previously reported results for the spinel phase,[25,30] the splitting of FT peaks corresponding to (Mn−Mn) shells induced by lithiation is not obvious for the present nanocrystalline compounds, which is well correlated with the XANES results.[26] Between both lithiated nanocrystals, the splitting of (Mn−Mn) shells is more well-resolved for Na-based material than for K-based one. These findings can be regarded as further evidence for the excellent endurance of the amorphous character of these nanocrystalline materials during Li insertion reaction, especially for the K-based nanocrystal. The peaks at 4−6 Å originated

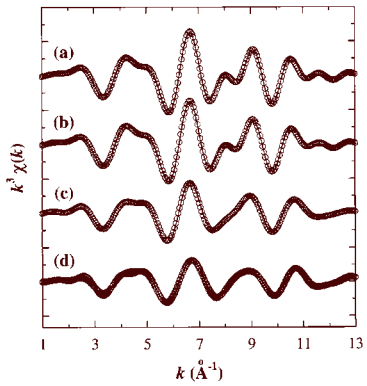


**Figure 8.** Fourier filtered Mn K-edge EXAFS spectra for the nanocrystalline A−Li−Mn−O−I compounds with A = (a) K and (b) Na and (c−d) their lithiated derivatives. The solid lines and empty circles represent the fitted and experimental data, respectively.

**TABLE 2: Results of Nonlinear Least-Squares Curve-Fitting Analysis for the Mn K-edge EXAFS Spectra of Nanocrystalline Manganese Oxyiodides and Their Lithiated Derivatives**

| sample | bond | CN[a] | $R$ (Å) | $\sigma^2$ ($10^{-3}$ × Å$^2$) |
|---|---|---|---|---|
| K−Li−Mn−O−I | (Mn−O) | 6.0 | 1.90 | 4.89 |
| | (Mn−Mn) | 4.2 | 2.86 | 6.22 |
| Na−Li−Mn−O−I | (Mn−O) | 6.0 | 1.90 | 4.95 |
| | (Mn−Mn) | 4.3 | 2.85 | 6.91 |
| | (Mn−$O_{eq}$) | 4 | 1.90 | 3.21 |
| Lithiated | (Mn−$O_{ax}$) | 2 | 2.33 | 10.60 |
| K−Li−Mn−O−I | (Mn−Mn) | 1.4 | 2.87 | 2.82 |
| | (Mn−Mn) | 2.8 | 3.02 | 9.99 |
| | (Mn−$O_{eq}$) | 4 | 1.90 | 4.08 |
| Lithiated | (Mn−$O_{ax}$) | 2 | 2.27 | 15.31 |
| Na−Li−Mn−O−I | (Mn−Mn) | 1.4 | 2.83 | 5.73 |
| | (Mn−Mn) | 2.8 | 3.02 | 15.11 |

[a] While the coordination numbers for (Mn−O) shells are fixed to the crystallographic values, those for (Mn−Mn) shells are set as variables in the curve-fitting analyses.

from the multiple scattering paths with focusing effect are nearly suppressed in the present compounds, in contrast to the well-crystalline $LiMnO_2$ and $LiMn_2O_4$ ones.[5,25] This confirms the nanocrystalline nature of the present manganese oxyiodides. To determine the structural parameters such as coordination number (CN), bond distance ($R$), and Debye−Waller factor ($\sigma^2$), these FT peaks were isolated by inverse Fourier transform to a $k$ space and then were curve-fitted. In light of micro-Raman results, we have tried to reproduce the spectra of nanocrystalline manganese oxyiodides and their lithiated derivatives on the basis of the crystal structures of rhombohedral layered and monoclinic layered phases, respectively, in such a way that we were able to get reasonable fitting results.[31] The best fitting results are compared to the experimental $k^3\chi(k)$ Fourier filtered data in Figure 8, and the obtained structural parameters are listed in Table 2. While the manganese ion in the nanocrystalline A−Li−Mn−O−I (A = K and Na) compounds is stabilized in a regular $MnO_6$ octahedron with six neighboring oxygen ions at the same distance, the manganese ion in the lithiated derivatives exists in a Jahn−Teller distorted $MnO_6$ octahedra, as supposed from micro-Raman study. Moreover, the average (Mn−O) and (Mn−Mn) bond distances of the nanocrystalline materials are found to be elongated by lithiation reaction, confirming the decrease of Mn oxidation state after reaction with $n$-BuLi. In addition, the coordination numbers are determined to be smaller

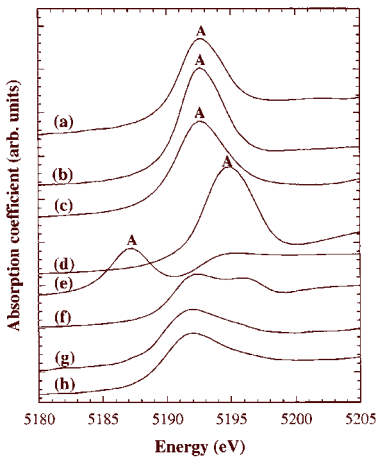


**Figure 9.** I $L_I$-edge XANES spectra for the nanocrystalline A−Li−Mn−O−I compounds with A = (a) K and (b) Na and (g−h) their lithiated derivatives, in comparison with the references (c) $KIO_3$, (d) $KIO_4$, (e) $I_2$, and (f) KI.

for (Mn−Mn) shells than for (Mn−O) shells, which reflects the nanocrystalline nature of the present samples leading to an incomplete coordination of manganese by distant shells.

**I $L_I$-Edge XANES Analysis.** As described in the Mn K-edge XANES section, another type of nanocrystalline manganate without iodine and potassium species crystallizes with edge- and corner-shared network of $MnO_6$ octahedra, in contrast to the present manganese oxyiodides. In this regard, it is a very interesting question what the role of iodine is. To give an answer to this question, we have studied the chemical bonding character of iodine species by performing I $L_I$-edge XANES analysis. The I $L_I$-edge XANES spectra of the nanocrystalline manganese oxyiodides and their lithiated derivatives are presented in Figure 9, in comparison with the reference spectra of KI, $I_2$, $KIO_3$, and $KIO_4$. All the reference spectra except for KI exhibit a characteristic white line (WL) peak at around 5185−5195 eV, which is ascribed to the transition from the 2s core level to the unoccupied 5p state.[32] Since the intensity of this WL feature is dependent on the density of the unoccupied 5p final state, the most intense peak is discernible for both $KIO_3$ and $KIO_4$ references having completely empty I 5p orbitals. On the contrary, this 2s → 5p transition is not possible for KI because of the full occupancy of I 5p orbital. In the pristine nanocrystalline materials, this WL peak shows almost the same position and intensity as the reference $KIO_3$, which indicates that the iodate species is stabilized in nanocrystalline manganate oxyiodides, as reported very recently.[26] There are two possibilities about the site of $IO_3^-$ cluster in these nanocrystalline compounds; one is the interlayer site and the other is the grain boundary or the sample surface. As shown in Figure 9, a notable depression of peak A upon lithiation can be observed for both nanocrystalline materials, suggesting that most of iodate ion is reduced to a negatively charged iodide ion. Considering the electrostatic repulsion between iodide and oxide anions, it is impossible for iodide ion to exist in the interlayer octahedral site of rhombohedral layered lattice. However, the elemental analyses reveal that there still remain lots of iodine species after lithiation, which implies that most of iodine species in nanocrystalline manganese oxyiodide is located in the grain boundary or on the surface. Since the iodate ion stabilized in the grain boundary prevents an effective crystal growth of lithium manganese oxide grains, it would help to maintain the nanocrystalline nature of this material before and after Li insertion.

Summarizing the present experimental findings, it is evident that manganese ion in the present nanocrystalline compounds is stabilized in the rhombohedral layered-type local structure, which is maintained by the presence of alkali metal pillar rather than by the existence of iodate cluster in interlayer space. In this context, a greater initial discharge capacity of K-based nanocrystal compared to Na-based one is interpreted as a result of the expanded interlayer spacing sustained by larger potassium ion, giving a better ability to accommodate the lithium ion in the interlayer space.

## Conclusion

In this study, an attempt has been made not only to determine the local structure of manganese in the nanocrystalline electrode materials but also to probe the effects of Li insertion on the atomic and electronic structures of these compounds by performing systematic micro-Raman and XAS analyses. The electrochemical measurements demonstrate that a newly prepared potassium-based lithium manganese oxyiodide shows a great initial discharge capacity of ~340 mAh/g at 0.2 mA/cm$^2$, which is larger than that of sodium-based homologue. According to the XRD analysis, the amorphous nature of the present samples is maintained before and after lithiation reaction. The Mn K-edge XANES and micro-Raman results reveal that the manganese ion is stabilized in the rhombohedral layered lattice, and the crystal symmetry is changed into a monoclinic symmetry upon lithiation reaction. Despite layered local crystal structure, the present nanocrystalline materials exhibit no significant change in discharge potential profiles during lithium insertion−extraction process, which is surely contrasted with the layered $LiMnO_2$ phase with well-crystalline structure showing a structural transition to spinel-type cation ordering. This can be regarded as evidence of the better structural stability of nanocrystalline materials with respect to well-crystalline ones. The Mn K-edge EXAFS analysis confirms that the structural distortion is less prominent for the nanocrystalline compounds than for the spinel lithium manganate, which gives an explanation for the greater initial discharge capacities of these nanocrystalline materials. On the other hand, I $L_I$-edge XAS spectra show that the iodine is stabilized as iodate species in the grain boundary or on the surface of the nanocrystalline manganese oxyiodide. Such an iodate species in the grain boundary is presumed to contribute to the maintenance of the nanocrystallinity of the present materials before and after Li insertion.

**Acknowledgment.** This work was supported in part by the Korean Ministry of Education (BSRI-99-3413) with the Brain Korea 21 fellowship for H. S. Park and by the Korean Ministry of Science and Technology through the National Research Laboratory Project (1999). C. W. Kwon thanks CROUS of Bordeaux in France for the financial support. Authors are also grateful to Prof. M. Nomura for helping us to get the XAS data in the Photon Factory.

## References and Notes

(1) Thackeray, M. M. *Prog. Solid State Chem.* **1997**, *25*, 1.
(2) Armstrong, A. R.; Bruce, P. G. *Nature* **1996**, *381*, 499.
(3) Capitaine, F.; Gravereau, P.; Delmas, C. *Solid State Ionics* **1996**, *89*, 197.
(4) Koetschau, I.; Richard, M. N.; Dahn, J. R.; Soupart, J. B.; Rousche, J. C. *J. Electrochem. Soc.* **1995**, *142*, 2906.

(5) Hwang, S. J.; Park, H. S.; Choy, J. H.; Campet, G. *Chem. Mater.* **2000**, *12*, 1818.
(6) Gummow, R. J.; Liles, D. C.; Goodenough, J. B. *Mater. Res. Bull.* **1993**, *28*, 1249.
(7) Thackeray, M. M.; David, W. I. F.; Bruce, P. G.; Goodenough, J. B. *Mater. Res. Bull.* **1983**, *18*, 469.
(8) Treuil, N.; Labrugère, C.; Menetrier, M.; Portier, J.; Campet, G.; Deshayes, A.; Frison, J. C.; Hwang, S. J.; Song, S. W.; Choy, J. H. *J. Phys. Chem. B* **1999**, *103*, 2100.
(9) (a) Kim, J.; Manthiram, A. *Nature* **1997**, *390*, 265. (b) Manthiram, A.; Kim, J. *Chem. Mater.* **1998**, *10*, 2895. (c) Kim, J.; Manthiram, A. *Electrochem. Solid-State Lett.* **1999**, *2*, 55.
(10) (a) Jeong, Y. U.; Manthiram, A. *Electrochem. Solid-State Lett.* **1999**, *2*, 421. (b) Jeong, Y. U.; Manthiram, A. *J. Solid State Chem.* **2001**, *156*, 331. (c) Manthiram, A.; Kim, J.; Choi, S. *MRS Symp. Proc.* **2000**, *575*, 9.
(11) Xu, J. J.; Kinser, A. J.; Owens, B. B.; Amyrl, W. H. *Electrochem. Solid-State Lett.* **1998**, *1*, 1.
(12) Leroux, F.; Nazar, L. F.*Solid State Ionics* **1997**, *100*, 103.
(13) Chen, R.; Whittingham, M. S. *J. Electrochem. Soc.* **1997**, *144*, L64.
(14) Hwang, S. J.; Park, H. S.; Choy, J. H.; Campet, G. *J. Phys. Chem. B* **2000**, *104*, 7612.
(15) Hwang, S. J.; Park, H. S.; Choy, J. H.; Campet, G.; Portier, J.; Kwon, C. W.; Etourneau, J. *Electrochem. Solid-State Lett.* **2001**, *4*, A123.
(16) Considering the fact that the charge capacity for the first charge process (~110 mAh/g) is much smaller than that for the following discharge process, the electrochemical activity of these electrode materials is considered to originate mainly from the insertion of lithium into the as-prepared nanocrystal. In this regard, we have probed the variation of the chemical bonding nature of nanocrystalline compounds before and after chemical lithiation reaction to understand the origin of its electrochemical activity.
(17) Oyanagi, H.; Matsushida, T.; Ito, M.; Kuroda, H. *KEK Report* **1984**, *83*, 30.
(18) Chen, R.; Zavalij, P.; Whittingham, M. S. *Chem. Mater.* **1996**, *8*, 1275.
(19) Kim, J.; Manthiram, A. *Electrochem. Solid-State Lett.* **1998**, *1*, 207.
(20) Kwon, C. W.; Campet, G.; Portier, J.; Poquet, A.; Fournes, L.; Labrugere, C.; Jousseaume, B.; Toupance, T.; Choy, J. H.; Subramanian, M. A. *Int. J. Inorg. Mater.* **2001**, *3*, 211.
(21) Campet, G.; Wen, S. J.; Han, S. D.; Shastry, M. C. R.; Portier, J.; Guizard, C.; Cot, L.; Xu, Y.; Salardennet, J. *Mater. Sci. Eng., B* **1993**, *18*, 201.
(22) Tsang, C.; Kim, J.; Manthiram, A. *J. Solid State Chem.* **1998**, *137*, 28.
(23) This material corresponds to the sample 2 in ref 22 with composition of $MnO_{1.89}$.
(24) Horne, C. R.; Bergmann, U.; Grush, M. M.; Perera, R. C. C.; Ederer, D. L.; Callcott, T. A.; Cairns, E. J.; Cramer, S. P. *J. Phys. Chem. B* **2000**, *104*, 9587.
(25) Hwang, S. J.; Park, H. S.; Choy, J. H.; Campet, G. *J. Phys. Chem. B* **2001**, *105*, 335.
(26) Horne, C. R.; Bergmann, U.; Kim, J.; Striebel, K. A.; Manthiram, A.; Cramer, S. P.; Cairns, E. J. *J. Electrochem. Soc.* **2000**, *147*, 395.
(27) Manceau, A.; Gorshkov, A. I.; Drits, V. A. *Am. Mineral.* **1992**, *77*, 1133.
(28) Inaba, M.; Iriyama, Y.; Ogumi, Z.; Todzuka, Y.; Tasaka, A. *J. Raman Spectrosc.* **1997**, *28*, 613.
(29) Jang, Y. I.; Huang, B.; Chiang, Y. M.; Sadoway, D. R. *Electrochem. Solid-State Lett.* **1998**, *1*, 13.
(30) Ammundsen, B.; Jones, D. J.; Rozière, J.; Villain, F. *J. Phys. Chem. B* **1998**, *102*, 7939.
(31) We have also tried to reproduce the experimental EXAFS data of lithiated derivatives on the basis of rhombohedral layered structure, but it gave poor fits and physically meaningless structural parameters.
(32) Hwang, S. J.; Park, N. G.; Kim, D. H.; Choy, J. H. *J. Solid State Chem.* **1998**, *138*, 66.

*Electrochemical and Solid-State Letters*, **4** (12) A213-A216 (2001)
1099-0062/2001/4(12)/A213/4/$7.00 © The Electrochemical Society, Inc.



# Micro-Raman Spectroscopic Study on Layered Lithium Manganese Oxide and Its Delithiated/Relithiated Derivatives

**Seong-Ju Hwang,[a,b] Hyo-Suk Park,[b] Jin-Ho Choy,[b] Guy Campet,[a,z] Josik Portier,[a] Chai-Won Kwon,[a] and Jean Etourneau[a]**

[a]*Institut de Chimie de la Matière Condensée de Bordeaux du CNRS, 33608 Pessac, France*
[b]*National Nanohybrid Materials Laboratory, School of Chemistry, Seoul National University, Seoul 151-747, Korea*

Micro-Raman spectroscopic analyses have been performed for the layered $LiMnO_2$ compound and its delithiated/relithiated derivatives in order to probe the effect of Li extraction/insertion on the local structure around manganese ion in this layered material. For this purpose, we have first tried to establish a spectroscopic measure for identifying the lithium manganates with closely related structures. From the detailed comparison among the Raman spectra of layered and spinel-structured lithium manganates, both phases can be easily differentiated from each other by using micro-Raman spectroscopy. Based on these experimental findings, we are able to conclude that the chemical or electrochemical deintercalation of lithium gives rise to the Mn migration into the interlayer lithium site, resulting in the creation of the spinel-like cation ordering.
 [DOI: 10.1149/1.1413704] 

Manuscript submitted May 17, 2001; revised manuscript received August 24, 2001. Available electronically October 15, 2001.

Recently, lithium manganese oxides have received considerable attention as promising cathode materials in lithium secondary batteries, since manganese is more abundant, less expensive, and less toxic than cobalt used in the currently commercialized lithium rechargeable batteries.[1-3] For this reason, intense research efforts have been directed not only to develop new types of manganese-based compounds but also to improve the electrochemical performance of existing lithium manganate cathode materials. Although the spinel $LiMn_2O_4$ is the most widely studied among the lithium manganate systems, there is increasing interest in other types of lithium manganese oxides such as layered $LiMnO_2$, orthorhombic $LiMnO_2$, nanocrystalline manganese oxyiodides, etc.[4-8] Among them, the layered $LiMnO_2$ exhibits the largest initial capacity for the 4 V region but it suffers from severe capacity fading after the first charge process.[4] Such a remarkable capacity loss would be attributed to the destabilization of layered structure induced by the electrochemical delithiation reaction.[9,10] In fact, most manganese oxides have been known to experience such a structural modification during extended electrochemical charge/discharge cycling.[11,12] Since the local atomic arrangement of the cathode material is closely related to its electrochemical performance, neutron and X-ray diffraction (XRD) analyses were performed to investigate the variation of the crystal structure of lithium manganese oxides during electrochemical cycling.[13,14] Although these diffraction methods have been reported to be useful in probing the average structure of electrode material, they cannot provide detailed information on the local structure around manganese ion. As an alternative tool, vibrational spectroscopy allows us to examine the local crystal structure of cathode materials including the electrochemically cycled derivative with poor crystallinity, since it does not need long range structural order.[15-20] Moreover, taking into account the fact that the vibrational spectrum is very sensitive to the crystal symmetry, this kind of spectroscopic method should be effective in differentiating various kinds of lithium manganese oxides whose atomic arrangements are closely related to one another. Especially, in contrast to infrared spectroscopy, micro-Raman spectroscopy enables us to probe the lattice vibration of this compound without any pretreatment, and hence, it can be one of the most suitable tools for studying the chemical bonding nature of electrode material. In spite of such advantages, there have been only a few Raman studies on lithium manganese oxides, because the relatively high electronic conductivity of these materials makes it difficult to obtain the reproducible spectra with high signal-to-noise (S/N) ratio.[16-18]

[z] E-mail: campet@icmcb.u-bordeaux.fr

In this work, we have applied micro-Raman spectroscopy to explore the evolution of the chemical bonding environment around manganese in layered $LiMnO_2$ upon chemical and electrochemical Li deintercalation/intercalation. For this purpose, the Raman spectra of spinel-structured lithium manganates were also collected to establish a measure for identifying the lithium manganese oxides with closely related crystal structures.

## Experimental

The layered $LiMnO_2$ polycrystal was prepared by ion exchange reaction of $\alpha$-$NaMnO_2$ with LiBr, whereas the spinel $LiMn_2O_4$ sample was obtained by using the conventional solid-state reaction method.[9,21] The chemical delithiation reaction for the $LiMnO_2$ compound was carried out by stirring this sample with 2.5 M $H_2SO_4$ solution, and then the lithium was reinserted by reacting the delithiated sample with 1.6 M *n*-BuLi in hexane at room temperature, as reported previously.[9] On the other hand, the lithiated tetragonal spinel $Li_2Mn_2O_4$ sample was synthesized by reacting the pristine cubic spinel with 1.6 M *n*-BuLi in hexane.[21]

The crystal structures of all the present materials were studied by XRD measurement using Ni-filtered Cu K$\alpha$ radiation with a graphite diffracted beam monochromator. As summarized in Table I, it becomes clear that the delithiation/relithiation reaction for $LiMnO_2$ induces a significant change in crystal structure from monoclinic symmetry to rhombohedral/cubic.[9] On the other hand, the effects of chemical delithiation and relithiation on the stoichiometry of layered $LiMnO_2$ were examined by performing atomic absorption (AA) spectrometry and thermogravimetric analysis, as listed in Table I. The electrochemical measurements were carried out with the cell of Li/1 M $LiPF_6$ in ethylene carbonate (EC): diethyl carbonate (DEC) (50:50 v/v)/$LiMnO_2$, which was assembled in a dry box. The composite cathode was prepared by mixing thoroughly the active $LiMnO_2$ cathode material (85%) with 10% acetylene black and 5% polytetrafluoroethylene (PTFE). The experiment was performed in a galvanostatic mode with an Arbin BT 2043 multichannel galvanostat/potentiostat in the voltage range of 2.2-4.3 V. A large initial capacity of ~220 mAh/g was obtained for the first charge process whereas it was significantly decreased to ~110 mAh/g for the subsequent discharge process, as reported previously.[4] From the observed charge capacities, the chemical formula of the first cycled sample could be estimated to be $Li_{0.62}MnO_2$, with the supposition that the charge capacity on the charge/discharge process originates wholly from the lithium deintercalation/intercalation reaction.

The Raman measurement was carried out at room temperature using a Jobin-Yvon/Atago Bussan T64000 triple spectrometer equipped with micro-optics. The samples were excited with the

**Table I. Lattice parameters, unit cell volumes ($V_c$), crystal symmetries, and chemical formulas of lithium manganese oxides.**

| Nominal formula | $a$ (Å) | $b$ (Å) | $c$ (Å) | β (°) | $V_c$ | Crystal symmetry | Chemical formula |
|---|---|---|---|---|---|---|---|
| $LiMnO_2$ | 5.443 | 2.810 | 5.392 | 116.012 | 74.12 | Monoclinic | $Li_{1.02}MnO_2$ |
| $LiMn_2O_4$ | 8.249 | | | | 561.29 | Cubic | $Li_{1.07}Mn_2O_4$ |
| $Li_2Mn_2O_4$ | 5.659 | | 9.291 | | 297.59 | Tetragonal | $Li_{2.34}Mn_2O_4$ |
| Delithiated $LiMnO_2$ | 2.859 | | 13.378 | | 284.10 | Rhombohedral | $H_{0.34}MnO_2$ |
| Relithiated $LiMnO_2$ | 8.234 | | | | 558.25 | Cubic | $Li_{0.36}H_{0.25}MnO_2$ |

514.5 nm line of an $Ar^+$ laser. All the present spectra were obtained by backscattering from the polycrystalline powdered sample. The resolution of the present spectra was 3-4 $cm^{-1}$. In order to prevent possible thermal damage of the samples, the power of the incident laser light was maintained at less than 5 mW. After each measurement, the sample surface was thoroughly checked to remove the possibility of spectral modification caused by surface degradation.

## Results and Discussion

In order to probe the evolution of the local crystal structure of layered $LiMnO_2$ upon chemical and electrochemical delithiation/relithiation, we have first attempted to establish a spectroscopic measure for identifying the lithium manganates with closely related structures by using micro-Raman spectroscopy. It is well known that there are close structural similarities between monoclinic layered $LiMn^{+III}O_2$ and tetragonal spinel $Li_2Mn^{+III}{}_2O_4$, and between rhombohedral layered $Li_{0.5}Mn^{+III}{}_{0.5}Mn^{+IV}{}_{0.5}$ $O_2$[c] and cubic spinel $LiMn^{+III}Mn^{+IV}O_4$, since the crystal symmetry of lithium manganate is closely related to the concentration of Jahn-Teller active $Mn^{+III}$ ion.[2] In this regard, the Raman spectra of the layered $LiMnO_2$ and $LiCoO_2$ are compared in Fig. 1 with those of the spinel-structured $Li_2Mn_2O_4$ and $LiMn_2O_4$, respectively. According to the group theoretical calculation,[15] the layered lithium metal oxide with rhombohedral $R\bar{3}m$ symmetry is predicted to show two Raman-active $A_{1g}$ + $E_g$ modes whereas there are three Raman-active $2A_g$ + $B_g$ modes for the monoclinic $C2/m$ phase. As expected from the factor group analysis, the rhombohedral $LiCoO_2$ compound exhibits two Raman bands at 486 and 596 $cm^{-1}$, which can be assigned as $E_g$ and $A_{1g}$ modes.[15] In the case of layered $LiMnO_2$ oxide, three Raman peaks are observed at 422, 481, and 603 $cm^{-1}$, confirming the monoclinic symmetry of this compound.[4] On the other hand, four Raman peaks are discernible for the present cubic spinel $LiMn_2O_4$ sample whereas the factor group analysis predicts five Raman active modes ($A_{1g}$ + $E_g$ + $3T_{2g}$) for this compound.[16]

On the basis of the theoretical calculation for the vibrational frequencies in $LiMn_2O_4$ spinel phase,[16] the strongest peak at 631 $cm^{-1}$ can be attributed to the symmetric $A_{1g}$ mode. In fact, such an intense peak around 630 $cm^{-1}$ was regarded as an indication of a cubic spinel lithium manganate phase.[17,18] The other weaker phonon lines at 270, 340, and 454 $cm^{-1}$ should be related to the $2T_{2g}$ and $E_g$ modes, while another $T_{2g}$ mode seems to be concealed by the large intensity of the strongest peak. In comparison with the previously reported spectrum of $LiMn_2O_4$ compound, the present spectrum shows small discrepancies in minor phonon lines except the strongest peak around 630 $cm^{-1}$.[16,18] Such a spectral inconsistency would be attributed to the different stoichiometry of the samples used for these studies which results in remarkable changes in the Raman spectra.[16,17] However, note that both the present and the previously reported spectra of cubic spinel $LiMn_2O_4$ compound are quite dissimilar to that of rhombohedral $LiCoO_2$ layered oxide showing two peaks in the frequency region of 450-600 $cm^{-1}$. Furthermore, very recently we have measured the Raman spectrum of lithium manganese oxyiodide nanoparticles with a rhombohedral layered structure, and found that there are two broad phonon lines at around 480 and 610 $cm^{-1}$, as are observed for $LiCoO_2$.[22] Such spectral features of rhombohedral layered lithium manganate can also be easily differentiated from those of cubic spinel $LiMn_2O_4$ phase. In the case of tetragonal spinel $Li_2Mn_2O_4$ compound, four phonon lines can be detected in the frequency range 200-650 $cm^{-1}$ as for the cubic spinel phase, even though a lowering of crystal symmetry from $Fd3m$ to $I4_1/amd$ increases the number of Raman active modes.[23] In addition, these spectral features of the tetragonal spinel are found to be more intense and sharper than those of the cubic one, which can be explained by a decrease of electrical conductivity leading to an enhancement of the optical skin depth of the incident laser beam.

Compared to the cubic spinel phase, all the Raman peaks of tetragonal spinel appear to shift toward low frequency, which should be related to the decrease of the Mn oxidation state. However, the absence of single crystal data and/or theoretical calculation prevents

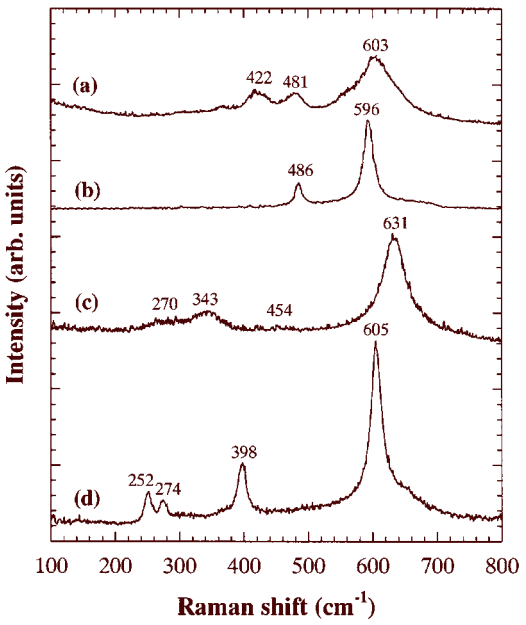


**Figure 1.** Micro-Raman spectra for (a) the monoclinic layered $LiMnO_2$, (b) the rhombohedral layered $LiCoO_2$, (c) the cubic spinel $LiMn_2O_4$, and (d) the tetragonal spinel $Li_2Mn_2O_4$ compounds. The data of $LiCoO_2$ are taken from Ref. 19.

[c] We cannot obtain the Raman spectrum of rhombohedral $Li_{0.5}MnO_2$experimentally, because the delithiation of layered $LiMnO_2$ via chemical or electrochemical way gives rise to a local structural transformation into spinel-like cation ordering (Ref. 9 and 10). For this reason, we present the spectrum of rhombohedral layered $LiCoO_2$ compound in Fig. 1, instead of that of rhombohedral layered lithium manganate.

*Electrochemical and Solid-State Letters*, **4** (12) A213-A216 (2001) 

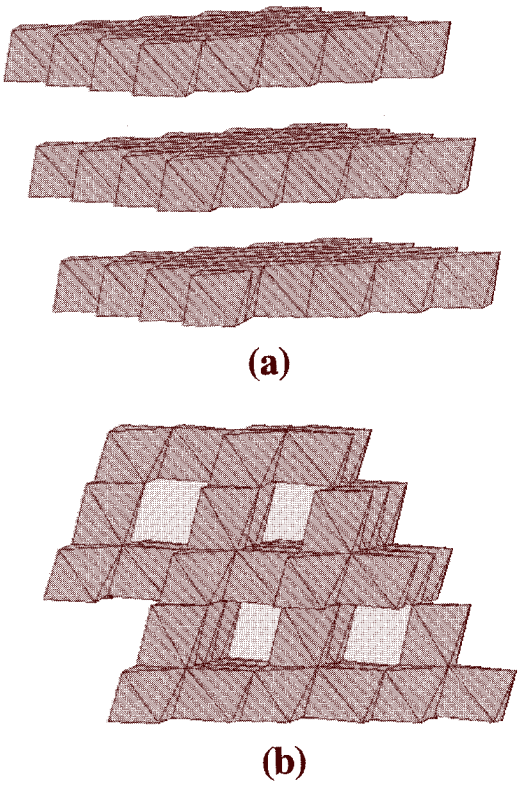


**Figure 2.** Schematic models for $MnO_2$ frameworks of (a) the layered and (b) the spinel-structured lithium manganese oxides.

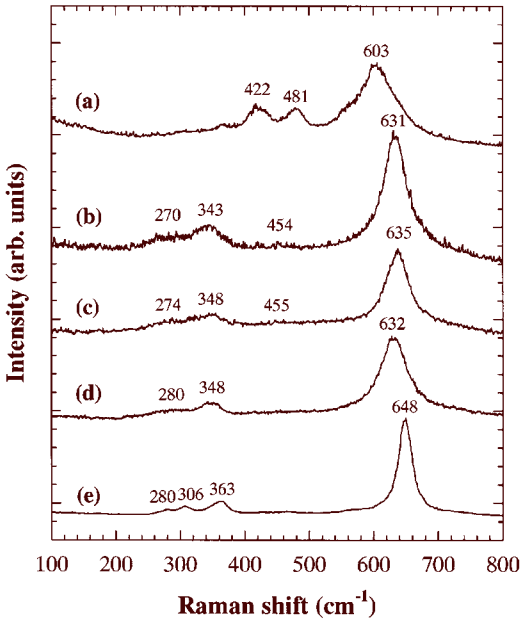


**Figure 3.** Micro-Raman spectra for (a) the monoclinic layered $LiMnO_2$, (b) the cubic spinel $LiMn_2O_4$, (c) the delithiated layered $LiMnO_2$, (d) the relithiated layered $LiMnO_2$, and (e) the electrochemically cycled $LiMnO_2$ compounds.

us from conclusively assigning the observed bands. Again, it is worthwhile to mention that the Raman spectrum of tetragonal spinel can be easily distinguished from that of monoclinic layered $LiMnO_2$. Taking into account the fact that the charge/discharge process frequently accompanies the structural transformation between layered and spinel lithium manganate phases,[2] it is very important to clearly identify both phases for understanding the intercalation mechanism for lithium manganate electrodes. However, as illustrated in Fig. 2, the $MnO_2$ frameworks of both structures are closely related to each other, that is, one fourth of the manganese ions in the spinel structure are located in the interlayer octahedral site of the layered structure whereas the remaining manganese ions are positioned in the same site for both structures. For this reason, it is quite difficult to discriminate these phases by using diffraction tools.[24] In this context, micro-Raman spectroscopy can be regarded as a powerful method to probe the local structural evolution of lithium manganate during Li deintercalation/intercalation, since it allows us to easily identify the lithium manganates with layered and spinel structures.

Based on the above comparative Raman results, we are able to investigate the influences of chemical and electrochemical delithiation/relithiation on the local crystal structure of layered $LiMnO_2$. As shown in Fig. 3, an intense peak around 630 $cm^{-1}$, characteristic of cubic spinel phase, is detected commonly for both delithiated and relithiated $LiMnO_2$ compounds, and moreover, their overall spectral features appear to be almost identical to those of cubic spinel lithium manganate, indicating a local structural modification from monoclinic layered structure to a spinel-like cation ordering. Such a structural transition can be achieved by the migration of one-fourth of Mn ions into the interlayer Li sites, as can be supposed from Fig. 2.[9] If this Mn migration does not occur during Li deintercalation, both the delithiated and relithiated compounds should crystallize with rhombohedral layered structure on the basis of the high Mn oxidation state of ≅3.5 (Table I). However, the present spectra of both compounds are surely different from that of the rhombohedral layered $LiCoO_2$ phase, confirming the structural change into the spinel-type cation ordering. On the other hand, considering that the XRD pattern of the delithiated compound can be indexed as a rhombohedral layered structure (Table I), the present Raman results emphasize the fact that the local cation arrangement unambiguously differs from the average crystal structure, which is fully consistent with the previous extended X-ray absorption fine structure (EXAFS) analysis and electrochemical measurement.[9,13] In addition, it is clear that the reaction of delithiated $LiMnO_2$ with *n*-BuLi does not lead to the formation of the tetragonal spinel $Li_2Mn_2O_4$ phase. This is in good agreement with the AA measurements, revealing that all the deintercalated lithium ions are not reintercalated into the crystal lattice of layered lithium manganese oxide (Table I). On the other hand, the overall spectral features of electrochemically cycled derivative are also observed to be rather similar to those of cubic spinel oxide but different from those of layered oxide, suggesting the structural transition to spinel-type cation ordering upon the electrochemical charge/discharge process. In comparison with the Raman spectrum of the reference $LiMn_2O_4$ spinel oxide, there are detectable peak shifts in the spectrum of the electrochemically cycled derivative. This would originate from the different chemical bonding environments for both compounds and/or from the matrix effect caused by phase mixing of spinel and

layered structures in the cycled derivative, as revealed by the recent transmission electron microscopic and EXAFS studies.[9,10] And it should be noted that, although the sample is discharged to 2.2 V, no tetragonal spinel phase is formed, which can be understood from the fact that the mixed state of spinel and layered structures prevents an effective reintercalation of lithium.

In conclusion, the present results clarify that micro-Raman spectroscopy is very effective in examining the local structural change of lithium manganese oxide upon electrochemical or chemical cycling process and in estimating the phase stability of lithium manganate cathode materials.

## Acknowledgments

This work was supported in part by the Korean Ministry of Education (BSRI-99-3413) with the Brain Korea 21 fellowship for H. S. Park, and by the Korean Ministry of Science and Technology through the National Research Laboratory Project (1999). Authors are grateful to Professor M. Yoshimura and Professor M. Kakihana for helping us to get the micro-Raman data.

*Institut de Chimie de la Matière Condensée de Bordeaux assisted in meeting the publication costs of this article.*

## References

1. K. Mizushima, P. C. Jones, P. J. Wiseman, and J. B. Goodenough, *Mater. Res. Bull.*, **15**, 783 (1980).
2. M. M. Thackeray, *Prog. Solid State Chem.*, **25**, 1 (1997).
3. J. R. Dahn, U. von Sacken, M. R. Jukow, and H. Al-Janaby, *J. Electrochem. Soc.*, **138**, 2207 (1991).
4. A. R. Armstrong and P. G. Bruce, *Nature*, **381**, 499 (1996).
5. F. Capitaine, P. Gravereau, and C. Delmas, *Solid State Ionics*, **89**, 197 (1996).
6. S. J. Hwang, H. S. Park, J. H. Choy, and G. Campet, *J. Phys. Chem. B*, **104**, 7612 (2000).
7. I. Koetschau, M. N. Richard, J. R. Dahn, J. B. Soupart, and J. C. Rousche, *J. Electrochem. Soc.*, **142**, 2906 (1995).
8. J. Kim and A. Manthiram, *Nature*, **390**, 265 (1997).
9. S. J. Hwang, H. S. Park, J. H. Choy, and G. Campet, *Chem. Mater.*, **12**, 1818 (2000).
10. Y. Shao-Horn, S. A. Hackney, A. R. Armstrong, P. G. Bruce, R. Gitzendanner, C. S. Johnson, and M. M. Thackeray, *J. Electrochem. Soc.*, **146**, 2404 (1999).
11. Y. I. Jang, B. Huang, H. Wang, D. R. Sadoway, and Y. M. Chiang, *J. Electrochem. Soc.*, **146**, 3217 (1999).
12. L. Croguennec, P. Deniard, and R. Brec, *J. Electrochem. Soc.*, **144**, 3323 (1997).
13. P. G. Bruce, A. R. Armstrong, and R. L. Gitzendanner, *J. Mater. Chem.*, **9**, 193 (1999).
14. I. M. Kotschau and J. R. Dahn, *J. Electrochem. Soc.*, **145**, 2672 (1998).
15. M. Inaba, Y. Iriyama, Z. Ogumi, Y. Todzuka, and A. Tasaka, *J. Raman Spectrosc.*, **28**, 613 (1997).
16. B. Ammundsen, G. R. Burns, M. S. Islam, H. Kanoh, and J. Rozière, *J. Phys. Chem. B*, **103**, 5175 (1999).
17. W. Huang and R. Trech, *J. Power Sources*, **81-82**, 616 (1999).
18. H. Kanoh, W. Tang, and K. Ooi, *Electrochem. Solid-State Lett.*, **1**, 17 (1998).
19. K. S. Han, S. W. Song, T. Watanabe, and M. Yoshimura, *Electrochem. Solid-State Lett.*, **2**, 63 (1999).
20. E. Zhecheva and R. Stoyanova, *Solid State Ionics*, **66**, 143 (1993).
21. S. J. Hwang, H. S. Park, J. H. Choy, and G. Campet, *J. Phys. Chem. B*, **105**, 335 (2001).
22. S. J. Hwang *et al.*, To be published.
23. J. Arsene, A. Erb, and M. Lenglet, *Ann. Chim. Fr.*, **6**, 399 (1981).
24. Y. I. Jang, B. Huang, Y. M. Chiang, and D. R. Sadoway, *Electrochem. Solid-State Lett.*, **1**, 13 (1998).

ELSEVIER

International Journal of Inorganic Materials 3 (2001) 211–214

International Journal of Inorganic Materials

# A new single molecular precursor route to fluorine-doped nanocrystalline tin oxide anodes for lithium batteries

C.W. Kwon[a], G. Campet[a,*], J. Portier[a], A. Poquet[a], L. Fournès[a], C. Labrugère[a], B. Jousseaume[b], T. Toupance[b], J.H. Choy[c], M.A. Subramanian[d]

[a]*Institut de Chimie de la Matière Condensée de Bordeaux (ICMCB), CNRS. 87 Avenue du Docteur A. Schweitzer, 33608 Pessac Cedex, France*
[b]*Laboratoire de Chimie Organique et Organométallique. Université Bordeaux I, 351 Cours de la Libération, 33405 Talence Cedex, France*
[c]*National Nanohybrid Materials Laboratory (NNML), School of Chemistry and Molecular Engineering, Seoul National University, Seoul 151-742, South Korea*
[d]*Dupont Company, Central Research and Development, P.O. Box 80328, Experimental Station, Wilmington, DE 19880-0328, USA*

Accepted 9 November 2000

**Abstract**

A fluorine-doped nanocrystalline tin oxide has been prepared by thermolysis of xerosol derived from a single molecular precursor. A fluorine to tin atomic ratio, as high as 0.14, was estimated from the results of elemental analysis. The oxidation state of Sn and conducting properties were determined by Mössbauer spectroscopy and resistivity measurements. According to the electrochemical experiments, a reversible capacity up to ~800 mAh/g has been achieved. 

*Keywords:* Tin oxide; Lithium battery; Fluorine doping; Electrochemistry

## 1. Introduction

Tin oxide is a well-known host material for lithium insertion and extraction. Its electrochemical behavior in non-aqueous electrolytes has been studied from the view point of electrochromism [1]. Recently, it has been reported that several tin oxide-based compounds can be used as anodes for lithium-ion batteries [2–7]. The common feature between them is that Li irreversibly decomposes the Sn oxides into metallic tin and then a subsequent Li–Sn alloy is formed [3,4]. The second reaction is reversible, leading to a high capacity of about 600 mAh/g. However, the reversible capacity varies severely depending on the synthetic condition and sample state [4–7]. A plausible explanation might be the enormous volume change during Li–Sn alloy formation, inducing large local stress and inhomogeneity, deteriorating the mechanical stability of the electrode [3,8]. In this respect, it is worthwhile to note that, generally, nanocrystalline or/and more conductive (doped) tin oxide powders have larger reversible capacities than well crystallized and undoped ones [4–7].

The way of enhancing the conductivity and electrochemical reversibility by doping Cl, Sb, Mo or F into tin oxide is a well-established strategy [5,9–12]. Among these dopants, the fluorine is known to be the most efficient doping agent for tin oxide to achieve the highest electrical conductivity which is ~$5\times10^{3}$ $\Omega^{-1}cm^{-1}$ for an optimum atomic F/Sn ratio of ~3% [13]. Preparation of nanostructured $SnO_2$ and its electrochemical properties have already been reported [4], however, to our knowledge, no investigation has been devoted to the synthesis and electrochemistry of similar F-doped tin oxide, although the enhancement of the conductivity due to F-doping may increase the reversible electrochemical capacity of this kind of materials. Furthermore, until recently, the concept of a single molecular precursor of F-doped $SnO_2$ prepared by the sol–gel route has rarely been investigated. Recently we have reported, for the first time, how to stabilize fluoroalcoxytin complexes, which are ideal precursors for preparing highly conductive F-doped $SnO_2$ nanocrystalline powders [14,15].

*Corresponding author. Tel.: +33-5-5684-6297; fax: +33-5-5684-2761.
*E-mail address:* campet@icmcb.u-bordeaux.fr (G. Campet).

1466-6049/01/$ – see front matter 
PII: S1466-6049(01)00021-6

In this study, we describe the preparation and electrochemical characteristics of nanocrystalline F-doped tin oxide powder, obtained from a mixed-valence fluorotin alkoxide.

## 2. Experimental

The nanocrystalline F-doped $SnO_2$ powder was prepared by the same method as reported in Ref. [15]. The simplified procedure is illustrated in Scheme 1. The thermolysis of xerosol was carried out at first by drying the powder at 50°C, and then calcined at 550°C in air for 15 min. For comparison, commercial $SnO_2$ powder was purchased from Aldrich Chemicals (99.9%).

Elemental analysis was conducted in the Center of Chemical Analysis of the CNRS (Vernaison, France). The crystallinity and structure of the samples were monitored by powder X-ray diffractometer (Phillips PW1820) using Cu Kα radiation ($\lambda$=1.5418 Å). The sample resistivity was estimated as quoted in Ref. [15].

The room temperature Mössbauer resonance spectrum was obtained using a Halder-type spectrometer equipped with a $Ca^{119}SnO_3$ source in the constant acceleration mode. The spectrum thus acquired was fitted to the sum of Lorentzians by least square refinements. All isomer shifts given refer to $CaSnO_3$ at 293 K.

Electrochemical measurements were performed using a computer-controlled potentiostat/galvanostat (Tacussel, PGS 201T). A button-type cell was used with the configuration of Li/1 M $LiClO_4$ in ethylene carbonate (EC)–dimethyl carbonate (DMC) (50:50, v/v)/$SnO_2$ composite electrode. The composite electrodes were prepared either by intimately mixing the active material with carbon black (25 wt.%) and polytetrafluoroethylene (PTFE, 5 wt.%) or by mixing with carbon black (15 wt.%) and ploy vinylidenedifluoride (PVDF, 10 wt.%) and spreading on Cu foil. All measurements and cell assembly were carried out in an argon-filled dry box. The potential range was set between 0 and 2 V vs. Li electrode and the current density was fixed at 20 mA/g in a galvanostatic mode.

## 3. Results and discussion

Fig. 1 shows the X-ray diffraction patterns of the dried xerosol precursor, the nanocrystalline F-doped $SnO_2$ and undoped $SnO_2$ powders. For the dried xerosol precursor, no distinguishable peak appears indicating an amorphous state or/and absence of long-range order. After heat-treatment at 550°C in air, as expected, XRD peaks appear to be broader compared to the well-crystalline Aldrich sample. All the XRD reflections are properly indexed with tetragonal symmetry, and the cell parameters obtained from the least-square fitting analysis are listed in Table 1.

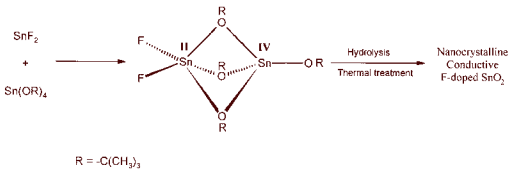


Scheme 1. The simplified synthetic procedure.

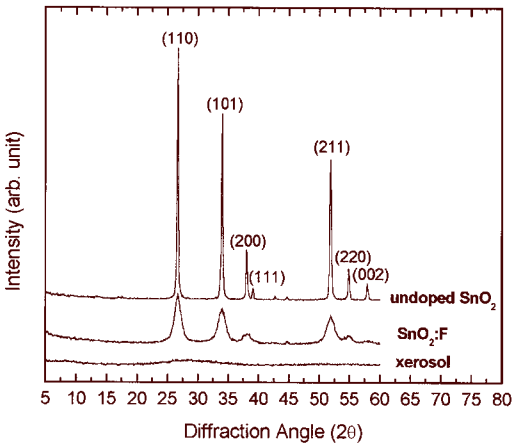


Fig. 1. The X-ray diffraction patterns of the dried xerosol precursor, the nanocrystalline F-doped and well-crystalline undoped (Aldrich) $SnO_2$ powders.

It is evident that the cell parameters become smaller for the F-doped nanocrystalline sample. The size of crystallites was estimated to be 7 nm using Scherrer's relation $t = 0.9\lambda/(B\cos\theta)$ where $\lambda$ is the X-ray wavelength, $\theta$ is the Bragg angle and $B$ is the angular full-width-half-maximum of the chosen ($hkl$) reflection in radian. For the doped sample, the F/Sn ratio of ~0.14, based on the results of elemental analysis, leads to a diminished resistivity of $\rho_s$~0.7 Ω cm, in agreement with Ref. [15]. On the contrary, for the undoped $SnO_2$, the resistivity is higher than $10^5$ Ω cm. At this point, it should be noted that the

Table 1
Elemental analysis, electrical resistivity, crystallite size and cell parameter data of the Aldrich $SnO_2$ and the nanocrystalline F-doped $SnO_2$

| | | Undoped $SnO_2$ | F-doped $SnO_2$ |
|---|---|---|---|
| Elemental analysis (mole ratio) | F/Sn | – | 0.14 |
| | C/Sn | – | <0.04 |
| Electrical resistivity | $\rho_s$(Ω cm) | $>10^5$ | 0.7 |
| Crystallite size | $l$ (nm) | >200 | ~7 |
| Cell parameters | $a$ (Å) | 4.73(8) | 4.69(3) |
| | $c$ (Å) | 3.18(7) | 3.17(6) |

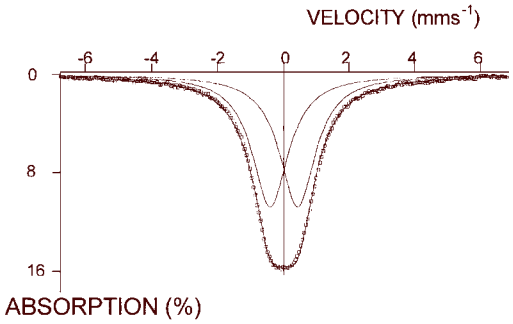


Fig. 2. The $^{119}$Sn Mössbauer spectrum of the F-doped nanocrystalline $SnO_2$ and its Lorentzian fits.

above reported F/Sn ratio of 0.14 is ~5 times higher than the maximum value which can be incorporated into the lattice [13]. It might be that some amorphous (as not detected by XRD) secondary phases exist at the grain boundary such as $Sn^{4+}F_4$ [13].

The oxidation state of tin in the nanocrystalline F-doped $SnO_2$ was determined by Mössbauer spectroscopy at room temperature. The $^{119}$Sn Mössbauer spectrum of the F-doped nanocrystalline $SnO_2$ and its Lorentzian fits are presented in Fig. 2. These spectra show the existence of the $Sn^{4+}$ state only, although this material was prepared by heating a mixed valence precursor [15]. This finding is consistent with the observed low resistivity (0.7 Ω cm), which implies indeed that the F-doping into $SnO_2$ may generate mobile electrons in the conduction band, instead of trapped electrons leading to $Sn^{2+}$ formation ($Sn^{4+} + 2e^- \rightarrow Sn^{2+}$).

Fig. 3 shows the first discharge curves for Li/$SnO_2$ cells. A distinctive plateau at about 1.0 V can be observed for the undoped $SnO_2$ sample, which is due to the initial formation of Sn. In contrast, the plateau is less obvious for the doped nanocrystalline sample. For the voltage region over 1.5 V, the F-doped $SnO_2$ shows a capacity of ~30 mAh/g, which is ~6 times larger than that of the undoped sample (~5 mAh/g). A similar phenomenon was also observed in the case of nanocrystalline $SnO_2$ prepared by the hydrolysis of $SnCl_4$ and heating at various temperatures [4]. As reported previously by our group, in general, a higher insertion voltage can be observed at the same insertion level for a n-type semiconducting electrode with smaller particles; moreover, the potential decreases more smoothly as the lithium-insertion progresses in these kinds of electrodes composed of nanocrystalline materials such as $Li_xSnO_2$, $Li_xTiO_2$, and $Li_xWO_3$ [16–20]. It suggests that a regular and smooth change of Fermi-energy in the electrode without undergoing any significant structural change, owing to the existence of many sub-band gap states between the valence and conduction bands, may be due to surface defects and/or surface dangling bonds [20]. It is worthy to note here that the first discharge capacity (~1800 mAh/g) of the doped sample is larger than the theoretical one (~1490 mAh/g), probably due to the influence of carbon black (25 wt.%). The first two cycling curves of the cells are shown in Fig. 4. The undoped sample shows the reversible capacity of ~600 mAh/g, which corresponds well to the literature values [3–7]. For the F-doped nanocrystalline $SnO_2$, the reversible capacity is close to the expected maximum one (~800 mAh/g) [21]. Thus, it seems that highly conductive nanoparticles may provide a way of forming the Li–Sn alloy more effectively, as they reach the ratio of 22:5 ($Li_{22}Sn_5$) [21]. On the whole, it can be rationalized that a nanocrystalline and conductive matrix facilitates the diffusion of Li and

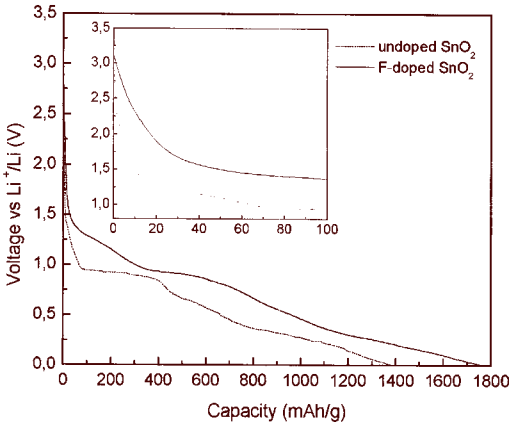


Fig. 3. The discharge curves of Li/$SnO_2$ and Li/F-doped nanocrystalline $SnO_2$ cells.

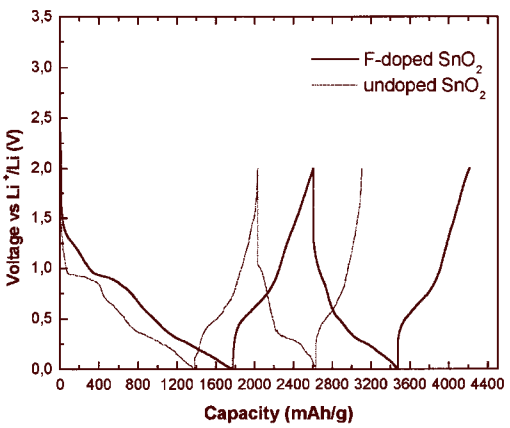


Fig. 4. The first two cycle curves of Li/$SnO_2$ and Li/F-doped nanocrystalline $SnO_2$ cells.

the dispersion of Sn atoms in the electrode and that the formation of an alloy around the Sn atoms occurs more intactly. Even though further systematic investigations should be done on the long term cycling behavior and on the microstructural change induced by the dopage of F, the F-doped nanocrystalline $SnO_2$ reported here is expected to be a promising anode material for Li-ion batteries.

## Acknowledgements

The authors are grateful to DuPont company for financial support. C.W. Kwon is also indebted finantially to the CROUS of Bordeaux (France).

## References

[1] Orel B, Stangar UL, Opara U, Gaberscek M, Kalcher K. J Mater Chem 1995;5:617.
[2] Idota Y, Kubota T, Matsufuji A, Maekawa Y, Miyasaka T. Science 1997;276:1395.
[3] Courtney IA, Dahn JR. J Electrochem Soc 1997;144:2045.
[4] Liu W, Huang X, Wang Z, Li H, Chen L. J Electrochem Soc 1998;145:59.
[5] Morales J, Sánchez L. J Electrochem Soc 1999;146:1640.
[6] Retoux R, Brousse T, Schleich DM. J Electrochem Soc 1999;146:2472.
[7] Nam SC, Kim YH, Cho WI, Cho BW, Chun HS, Yun KS. Electrochem Solid State Lett 1999;2:9.
[8] Yang J, Winter M, Besenhard JO. Solid State Ionics 1996;90:281.
[9] Maruyama T, Tabata K. J Appl Phys 1990;68:4282.
[10] Messad A, Bruneaux J, Cachet H, Bruneaux J. J Mater Sci 1994;29:5095.
[11] Bruneaux J, Cachet H, Froment M, Messad A. Thin Solid Films 1991;197:129.
[12] Bruneaux J, Cachet H, Froment M, Messad A. Electrochim Acta 1994;39:1251.
[13] Geoffroy C. Doctoral thesis, University of Bordeaux, 1990.
[14] Gamard A, Jousseaume B, Toupance T, Campet G. Inorg Chem 1999;38:4671.
[15] Boegeat D, Jousseaume B, Toupance T, Campet G, Fournès L. Inorg Chem 2000;39:3924.
[16] Han SD, Treuil N, Campet G, Portier J, Delmas C, Lassègues JC, Pierre A. In: Rouxel J, Tournoux M, Brec R, editors, Soft chemistry routes to new materials, Materials science forum, Vol. 152–153, Trans Tech Publications, 1994.
[17] Han SD, Campet G, Huang SY, Shastry MCR, Portier J, Lassègues JC, Dweik HS. Active Passive Elec Comp 1995;18:39.
[18] Han SD, Huang SY, Campet G, Pulcinnelli SH, Santilli CV. Active Passive Elec Comp 1995;18:61.
[19] Couput JP, Campet G, Chabagno JM, Bourrel M, Muller D, Garrié R, Delmas C, Morel B, Portier J, Salardenne J. World Patent Number W.O. 9101510, 1991.
[20] Campet G, Wen SJ, Han SD, Shastry MCR, Portier J, Guizard C, Cot L, Xu Y, Salardenne J. Mater Sci Eng 1993;B18:201.
[21] Dunlap RA, Small DA, MacNeil DD, Obrovac MN, Dahn JR. J Alloys Compd 1999;289:135.

# General Conclusion

# *General Conclusion*

To develop novel electrode materials for Li batteries, three kinds of approaches have been performed as follows :

i) lamellar organic-inorganic hybrid materials synthesized by intercalation of monomer of conductive polymer (intercalation strategy)
ii) 3-dimensional transition metal oxide nanoparticles coated by conductive polymer (core-shell strategy)
iii) nanocrystalline materials

First, for the intercalation strategy, we have developped a novel method of inserting PEDOT between the layers of $V_2O_5$ using a soft process of intercalation. The reaction takes place with the *in-situ* polymerization of EDOT within the framework of $V_2O_5$ with different nominal EDOT/$V_2O_5$ ratios. The interlayer distance of $V_2O_5$ expands upon the incorporation of polymer step-by-step, first forming monolayer and then double layers depending on the amount of incorporated polymer. IR spectra suggest the occurrence of $V^{4+}$ centers upon the insertion reaction and a strong interaction between vanadyl group and the incorporated polymer. From the electron microscopy and XRD results, it has been found that the incorporation of PEDOT increases bidimensionality of the $V_2O_5$ host by the layer separation. According to electrochemical measurements, the hybrids showed reversible specific capacities up to ~330 mAh/g at 15 mA/g between 2 ~ 4.4 V vs. $Li^+$/Li. This improvement of

electrochemical performance compared with pristine $V_2O_5$ is attributed to higher electric conductivity and enhanced bidimensionality.

For the second approach, core-shell strategy, PPY/maghemite hybrid was prepared by the polymerization of pyrrole on the surface of maghemite nanoparticles. IR and XRD experiments showed that it was a surface modification keeping the core particles unchanged. From the chemical composition analysis and TEM results, it was found that the polypyrrole partially covers the maghemite particles. Electrochemical measurements showed that the surface modification with polypyrrole not only increases the capacity but also enhances reversibility of maghemite nanoparticles. The hybrid delivers up tp ~ 270 mAh/g between 1.3 ~ 4.3 V vs. $Li^+/Li$.

The last methodology deals with electrochemistry of various nanocrystalline materials, which differs from that of traditional well-crystalline ones due to their significant surface effects. It is proved that they can be profitably used as lithium insertion electrodes *e.g.* to overcome phase transition problem for potassium manganese oxyiodide, to solve conductivity problem by shortening diffusion length for $\gamma$-$Fe_2O_3$, and to facilitate alloy formation with a judicious molecular precursor approach for F-doped $SnO_2$. The above-presented electrochemical grafting concept would be advantageously served for a qualitative comprehension of such “nano-phenomena” occuring at the surface of the nanocrystalline electrodes.

Therefore, these three new approaches suggest a way to design and develop novel kinds of electrode materials.

## RESUME EN FRANÇAIS

Trois voies de recherche ont été explorées, portant sur des matériaux d'electrodes pour batteries au lithium. La première concerne des systèmes hybrides à structure lamellaire, synthétisés par intercalation de polymères conducteurs dans une structure hôte bidimensionnelle de façon à accroître la bidimensionnalité tout en stabilisant la structure. La deuxième porte sur des nanohybrides de type 'core-shell', c'est à dire qui sont constitués de nanoparticules d'oxydes enrobées par des polymères conducteurs. La troisième voie de recherche explore des oxydes nanocristallins originaux dont le comportement électrochimique s'explique en faisant intervenir le greffage réversible des ions lithium sur la surface des nanograins.

## TITRE EN ANGLAIS

Novel electrodes based on hybrid or nanocrystalline materials for lithium batteries

## RESUME EN ANGLAIS

Three different methods were explored on the electrode materials for lithium batteries. The first one is lamellar hybrid system synthesized by intercalation of conductive polymers into layered host structure, which exhibits enhanced bidimensionality and structural stability. The second system is a core-shell-type nanohybrid, composed of oxide nanoparticles coated by conductive polymer. The last strategy investigates nanocrystalline materials, whose electrochemical behaviors may be explained by grafting of lithium ions on the surface of nanograins.

## DISCIPLINE

Sciences chimiques

## MOTS CLES

Lithium battery
Conductive polymer
Intercalation
Polymer coating
Organic–inorganic hybrid
Nanocrystalline material
Electrochemistry
X-ray absorption spectroscopy
X-ray photoelectron spectroscopy

## INTITULE ET ADRESSE DE L'U.F.R. OU DU LABORATOIRE

Institut de Chimie de la Matière Condensée de Bordeaux (I.C.M.C.B.-C.N.R.S.),
87, av. Dr. A. Schweitzer, 33608 Pessac CEDEX, France